Transport signatures of spin-orbit coupling in graphene-based materials

Thesis by

Min-Feng Tu

In Partial Fulfillment of the Requirements for the
Degree of
Doctor of Philosophy

CALIFORNIA INSTITUTE OF TECHNOLOGY
Pasadena, California

2019
Defended Aug 9, 2018

To my father

ACKNOWLEDGEMENTS

I dedicate this thesis to my father, who has been a great support for me throughout my life. Even though he had his own plan for my life and did not know much about being a scientist, he still offered his support and encouragement for me to pursue my goals. Without his kindness and love, it is impossible for me to have ever come to the United States and become a scientist.

My deep gratitude goes to my advisor Jason Alicea for his support, patience, and dedication to my research and career. He provided direction when I struggled and examined my work carefully despite my developing English speaking and writing abilities. I have learned numerous valuable things from our discussions, from his insightful comments, and from his rigor in science. It has been a great privilege to be a student of his.

I acknowledge my collaborators, Roger Mong, Bowen Yang, Jeongwoo Kim, Ruqian Wu, Jing Shi, and Torsten Karzig. It has been a great pleasure to work and learn from them. The development of many of the ideas in this thesis would not have been possible without their hard work. I would like to especially thank Roger for his mentoring, friendship, and humor. I would often come to him with questions and he provided not only a brilliant idea or answer, but also much joy and laughter.

I would also like to thank my family members, fellow physicists, Loly Ekmekjian, roommates, ACT friends, Church friends, snowboarding/climbing friends, and many other friends for their company and support. They have shown me a life outside of physics, explored the beautiful landscapes and diverse cultures of America with me, and encouraged me through the ups and downs of my PhD.

ABSTRACT

Topological materials have been a fastest growing research topic in the recent decade. Out of the numerous new phases proposed and/or discovered, “topological insulators" (TIs) are one of the most promising materials that could lead to further advances in high-performance electronics and to applications in quantum computing. Similar to the ordinary semiconductors, TIs have a bulk gap; yet they host robust edge/surface states which are protected from non-magnetic disorder and interactions while the gap remains open. This feature is a manifestation of the non-trivial topology of TIs, the crucial feature that distinguishes them from ordinary semiconductors. Although the search for more topological materials continues, discovered TI currently are limited by practical difficulties that prevent industrialization.

In this thesis, we study graphene, which is the first proposed TI candidate in the history, and its derivatives. With the intrinsic spin-orbital coupling (SOC) on graphene, one can open a topologically nontrivial band gap at the Dirac cones, although the SOC of the carbon atoms is exceedingly small for topological insulation to be observed in experiments. Many proposals exist to enhance the SOC on graphene by doping with adatoms, changing the functionality of the surface, placing graphene on top of other strong SOC materials, etc. However, few proposed TI signatures have been found experimentally. Furthermore, measuring these intrinsic SOCs through magnetoconductance is challenging due to their relatively weak signatures in transport. This work addresses the challenges in transport measurements from both analytical and numerical approaches on various graphene-based materials.

Graphene’s Dirac band structure and open geometry underlie its exciting prospects for engineering new physics via impurity-induced spin-orbit coupling. As a tantalizing example, previous theory works predicted a robust quantum-spin-Hall phase in graphene covered with dilute heavy adatoms such as In, Tl, and Os, although experiments to date have not detected the required enhancement of spin-orbit coupling. Motivated by these experiments, we explore the consequences of adatom-generated spin-orbit couplings on magneto-transport in graphene. We attack the problem using diagrammatic techniques and the Landauer-Buttiker transport simulation informed by microscopics, and study various coverages, chemical potentials, and disorder types. We find that the induced spin-orbit couplings can contribute to magneto-conductance differently from conventional intrinsic and Rasbha spin-orbit couplings. Our results provide a possible rationale for the absence of spin-orbit signatures in recent experiments, and also highlight a roadmap for their discovery in future work.

In addition to the adatom-dedoped graphene, we also study graphene placing on top of strong SOC substrate, WS_2, by jointing theory, numerics, and experiment. We demonstrate, in experiment, a clear weak anti-localization (WAL) effect arising from induced Rashba spin–orbit coupling (SOC) in WS_2-covered single-layer and bilayer graphene devices. Contrary to the uncovered region of a shared single-layer graphene flake, WAL in WS_2-covered graphene occurs over a wide range of carrier densities on both the electron and hole sides. At high carrier densities, we estimate the Rashba SOC relaxation rate to be $\sim 0.2\,\mathrm{ps}^{-1}$ and show that it can be tuned by transverse electric fields. In addition to the Rashba SOC, we also predict the existence of a 'valley-Zeeman' SOC from first-principles calculations. The interplay between these two SOC's can open a non-topological but interesting gap in graphene; in particular, zigzag boundaries host four sub-gap edge states protected by time-reversal and crystalline symmetries. The graphene/WS_2 system provides a possible platform for these novel edge states.

PUBLISHED CONTENT AND CONTRIBUTIONS

[Intentionally Left Blank]

TABLE OF CONTENTS

LIST OF ILLUSTRATIONS

LIST OF TABLES

Chapter 1

INTRODUCTION

One of the most fast growing research topics in the recent decade is topological materials. Topology is the study of geometric properties that are insensitive to smooth deformation (bending, stretching, etc.). Two topologically distinct objects can not transform into each other without breaking or cutting. A disc, for example, can be bent and smoothed out into a square but it is impossible to deform it into a circle without drilling a hole somewhere. These ideas of topology and geometry inherently manifest themselves in physical phenomena, and in particular, in topological materials.

Two topologically distinct phases of matter cannot be deformed into each other without the breakdown of the adiabaticity (possibly up to symmetry constraints). It is in this sense, phases of matter can be classified by topology in addition to the usual identifiers of symmetry and dimensionality [17]. Out of the numerous new phases, “topological insulators"(TI) are one of the most promising materials which can lead to high-performance electronics and applications in quantum computing [63]. Topological insulators were predicted [25, 39, 40, 52, 58] to exist and confirmed experimentally in HgTe quantum wells and thermo-electric materials Bi_2Se_3 and Bi_2Te_3 [12, 16, 32, 43, 72]. They have an insulating bulk but support robust gapless (i.e. metallic) edge/surface conducting states. In three dimensions, a nice analogy from Charlie Kane is that of a Hershey’s kiss which starts of initially wrapped in aluminum foil. However, in this case, when you cut it Hershey’s kiss in half, it turns into two complete and still-fully-wrapped Hershey’s kisses (which is probably quite annoying if you want to eat it!) There are two striking and important properties of these topological insulators: one is that its surface behavior leads to dissipation-less conduction; the other is that if we induce superconductivity (e.g. by the proximity effect) on the edges of a TI, one can localize exotic electronic excitations known as Majorana modes. These Majorana modes, which are robust against deformations of the Hamiltonian, have non-abelian braiding properties [57] that are useful for topological quantum computing.

The search for more TIs has continued over the past decade. Many 3D TIs have been discovered; numerous 2D TIs theoretical proposals and first-principles calculations [12, 16, 25, 32, 39, 40, 43, 52, 58, 72] existed though many of them are not confirmed experimentally. Two dimensional TIs were first predicted to arise in graphene [39]. However, its topological aspects were not observable due to the extremely weak spin-orbit coupling [7-11], a key ingredient that often promotes topological insulating behavior. Later on, Bernevig *al et.* proposed another 2D TI candidate, the CdTe/HgTe/CdTe quantum well, which inverts the bulk subbands to achieve a topological phase by changing the thickness of HgTe [10]. This proposal was subsequently confirmed by experiments [12]. Other similar proposals for a 2D TI include InAs/GaSb quantum wells [47] and bilayer bismuth [54]. While this milestone experiment confirmed the existence of a 2D TI, the engineering and experimental applications are still limited by many practical difficulties related to this structure. In this regard, graphene has greater industrial and application potential if we can achieve topological phases by enhance its SOC.

Fortunately, the open two-dimensional honeycomb structure of graphene allows tailoring of the SOC strength by coupling to foreign atoms or materials [13, 21, 24, 34, 38, 50, 70]. Several experiments have pursued approaches of graphene hydrogenation [7, 41] or fluorination [31] as well as heavy-adatom decoration [15, 36]; these methods tend to decrease transport quality, and moreover the induced SOC appears to be difficult to reproduce [7, 41] and/or detect [15, 31, 36]. A different approach has recently been employed by several groups: placing graphene on target substrates featuring heavy atoms. Proximity to the substrates not only provides desirable properties such as ferromagnetic ordering and large SOC, but also reduces adverse effects on the target materials [6, 37, 68, 69]. Yet no solid evidence for the signature of 2D TI have been found on these materials, people have explored its applications in multifunctional 2D spintronic devices as in Refs. [18, 27, 49, 74].

In contrast to aforementioned 2D TIs, many existing 3D TIs have been discovered. The first generation was the $Bi_{1-x}Sb_x$ binary alloy ($x = 0.07-0.22$), which, however, has the complicated surface structure and the narrow gap makes further experimental development difficult [32, 46]. The second generation, including Bi_2Se_3, Bi_2Te_3 and Sb_2Te_3 [77], are all hexagonal structures with narrow gaps [5]. The surface states of these TIs have been experimentally observed by angle-resolved photoemission spectroscopy [72]. These TIs are most widely used due to their simple structures and strong TI nature (only one Dirac cone) [33]. Another type of 3D TIs are topological crystalline insulators (TCIs) [48], which have a gapped bulk and a boundary state with spin filter properties protected by mirror symmetry (001) on the surface. This novel topological phase could be achieved on films of SnTe, $\mathrm{Pb}_x\mathrm{Sn}_{1-x}$Se(Te) (001), and $\mathrm{Pb}_{1-x}\mathrm{Sn}_x$Se [45, 55, 59]. The gap of a TCI can be controlled by an electric field which breaks the mirror symmetry. Furthermore, a variety of novel topological phenomena can be observed in TCIs such as Dirac mass generation via ferroelectric distortion and flat band superconductivity. All of the above properties make TCIs a great platform for engineering quantum devices in spintronics. However, for most existing 3D TIs, controlling the Fermi level (e.g., doping) is still quite challenging and although there has been much improvement, the precision has still not reached the levels needed for industrialization [64]. The search for new topological materials and their applications is an ongoing mission.

The purpose of this chapter is to introduce and briefly review the theoretical concepts and phenomenology of topology, topological insulators, and graphene-based TIs. We will also discuss transport tools for measuring TI signatures on graphene and a provide an overview of disorder physics in mesocopic systems. There are a number of excellent topical reviews covering the field in much greater depth than permitted here. The reader is encouraged to consult to Refs. [3, 14, 20, 26, 29, 30, 53, 57] for a much more comprehensive review of the subject.

1.1 Brief introduction of topological phases

In this section, we discuss a simple example: a particle on a ring, showing how *topology* plays a role in condensed matter physics. Next, we will describe the first discovered topological phase - quantum Hall effect (QHE), and define a topological index known as the Chern number. If we adjoin two copies of quantum Hall systems with opposite Chern number and spin, i.e., adjoin two copies that are time-reversal symmetric partners, we obtain a new time-reversal symmetric topological phase—a 2D TI or alternatively known as the quantum spin Hall effect (QSHE). Finally, we focus on how to calculate the corresponding topological number and bulk/edge correspondence.

Motivating example—a particle on a ring

Consider a particle with the moment of inertia I on a ring [1]. As shown in the Fig. 1.1, there is a homogeneous magnetic field B in the center, $r < r_c$, of the ring, but the particle on the ring is experiences no field. We choose the vector potential

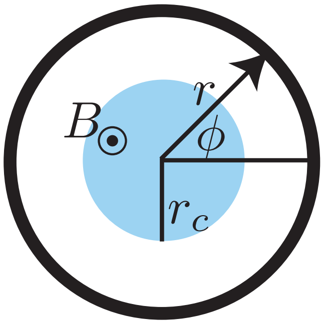

Figure 1.1: The cartoon picture of a particle on a ring.

as $\vec{A} = A\hat{e}_\phi$ with

$$A = \begin{cases} \frac{Br_c^2}{2r} = \frac{\Phi}{2\pi r} & \text{if } r > r_c \\ \frac{Br}{2} & \text{if } r < r_c. \end{cases} \tag{1.1}$$

The corresponding classical action $\mathcal{S}$, Lagrangian $\mathcal{L}_{\text{cl}}$, and Hamiltonian $\mathcal{H}_{\text{cl}}$ of the particle respectively read

$$\mathcal{S}[\phi] = \int dt \mathcal{L}_{\text{cl}}(\phi, \dot{\phi}) = \int dt[p\dot{\phi} - \mathcal{H}_{\text{cl}}(p, \phi)], \tag{1.2a}$$

$$\mathcal{L}_{\text{cl}} = \frac{I}{2}\dot{\phi}^2 + eAr\dot{\phi}, \tag{1.2b}$$

$$\mathcal{H}_{\text{cl}} = \frac{1}{2I}(p - eAr)^2. \tag{1.2c}$$

The angle $\phi(t)$ denotes the angular coordinate of the particle on a ring and $p = \frac{\partial L}{\partial \dot{\phi}}$ denotes the momenta. Although both $\mathcal{L}_{\text{cl}}$ and $\mathcal{H}_{\text{cl}}$ depend on A, the vector potential does not affect the equation of motion

$$I\ddot{\phi} = 0. \tag{1.3}$$

This matches our classical expectation: the electron on the ring experiences no field and hence no force acts upon it. Even with the nontrivial topology of the ring $\phi = \phi + 2\pi$, topology does not matter since we can always think of ϕ as taking real values from $-\infty$ to ∞ and remove A by a simple canonical transformation $p \longrightarrow p + A$. Thus, the gauge of A is not important classically.

Consider now a quantum particle on a ring. The Hamiltonian is similar

$$\mathcal{H}_q = \frac{1}{2I}(-i\hbar\partial_\phi - eAr)^2 \tag{1.4}$$

with the eigenstates and eigen-energies

$$\psi_m = e^{im\phi}, \tag{1.5}$$

$$E_m = \frac{\hbar^2}{2I}(m - \frac{eAr}{\hbar})^2 = \frac{\hbar^2}{2I}(m - \frac{\Phi}{\Phi_0})^2 \tag{1.6}$$

where $m = 0, \pm 1, \pm 2, ...$ and Φ_0 denotes the number of flux quanta $\frac{h}{e}$. Surprisingly, the quantum system is sensitive to A because of the quantization of p. If we try to remove A by making a transformation $\psi \longrightarrow e^{iA\phi}\psi$ and obtain $p \longrightarrow p + A$, the boundary conditions will not match $\psi(\phi + 2\pi) = e^{i2\pi A}\psi(\phi)$. Therefore, A can be removed from H by absorbing it into the boundary conditions, but it is not possible to remove the physical effect of the A term in quantum mechanics by any adiabatic transformation.

The A term is directly associated with the topology of the ring and manifests itself as the topological term in the Lagrangian

$$S_{\text{topo}} = er \int_{t_1}^{t_2} dt A\dot{\phi} = 2\pi er A \frac{\phi_2 - \phi_1}{2\pi} = \theta \frac{\Delta\phi}{2\pi}. \tag{1.7}$$

The phase $\theta = 2\pi er A = h\frac{\Phi}{\Phi_0}$ denotes the change of action whenever the particle travels a full circle around the ring. More specifically, it is the number of flux quanta piercing through the ring which changes the eigen-energy of the system. This type of topological term is also called a topological theta-term. A similar concept is found in the quantum Hall effect.

Integer Quantum Hall effect

In 1879, Edwin Hall performed a magneto-transport experiment with a thin gold leaf in the xy-plane and a fixed magnetic field B_z in the z-direction. He found that the magnetic field altered the charge distribution when the current flows by: while applying the magnetic field perpendicular to the conductor, he found a nonzero voltage difference across the electrical conductor, transverse to the electric current—the *Hall effect*.

We now discuss the theory of the Hall effect and generalize it to the quantum Hall effect. Consider the Hall experiment for a sample in the x, y-plane with magnetic field B_z. In the linear response regime, the conductivity and resistivity tensors defined through $\mathbf{j} = \sigma\mathbf{E}$ and $\mathbf{E} = \rho\mathbf{j}$ respectively are

$$\sigma = \begin{bmatrix} \sigma^{xx} & \sigma^{xy} \\ \sigma^{yx} & \sigma^{yy} \end{bmatrix}, \quad \rho = \begin{bmatrix} \rho^{xx} & \rho^{xy} \\ \rho^{yx} & \rho^{yy} \end{bmatrix}. \tag{1.8}$$

The matrices are related by $\sigma\rho = 1$. The classical Hall experiment shows that the Hall resistivity is proportional to B_z,

$$\rho^{xy} = -\frac{B_z}{ne} \tag{1.9}$$

where n is the density of electrons in the sample. This Hall resistivity equation turns out to be an important diagnostic tool for investigating the carriers of electric current.

In 1980, von Klitzing discovered a *quantized* Hall conductivity of a 2D electron gas (conductor), as opposed to the proportionality to B_z [42, 67] found by Edwin Hall:

$$\rho^{xy} = -\frac{h}{\nu e^2} \tag{1.10}$$

where ν is an integer. Furthermore, the diagonal resistivity ρ^{xx} vanishes at these plateau as shown in the Fig. 1.1. This phenomena cannot be explained classically. One can solve the Hamiltonian of a 2D electron gas under a perpendicular magnetic field, and obtain the so-called Landau energy levels which are highly degenerate with degeneracy

$$N_l \sim \frac{A_0}{2\pi l_B^2} = \frac{\Phi}{\Phi_0}. \tag{1.11}$$

Here Φ is the total magnetic flux, $\Phi_0 = \frac{h}{e}$ is the quantum of flux, and A_0 is the area of the device. The magnetic length $l_B = \sqrt{\frac{\hbar}{m\omega}}$ is defined by the electron mass m and the cyclotron frequency $\omega = eB/m$. In the simplest treatment, we can estimate the total number of electrons of a system with N filled bands as NN_l. Then plugging the electron density $n = \frac{N_l}{A_0}$ into Eq. 1.9, we obtain the QHE resistivity

$$\rho^{xy} = -\frac{B_z}{ne} = -\frac{2\pi l_B^2 B_z}{e}\frac{1}{N} = -\frac{h}{e^2}\frac{1}{N} \tag{1.12}$$

which is the same as Eq. 1.10. However, this approach can not explain why QHE is a universal phenomena even in the presence of disorder and interaction. We will need to look into the Berry curvature.

Chern integer and topology

The QHE is actually a universal phenomena, regardless of the material geometry, disorder, and electron interactions. By analyzing gauge invariance carefully, Thouless *et al.* [65] along with Simon [61] connected the quantized conductivity to Bloch wavefunctions, and showed that the integer in the QHE is the first Chern number.

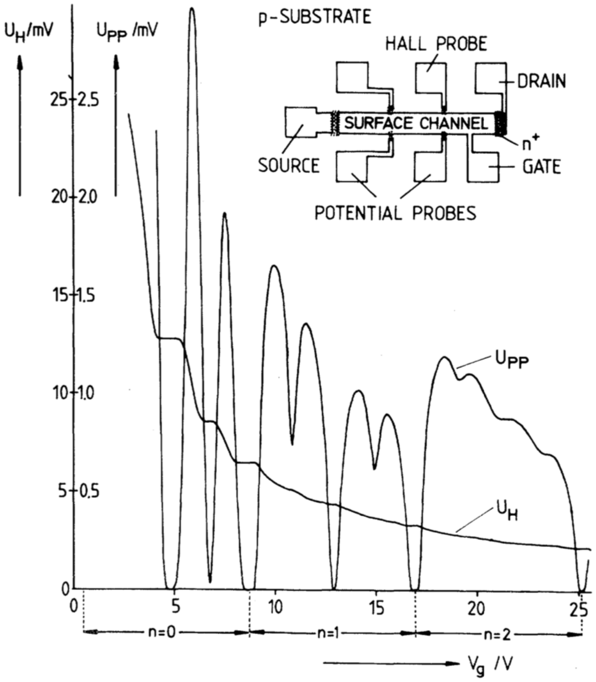

Figure 1.2: Quantum Hall effect taken from Ref. [42]. *This figure is adapted from “New Method for High-Accuracy Determination of the Fine-Structure Constant Based on Quantized Hall Resistance,” by Klitzing, K. v. and Dorda, G. and Pepper, M., 1980, Phys. Rev. Lett., 45, p. 494–497. Copyright 1980 by American Physical Society.*

The Chern number properly distinguishes the gapped phase in the QHE from that of an ordinary insulator.

For electrons in a crystal, the electronic states are described by Bloch wave functions

$$\psi_{n,\mathbf{k}}(\mathbf{r}) = e^{i\mathbf{k}\cdot\mathbf{r}} u_{n,\mathbf{k}}(\mathbf{r}), \quad u_{n,\mathbf{k}}(\mathbf{r}+\mathbf{R}) = u_{n,\mathbf{k}}(\mathbf{r}). \tag{1.13}$$

$\psi_n(\mathbf{r})$ is the quasi-periodic eigenstates of $n-$th band function. Due to the translational symmetry, each Bloch wave function lives on a Brillouin zone which is topologically a torus. The Hall conductivity for a 2D system can be shown in relation to the these eigenstates as,

$$\nu = \frac{h}{e^2}\sigma^{xy} = \sum_{n\in\text{occ.}} \int_{\text{BZ}} \frac{i}{2\pi}(\langle \partial_{k_x} u_{n,\mathbf{k}} | \partial_{k_y} u_{n,\mathbf{k}}\rangle - \langle \partial_{k_y} u_{n,\mathbf{k}} | \partial_{k_x} u_{n,\mathbf{k}}\rangle) dk_x dk_y \tag{1.14}$$

where the n is summed over all occupied bands and the integral is performed over the entire Brillouin zone (BZ). The above, seemingly complicated expression, is nothing but the integral of the gauge-invariant Berry curvature $\mathcal{F}$,

$$\nu = \frac{1}{2\pi} \int_{\mathrm{BZ}} \mathcal{F} d^2\mathbf{k}. \tag{1.15}$$

The Berry curvature is the curl of the Berry gauge field $\mathcal{A} = \sum_{n\in \mathrm{occ}} \langle u_{n,\mathbf{k}} | i\nabla_{\mathbf{k}} | u_{n,\mathbf{k}} \rangle$. From Stoke's theorem, we know that ν is an integral of A over the boundary of the BZ. If $\mathcal{A}$ is continuous, then ν becomes zero and so does the conductivity because a torus (the BZ) has no boundary. Therefore, $\mathcal{A}$ can not be a continuous function in order to agree with experimental results.

Before analyzing discontinuous $\mathcal{A}$, we first consider the wavefunction of the $n-$th energy level. Under a smooth gauge transformation, $u_{n,\mathbf{k}}$ turns to

$$u'_{n,\mathbf{k}} = e^{if(\mathbf{k})} u_{n,\mathbf{k}} \tag{1.16}$$

where $f(k)$ is a smooth function over part of the BZ. The corresponding gauge transformation on Berry potential $\mathcal{A}_n$ is

$$\mathcal{A}'_n = \mathcal{A}_n + \nabla f(k). \tag{1.17}$$

Now since $\mathcal{A}_n$ is not continuous in the BZ (otherwise conductivity is zero), it must be true that we can not find a smooth gauge $f(k)$ at part of the BZ—k_s. Let's now separate the BZ into two parts: one is the regime where the wavefunction ψ_1 is smoothly defined; another one is some small circles $\mathbf{R}_s$ which surround the zeros $\mathbf{k}_s$. In the latter regime, we can pick another phase $g(k)$ for which wavefunction ψ_2 is smoothly defined inside the small circles. At the boundary between these two regimes, the wavefunctions can be connected by

$$\psi_2 = e^{i(g(k)-f(k))}\psi_1 = e^{i\chi(k)}\psi_1 \tag{1.18}$$

and their Berry potentials are related by

$$\mathcal{A}_2 = \mathcal{A}_1 + i\nabla\chi(k). \tag{1.19}$$

Since these two areas share the same boundary, we can plug these two Berry potentials into Eq. 1.14 and further simplify the invariant ν

$$\nu = \frac{1}{2\pi i} \int_{\partial(\mathbf{R}_s)} d\mathbf{k} \cdot i\nabla\chi(\mathbf{k}) = n \tag{1.20}$$

where n is the so-called winding number of the gauge transformation on the boundary of the piecewise definition of the wavefunctions. This number has to be an integer because upon a full revolution around the point $\mathbf{k}_s$, $\chi(\mathbf{k}_s+\varepsilon e^{i2\pi-0^-})-\chi(\mathbf{k}_s+\varepsilon) = 2m\pi$ has to be satisfied. This gauge invariant parameter ν came to be known as the TKNN/Chern number. Because of the quantization of ν, it must be a constant under continuous changes to the system, as long as the number of occupied bands remains fixed (gapped insulator).

In the presence of disorder, the Landau levels will be broadened but the states in the Landau level tails are localized in space, while only states in the center of Landau levels are extended states. These localized states can help us to spot the plateaus. When the chemical potential lies between two Landau level centers, electrons will be localized, not contributing to the conductivity. (Note that there exist some edge states which contribute to the none-zero constant conductivity in this case.) If the chemical potentials lies at the center of a Landau level, the conductivity will move to higher quantized value, since the occupation of the extended states has changed. Also σ^{xx} is non-zero at this transition because the dissipation is no longer suppressed in these extended states.

In the aforementioned paragraph, we mentioned that the conductivity between two centers of Landau levels comes from the edge currents. While the bulk states are localized, these edge states carry a current because of electron drift on the potential gradient. More specifically, each edge state contributes to conductivity $\frac{e^2}{h}$. The edge states are chiral and topologically protected as long as the bulk gap exists. The edge states are perfect 1D conducting channels against impurities and defects because the right- and left-moving currents are spatially separated and hence back-scattering is prohibited. The relation between insulating bulk spectrum and gapless edge states is generally referred to as the “bulk/edge correspondence." This correspondence states that a gapless excitation must exist at the interface between two different topological classes of materials. The bulk gap of a topological class can not smoothly connected to another system with different topology without closing the gap.

The quantum Hall effect may be regarded as the first topological insulator, with the Hall conductivity being a topological response function of the system. One may perturb a quantum Hall system – but as long as the material remains insulating, σ^{xy} is invariant under adiabatic changes to the system. To change the Hall conductivity, the system must pass a singularity in the Berry connection and Bloch functions. When that happens, the band insulators can not continuously deformed from one to another while maintaining a gapped system (since they haver different Chern number); the gap has to close and reopen to make that transition.

Quantum spin Hall effect

The Quantum Hall experiment explicitly breaks time-reversal symmetry by applying an external magnetic field. The Hall conductivity $\sigma^{xy} = j_x/E_y$ is also time-reversal breaking, where j_x is odd under time-reversal but E is even. We wonder whether it is possible to realize a TI which respects to the time-reversal symmetry.

In 2005, Kane and Mele proposed a time-reversal symmetric topological insulator by combining two copies of the QH system with opposite Chern numbers and spin [39]. These two copies are connected by time reversal symmetry. This type of TI is based on graphene with $z \to -z$ inversion symmetric spin-orbital coupling (SOC), i.e. the so-called intrinsic SOC or Kane-Mele SOC as shown in Fig. 1.3. Since s_z is still a good quantum number, we can split the Hamiltonian of graphene into two copies — spin up and spin down. The SOC for the spin up copy acts like a positive out-of-plane magnetic field and turns half of the system into a $\nu_\uparrow = 1$ QH state. Similarly, the SOC for the spin down copy serves as a negative out-of-plane magnetic field, and makes another QH with $\nu_\downarrow = -1$. Finally the SOC opens a gap in the band diagram, which turns out to also be topologically nontrivial yielding a quantized spin Hall conductivity $\sigma_s^{xy} = e/2h$. This state is a $\mathbb{Z}$ topologically trivial state since $\nu_\downarrow + \nu_\uparrow = 0$; however, it belongs to another topologically nontrivial class: $\mathbb{Z}_2$. The edges of the system host two helical edge states, like two copies of chiral edge currents of QHE stacked on each other but traveling with opposite chirality. This phenomenon is called quantum spin Hall effect (QSHE).

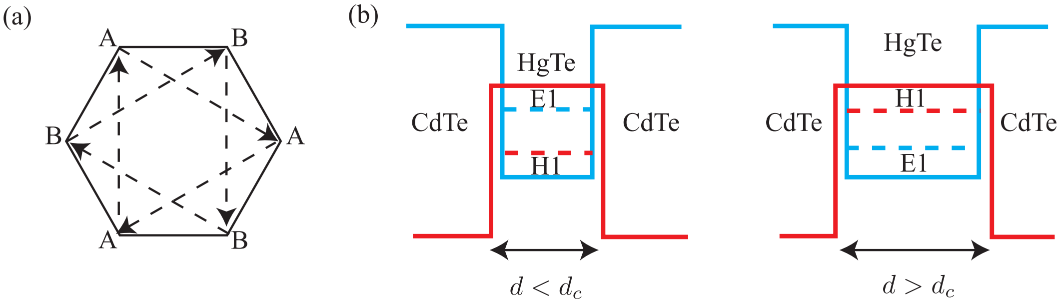

Figure 1.3: Microscopic model for Quantum spin Hall effect on (a) graphene and (b) quantum wells. The Kane-Mele model consists of a hopping term between nearest-neighbor with coefficient t_2. The dashed arrows are of the form $-it_2\sigma_z$ for spin-up, where t_2 is the second nearest-neighbor hopping amplitude. (Hopping against dashed arrow is $it_2\sigma_z$.) The hopping term for spin down is the same with inverted sign.

It was soon realized that the SOC of carbon atoms is exceedingly small for the QSHE being observed in experiments on graphene. Bernevig *et al.* [10] suggested a possible realization of a 2D topological insulator involving HgTe sandwiched between CdTe layers to create a 2D quantum well, which was soon confirmed by König *et al.* [43] in an experiment. Instead of opening the topological gap by bringing in SOC into the system, they open the topological gap by tuning the width of the sample and engineer the QSH phase via band inversion on strong SOC materials, which is a generic and common way to realize many TIs.

The quantum well is composed of barrier material-CdTe, which is a normal semiconductor with Γ_6 s-type band lying above the Γ_8 p-type one, and the well material-HgTe having inverted bands with Γ_8 p-type band lying above the Γ_6 s-type band as shown in the Fig. 1.3. Considering the SOC, these bands can be grouped into three subband states $E1$, $H1$, $L1$, where only the first two are relevant near the Fermi level. These two subbands states have the opposite parity- $E1$ has $m_J = \pm\frac{1}{2}$ and $H1$ has $m_J = \pm\frac{3}{2}$; the Hamiltonian constructed by these states reads

$$H_{\text{eff}}(k_x, k_y) = \begin{bmatrix} H(\mathbf{k}) & 0 \\ 0 & H^*(-\mathbf{k}) \end{bmatrix}, \quad H(\mathbf{k}) = \varepsilon(\mathbf{k}) + d_i\sigma_i, \tag{1.21}$$

where σ_i are the Pauli matrices. By the symmetry constraints, each Hamiltonian block to the lowest order in k can be expanded in the following form:

$$\begin{aligned} d_1 + id_2 &= A(k_x + ik_y) = Ak_+, \\ d_3 &= M - B(k_x^2 + k_y^2), \\ \varepsilon_k &= C - D(k_x^2 + k_y^2), \end{aligned} \tag{1.22}$$

where A, M, C, and D are determined by the microscopic models for specific materials. The Hall conductance for each subblock is

$$\sigma^{xy} = -\frac{1}{8\pi^2} \int d\mathbf{k}(\hat{\mathbf{d}}) \cdot \left(\partial_x(\hat{\mathbf{d}}) \times \partial_y(\hat{\mathbf{d}})\right) \tag{1.23}$$

in e^2/h. Interesting, one can easily change the parameters A, M, C, and D by modifying the width of the well material d, and there is a transition point $d = d_c$ across which the Hall conductance is changed by $2e^2/h$ and the number of pairs of helical edge states is changed by 1. For thickness $d < d_c$, the bands are still dominated by CdTe and the quantum well is in the normal phase; for $d > d_c$, the HgTe is thick enough to invert the bands, leading to the topological phase.

With a six-terminal transport probe, experimentalists measured the quantized conductance e^2/h for each edge of the system, thereby confirming the helical edge nature of the QSH insulator. The details of the experiments are presented in Refs. [43, 44].

$\mathbb{Z}_2$ invariant and bulk-edge correspondance

The quantum spin Hall effect is the so-called 2D $\mathbb{Z}_2$ topological insulator. Systems under time-reversal symmetry are characterized by the $\mathbb{Z}_2$ topological numbers. By time-reversal symmetry T, the Bloch wavefunctions $u_{n,\mathbf{k}}$ and $Tu_{n,\mathbf{k}}$ are degenerate and orthogonal to each other. Built from the matrix of overlaps of the ith eigenstate with the time reversal of the jth eigenstate $w_{mn}(\mathbf{k}) = \langle u_{m,\mathbf{k}}|\Theta|u_{n,-\mathbf{k}}\rangle$, we can define the $\mathbb{Z}_2$ invariant as

$$\delta_a = \mathrm{Pf}[w(\Lambda_a)]/\sqrt{\mathrm{Det}[w(\Lambda_a)]} = \pm 1 \tag{1.24}$$

where $\mathrm{Ph}[w(\Lambda_a)]$ is the Pfaffian of the matrix $w(\Lambda_a)$. Then the $\mathbb{Z}_2$ invariant ν is defined by

$$(-1)^\nu = \prod_{a=1}^{4} \delta_a. \tag{1.25}$$

Here a is one of the four special points Λ_a in the bulk of 2D BZ where $\mathbf{k}$ and $-\mathbf{k}$ differ by a reciprocal lattice vector. Note that this simple approach is only valid in the presence of the additional symmetry-inversion symmetry. There are also other approaches for general systems as shown in Refs. [22, 60, 62]. The calculation of this number becomes a nice indicator either analytically or numerically of confirming a certain structure of materials being TIs.

The QSH states (or 2D TI) have *gapless edge modes* by the bulk-boundary correspondence. For a gapped 2D TI state, there is always an odd number of Kramers pair (time-reversal polarization) edge states traveling in the opposite direction. Kramers pair are related by time reversal symmetry; the same symmetry also prevents electrons in one edge state from backscattering into its Kramers partner [4, 8, 73]. This protection yields a TI phase robust against most disorder, except for magnetic impurities that break time reversal symmetry. For more details, we refer the readers to Ref. [29].

1.2 Gaphene-based topological insulators

Though QSHE was already realized in the quantum well structure, many experimental activities on the QSHE effect are still limited by some practical difficulties. On the contrary, the open surface, high conductivity, and easy fabrication makes graphene more amendable for experimental and industrial investigation. The only lacking ingredient in engineering QSHE on graphene is strong SOC, especially the intrinsic SOC. In this spirit, many proposals exist to enhance SOC on graphene by doping adatoms, changing functionality of the surface, placing graphene on top of other strong SOC materials, etc.[13, 21, 24, 34, 38, 50, 70, 75, 76]. In this section, we establish a mathematical setup to study this problem, and clarify all the notations which will be used in the following chapters.

Graphene

Graphene is made of carbon atoms distributed at the edges of hexagons as shown in the figure (a) of Table 1.2. Carbon is a light element with outer shell $2p$ orbitals, specifically $2p_z$ orbitals (or π states). Electrons in the $2p_z$ state can hop easily between neighboring atoms. The Dirac physics of graphene relies on this hopping process in graphene. To describe this system, we define the creation operator $c^\dagger_{\mathbf{r}}$ which adds an electron to a p_z orbital at site r, and construct the minimum Hamiltonian H in real space with a tight binding model,

$$H = \sum_{\langle \mathbf{r},\mathbf{r}' \rangle} (c^\dagger_{\mathbf{r}} c_{\mathbf{r}'} + h.c.) \tag{1.26}$$

where t is the hopping amplitude. Here and below, spin indices are implicitly summed whenever suppressed. The honeycomb lattice is viewed as a Bravais lattice (triangular) built with unit cells of two atoms, say A and B. Each unit cell is connected via the superposition of two vectors $\mathbf{a}_1$ and $\mathbf{a}_2$ as defined in Table 1.2.

Performing the Fourier transformation of Eq. (1.26), we obtain the

$$H = \int_{\mathbf{k}} c^\dagger_{\mathbf{k}} \begin{bmatrix} 0 & -tf(\mathbf{k}) \\ -tf^*(\mathbf{k}) & 0 \end{bmatrix} c_{\mathbf{k}} \tag{1.27}$$

with a geometrical factor

$$f(\mathbf{k}) = \sqrt{1 + 4\cos^2(k_x \frac{\sqrt{3}a}{2}) + 4\cos(k_x \frac{\sqrt{3}a}{2})\cos(k_y \frac{3a}{2})}. \tag{1.28}$$

Here $c_{\mathbf{k}}$ is a four-component object with spin and sub-lattices (A, B). The reciprocal lattice of a honeycomb lattice is also a honeycomb with reciprocal lattice vectors $\mathbf{G}_1$ and $\mathbf{G}_2$. The corresponding energy spectrum is simply

$$E(\mathbf{k}) = \pm t|f(\mathbf{k})| \tag{1.29}$$

which contains two Dirac cones with Dirac points $\mathbf{K}$, $\mathbf{K}'$ at zero energy. This energy diagram is especially interesting and important because its low energy excitations follow a linear dispersion, the same as that of the light cone for fundamental electrons. These low energy states are also known as Dirac states—a “relativistic" state.

We now expand Eq. (1.27) around $\mathbf{K}$ and $\mathbf{K}'$ up to the first order in momentum $\mathbf{k}$. The effective low-energy Hamiltonian reduces to the linear model as follows,

$$H_{\text{eff}} = v_F \int_{\mathbf{k}} \psi^\dagger_{\mathbf{k}} (\tau_z \sigma_x \mathbf{k}_x + \sigma_y \mathbf{k}_y) \psi_{\mathbf{k}} \tag{1.30}$$

where $\psi^\dagger_{\mathbf{k}}$ is the low-energy electron creation operator with 8 components,

$$\psi^\dagger_{\mathbf{k}} = (c^\dagger_{\mathbf{K}+\mathbf{k},A,\uparrow}, c^\dagger_{\mathbf{K}+\mathbf{k},A,\downarrow}, c^\dagger_{\mathbf{K}+\mathbf{k},B,\uparrow}, c^\dagger_{\mathbf{K}+\mathbf{k},B,\downarrow}, c^\dagger_{\mathbf{K}'+\mathbf{k},A,\uparrow}, c^\dagger_{\mathbf{K}'+\mathbf{k},A,\downarrow}, c^\dagger_{\mathbf{K}'+\mathbf{k},B,\uparrow}, c^\dagger_{\mathbf{K}'+\mathbf{k},B,\downarrow}). \tag{1.31}$$

Here τ is the Pauli matrix for valleys $(\mathbf{K}, \mathbf{K}')$, σ is for sub-lattices (A, B), and $v_F = \frac{3}{2}at \sim 10^6$ m/s is the Fermi velocity. The spin states $(\uparrow, \downarrow)$ and its corresponding Pauli matrices $s_{x,y,z}$ will be used later in a spin-dependent Hamiltonian. The corresponding energy dispersion reads

$$E^{\pm} = \pm\hbar v_F |\mathbf{k}|. \tag{1.32}$$

The *Dirac Hamiltonian* of graphene gives an experimentally accessible system in which to study relativistic physics. For more interesting properties of graphene, we refer the readers to Refs. [14, 19].

(a) real space

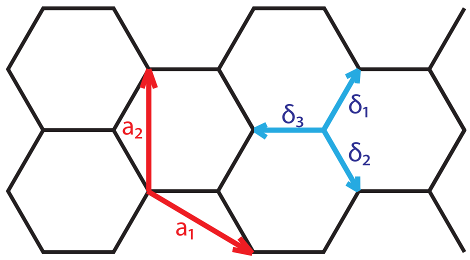

(b) momentum space

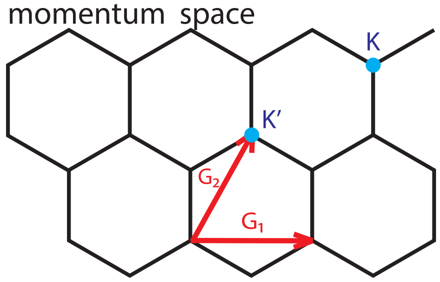

- Lattice spacing a.
- $\vec{a}_1 = (\frac{3}{2}a, -\frac{\sqrt{3}}{2}a)$, $\vec{a}_2 = (0, \sqrt{3}a)$
- $\vec{\delta}_1 = (\frac{a}{2}, \frac{\sqrt{3}}{2}a)$, $\vec{\delta}_2 = (\frac{a}{2}, -\frac{\sqrt{3}}{2}a)$, $\vec{\delta}_3 = (-a, 0)$
- $G_1 = \frac{4\pi}{3a}(1, 0)$, $G_2 = \frac{4\pi}{3a}(\frac{1}{2}, \frac{\sqrt{3}}{2})$
- Dirac point $K = \frac{4\pi}{3a}(\frac{1}{2}, \frac{1}{2\sqrt{3}})$, $K' = -K$
- energy $\epsilon_{\pm} = \pm t\sqrt{3 + 2\cos\sqrt{3}k_y a + 4\cos\frac{3}{2}k_x a \cos\frac{\sqrt{3}}{2}k_y a}$

Quantum spin Hall effect on graphene

Before discussing the QSHE on graphene, it is useful to start by introducing the Chern insulator (a.k.a. Haldane model) on the honeycomb lattice which is historically the first topological insulator without a magnetic field. Haldane wanted to mimic an integer QHE on graphene in the absence of external magnetic field [28]. He realized that the crucial ingredient for topological insulation that the magnetic field provided was time-reversal symmetry breaking. Following this insight, he engineered a system which breaks time-reversal symmetry, but which has no net magnetic flux per unit cell, by introducing a magnetic phase ϕ on the next-nearest-neighbor hopping amplitude. The Hamiltonian reads

$$H = -t \sum_{\langle \mathbf{r},\mathbf{r}' \rangle} c^\dagger_{\mathbf{r}} c_{\mathbf{r}'} + t_2 \sum_{\langle\langle \mathbf{r},\mathbf{r}' \rangle\rangle} e^{-i\nu_{\mathbf{r}\mathbf{r}'}\phi} c^\dagger_{\mathbf{r}} c_{\mathbf{r}'} + M \sum_{\mathbf{r}} \epsilon_{\mathbf{r}} c^\dagger_{\mathbf{r}} c_{\mathbf{r}} \tag{1.33}$$

where the parameter $\epsilon_{\mathbf{r}} = \pm 1$ depends on $\mathbf{r} = A$ or B sublattice, t_2 is the next-nearest neighbor hopping energy, and M is an on-site inversion symmetry-breaking term (mass term). The sign of the phase in next-nearest neighbor hopping amplitude is determined by the hopping direction $\nu_{\mathbf{r}\mathbf{r}'} = \mathrm{sign}(\hat{d}_{\mathbf{r}} \times \hat{d}_{\mathbf{r}'})_z = \pm 1$ where $\hat{d}_i$ is the position relative the center of each hexagon: $\mathbf{r} - \mathbf{r}_\mathrm{c}$. The t_2 term and mass M term break the time-reversal symmetry and the inversion symmetry respectively. Both open a band gap but as we will see later, these two band gaps have different topological nature.

To get the band structure, we derive the corresponding low energy Hamiltonian $H = \int_{\mathbf{k}} c^\dagger_{\mathbf{k}} h(\mathbf{k}) c_{\mathbf{k}}$ at Dirac cones with

$$h(\mathbf{k}) = \varepsilon(\mathbf{k}) + d_i(\mathbf{k})\sigma_i \tag{1.34}$$

where

$$\begin{aligned} \varepsilon(\mathbf{k}) &= -3t_2 \cos(\phi) \\ d_x(\mathbf{k}) &= \frac{3}{2} t\tau k_x \\ d_y(\mathbf{k}) &= \frac{3}{2} t k_y \\ d_z(\mathbf{k}) &= M - 3\sqrt{3} t_2 \sin(\phi)\tau \end{aligned} \tag{1.35}$$

where $\tau = 1$ corresponds to Dirac point $\mathbf{K}$ and $\tau = -1$ to $\mathbf{K}'$. The corresponding Hall conductance of the above Hamiltonian depends on the details of the parameters, especially M and ϕ. Without loss of generality, we assume $0 < \phi < \pi$), $t_2 > 0$. In the case of $M \gg t_2$, the system is dominated by the mass term and opens a topologically trivial gap with wavefunctions localizing on the A or B sites. If we lower M, the $\mathbf{K}'$ Dirac fermion goes through a gap-closing and reopening transition at

$$M = 3\sqrt{3} t_2 \sin\phi. \tag{1.36}$$

In the mean time, the Hall conductance from $\mathbf{K}'$ cone changes from $-\frac{e^2}{2h}$ to $\frac{e^2}{2h}$ with a change of $\frac{e^2}{h}$, while the gap at $\mathbf{K}'$ stays open all the time. If we keep lowering M, the $\mathbf{K}$ Dirac fermion also goes through a gap-closing and reopening transition at

$$M = -3\sqrt{3}t_2 \sin\phi \tag{1.37}$$

with a change in Hall conductance of $-\frac{e^2}{h}$, while point $\mathbf{K}'$ remains gapped. Beyond this point, the phase is trivially insulating again, and is smoothly connected to the $M = -\infty$ phase. The phase diagram of Haldane model is summarized in the Fig. 1.2.

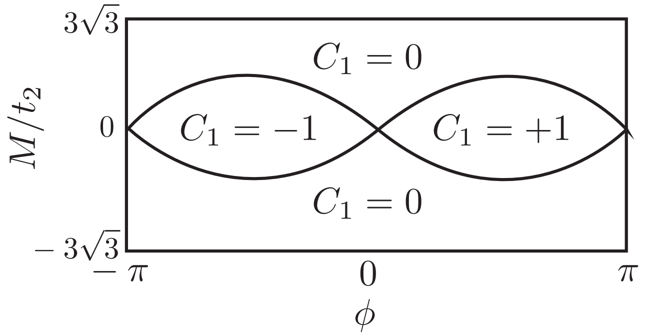

Figure 1.4: Phases of the Haldane model characterized by the first Chern number C_1.

One may wonder: is breaking time-reversal symmetry the only way to realize a topological phase? Kane and Mele answered no to the above question with intrinsic spin-orbital coupling $\tau_z\sigma_z s_z$ [39]. The idea is that, by adding a spin degree of freedom, one can stack two Haldane models together and realize another topological state while preserving TR symmetry. The full tight binding model of proposed Hamiltonian reads

$$H = -t \sum_{\langle i,j\rangle} c_i^\dagger c_j + i\lambda_{so} \sum_{\langle\langle i,j\rangle\rangle} e^{i\nu_{ij}} c_i^\dagger s_z c_j, \tag{1.38}$$

where ν_{ij} are the bonds as in the Haldane model. The new SOC term respects TR symmetry. In the low energy limit, the intrinsic SOC can be written as

$$H_{\text{so}} = \Delta_{so} \int_{\mathbf{k}} c_{\mathbf{k}}^\dagger \left[\tau_z\sigma_z s_z\right] c_{\mathbf{k}}, \quad \Delta_{so} = 3\sqrt{3}\lambda_{so}. \tag{1.39}$$

As shown in the Fig. 1.5, the corresponding bulk energy spectrum has a gap at the Dirac points with a pair of counter-propagating edge modes on a graphene strip with open boundary conditions: spin up current goes counter-clockwise while spin down current goes clockwise. These two edge modes cross at a TR-invariant point; the crossing is protected by TR symmetry and cannot be absorbed into the bulk (unless the symmetry is broken). This state is not the same $\mathbb{Z}$ topological state as in the Haldane model since its charge Hall conductivity is 0; however, it can be shown to be a $\mathbb{Z}_2$ topological insulator - also QSHE- in Ref. [40], of which the derivation will not be repeated here. This topological state is robust against weak interactions and disorder (but preserving TR), but can be destroyed by magnetic impurities or any term which breaks TR symmetry.

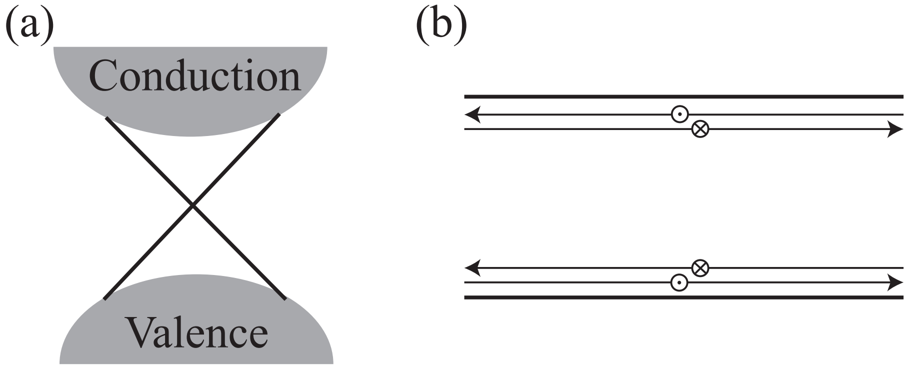

Figure 1.5: (a) A cartoon phase diagram with edge states for Kane-Mele model. (b) The edge states in real space.

The above model is the simplest model for a 2D TI on graphene, of which the spin s_z is still a good quantum number. However, the actual atomic SOC arises from $\nabla V(\mathbf{r}) \times \mathbf{p} \cdot \sigma$ which includes a spin-conserving term s_z and/or a spin-flipping term $s_{x,y}$, especially the latter one is a common spin type in experiments. For example, the Rashba SOC

$$H_R = \lambda_R \int_{\mathbf{k}} c_{\mathbf{k}}^{\dagger} \left[\sigma_x \tau_z s_y - \sigma_y s_x \right] c_{\mathbf{k}}, \quad \Delta_{so} = 3\sqrt{3}\lambda_{so} \tag{1.40}$$

is a common spin-flipping SOC seen in the experiments. It also preserves time reversal symmetry, but breaks the out-of-plane inversion symmetry. Rashba SOC has been found in many experiments [7, 31, 41, 75].

When Rashba SOC and intrinsic SOC appear in graphene together, the s_z quantum number is no longer conserved. One may ask that, if the system can not be separated into spin-up and spin-down copies, does the topology still exist in the presence of

Rashba SOC? To answer this question, we can study graphene with both intrinsic SOC Δ_{so} and Rashba SOC λ_R. When $\lambda_{so} \neq 0$ and $\lambda_R = 0$, the system has a topologically nontrivial gap. If we slowly turn on λ_R, the topological gap slowly decreases as $2(\Delta_{so} - \lambda_R)$. The gap is smaller but the edge states still exist. This suggests that when $\lambda_R < \Delta_{so}$, the system can be smoothly connected to the topological phase of $\lambda_R = 0$. However, since the spin s_z is no longer a good quantum number, the system does not have quantized spin-Hall conductance, but spin still gets pumped. In this case, we say that the system has a quantized TR polarization [39]. When $\lambda_R > \Delta_{so}$, the gap will close and the system becomes a trivial conductor. Note that it is possible to have edge states if the edge is of zig-zag type, but they will not cross the bulk gap and not be robust against disorder.

To sum up, the key ingredient of realizing the QSHE on graphene is SOC, especially the intrinsic SOC. A few adverse factors such as Rashba SOC, strong disorder and interactions, or magnetic impurities would destroy QSH phase. Therefore, one must be very careful in avoiding these factors while coupling graphene to adatoms or other materials to enhance SOC. Combining analytical modeling and DFT, there are many proposals to engineer a 2D TI on graphene, yet no solid evidence such as a gap or quantized edge states have been found so far. More importantly, we do not really have a good tool to tell whether graphene actually inherits these SOCs, especially the intrinsic SOC, from other materials. Common SOC measurements such as spin Hall transport and magneto-conductance have some difficulties in reading intrinsic SOC. More details will be mentioned in the following sections.

1.3 Disordered Mesocopic system

Disorder physics has been investigated for decades and continues to be a rich field of research. In real experiments, disorder is unavoidable, ranging from a few impurities to the strong disorder limit in alloys. Furthermore, disorder is a key ingredient for some interesting physics phenomena such as quantum interference, the topological Anderson insulator, and many-body localization.

In this section, we will briefly describe the disorder-induced metal-to-insulator transition and then specifically focus on the two-dimensional case. Next, we will discuss the microscopic origin of weak-localization/weak anti-localization, quantum interference, and its application in identifying SOC in 2D materials. Lastly, we will talk about 2D mesoscopic systems which are great platforms for observing quantum interference effects and all its related length scales.

Disorder classes

Beginning with a perfect metallic system, we may put disorder in the system either by increasing the number of impurities or by increasing the disorder strength. Depending on the symmetries and the dimensionality of the system, the system may experience a disorder transition, the so called metal-to-insulator phase transition (MIT). By using a one-parameter renormalization group approach, Abrahams *et al.* found that the finite size scaling of the conductance in a metal is different from an insulator [2]:

$$g \sim L^{d-2} \quad \text{when metallic;} \tag{1.41}$$

$$g \sim e^{-2L/\xi} \quad \text{when insulating.} \tag{1.42}$$

Here L^d denotes the system size in $d-$dimension. We can thus define a function β to describe the scaling variable $g(L)$ as

$$\beta(g) = \frac{d \ln g}{d \ln L} \sim \begin{cases} d-2 & \text{when metallic, i.e.} g \rightarrow \infty, \\ \ln g & \text{when insulating, i.e.} g \rightarrow 0. \end{cases} \tag{1.43}$$

From the schematic flow diagram in Fig. 1.3, we observe that there is no MIT for $d < 2$. The system is immediately localized with infinitesimal disorder. On the other hand, there is always a transition point between the metallic and insulating phases for $d > 2$. The $d = 2$ cases is a marginal case. The existence of a MIT further depends on the symmetry (time reversal and spin rotation) and can be categorized into weak localization (with no MIT), weak anti-localization (with MIT), and unitary (marginal case). Therefore, the phenomena of weak-localization (WL) and weak anti-localization (WAL) can be very useful tool to distinguish the symmetry/disorder class of a 2D system.

Weak localization for 2D electron gas

Unlike the strong disorder regime in which the single-particle wavefunctions are exponentially localized at zero temperature, a conductor/semiconductor, in the presence of weak disorder, has single-particle wavefunctions that extend throughout the whole system. Here we will focus on an interesting quantum interference phenomenon on a 2D material with weak disorder.

Consider a metallic system with weak disorder. Naively, we would expect a monotonic decrease in conductance and zero interference effects because the phases of various paths completely are randomized. However, this is not exactly correct. To

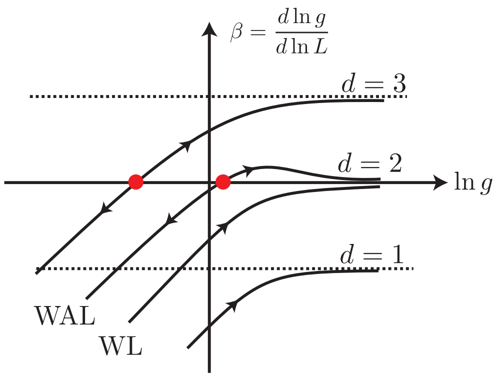

Figure 1.6: Renormalization group flows of the β function for the zero temperature conductance of a disordered system with dimensionality d.

clarify this point, let's focus on a scattering path in which an incident electron in mode m is reflected into mode n with intermediate scattering process $m_1, m_2, \ldots$ with the probability $R(m \longrightarrow n)$. By squaring the sum of all possible Feynman paths connecting the initial and final states, the probability $R(m \longrightarrow n)$ reads

$$\begin{aligned} R(m \longrightarrow n) &= |A_1(m \longrightarrow n) + A_2(m \longrightarrow n) + \ldots|^2 \\ &= \sum_i |A_i|^2 + \sum_{i,j,i \neq j} A_i A_j \end{aligned}$$

where

$$A(m \longrightarrow n) = |A| \exp[i(k_m l_m + k_{m_1} l_{m_1} + k_{m_2} l_{m_2} + \ldots + k_n l_n)]$$

Usually the phases of the various paths are all random and any interference effects cancel out upon averaging yielding $R(m \longrightarrow n) \longrightarrow \sum_i |A_i|^2$. However, this is not the case when the initial and final states are the same. For each such process

$$m \longrightarrow m_1 \longrightarrow m_2 \ldots m_{N-1} \longrightarrow m_N \longrightarrow m,$$

there is a time reversed path which also has the same initial and final states

$$m \longrightarrow m_N \longrightarrow m_{N-1} \ldots m_2 \longrightarrow m_1 \longrightarrow m.$$

The probability of transitioning from m to m state is simply

$$R(m \longrightarrow m) = |(A_1 + A_2 + \ldots) + (A_{1R} + A_{2R} + \ldots)|^2 = |A + A_R|^2 \qquad (1.44)$$

where A is the collection of the paths of $m \longrightarrow m$ and A_R is the time reversal of A. The amplitude of A and A_R are the same but the phases, θ and θ_R, can be different. Therefore, the Eq. (1.44) can be rewritten as

$$R(m \longrightarrow m) = 2|A|^2 + 2|A|^2 \cos(\theta - \theta_R). \tag{1.45}$$

Depending on the phase difference, the system will present different transport behaviors,

$$\begin{aligned} \cos(\theta - \theta_R) &= 0 \longrightarrow \text{incoherent backscattering} \\ \cos(\theta - \theta_R) &= 1 \longrightarrow \text{constructive interference} \\ \cos(\theta - \theta_R) &= -1 \longrightarrow \text{destructive interference.} \end{aligned}$$

If the quantum interference is constructive, electrons tend to localize in the system and the conductivity decreases. This phenomena is the so-called *weak localization* (WL). On the other hand, if the quantum interference is destructive, electrons tend to travel through the system, more than without quantum interference. This phenomena is *weak anti-localization* (WAL). For a spinless particle in 2D, the phases acquired from disorder are the same and this system shows WL behavior.

There are two major features of weak localization. The first is the logarithmic divergence of the resistance at low temperature. However, the same divergence scaling can also be caused by impurity-induced electron-electron interaction. The second feature is magnetoconductance (MC) and can be used to distinguish these two effects. The idea of MC is to alter the phase of the interferences of the self-intersecting paths by applying a magnetic field. The reflection probability becomes

$$R(m \longrightarrow m) = 2|A|^2 + 2|A|^2 \cos(\theta - \theta_R - 2\theta_B) \tag{1.46}$$

where θ_B is the phase induced by magnetic field. Therefore, the MR will oscillate when the magnetic field increases. From the dispersion of the MR at $B = 0$, we can distinguish the type of localization. Near $B = 0$, if the MC increases while B increases, it means that the conductance is suppressed by the interference and the material is weakly localized. On the other hand, if the MC decreases, it suggests that the quantum interference is destructive and the electrons tends to anti-localize.

In conventional spin-independent 2D system, a small amount of disorder cause weak localization. However, Bergman found that we can actually have WAL in 2D by introducing SOC into the system, and this idea was later confirmed by the experiments shown in Fig. 1.7 [9]. Bergman performed a magneto-transport measurement on a Mg film which has little SOC and found increasing MC, suggesting WL. Next, they placed some Au atoms on the film to enhance the SOC and found that the MC decreased gradually and, eventually, turned to negative MC. It showed that SOC can turn a 2D material from WL to WAL. This result is not too surprising. When SOC happens during a back-scattering process, the wavefunction gains an extra phase. Due to the different directions of A and A_R, there exists a 2π phase between A and A_R in the spin degrees of freedom, leading to a minus sign of the wavefunction because of the property of electrons. The drastic change in MC makes MC transport experiments a nice indicator for the existence of SOC for 2D electron gas.

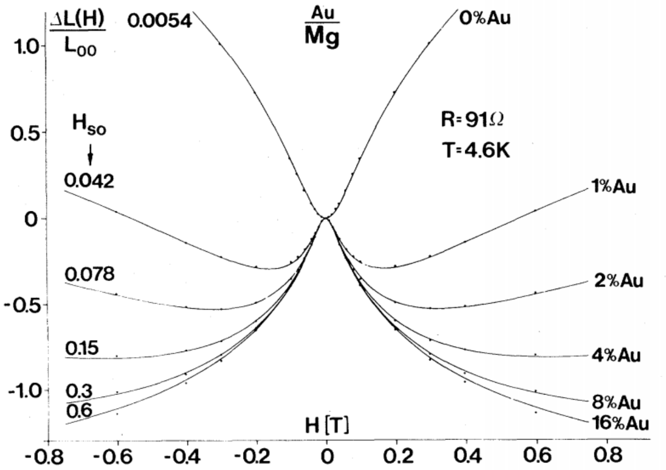

FIG. 1. The magnetoconductance curves of a Mg film (R = 91 Ω) with different coverages of Au. The numbers at the right give the Au coverage of the Mg surface in percent of an atola. The numbers at the left give the adjusted spin-orbit coupling fields. The dots are measured and the full curves are calculated with the theory by Hikami, Larkin, and Nagaoka.

Figure 1.7: The figure is take from Bergman(1982) [9]

It it worth mentioning another perspective for classifying disorder. Wigner and Dyson modeled the statistics of single particle states of non-interacting systems with external disorder potentials by standard Random matrix ensembles [23, 71]. Random matrices for a disordered system can be classified into three distinct invariant ensembles based on symmetries, such as time-reversal (TR) and spin-rotation (S) symmetry. The three ensembles are Gaussian Unitary Ensemble (breaks T), Gaussian Orthogonal Ensemble (respects both T and S), and Gaussian Symplectic Ensemble (respects T, breaks S) as shown in the Table. 1.1. Each of these specifies a disorder class: weak localization and anti-localization are classified according to orthogonal and symplectic ensembles respectively. By examine the symmetry of a 2D Hamiltonian, one can easily tell the WL or WAL disorder class.

Class	Time-reversal	Spin rotation
Orthogonal	✓	✓
Unitary	✗	not applicable
Symplectic	✓	✗

Table 1.1: Classification of the different Random matrix ensembles proposed by Wigner and Dyson.

Weak localization in Graphene

In the low energy graphene physics, a relevant quantity used to characterize the eigen-functions' chirality is defined as the projection of the momentum along the pseudo-spin direction $\mathbf{p} \cdot \sigma$,

$$(\mathbf{p} \cdot \sigma)\psi_{\mathbf{K}}(\mathbf{r}) = \pm\frac{1}{2}\psi_{\mathbf{K}}(\mathbf{r}). \tag{1.47}$$

States around Dirac points can be categorized by chirality: electrons at $\mathbf{K}$ have positive chirality while the holes have negative chirality. The chirality at $\mathbf{K}'$ is the same but with the opposite sign. This chirality is similar to SOC, leading to an extra Berry phase gain in a back-scattering process within the Dirac cone; this phase changes the sign of the amplitude of one path with respect to the time-reversed path and thus graphene with smooth disorder is predicted to exhibit WAL. However, strong inter-valley scattering, which typically arises in ordinary-quality samples, suppresses the chirality-related WAL and generates weak localization (WL) [29, 39]. The whole classification becomes more complicated when spins are included in the system since the interplay of spins, pseudo-spins, valleys, and their corresponding phase become non-trivial.

Imura and McCann have done extensive work on analyzing the localization properties of graphene in the presence of different scattering and SOC mechanisms. Different localization classes are controlled by the number of effective internal degree of freedom, i.e. spin s and pseudo-spin for sub-lattices σ and valleys τ. Imura [35] used a set of effective time-reversal symmetries T_Σ, where $\Sigma = \{\vec{\sigma}\}, \{\vec{\sigma}, \vec{\tau}\}, \{\vec{\sigma}, \vec{s}\}\{\vec{\sigma}, \vec{\tau}, \vec{s}\}$, to categorize the localization behavior for different scattering process as shown in Fig. 1.8. Their explicit forms are given by

$$\begin{aligned} T_{\sigma} &= -i\sigma_y\mathcal{K}, \quad T_{\sigma,\tau} = \tau_x\mathcal{K}, \\ T_{\sigma s} &= (-i\sigma_y)(-is_y)\mathcal{K}, \quad T_{\sigma,\tau,s} = \tau_x(-is_y)\mathcal{K}, \end{aligned} \tag{1.48}$$

where $\mathcal{K}$ is complex conjugation. The Hamiltonian of graphene with spin-independent disorder and Rashba coupling respects all the effective time reversal symmetries. Thus their localization properties are determined by the number of activated spin degrees of freedoms, N_s. One can verify $T_\Sigma^2 = 1$ if N_s is even, and $T_\Sigma^2 = -1$ if N_s is odd. The former (latter) corresponds to the orthogonal (symplectic) class. The Kane-Mele term and mass term σ_z possibly break some effective TRS operators and drive the system to unitary class.

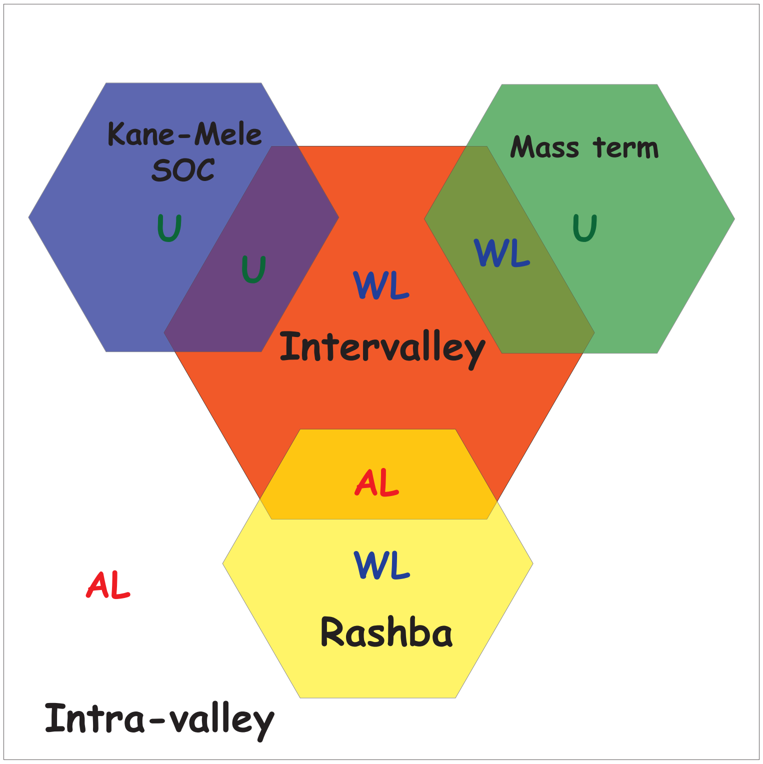

Figure 1.8: Weak localization class diagram of grapheme-based models with different types of the mass and impurity scattering. WL, AL and U refer to weak localization (orthogonal class), weak anti-localization (symplectic class) and absence of WL (unitary class), respectively.

The precise crossover between different regimes depends on the competition of scattering and/or SOC relaxation rates, as shown in Fig. 1.9. By using diagrammatic techniques, McCann analyzed disordered graphene, deriving the weak localization

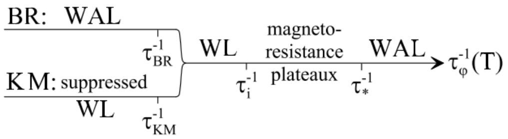

Figure 1.9: The disorder class in monolayer is determined by the magnitude of the inelastic dephasing rate τ_ϕ^{-1} relative to characteristic relaxation rates describing intra-valley symmetry-breaking τ_*^{-1} and inter-valley scattering τ_i^{-1}. The left side shows the expected behavior when the defacing rate is smaller than scattering rates related to either Bychkov-Rashba (BR) or Kane-Mele (KM) spin-orbit coupling

correction to the magneto-conductance [51],

$$\begin{aligned}\Delta\rho(B) =&\frac{e^2\rho^2}{2\pi h}[F(\frac{B}{B_\phi}) - F(\frac{B}{B_\phi + 2B_i}) - 2F(\frac{B}{B_\phi + B_z})\\ &- 2F(\frac{B}{B_\phi + B_{BR} + B_{KM}}) + 2F(\frac{B}{B_\phi + 2B_i + B_{BR} + B_{KM}})\\ &+ 4F(\frac{B}{B_\phi + B_z + B_{BR} + B_{KM}})\\ &- F(\frac{B}{B_\phi + B_{BR}}) + F(\frac{B}{B_\phi + 2B_i + 2B_{BR}}) + 2F(\frac{B}{B_\phi + B_z + 2B_{BR}})] \quad (1.49)\end{aligned}$$

where $B_{\phi,i,z,BR,KM} = (\hbar c/4De)\tau_{\phi,i,z,BR,KM}^{-1}$ with diffusion coefficient $D = v^2\tau_{tr}/2$. The parameters are defined as follows: the transport time $\tau_{tr} = 2\tau_0$, $F(z) = \ln z + \psi(1/2 + 1/z)$, τ_ϕ^{-1} is the inelastic decoherence rate, τ_z^{-1} is the intra-valley scattering rate, τ_i^{-1} is the inter-valley scattering rate. The total elastic scattering rate is $\tau_0^{-1} = \tau_z^{-1} + \tau_i^{-1}$. The Kane-Mele (intrinsic) and Rashba SOC rates are described by τ_{KM}^{-1} and τ_{BR}^{-1} respectively. Here we would like to address the effects of each rate in quantum interference:

1. The decoherence, or dephasing, rate τ_ϕ^{-1} characterizes the suppression of quantum interference. Therefore, the MC change is more significant in a system with smaller decoherence rate.

2. The inter-valley scattering couples two valleys. The system with only intra- and inter-valley scattering is an orthogonal disorder class (WL behavior).

3. Adding Kane-Mele SOC will turn the spin-independent disordered graphene from WAL/WL to the unitary class, which shows suppressed WL in the magneto-transport data. It is challenging to distinguish the unitary class

from WL, because both inelastic scattering and Kane-Mele SOC show the suppressed WL in MC.

4. The Rashba SOC flips WAL to WL or vice versa. It is the most obvious change than the other scattering mechanisms or SOCs.

Due to multiples parameters, it is a challenging task to extract all the relevant rates by fitting the above MC equation to the experimental data. Also, the above equation is only valid under the assumption of only local disorder, $\langle V(x)V(x')\rangle \sim \delta(x-x')$, and no correlation between different disorder types. Therefore, one should be careful in using the above equations to extract SOC rates from experimental MC data.

Relevant length scales

There are a few important length scales in transport in a 2D mesoscopic system: wavelength $\lambda = \frac{2\pi}{k}$, correlation length of the disorder ξ, mean free path l_e, localization length ξ_{loc}, and system size L.

A magnetic field introduces two additional effective length scales into the problem. First, the electron trajectories become curved with the classical cyclotron orbit radius $l_{cyc} = m^* v/eB$, where m^* denotes the electron effective mass. Secondly, the effect of the magnetic field on the phase of the electron wavefunction is characterized by the magnetic length $l_B = [\hbar/eB]^{1/2}$.

Depending on the disorder or SOC details, more related scattering lengths (or rates) are included in the system, such as $l_{\phi,i,z,BR,KM}$ which stands for decoherence length, inter-valley scattering length, intra-valley scattering length, Rashba spin relaxation length, and Kane-Mele (intrinsic) spin relaxation length respectively. In the following, I will explain the physical meaning of each relaxation rate.

1. Fermi wave-vector k_F and Fermi wavelength λ

   The wave-vector $k_F = E_F/\hbar v_F = \frac{2\pi}{\lambda}$ and the associated parameter $(k_F l_e)^{-1}$ characterize the "disorderness" of the system. When $(k_F l_e)^{-1}$ is much greater than 1, it suggests the system is either in the Anderson localization regime or in another subtle regime at the Dirac point, where Boltzmann theory and diagrammatic calculations fail.

2. Decoherence/dephasing rate τ_ϕ^{-1}

Coherence/dephasing time measures how long it takes for an electron to lose its phase coherence through inelastic scattering from, or entanglement with, the environment, e.g., the phonons. For example, we can change the dephasing rate by changing temperature. The dephasing length is defined as $L_\phi = (D\tau_\phi)^{1/2}$ where $D = v_F^2\tau_{\rm tr}/2$ is the diffusion constant and $\tau_{\rm tr}$ is the transport time. In a finite-size system, the L_ϕ is determined by the minimum length of the inelastic scattering length, system size, and magnetic length:[20]

$$L_\phi = \min\{L, L_T, l_B\}. \tag{1.50}$$

Here, L is the system size, L_T is the Thouless length, and l_B is the magnetic length.

3. Intra-valley scattering rate τ_z^{-1} and Inter-valley scattering rate τ_i^{-1}

   The intra-valley and inter-valley scattering together contribute to elastic scattering. With presence of long range disorder, the graphene system has mostly intra-valley scattering. On the other hand, when the disorder is short-ranged (even uncorrelated), large angle scatterings are allowed and the inter-valley scattering would be more important. Both associated scattering rates can be estimated by Fermi's Golden rule.

4. KM relaxation rate τ_{KM}^{-1}

   This spin relaxation term is associated with the homogeneous Kane-Mele (intrinsic) SOC,

$$\Delta_{so}\sigma_z\tau_z s_z. \tag{1.51}$$

One can easily check that s_z is a good quantum number for the graphene+Kane-Mele SOC: $[H, s_z] = 0$ but $s_{x(y)}$ is not. The eigenstates are still eigenstates of s_z, so that the spin up (or down) in z-direction will not relaxed. However, in experiments, the spin can be in other orientation which can be relaxed. To be more precise, let's consider the states in the band structures that are s_x eigenstates, those that are not eigenstates of Hamiltonian. If a collision event with non-magnetic impurities changes the momentum of an electron, it changes the spin as well because the spin orientation associated with the momentum are never mutually parallel. Such a spin changing process is called the "Elliot-Yafet" mechanism and the spin relaxation rate is estimated to be

$$\tau_{KM}^{-1} = \tau_0^{-1}(\frac{\Delta_{so}}{E_F})^2. \tag{1.52}$$

Since the elastic scattering is the main source in flipping spin, the spin relaxation rate is proportional to the elastic scattering rate.

5. Rashba relaxation rate τ_{BR}^{-1}

   When inversion symmetry is broken, homogeneous Rashba SOC will appear and lift the spin degeneracy,

   $$\lambda_R(\sigma_x \tau_z s_y - \sigma_y s_x). \tag{1.53}$$

   None of $s_{x,y,z}$ is a good quantum number in this system (graphene+Rashba SOC). The Rashba SOC induces a more efficient spin relaxation process. Since the conduction energy bands are spilt, the spin of each momentum state will precess as if there is an internal magnetic field for each momentum. Unlike the intrinsic SOC, the spin orientation changes during the precession but the electron loses the rotating information once it is scattered into another state. Thus, the scattering event acts against the spin relaxation in this case, which is also known as D'yakonov-Perel mechaism:

   $$\tau_{BR}^{-1} = 2\tau_0(\frac{\lambda_R}{\hbar})^2. \tag{1.54}$$

   The spin-diffusion length is $l_{BR} = \sqrt{D\tau_{BR}} \sim \frac{\hbar v_F}{\lambda_R}$. The following picture is a summary of the relation between spin relation rate and the elastic scattering rate for the EY and DP mechanisms [11].

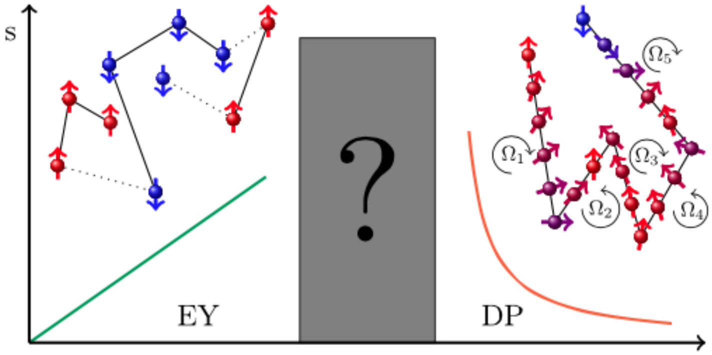

The real spin relaxation mechanism in graphene and its source is still in debate. The above theoretical argument is used by many research works [51, 56], but is not confirmed in experiments yet. First, a wide variety of experiments suggest a linear scaling between τ_s and τ_0 with independence of the carrier concentration. Also, the spin relaxation time is much shorter than expected. These data suggest the failure of the EY mechanism. A more recent experimental paper studying the DP mechanism [66] shows that none of these conventional mechanisms can describe the experimental results of graphene spintronic properties.

Length scale comparison in a MC experiment

In a typical magneto-transport measurement, the length scales at higher carrier density are in the order of

$$L_\varphi > l_{\mathrm{tr}} > \lambda > \xi > a. \tag{1.55}$$

This length scale order describes diffusive mesoscopic system with weak finite-range correlated disorder $k_F l \ll 1$. We will strive to prepare such a system later in our simulation. However, this length scale order is not applicable at low carrier density, where $k_F l \gg 1$. Close to the Dirac points, the carrier density saturates at a non-zero value $\sim 10^{10} - 10^{11} cm^{-2}$ due to inhomogeneities (such as electron-hole puddles.) Another fundamental mystery in graphene transport is the absence of any strong localization-induced insulating phases around the Dirac point, though where $k_F l \ll 1$ due to the infinitesimal k_F at the charge neutrality point. This is a manifest violation of the Ioffe-Reggel criterion which predicts strong localization for $k_F l < 1$. It is conceivable, but does not seem likely, that graphene may go insulating due to strong localization at lower temperatures.

1.4 Overview of the thesis

This thesis focuses on enhancing SOCs on graphene and extracting SOC information by using numerical and analytical methods.

In Chapter 2, we give a detailed derivation of the magneto-conductance for different graphene-based systems by using diagrammatic theory. In Chapter 3 and 4, we discuss the theory of simulating magneto-conductance by using the Landauer-Büttiker formalism, and explore various important factors in the magneto-conductance simulation. In Chapter 5, we study the graphene/WS$_2$ system from experimental, numerical, and analytical perspectives. We find that the SOC on such system is greatly enhanced and discuss the underlying physics mechanisms. In Chapter 6, we study heavy adatom-doped graphene in the hope of engineering a 2D TI by a proximity effect. We propose a way to measure the SOC signatures which are precursor signatures of 2D TI, and confirm this idea both analytically and numerically. Lastly, we summarize our work in Chapter 7.

BIBLIOGRAPHY

[1] Abanov A. *Topology and Condensed Matter Physics*. Springer, Singapore, 2017. doi: 10.1007/978-981-10-6841-6_12.

[2] E. Abrahams, P. W. Anderson, D. C. Licciardello, and T. V. Ramakrishnan. Scaling theory of localization: Absence of quantum diffusion in two dimensions. *Phys. Rev. Lett.*, 42:673–676, Mar 1979. doi: 10.1103/PhysRevLett.42.673.

[3] Eric Akkermans and Gilles Montambaux. *Mesoscopic Physics of Electrons and Photons*. Cambridge University Press, 1 edition, 2007. ISBN 9780521855129.

[4] Tsuneya Ando and Hidekatsu Suzuura. Presence of perfectly conducting channel in metallic carbon nanotubes. *Journal of the Physical Society of Japan*, 71 (11):2753–2760, 2002. doi: 10.1143/JPSJ.71.2753.

[5] Saji Augustine and Elizabeth Mathai. Growth, morphology, and microindentation analysis of bi$_2$se$_3$, bi$_{1.8}$in$_0$.2se$_3$, and bi$_2$se$_{2.8}$te$_{0.2}$ single crystals. *Materials Research Bulletin*, 36(13):2251 – 2261, 2001. ISSN 0025-5408. doi: https://doi.org/10.1016/S0025-5408(01)00717-6.

[6] A. Avsar, J. Y. Tan, T. Taychatanapat, J. Balakrishnan, G.K.W. Koon, Y. Yeo, J. Lahiri, A. Carvalho, A. S. Rodin, E.C.T. O'Farrell, G. Eda, A. H. Castro Neto, and B. Ozyilmaz. Spin-orbit proximity effect in graphene. *Nat Commun*, 5:4875, Sep 2014. doi: 10.1038/ncomms5875.

[7] J. Balakrishnan, G. K. W. Koon, M. Jaiswal, A. H. C. Neto, and B. Colossal Ozyilmaz. enhancement of spin-orbit coupling in weakly hydrogenated graphene. *Nat. Phys.*, 9:284–287, Mar 2013. doi: doi:10.1038/nphys2576.

[8] J H Bardarson. A proof of the kramers degeneracy of transmission eigenvalues from antisymmetry of the scattering matrix. *Journal of Physics A: Mathematical and Theoretical*, 41(40):405203, 2008.

[9] Gerd Bergman. Influence of spin-orbit coupling on weak localization. *Phys. Rev. Lett.*, 48:1046–1049, Apr 1982. doi: 10.1103/PhysRevLett.48.1046.

[10] B. Andrei Bernevig, Taylor L. Hughes, and Shou-Cheng Zhang. Quantum spin hall effect and topological phase transition in hgte quantum wells. *Science*, 314 (5806):1757–1761, 2006. ISSN 0036-8075. doi: 10.1126/science.1133734.

[11] Péter Boross, Balázs Dóra, Annamária Kiss, and Ferenc Simon. A unified theory of spin-relaxation due to spin-orbit coupling in metals and semiconductors. *Scientific Reports*, 3:3233, nov 2013.

[12] B Büttner, C X Liu, , G Tkachov, E G Novik, C Brüne, H Buhmann, E M Hankiewicz, P Recher, B Trauzettel, S C Zhang, and L W Molenkamp. Single valley dirac fermions in zero-gap hgte quantum wells. *Nature Physics*, 7: 418–422, 2011. doi: 10.1038/nphys1914.

[13] A. H. Castro Neto and F. Guinea. Impurity-induced spin-orbit coupling in graphene. *Phys. Rev. Lett.*, 103:026804, Jul 2009. doi: 10.1103/PhysRevLett.103.026804.

[14] A. H. Castro Neto, F. Guinea, N. M. R. Peres, K. S. Novoselov, and A. K. Geim. The electronic properties of graphene. *Rev. Mod. Phys.*, 81:109–162, Jan 2009. doi: 10.1103/RevModPhys.81.109.

[15] U. Chandni, Erik A. Henriksen, and J. P. Eisenstein. Transport in indium-decorated graphene. *Phys. Rev. B*, 91:245402, Jun 2015. doi: 10.1103/PhysRevB.91.245402.

[16] Y. L. Chen, J. G. Analytis, J.-H. Chu, Z. K. Liu, S.-K. Mo, X. L. Qi, H. J. Zhang, D. H. Lu, X. Dai, Z. Fang, S. C. Zhang, I. R. Fisher, Z. Hussain, and Z.-X. Shen. Experimental realization of a three-dimensional topological insulator, bi2te3. *Science*, 325(5937):178–181, 2009. ISSN 0036-8075. doi: 10.1126/science.1173034.

[17] Ching-Kai Chiu, Jeffrey C. Y. Teo, Andreas P. Schnyder, and Shinsei Ryu. Classification of topological quantum matter with symmetries. *Rev. Mod. Phys.*, 88:035005, Aug 2016. doi: 10.1103/RevModPhys.88.035005.

[18] Aron W. Cummings, Jose H. Garcia, Jaroslav Fabian, and Stephan Roche. Giant spin lifetime anisotropy in graphene induced by proximity effects. *Phys. Rev. Lett.*, 119:206601, Nov 2017. doi: 10.1103/PhysRevLett.119.206601.

[19] S. Das Sarma, Shaffique Adam, E. H. Hwang, and Enrico Rossi. Electronic transport in two-dimensional graphene. *Rev. Mod. Phys.*, 83:407–470, May 2011. doi: 10.1103/RevModPhys.83.407.

[20] Supriyo Datta. *Electronic Transport in Mesoscopic Systems*. Cambridge University Press, 3 edition, 1995. ISBN 9780511805776.

[21] Jun Ding, Zhenhua Qiao, Wanxiang Feng, Yugui Yao, and Qian Niu. Engineering quantum anomalous/valley hall states in graphene via metal-atom adsorption: An *ab-initio* study. *Phys. Rev. B*, 84:195444, Nov 2011. doi: 10.1103/PhysRevB.84.195444.

[22] D. P. DiVincenzo and E. J. Mele. Self-consistent effective-mass theory for intralayer screening in graphite intercalation compounds. *Phys. Rev. B*, 29: 1685–1694, Feb 1984. doi: 10.1103/PhysRevB.29.1685.

[23] Freeman J. Dyson. Statistical theory of the energy levels of complex systems. i. *Journal of Mathematical Physics*, 3(1):140–156, 1962. doi: 10.1063/1.1703773.

[24] Aires Ferreira, Tatiana G. Rappoport, Miguel A. Cazalilla, and A. H. Castro Neto. Extrinsic spin hall effect induced by resonant skew scattering in graphene. *Phys. Rev. Lett.*, 112:066601, Feb 2014. doi: 10.1103/PhysRevLett.112.066601.

[25] Liang Fu, C. L. Kane, and E. J. Mele. Topological insulators in three dimensions. *Phys. Rev. Lett.*, 98:106803, Mar 2007. doi: 10.1103/PhysRevLett.98.106803.

[26] A K Geim and K S Novoselov. The rise of graphene. *Nature Materials*, 6:183, mar 2007.

[27] Martin Gmitra and Jaroslav Fabian. Proximity effects in bilayer graphene on monolayer wse$_2$: Field-effect spin valley locking, spin-orbit valve, and spin transistor. *Phys. Rev. Lett.*, 119:146401, Oct 2017. doi: 10.1103/PhysRevLett.119.146401.

[28] F. D. M. Haldane. Model for a quantum hall effect without landau levels: Condensed-matter realization of the "parity anomaly". *Phys. Rev. Lett.*, 61:2015–2018, Oct 1988. doi: 10.1103/PhysRevLett.61.2015.

[29] M. Z. Hasan and C. L. Kane. Colloquium: Topological insulators. *Rev. Mod. Phys.*, 82:3045–3067, Nov 2010. doi: 10.1103/RevModPhys.82.3045.

[30] M. Zahid Hasan and Joel E. Moore. Three-dimensional topological insulators. *Annual Review of Condensed Matter Physics*, 2(1):55–78, 2011. doi: 10.1146/annurev-conmatphys-062910-140432.

[31] X. Hong, S.-H. Cheng, C. Herding, and J. Zhu. Colossal negative magnetoresistance in dilute fluorinated graphene. *Phys. Rev. B*, 83:085410, Feb 2011. doi: 10.1103/PhysRevB.83.085410.

[32] D Hsieh, D Qian, L Wray, Y Xia, Y S Hor, R J Cava, and M Z Hasan. A topological dirac insulator in a quantum spin hall phase. *Nature*, 452(7190):970–4, apr 2008. ISSN 1476-4687. doi: 10.1038/nature06843.

[33] D. Hsieh, Y. Xia, D. Qian, L. Wray, F. Meier, J. H. Dil, J. Osterwalder, L. Patthey, A. V. Fedorov, H. Lin, A. Bansil, D. Grauer, Y. S. Hor, R. J. Cava, and M. Z. Hasan. Observation of time-reversal-protected single-dirac-cone topological-insulator states in bi$_2$te$_3$ and sb$_2$te$_3$. *Phys. Rev. Lett.*, 103:146401, Sep 2009. doi: 10.1103/PhysRevLett.103.146401.

[34] Jun Hu, Jason Alicea, Ruqian Wu, and Marcel Franz. Giant topological insulator gap in graphene with 5d adatoms. *Phys. Rev. Lett.*, 109:266801, Dec 2012. doi: 10.1103/PhysRevLett.109.266801.

[35] K.-I. Imura, Y. Kuramoto, and K. Nomura. Anti-localization of graphene under the substrate electric field. *EPL (Europhysics Letters)*, 89(1):17009, 2010.

[36] Zhenzhao Jia, Baoming Yan, Jingjing Niu, Qi Han, Rui Zhu, Dapeng Yu, and Xiaosong Wu. Transport study of graphene adsorbed with indium adatoms. *Phys. Rev. B*, 91:085411, Feb 2015. doi: 10.1103/PhysRevB.91.085411.

[37] Zilong Jiang, Cui-Zu Chang, Chi Tang, Peng Wei, Jagadeesh S. Moodera, and Jing Shi. Independent tuning of electronic properties and induced ferromagnetism in topological insulators with heterostructure approach. *Nano Letters*, 15(9):5835–5840, 2015. doi: 10.1021/acs.nanolett.5b01905. PMID: 26288309.

[38] Kyung-Hwan Jin and Seung-Hoon Jhi. Proximity-induced giant spin-orbit interaction in epitaxial graphene on a topological insulator. *Phys. Rev. B*, 87: 075442, Feb 2013. doi: 10.1103/PhysRevB.87.075442.

[39] C. L. Kane and E. J. Mele. Quantum spin hall effect in graphene. *Phys. Rev. Lett.*, 95:226801, Nov 2005. doi: 10.1103/PhysRevLett.95.226801.

[40] C. L. Kane and E. J. Mele. Z_2 topological order and the quantum spin hall effect. *Phys. Rev. Lett.*, 95:146802, Sep 2005. doi: 10.1103/PhysRevLett.95.146802.

[41] A. A. Kaverzin and B. J. van Wees. Electron transport nonlocality in monolayer graphene modified with hydrogen silsesquioxane polymerization. *Phys. Rev. B*, 91:165412, Apr 2015. doi: 10.1103/PhysRevB.91.165412.

[42] K. v. Klitzing, G. Dorda, and M. Pepper. New method for high-accuracy determination of the fine-structure constant based on quantized hall resistance. *Phys. Rev. Lett.*, 45:494–497, Aug 1980. doi: 10.1103/PhysRevLett.45.494.

[43] Markus König, Steffen Wiedmann, Christoph Brüne, Andreas Roth, Hartmut Buhmann, Laurens W. Molenkamp, Xiao-Liang Qi, and Shou-Cheng Zhang. Quantum spin hall insulator state in hgte quantum wells. *Science*, 318(5851): 766–770, 2007. ISSN 0036-8075. doi: 10.1126/science.1148047.

[44] Markus König, Hartmut Buhmann, Laurens W. Molenkamp, Taylor Hughes, Chao-Xing Liu, Xiao-Liang Qi, and Shou-Cheng Zhang. The quantum spin hall effect: Theory and experiment. *Journal of the Physical Society of Japan*, 77(3):031007, 2008. doi: 10.1143/JPSJ.77.031007.

[45] Tian Liang, Quinn Gibson, Jun Xiong, Max Hirschberger, Sunada P. Koduvayur, R.J. Cava, and N.P. Ong. Evidence for massive bulk dirac fermions in $\mathrm{pb}_{1-x}\mathrm{sn}_x\mathrm{se}$ from nernst and thermopower experiments. *Nature Communications*, 4:2696, 2013. doi: 10.0.4.14/ncomms3696.

[46] Yu-Ming Lin, O. Rabin, S. B. Cronin, Jackie Y. Ying, and M.S. Dresselhaus. Semimetal-semiconductor transition in $\mathrm{bi}_{1-x}\mathrm{sb}_x$ alloy nanowires and their thermoelectric properties. *Applied Physics Letters*, 81(13):2403–2405, 2002. doi: 10.1063/1.1503873.

[47] Chaoxing Liu, Taylor L. Hughes, Xiao-Liang Qi, Kang Wang, and Shou-Cheng Zhang. Quantum spin hall effect in inverted type-ii semiconductors. *Phys. Rev. Lett.*, 100:236601, Jun 2008. doi: 10.1103/PhysRevLett.100.236601.

[48] Junwei Liu, Timothy H. Hsieh, Peng Wei, Wenhui Duan, Jagadeesh Moodera, and Liang Fu. Spin-filtered edge states with an electrically tunable gap in a two-dimensional topological crystalline insulator. *Nature Materials*, 13:178–183, 2014. doi: 10.0.4.14/nmat3828.

[49] Yunqiu Kelly Luo, Jinsong Xu, Tiancong Zhu, Guanzhong Wu, Elizabeth J. McCormick, Wenbo Zhan, Mahesh R. Neupane, and Roland K. Kawakami. Opto-valleytronic spin injection in monolayer mos2/few-layer graphene hybrid spin valves. *Nano Letters*, 17(6):3877–3883, 2017. doi: 10.1021/acs.nanolett.7b01393. PMID: 28534400.

[50] Dongwei Ma, Zhongyao Li, and Zhongqin Yang. *Carbon*, 50(1):297 – 305, 2012. ISSN 0008-6223. doi: http://dx.doi.org/10.1016/j.carbon.2011.08.055.

[51] Edward McCann and Vladimir I. Fal'ko. $z \to -z$ symmetry of spin-orbit coupling and weak localization in graphene. *Phys. Rev. Lett.*, 108:166606, Apr 2012. doi: 10.1103/PhysRevLett.108.166606.

[52] J. E. Moore and L. Balents. Topological invariants of time-reversal-invariant band structures. *Phys. Rev. B*, 75:121306, Mar 2007. doi: 10.1103/PhysRevB.75.121306.

[53] Joel Moore. The next generation. *Nature Physics*, 5:378, jun 2009.

[54] Shuichi Murakami. Quantum spin hall effect and enhanced magnetic response by spin-orbit coupling. *Phys. Rev. Lett.*, 97:236805, Dec 2006. doi: 10.1103/PhysRevLett.97.236805.

[55] Yoshinori Okada, Maksym Serbyn, Hsin Lin, Daniel Walkup, Wenwen Zhou, Chetan Dhital, Madhab Neupane, Suyang Xu, Yung Jui Wang, R. Sankar, Fangcheng Chou, Arun Bansil, M. Zahid Hasan, Stephen D. Wilson, Liang Fu, and Vidya Madhavan. Observation of dirac node formation and mass acquisition in a topological crystalline insulator. *Science*, 341(6153):1496–1499, 2013. ISSN 0036-8075. doi: 10.1126/science.1239451.

[56] Dmytro Pesin and Allan H. MacDonald. Spintronics and pseudospintronics in graphene and topological insulators. *Nature Materials*, 11(5):409–416, 5 2012. ISSN 1476-1122. doi: 10.1038/nmat3305.

[57] Xiao-Liang Qi and Shou-Cheng Zhang. Topological insulators and superconductors. *Rev. Mod. Phys.*, 83:1057–1110, Oct 2011. doi: 10.1103/RevModPhys.83.1057.

[58] Rahul Roy. Topological phases and the quantum spin hall effect in three dimensions. *Phys. Rev. B*, 79:195322, May 2009. doi: 10.1103/PhysRevB.79.195322.

[59] Muhammad Safdar, Qisheng Wang, Misbah Mirza, Zhenxing Wang, Kai Xu, and Jun He. Topological surface transport properties of single-crystalline snte nanowire. *Nano Letters*, 13(11):5344–5349, 2013. doi: 10.1021/nl402841x. PMID: 24175637.

[60] D. N. Sheng, Z. Y. Weng, L. Sheng, and F. D. M. Haldane. Quantum spin-hall effect and topologically invariant chern numbers. *Phys. Rev. Lett.*, 97:036808, Jul 2006. doi: 10.1103/PhysRevLett.97.036808.

[61] Barry Simon. Holonomy, the quantum adiabatic theorem, and berry's phase. *Phys. Rev. Lett.*, 51:2167–2170, Dec 1983. doi: 10.1103/PhysRevLett.51.2167.

[62] Alexey A. Soluyanov and David Vanderbilt. Computing topological invariants without inversion symmetry. *Phys. Rev. B*, 83:235401, Jun 2011. doi: 10.1103/PhysRevB.83.235401.

[63] Ady Stern and Netanel H. Lindner. Topological quantum computation—from basic concepts to first experiments. *Science*, 339(6124):1179–1184, 2013. ISSN 0036-8075. doi: 10.1126/science.1231473.

[64] Joonki Suh, Deyi Fu, Xinyu Liu, Jacek K. Furdyna, Kin Man Yu, Wladyslaw Walukiewicz, and Junqiao Wu. Fermi-level stabilization in the topological insulators bi_2se_3 and bi_2te_3: Origin of the surface electron gas. *Phys. Rev. B*, 89:115307, Mar 2014. doi: 10.1103/PhysRevB.89.115307.

[65] D. J. Thouless, M. Kohmoto, M. P. Nightingale, and M. den Nijs. Quantized hall conductance in a two-dimensional periodic potential. *Phys. Rev. Lett.*, 49:405–408, Aug 1982. doi: 10.1103/PhysRevLett.49.405.

[66] Dinh Van Tuan, Frank Ortmann, Aron W Cummings, David Soriano, and Stephan Roche. Spin dynamics and relaxation in graphene dictated by electron-hole puddles. *Scientific Reports*, 6:21046, feb 2016. ISSN 2045-2322. doi: 10.1038/srep21046.

[67] Klaus von Klitzing. Developments in the quantum hall effect. *Philosophical Transactions of the Royal Society of London A: Mathematical, Physical and Engineering Sciences*, 363(1834):2203–2219, 2005. ISSN 1364-503X. doi: 10.1098/rsta.2005.1640.

[68] Zhe Wang, Dong-Keun Ki, Hua Chen, Helmuth Berger, Allan H. MacDonald, and Alberto F. Morpurgo. Strong interface-induced spin-orbit interaction in graphene on ws2. *Nat Commun*, 6:8339, Sep 2015. doi: doi:10.1038/ncomms9339.

[69] Zhiyong Wang, Chi Tang, Raymond Sachs, Yafis Barlas, and Jing Shi. Proximity-induced ferromagnetism in graphene revealed by the anomalous hall effect. *Phys. Rev. Lett.*, 114:016603, Jan 2015. doi: 10.1103/PhysRevLett.114.016603.

[70] Conan Weeks, Jun Hu, Jason Alicea, Marcel Franz, and Ruqian Wu. Engineering a robust quantum spin hall state in graphene via adatom deposition. *Phys. Rev. X*, 1:021001, Oct 2011. doi: 10.1103/PhysRevX.1.021001.

[71] Eugene P. Wigner. On a class of analytic functions from the quantum theory of collisions. *Annals of Mathematics*, 53(1):36–67, 1951. ISSN 0003486X.

[72] Y Xia, D Qian, D Hsieh, L Wray, A Pal, H Lin, A Bansil, D Grauer, Y S Hor, R J Cava, and M Z Hasan. Observation of a large-gap topological-insulator class with a single Dirac cone on the surface. *Nature Physics*, 5:398, may 2009.

[73] Cenke Xu and J. E. Moore. Stability of the quantum spin hall effect: Effects of interactions, disorder, and $\mathbb{Z}_2$ topology. *Phys. Rev. B*, 73:045322, Jan 2006. doi: 10.1103/PhysRevB.73.045322.

[74] Wenjing Yan, Oihana Txoperena, Roger Llopis, Hanan Dery, Luis E Hueso, and Fèlix Casanova. A two-dimensional spin field-effect switch. *Nature Communications*, 7:13372, nov 2016. URL `http://dx.doi.org/10.1038/ncomms13372http://10.0.4.14/ncomms13372https://www.nature.com/articles/ncomms13372{\#}supplementary-information`.

[75] Bowen Yang, Mark Lohmann, David Barroso, Ingrid Liao, Zhisheng Lin, Yawen Liu, Ludwig Bartels, Kenji Watanabe, Takashi Taniguchi, and Jing Shi. Strong electron-hole symmetric rashba spin-orbit coupling in graphene/monolayer transition metal dichalcogenide heterostructures. *Phys. Rev. B*, 96:041409, Jul 2017. doi: 10.1103/PhysRevB.96.041409.

[76] Hongbin Zhang, Cesar Lazo, Stefan Blügel, Stefan Heinze, and Yuriy Mokrousov. Electrically tunable quantum anomalous hall effect in graphene decorated by $5d$ transition-metal adatoms. *Phys. Rev. Lett.*, 108:056802, Feb 2012. doi: 10.1103/PhysRevLett.108.056802.

[77] Wei Zhang, Rui Yu, Hai-Jun Zhang, Xi Dai, and Zhong Fang. First-principles studies of the three-dimensional strong topological insulators $\mathrm{bi}_2\ \mathrm{te}_3$, $\mathrm{bi}_2\ \mathrm{se}_3$ and $\mathrm{sb}_2\ \mathrm{te}_3$. *New Journal of Physics*, 12(6):065013, 2010.

Chapter 2

DIAGRAMMATIC THEORY

An applied uniform magnetic field provides a sensitive probe for the measurement of quantum interference correction, leading to various of applications. The diagrammatic theory is a great quantitative tool to study the coherent effects in weakly disordered metals, especially in a larger system.

In this chapter, we outline the derivation of magneto-conductance(MC) of graphene. Firstly, we will construct the Hamiltonian of graphene in a new basis which simplifies the calculation and also matches QED 2+1 theory. Then we use the diagrammatic method to calculate the conductivity and spin-relaxation rates. Notably, we will use two approaches; one is the straightforward diagrammatic evaluation by following Ref. [1, 5], and another one is converting the coordinate to the hidden symmetry representations as in Refs. [4]. The first method is more powerful in evaluating all kind of cases while the latter one can be very efficient in tackling special cases. We will use each method to deal with one type of disorder as an example- straightforward approach for adatom-doped graphene (local scatters) and hidden symmetry one for graphene on various fo substrates (homogeneous disorder landscape).

2.1 Hamiltonian

To simplify the calculation and match QED 2+1 theory, we change the basis from $(\psi_{\mathbf{K}A}, \psi_{\mathbf{K}B}, \psi_{\mathbf{K}'A}, \psi_{\mathbf{K}'B})$ to two sets of 4×4 Hermitian matrices for sublattice "iso-spin" Σ^{μ} and valley "pseudo-spin" Λ^{μ} respectively,

$$\begin{aligned} \Sigma^x &= \tau^z \otimes \sigma^x, & \Sigma^y &= \sigma^y, & \Sigma^z &= \tau^z \otimes \sigma^z, \\ \Lambda^x &= -\tau^y \otimes \sigma^y, & \Lambda^y &= \tau^x \otimes \sigma^y, & \Lambda^z &= \tau^z \otimes \sigma^0, \end{aligned} \tag{2.1}$$

with algebraic relations $\Sigma^{\alpha}\Sigma^{\beta} = i\epsilon_{\alpha\beta\gamma}\Sigma^{\gamma}$ and $\Lambda^{\alpha}\Lambda^{\beta} = i\epsilon_{\alpha\beta\gamma}\Lambda^{\gamma}$; the two sets are mutually independent. The time-reversal operator in this basis is $\Theta = \Lambda^y\Sigma^y s^y\mathcal{K}$.

These two sets of matrices are particularly useful to construct a general time-invariant Hamiltonian and calculate the quantum interference due to their time reversal asymmetric nature. The (time-reversal invariant) Hamiltonian of graphene with generic disorder, for example, can be written as

$$H = \hbar v_F \vec{\Sigma} \cdot \vec{p} + \hat{I} u(r) + \sum_{n,m} u_{nm}(r)\Sigma^n \Lambda^m + \sum_{n,m} \alpha_{nm}(r)\Sigma^n s^m + \sum_{n,m} \beta_{nm}(r)\Lambda^n s^m \tag{2.2}$$

where $u(r)$ and u_{nm} describe the spatial distribution of each disorder. Similarly, the possible SOC types include $\Sigma^n s_m$ and $s_n \Lambda^m$. This type of disorders are already derived in Refs. [3, 4] so that we will not repeat the calculation here. Now we consider two types of disorder in the following.

Adatom Hamiltonian

According to Chapter. 6, we focus on the disorder induced by $p, d-$orbital adatoms. For d-orbital adatoms, the low-energy effective Hamiltonian for a single adatom scatters at $\mathbf{R}_I$ can be approximated to

$$\begin{aligned} \delta\mathcal{H}^{(d)}_{\mathbf{R}_I} = \Big[& V_0 \mathbb{I} + e^{i(\Delta\mathbf{K}\cdot\mathbf{R}_I)\Lambda^z}(V_i \Lambda^x \Sigma^z - \lambda_i \Lambda^x s^z) \\ & + \lambda_{\mathrm{KM}} \Sigma^z s^z + \lambda_{\mathrm{R}}(\Sigma^x s^y + \Sigma^y s^x) \Big] \delta(\mathbf{r} - \mathbf{R}_I). \end{aligned} \tag{2.3}$$

where $\Delta\mathbf{K} = \left(\frac{8\pi}{3\sqrt{3}a}, 0\right)$. Similarly, the induced potential by p-orbital adatoms can be written as

$$\delta\mathcal{H}^{(p,0)}_{\mathbf{R}} = A_{\hexagon}\delta(\mathbf{r} - \mathbf{R})\left[V_0 \mathbb{I} + \lambda_{\mathrm{KM}} \Sigma^z s^z + e^{i\Delta\mathbf{K}\cdot\mathbf{R}_I\Lambda^z}(V_i \Lambda^x \Sigma^z - \lambda_i \Lambda^x s^z)\right] \tag{2.4}$$

and

$$\psi^\dagger \delta\mathcal{H}^{(p,1)}_{\mathbf{R}_I} \psi = A_{\hexagon}\delta(\mathbf{r} - \mathbf{R}_I)\left[\psi^\dagger \mathbf{\Omega} \cdot (-i\nabla\psi) + h.c.\right] \tag{2.5}$$

with

$$\begin{aligned} \Omega_x = & \, aV_0^{(1)}\Sigma^x - a\lambda_i^{(1)}\Lambda^x\Sigma^x s^z e^{i\Delta\mathbf{K}\cdot\mathbf{R}_I\Lambda^z} \\ & + a\lambda_{\mathrm{R}}^{(1)}(s^y + \Lambda^z\Sigma^x s^y - \Lambda^z\Sigma^y s^x) \\ & - a\lambda_{\mathrm{R}}^{(1)} e^{i\Delta\mathbf{K}\cdot\mathbf{R}_I\Lambda^z}(\Lambda^y\Sigma^y s^y + \Lambda^y\Sigma^x s^x + \Lambda^x\Sigma^z s^y) \\ \Omega_y = & \, aV_0^{(1)}\Sigma^y + a\lambda_i^{(1)}\Lambda^x\Sigma^y s^z e^{i\Delta\mathbf{K}\cdot\mathbf{R}_I\Lambda^z} \\ & + a\lambda_{\mathrm{R}}^{(1)}(-s^x + \Lambda^z\Sigma^y s^y + \Lambda^z\Sigma^x s^x) \\ & - a\lambda_{\mathrm{R}}^{(1)} e^{i\Delta\mathbf{K}\cdot\mathbf{R}_I\Lambda^z}(\Lambda^y\Sigma^y s^x - \Lambda^y\Sigma^x s^y - \Lambda^x\Sigma^z s^x). \end{aligned} \tag{2.6}$$

Here $V_0^{(1)} = -\frac{3}{2}\frac{t_1^2}{\epsilon_1}$ and $\lambda_i^{(1)} = \lambda_{\mathrm{R}}^{(1)}$. Adatoms are short-ranged disorder, providing both intra- and inter-valley scattering. Also, the spin-independent scattering terms can be re-normalized into the other inevitable disorder source, e.g. from substrate, and has little contribute to the change of MC. Thus, these terms will be neglected in the following calculation. Lastly, each disorder types are highly correlated since they are from the same adatom, unlike the uncorrelated assumption in Ref. [4]. Therefore, we should be more careful in treating different types of disorder.

Homogeneous Disorder Landscape

Here we consider proximity induced phenomena or periodically functionalized structure. SOCs induced from periodically structures are homogeneous and thus undergo a different spin relaxation process than the local adatom case. These SOCs may be induced to graphene on a substrate which breaks various of symmetries. In the work of Denis Kochan *e*t al. [2] who have constructed low energy effective model for structures with global point group symmetries D_{6h}, D_{3d} , D_{3h}, C_{6v}, and C_{3v} that represent, for example, pristine graphene, graphene mini-ripple, planar boron nitride, graphene on a substrate, and free standing graphone,respectively. By reducing symmetry step by step, they find the emergence of certain spin-orbit couplings by specific point group symmetries. Based on their work, we will discuss the transport signatures of for these SOCs,

1. Pristine graphene D_{6h}: intrinsic SOC-$\Sigma^z s^z$.
2. Rippling structure D_{3d}: intrinsic SOC and momentum-dependent SOC (PIA SOC)-$k_x s^y - k_y s^x$.
3. Sub-lattice inversion asymmetry D_{3h}: intrinsic SOC and valley-Zeeman SOC-$\Lambda^z s^z$.
4. Transverse electric field $C_6 v$: intrinsic SOC and Rashba SOC-$\Sigma^x s^y - \Sigma^y s^x$

Unlike local impurities, these SOCs are homogenous induced on graphene and thus technically they do not relax spin orientations because the propagating states are the eigenstates of Hamiltonian of graphene and these SOCs, $H_g + H_{\text{so}}$. However, spins may be relaxed when there is any spin-independent static disorder scattering. The detail scattering mechanisms are discussed in the Chapter. 6.

2.2 Direct approach - adatom disorder

Disorder Correlator

For simplicity, we denote the general disorder as V, which can be background disorder $\mathcal{H}_{\text{dis}}$, adatoms $\delta\mathcal{H}_{\mathbf{R}_I}$, or others. Correlator $B(\mathbf{k}, \mathbf{k}') = \langle V(\mathbf{k}, \mathbf{k}')V(\mathbf{k}', \mathbf{k})\rangle$, the product of transition amplitudes, is the elementary vertex in the diagrams. We also use slightly different correlators for diffuson and Cooperon,

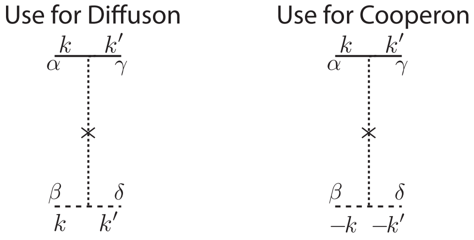

(2.7)

of which the mathematical forms read:

$$B^{(d)}_{\alpha\beta,\gamma\delta} = V(\mathbf{k},\mathbf{k}')_{\alpha\gamma} V(\mathbf{k}',\mathbf{k})_{\delta\beta} \tag{2.8}$$

$$B^{(c)}_{\alpha\beta,\gamma\delta} = V(\mathbf{k},\mathbf{k}')_{\alpha\gamma} V^{*}(-\mathbf{k}',-\mathbf{k})_{\delta\beta}. \tag{2.9}$$

Here we evaluate the correlators for $B^{(d)}_{\alpha\beta,\gamma\delta}$:

Scalar Potential For scalar potential $u\mathbb{I}$ with density n_i, the correlator is simply $B(\mathbf{k},\mathbf{k}') = n_i u^2 \mathbb{I}\otimes\mathbb{I}$, and $B^{(d)}_{\alpha\beta,\gamma\delta} = B^{(c)}_{\alpha\beta,\gamma\delta}$.

d-orbital adatom Assuming that the adatoms are randomly but homogeneously distributed on graphene with the density n_I, the associated scattering cross section for the state $|\mathbf{k},\alpha\rangle$ with $\alpha = (\tau,\sigma,s)$ is described by

$$\begin{aligned} V(\mathbf{k},\mathbf{k}')_{\alpha\beta} &= \langle \mathbf{k},\alpha|V|\mathbf{k}',\beta\rangle \\ &= V_0\hat{I} + e^{i\Delta\mathbf{K}\cdot\mathbf{R}_I\Lambda^z}(V_i\Lambda^x\Sigma^z - \lambda_i\Lambda^x s^z) \\ &\quad + \lambda_{\mathrm{KM}}\Sigma^z s^z + \lambda_R(\Sigma^x s^y - \Sigma^y s^x) \end{aligned} \tag{2.10}$$

and the correlator is

$$\begin{aligned} B_{\alpha\beta,\delta\gamma}(\mathbf{k},\mathbf{k}') &= n_I V^{\mathrm{intra}}_{\alpha,\gamma}(\mathbf{k},\mathbf{k}') V^{\mathrm{intra}}_{\delta,\beta}(\mathbf{k}',\mathbf{k}) \\ &\quad + n_I V^{\mathrm{inter}}_{\alpha,\gamma}(\mathbf{k},\mathbf{k}') V^{\mathrm{inter}}_{\delta,\beta}(\mathbf{k}',\mathbf{k}) \end{aligned} \tag{2.11}$$

where

$$\begin{aligned} V^{intra} &= V_0\hat{I} + \lambda_{\mathrm{KM}}\Sigma^z s^z + \lambda_{\mathrm{R}}(\Sigma^x s^y - \Sigma^y s^x) \\ V^{inter} \otimes V^{inter} &= \\ &\frac{1}{2}\left[(V_i\Lambda^x\Sigma^z - \lambda_i\Lambda^x S^z)\otimes(V_i\Lambda^x\Sigma^z - \lambda_i\Lambda^x S^z)\right] \\ &+ \frac{1}{2}\left[(V_i\Lambda^y\Sigma^z - \lambda_i\Lambda^y S^z)\otimes(V_i\Lambda^y\Sigma^z - \lambda_i\Lambda^y S^z)\right]. \end{aligned} \tag{2.12}$$

There are a few things to note. Firstly, the intervalley and intravalley correlators are decoupled because the phase for $V^{\mathrm{intra}}V^{\mathrm{inter}}$ is $\sim e^{iQr}$, averaging to 0. In addition, one needs to be careful in dealing with the phase of intervalley scattering. The term $e^{i\Delta\mathbf{K}\cdot\mathbf{R}_I\Lambda^z}\Lambda^x\Sigma^z$ includes more than $\Lambda^x\Sigma^z$ scattering process; it is a mix of two scattering process $\Lambda^x\Sigma^z$, $\Lambda^y\Sigma^z$ after averaging all the disorder. Again, $B^{(d)}_{\alpha\beta,\gamma\delta} = B^{(c)}_{\alpha\beta,\gamma\delta}$.

p-orbital adatom The correlators between zeroth order corrections are the same as the d-orbital case, except λ_{R}. However the momentum dependent disorder correlators should be dealt different while evaluating Diffuson and Cooperon. Take the $B^{(d)}$ for example, the adatom potential has three pieces

$$\begin{aligned} V(\mathbf{k},\mathbf{k}') =& V^{\text{intra}} + e^{i\varphi\Lambda^z}\left[\Lambda^x V^{\text{inter},x} + \Lambda^y V^{\text{inter},y}\right] \\ =& V^{\text{intra}} + (\cos\varphi\Lambda^x - \sin\varphi\Lambda^y)V^{\text{inter},x} + (\cos\varphi\Lambda^y + \sin\varphi\Lambda^x)V^{\text{inter},y} \end{aligned} \tag{2.13}$$

where the last two describe the intervalley scattering with $\Lambda^{x/y}$ respectively. The disorder-averaged correlator will be

$$\begin{aligned} B^{(d)}_{\alpha\beta,\delta\gamma}(\mathbf{q}) =& V^{\text{intra}}(\mathbf{q}) \otimes V^{\text{intra}}(\mathbf{q}) \\ &+ \frac{1}{2}\Lambda^x V^{\text{inter},x}(\mathbf{q}) \otimes \Lambda^x V^{\text{inter},x}(\mathbf{q}) + \frac{1}{2}\Lambda^x V^{\text{inter},x}(\mathbf{q}) \otimes \Lambda^y V^{\text{inter},y}(\mathbf{q}) \\ &+ \frac{1}{2}\Lambda^y V^{\text{inter},y}(\mathbf{q}) \otimes \Lambda^x V^{\text{inter},x}(\mathbf{q}) + \frac{1}{2}\Lambda^y V^{\text{inter},y}(\mathbf{q}) \otimes \Lambda^y V^{\text{inter},y}(\mathbf{q}) \\ &+ \frac{1}{2}\Lambda^y V^{\text{inter},x}(\mathbf{q}) \otimes \Lambda^y V^{\text{inter},x}(\mathbf{q}) - \frac{1}{2}\Lambda^y V^{\text{inter},x}(\mathbf{q}) \otimes \Lambda^x V^{\text{inter},y}(\mathbf{q}) \\ &- \frac{1}{2}\Lambda^x V^{\text{inter},y}(\mathbf{q}) \otimes \Lambda^y V^{\text{inter},x}(\mathbf{q}) + \frac{1}{2}\Lambda^x V^{\text{inter},y}(\mathbf{q}) \otimes \Lambda^x V^{\text{inter},y}(\mathbf{q}) \end{aligned} \tag{2.14}$$

where $\mathbf{k}' + \mathbf{k} = \mathbf{q}$. Note that the transition probability $V(\mathbf{q})$ depends on the sum of incoming and outgoing wave-vectors, instead of their difference. The exact reason for this dependence remains unclear.

Green function and self energy

The propagation of an electron on adatom-doped graphene can be described by retarded and advanced Green's functions $G^{r/a}$

$$\left[E - v\vec{\Sigma}\cdot\vec{p} - \Sigma \pm i\eta\right] G^{r/a} = \mathbb{I} \tag{2.15}$$

with self-energy Σ is energy contribution from disorder V. The self energy in the leading order in V can be written as

$$\Sigma_0^{r,a}(k,\omega) = \int \frac{d^2\mathbf{k}}{(2\pi)^2}\langle V(\mathbf{k},\mathbf{k}')G_0^{r,a}(\mathbf{k}',\omega)V(\mathbf{k}',\mathbf{k})\rangle \tag{2.16}$$

where G_0 is the bare Green function. The non-zero disorder correlator, and also its corresponding self-energy, implies that the eigenstate of the free Hamiltonian has the average lifetime $\tau(\mathbf{k}) = -\frac{\hbar}{2\mathrm{Im}\Sigma^R}$.

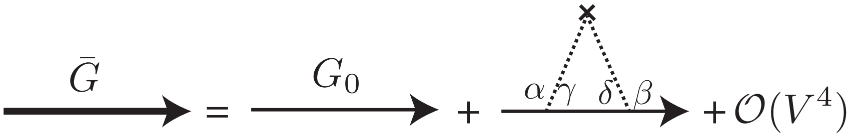

Figure 2.1: Diagrammatic expansion of the average Green function and self-energy, up to the leading order.

Self-energy and life times

d-orbital adatom

The life times of a particle is determined by the imaginary part of the self-energy as $\tau_\alpha(\mathbf{k}) = -\frac{\hbar}{2\mathrm{Im}\Sigma^R}$. The self-energy is given by $\Sigma^a(E, \mathbf{k}) = V(\mathbf{k}, \mathbf{k}) + \int \frac{d\mathbf{q}}{(2\pi)^2} V(\mathbf{k}, \mathbf{q}) G^a(E, \mathbf{q}) V(\mathbf{q}, \mathbf{k})$, averaged over disorder realizations. The anti-Hermitian part of Green's function is

$$\begin{aligned} \mathrm{Im} \int \frac{d^2\mathbf{q}}{(2\pi)^2} G_0^a(\mathbf{q}, E) &= \frac{1}{(2\pi)^2} \int d\theta_{\mathbf{q}} \frac{\pi}{\hbar v} P_{\mathbf{q}}^{(\mathrm{sgn}\, E)} \\ &= \pi \nu_0(E) \frac{\mathbb{I}}{2} \end{aligned} \tag{2.17}$$

where $P_{\mathbf{q}}^{\pm} = \frac{1 \pm \vec{\Sigma} \cdot \hat{\mathbf{q}}}{2}$ is the projection on to the conduction/valence band at $\mathbf{q}$, and $\nu(E_F) = \frac{k_F}{2\pi\hbar v_F} A_{\hexagon}$ is the density of states per unit cell, for a single valley and spin. Then, the antiHermitian part of the self-energy reads

$$2\,\mathrm{Im}\,\Sigma^a = \Gamma_a \mathbb{I} + \Gamma_b \Sigma^z s^z + \Gamma_c (\Sigma^x s^y + \Sigma^y s^x), \tag{2.18}$$

where

$$\begin{aligned} \Gamma_a &= \pi \nu n_a (V_0^2 + \lambda_{\mathrm{KM}}^2 + 2\lambda_{\mathrm{R}}^2 + V_i^2 + \lambda_i^2), \\ \Gamma_b &= 2\pi \nu n_a (V_0 \lambda_{\mathrm{KM}} - V_i \lambda_i + \lambda_{\mathrm{R}}^2), \\ \Gamma_c &= 2\pi \nu n_a \lambda_{\mathrm{R}} (V_0 + \lambda_{\mathrm{KM}}). \end{aligned} \tag{2.19}$$

Consider more types of disorder u_{sl} in Eq. (2.2), which are uncorrelated with each other, along with the adatoms. We find that the self-energy is still the same except that Γ_a has additional terms such as $\sum \pi \nu n_{sl} u_{sl}^2$. By projecting the Eq. (2.18) into the subspace spanned by $P_{\mathbf{k}}^{\pm}$, we obtain

$$P_{\mathbf{k}}^{\pm} (2\,\mathrm{Im}\,\Sigma) P_{\mathbf{k}}^{\pm} = \left[\Gamma_a \pm \Gamma_c (\cos\theta_{\mathbf{k}} s^y - \sin\theta_{\mathbf{k}} s^x)\right] P_{\mathbf{k}}^{\pm} \tag{2.20}$$

with eigenvalues $\Gamma_a + \Gamma_c$ and $\Gamma_a - \Gamma_c$.

We define

$$\tau_+ = \frac{\hbar}{\Gamma_a - \Gamma_c}, \qquad \tau_0 = \frac{\hbar}{\Gamma_a}, \qquad \tau_- = \frac{\hbar}{\Gamma_a + \Gamma_c}, \tag{2.21}$$

being the lifetimes.

p-orbital adatom

To evaluate the self energy for momentum dependent disorder, we set $\theta_{\mathbf{k}} = 0$ for simplicity (and WLOG). The disorder $V(\mathbf{q} = \mathbf{k}' + \mathbf{k})$ depends on the sum of wave-vectors $\mathbf{q}_x = k' \cos\theta + k$ and $\mathbf{q}_y = k' \sin\theta$. Note that the Green function is peaked at Fermi level, so that we assume that the amplitude of the wave-vectors $k = k' = \frac{E}{\hbar v}$.

The imaginary part of self-energy Σ is

$$\begin{aligned} \operatorname{Im}\Sigma(\mathbf{k},\omega) &= \int \frac{k'dk'd\theta}{(2\pi)^2} \langle V(\mathbf{k},\mathbf{k}') G_0^{r,a}(\mathbf{k}',\omega) V(\mathbf{k}',\mathbf{k})\rangle \\ &= \frac{1}{(2\pi)^2} \int d\theta \frac{k\pi}{\hbar v} \langle V(\mathbf{k},\mathbf{k}') P_{\mathbf{k}'} V(\mathbf{k}',\mathbf{k})\rangle \\ &= \frac{\nu\pi}{2}\left[\Gamma_a \mathbb{I} + \Gamma_b s^y + \Gamma_c \Sigma^x + \Gamma_d \Sigma^x s^y + \Gamma_e \Sigma^y s^x + \Gamma_f \Sigma^z s^z\right] \end{aligned} \tag{2.22}$$

where $\Gamma = \Gamma' n_a \pi \nu$ and Γ's are

$$\begin{aligned} \Gamma'_a &= V_0^2 + 2V_0 V_0^{(1)} ka + V_i^2 + \lambda_i^2 + \lambda_{\mathrm{KM}}^2 \\ \Gamma'_b &= ka\lambda_{\mathrm{R}}^{(1)}(2V_0 - 2V_i) \\ \Gamma'_c &= 2ka(V_0^{(1)} V_0 + \lambda_i^{(1)}\lambda_i) \\ \Gamma'_d &= ka\lambda_{\mathrm{R}}^{(1)}(V_0 + V_i + \lambda_i - \lambda_{\mathrm{KM}}) \\ \Gamma'_e &= -ka\lambda_{\mathrm{R}}^{(1)}(V_0 + V_i + \lambda_i - \lambda_{\mathrm{KM}}) \\ \Gamma'_f &= 2((V_0 + kaV_0^{(1)})\lambda_{\mathrm{KM}} - V_i\lambda_i). \end{aligned} \tag{2.23}$$

Since we only focus on the qualitative contribution, i.e. momentum-dependent Rashba SOC, here we assume $\lambda_i^{(1)} = V_0^{(1)} = 0$ and further simplify the Γ's. Projected into the subspace spanned by $P_{\mathbf{k}}$, $P_{\mathbf{k}}^{\pm}(2\operatorname{Im}\Sigma)P_{\mathbf{k}}^{\pm}$ equals to

$$\left[\Gamma_a + \Gamma_b s^y\right] P_{\mathbf{k}}^{\pm} \tag{2.24}$$

with eigenvalues

$$\Gamma_{\mp} = \Gamma_a \pm |\Gamma_b|. \tag{2.25}$$

which defines the two relevant scattering times $\tau_\pm$ respectively. We can also define the projection operators for each eigenvalue-

$$\mu_{\mathbf{k}}^{\pm} = \frac{1}{2}\left(\mathbb{I} \pm s^y\right). \tag{2.26}$$

Then again we define three life times,

$$\tau_+ = \frac{\hbar}{\Gamma_a - |\Gamma_b|}, \qquad \tau_- = \frac{\hbar}{\Gamma_a + |\Gamma_b|}, \tag{2.27}$$

and $\tau_0 = \frac{\hbar}{\Gamma_a}$.

Drude-Boltzmann Conductivity

Now we evaluate the diagonal conductivity $\sigma_{xx}(\omega)$ of which the real part at zero temperature is given by Kubo formula,

$$\sigma_{xx} = \frac{\hbar}{\pi\Omega}\mathrm{ReTr}\left[\hat{j}_x G^r \hat{j}_x G^a\right] \tag{2.28}$$

where $\hat{j}_x = -ev_F\Sigma^x$ is the current operator in x-direction. The system size is Ω, the Green functions are given by equation (2.15), and the disorder averaged conductivity is denoted as $\sigma(\omega) = \overline{\sigma}_{xx}(\omega)$. Out of numerous disorder scattering processes, three leading contributions to conductivity are Drude-Boltzmann process, the diffuson, and the Cooperon as shown in Fig.2.2. In this section, we will evaluate the contribution of the first scattering diagram.

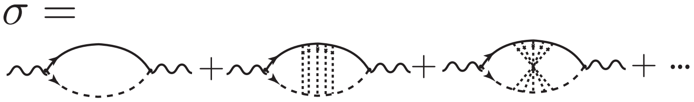

Figure 2.2: The diagrams of leading contributions to conductivity. The first one is Drude-Boltzmann, the second one is the diffuson, and the third one is Cooperon.

d-Orbit Doped Adatom

The bare conductivity is

$$\sigma_0(\omega) = \frac{e^2}{h}\int_{\mathbf{k}} \hbar^2 v_F^2 \,\mathrm{Tr}\left[\Sigma^x G^r(\epsilon_+, \mathbf{k})\Sigma^x G^a(\epsilon_-, \mathbf{k})\right] \tag{2.29}$$

$$= e^2\nu(\epsilon_F)v_F^2\left(\frac{\hbar}{\Gamma_a + \Gamma_c - i\hbar\omega} + \frac{\hbar}{\Gamma_a - \Gamma_c - i\hbar\omega}\right) \tag{2.30}$$

which can be reduced to

$$\sigma_0(\omega = 0) = e^2\nu(\epsilon_F)v_F^2(\tau_+ + \tau_-). \tag{2.31}$$

with the elastic scattering rate $\tau_e = \frac{\tau_+ + \tau_-}{2}$. When the onsite scalar disorder u is much stronger than adatom disorder, this equation turns to, $\tau_+ + \tau_- \longrightarrow 2\tau_0$.

p-orbit Doped Adatom

The bare conductivity is

$$\begin{aligned}\sigma_0(\omega) &= \frac{e^2}{h}\int_{\mathbf{k}} \hbar^2 v_F^2 \,\mathrm{Tr}\left[\Sigma^x G^r(\epsilon_+, \mathbf{k})\Sigma^x G^a(\epsilon_-, \mathbf{k})\right] && (2.32)\\ &= e^2 \nu(\epsilon_F) v_F^2 \left(\frac{\hbar}{\Gamma_a + \Gamma_b - i\hbar\omega} + \frac{\hbar}{\Gamma_a - \Gamma_b - i\hbar\omega}\right) && (2.33)\end{aligned}$$

This is the same for as the $d-$orbital adatoms, except different Γs. Note that $\Gamma_b = \Gamma_b(k_F)$ here.

Diffuson

The next order of classical conductivity correction is diffuson, which is the second diagram in Fig. 2.2. The conductivity for diffuson is

$$\sigma_d = \frac{e^2 v_F^2 \hbar}{2\pi} Tr\left[V_x(\mathbf{k}, \epsilon^-, \epsilon^+)\tilde{P}(\mathbf{k}, \mathbf{k}', \epsilon) V_x(\mathbf{k}', \epsilon^+, \epsilon^-)\right] \tag{2.34}$$

where V_x is the current vertex (related to $\hat{j}_x$) connected two Green's functions as

$$V_x(\mathbf{k}, \epsilon_1, \epsilon_2) = G^r(\mathbf{k}_+, \epsilon_1) v_x(\mathbf{k}, \epsilon_1, \epsilon_2) G^a(\mathbf{k}_-, \epsilon_2), \tag{2.35}$$

and $P(\mathbf{k}, \mathbf{k}', \epsilon)$ is the diffuson satisfying the recursive relation,

$$P(\mathbf{k}, \mathbf{k}', \mathbf{q}, \epsilon) = 1 + \int \frac{d^2\mathbf{k}''}{(2\pi)^2} B(\mathbf{k}, \mathbf{k}'', \epsilon) G^r(\mathbf{k}''_+, \epsilon_+) G^a(\mathbf{k}''_-, \epsilon_-) P(\mathbf{k}'', \mathbf{k}', \mathbf{q}, \epsilon) \tag{2.36}$$

where $B(\mathbf{k}, \mathbf{k}')$ is the correlator. Note that these matrices are connected as in the figure 2.3 instead of inner product.

d-Orbit Doped Adatom

The scatters are static and momentum-independent, therefore all internal integration become independent and the diffuson only depends on $\mathbf{q}$. We first define pair propagator $\rightleftarrows$ as

$$\begin{aligned}\rightleftarrows (\varepsilon, \omega, q)^{\alpha\beta}_{\gamma\delta} &= \int_{\mathbf{k}} G^r(\varepsilon_+, \mathbf{k}_+) \otimes G^a(\varepsilon_-, \mathbf{k}_-)\\ &= \int \frac{d^2\mathbf{k}}{(2\pi)^2} G^r(\varepsilon + \hbar\omega, \mathbf{k})_{\alpha\beta} G^a(\varepsilon, \mathbf{k} - \mathbf{q})_{\delta\gamma} && (2.37)\\ &= \int \frac{d\varphi}{2\pi} \int \frac{k dk}{2\pi} \frac{1}{\varepsilon_+ - \hbar v \mathbf{k} \cdot \vec{\Sigma} + i\eta} \otimes \frac{1}{\varepsilon_- - \hbar v \mathbf{k}_- \cdot \vec{\Sigma} - i\eta}\end{aligned}$$

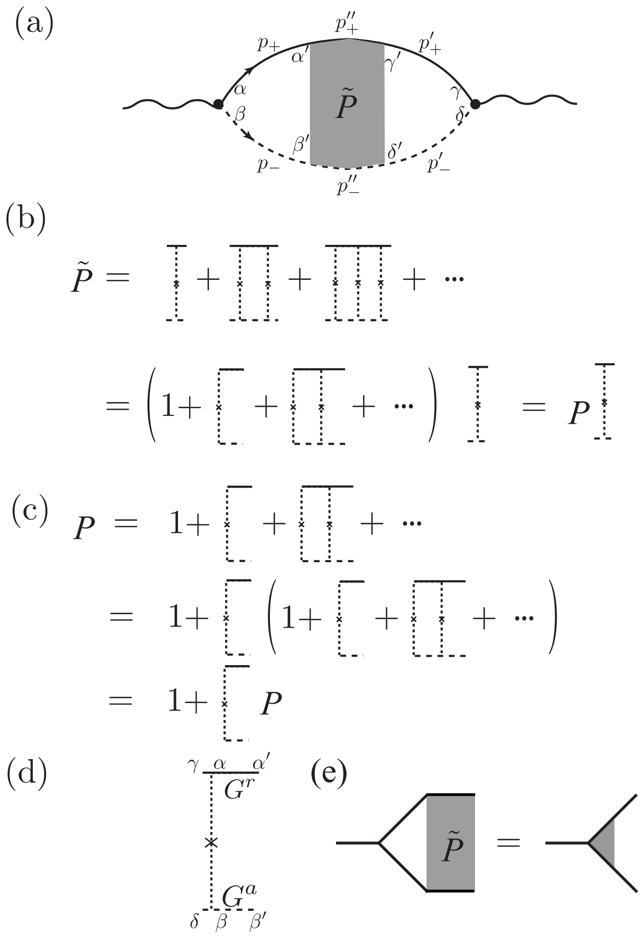

Figure 2.3: Diffuson. Note that p refers to $\mathbf{k}$ here and $\mathbf{k}_\pm = \mathbf{k} \pm \mathbf{q}/2$, $\epsilon_\pm = \epsilon \pm \hbar\omega/2$.

where $\mathbf{k}_- = \mathbf{k} - \mathbf{q}$, $\epsilon_+ = \epsilon + \hbar\omega$, $\epsilon_- = \epsilon$. To simplify the calculation, we restrict ourselves at $\mathbf{q} \rightarrow 0$ and project the propagator into energy eigenstates.

$$\rightleftarrows (\varepsilon, \omega, \mathbf{q} = 0)^{\alpha\beta}_{\gamma\delta} = \sum_{x,y} \int \frac{d\theta_k}{2\pi} \int \frac{kdk}{2\pi} \frac{P_{\mathbf{k}}\mu^x_{\mathbf{k}} \otimes P_{\mathbf{k}}\mu^y_{\mathbf{k}}}{(\varepsilon + \hbar\omega - \hbar vk + i\frac{\Gamma_x}{2})(\varepsilon - \hbar vk - i\frac{\Gamma_y}{2})} \tag{2.38}$$

$$= 2\pi\nu(k_F) \int \frac{d\theta_k}{2\pi} \sum_{x,y} \frac{P_{\mathbf{k}}\mu^x_{\mathbf{k}} \otimes P_{\mathbf{k}}\mu^y_{\mathbf{k}}}{\frac{\Gamma_x + \Gamma_y}{2} - i\hbar\omega} \tag{2.39}$$

$$= 2\pi\nu(k_F) \int \frac{d\theta_k}{2\pi} \left[\frac{P_{\mathbf{k}}\mu^+_{\mathbf{k}} \otimes P_{\mathbf{k}}\mu^+_{\mathbf{k}}}{\Gamma_+ - i\hbar\omega} + \frac{P_{\mathbf{k}}\mu^-_{\mathbf{k}} \otimes P_{\mathbf{k}}\mu^-_{\mathbf{k}}}{\Gamma_- - i\hbar\omega} + \frac{P_{\mathbf{k}}\mu^+_{\mathbf{k}} \otimes P_{\mathbf{k}}\mu^-_{\mathbf{k}}}{\Gamma_0 - i\hbar\omega} + \frac{P_{\mathbf{k}}\mu^-_{\mathbf{k}} \otimes P_{\mathbf{k}}\mu^+_{\mathbf{k}}}{\Gamma_0 - i\hbar\omega} \right] \tag{2.40}$$

where $P_{\mathbf{k}}$ and $\mu^{\pm}_{\mathbf{k}}$ are defined as

$$P_{\mathbf{k}} = \frac{1}{2}\left(\mathbb{I} + \cos\theta_{\mathbf{k}}\Sigma^x + \theta_{\mathbf{k}}\Sigma^y\right) \tag{2.41a}$$

$$\mu^{\pm}_{\mathbf{k}} = \frac{1}{2}\left(\mathbb{I} \pm \left(\cos\theta_{\mathbf{k}} s^y + \sin\theta_{\mathbf{k}} s^x\right)\right). \tag{2.41b}$$

Now we evaluate the bare conductivity with the above pair propagator: $\sigma_0 = \frac{e^2}{h}\hbar^2 v^2 \mathrm{Tr}\left[\rightleftarrows^{\alpha\beta}_{\delta\gamma} \Sigma^x_{\alpha\delta}\Sigma^x_{\beta\gamma}\right]$. The diffuson contribution can be renormalized into current operator $j \longrightarrow \tilde{j}$ as shown in Fig. 2.3 (e). The classical conductivity is

$$\frac{\pi}{e^2 v^2 \hbar}\sigma_{cl} = \mathrm{Tr}\left[\Sigma^x_{\alpha\delta} \rightleftarrows^{\alpha\beta}_{\delta\gamma} \Sigma^x_{\beta\gamma}\right] + \mathrm{Tr}\left[\Sigma^x_{\alpha\delta} \rightleftarrows^{\alpha\beta}_{\delta\gamma} P^{\beta\beta'}_{\gamma\gamma'} \rightleftarrows^{\beta'\alpha'}_{\gamma'\delta'} \Sigma^x_{\alpha'\delta'}\right] \tag{2.42}$$

From Fig. 2.3(c), we know that $P(VV)^{-1} = \mathbb{I} + P \rightleftarrows$ so the above equation can be simplified to

$$\frac{\pi}{e^2 v^2 \hbar}\sigma_{cl} = \mathrm{Tr}\left[\Sigma^x_{\alpha\delta} \rightleftarrows^{\alpha\beta}_{\delta\gamma} P^{\beta\beta'}_{\gamma\gamma'} \langle VV\rangle^{-1}_{\beta'\gamma',\alpha'\delta'} \Sigma^x_{\alpha'\delta'}\right] \tag{2.43}$$

$$= \mathrm{Tr}\left[\Sigma^x_{\alpha\delta} \rightleftarrows^{\alpha\beta}_{\delta\gamma} \tilde{\Sigma}^x_{\beta\gamma}\right] \tag{2.44}$$

where $\tilde{\Sigma}^x = \Sigma^x + P \rightleftarrows \Sigma^x = P(VV)^{-1}\Sigma^x = (1 - VV \rightleftarrows)^{-1}\Sigma^x$. Note that in the limit of $\mathbf{q} \rightarrow 0$, the diffuson is no longer invertible because these diffuson channels indeed possess long wave length diffusive modes. However, we can explicitly check that the contraction $P(\mathbf{q})\Sigma^x$ is valid.

Due to the high correlation nature of different scattering types of adatoms, there is no simple analytical form for this case. However, in the presence of strong background disorder or uncorrelated case $\Gamma_{i\neq a} \ll \Gamma_a$, the above current modification can be approximated to be

$$\tilde{j} = 2j. \tag{2.45}$$

Otherwise, the exact contribution from diffuson can be solved numerically.

p-Orbit Doped Adatom The diffuson contribution of p-orbit doped adatom is the same as the d-orbital one, except that the Γs are different.

Cooperon

In Cooperon calculation, we first define two quantities- pair propagator and current current propagator. The pair propagator $\rightrightarrows$ is defined as

$$\rightrightarrows(\varepsilon, \omega, \mathbf{Q})^{\alpha\beta}_{\gamma\delta} = \int \frac{d^2\mathbf{k}}{(2\pi)^2} G^r(\varepsilon + \hbar\omega, \mathbf{k})_{\alpha\beta} G^a(\varepsilon, \mathbf{Q} - \mathbf{k})_{\gamma\delta}. \tag{2.46}$$

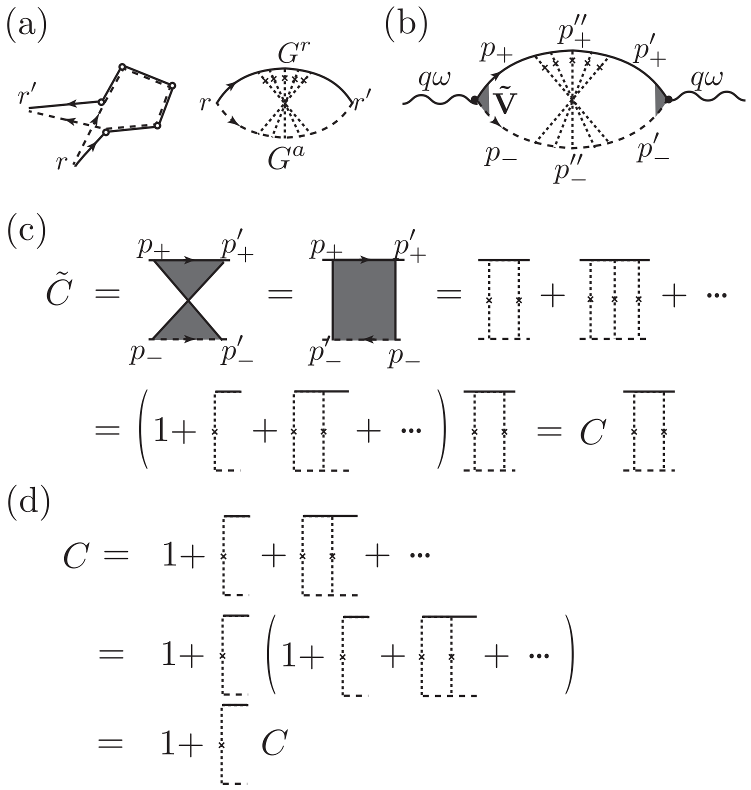

Figure 2.4: (a) A process of collisions contributed to quantum interference and the same process after disorder averaging which is also called Cooperon. (b)Cooperon, maximally cross diagram, in momentum representation. (c) The definition of Cooperon $\tilde{C}$ and modified Cooperon C.

or more succinctly $\rightrightarrows = \int_{\mathbf{k}} G^r(\varepsilon_+, \mathbf{k}_+) \otimes G^a(\varepsilon_-, \mathbf{k}_-)$.

In polar coordinates,

$$\rightrightarrows = \int \frac{d\varphi}{2\pi} \int \frac{k\,dk}{2\pi} \frac{1}{\varepsilon_+ - \hbar v \mathbf{k} \cdot \vec{\Sigma} + i\eta} \otimes \frac{1}{\varepsilon_- - \hbar v \mathbf{k}_- \cdot \vec{\Sigma} - i\eta} \tag{2.47}$$

which in low limit $Q = 0$ can be simplified to be

$$\begin{aligned}\rightrightarrows &= \frac{1}{\hbar v} \sum_{x,y} \frac{\frac{\varepsilon}{\hbar v} P_{\mathbf{k}} \mu^x_{\mathbf{k}} \otimes P_{\mathbf{k}_-} \mu^y_{\mathbf{k}_-}}{\frac{\Gamma_x + \Gamma_y}{2} - i\hbar\omega} \\ &\approx 2\pi\nu(\varepsilon) \sum_{x,y} \frac{P_{\mathbf{k}} \mu^x_{\mathbf{k}} \otimes P_{-\mathbf{k}} \mu^y_{-\mathbf{k}}}{\frac{\Gamma_x + \Gamma_y}{2} - i\hbar\omega} \\ &= 2\pi\nu(\epsilon) \left(\frac{P_{\mathbf{k}} \mu^+_{\mathbf{k}} \otimes P_{-\mathbf{k}} \mu^+_{-\mathbf{k}}}{\Gamma_+ - i\hbar\omega} + \frac{P_{\mathbf{k}} \mu^-_{\mathbf{k}} \otimes P_{-\mathbf{k}} \mu^-_{-\mathbf{k}}}{\Gamma_- - i\hbar\omega} + \frac{P_{\mathbf{k}} \mu^+_{\mathbf{k}} \otimes P_{-\mathbf{k}} \mu^-_{-\mathbf{k}} + P_{\mathbf{k}} \mu^-_{\mathbf{k}} \otimes P_{-\mathbf{k}} \mu^+_{-\mathbf{k}}}{\Gamma_0 - i\hbar\omega} \right).\end{aligned} \tag{2.48}$$

This describes the pair propagator in the diagrams and is applicable for both $p-$ and $d-$orbital adatom-doped graphene. Now we define another physics quantity, describing the current-current vortices, pair-j-pair propagator:

$$\overset{j}{\underset{j}{\Leftarrow\vdots\Leftarrow}}\,(\varepsilon,\omega;\mathbf{k}+\mathbf{k}') \quad \sim$$

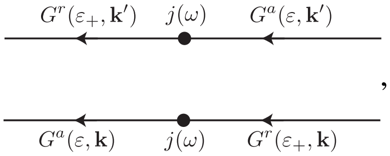

, (2.49)

with the mathematical form,

$$\overset{j}{\underset{j}{\Leftarrow\vdots\Leftarrow}}\,(\varepsilon,\omega;\mathbf{Q}) = \int \frac{d^2\mathbf{k}}{(2\pi)^2} G^R(\varepsilon+\hbar\omega,\mathbf{Q}-\mathbf{k})\Sigma^x G^A(\varepsilon,\mathbf{Q}-\mathbf{k}) \otimes G^A(\varepsilon,\mathbf{k})\Sigma^x G^R(\varepsilon+\hbar\omega,\mathbf{k}). \tag{2.50}$$

Here we keep total momenta $\mathbf{Q} = \mathbf{k}+\mathbf{k}'$ fixed. In the low $\mathbf{Q}$ limit (setting $\mathbf{Q}=0$), the current-current operator can be reduced to

$$\begin{aligned}\overset{j}{\underset{j}{\Leftarrow\vdots\Leftarrow}}\,(\varepsilon,\omega;0) = {} & \frac{4\pi\nu}{(\Gamma_+ - i\hbar\omega)^3} P_{-\mathbf{k}}\Sigma^x P_{-\mathbf{k}}\mu^+_{-\mathbf{k}} \otimes P_{\mathbf{k}}\Sigma^x P_{\mathbf{k}}\mu^+_{\mathbf{k}} \\ & + \frac{4\pi\nu}{(\Gamma_- - i\hbar\omega)^3} P_{-\mathbf{k}}\Sigma^x P_{-\mathbf{k}}\mu^-_{-\mathbf{k}} \otimes P_{\mathbf{k}}\Sigma^x P_{\mathbf{k}}\mu^-_{\mathbf{k}} \\ & + \frac{4\pi\nu\left[P_{-\mathbf{k}}\Sigma^x P_{-\mathbf{k}}\mu^+_{-\mathbf{k}} \otimes P_{\mathbf{k}}\Sigma^x P_{\mathbf{k}}\mu^-_{\mathbf{k}} + P_{-\mathbf{k}}\Sigma^x P_{-\mathbf{k}}\mu^-_{-\mathbf{k}} \otimes P_{\mathbf{k}}\Sigma^x P_{\mathbf{k}}\mu^+_{\mathbf{k}}\right]}{(\Gamma_0 - i\hbar\omega)(\Gamma_+ - i\hbar\omega)(\Gamma_- - i\hbar\omega)}.\end{aligned} \tag{2.51}$$

Consider a degenerate Dirac Fermi gas with $\hbar\omega$, $kT \ll \epsilon_F$ with weak disorder $k_F l \gg 1$. Under this limit, we calculate the conductivity corresponding to the maximally crossed diagrams (Cooperon) in Fig. 2.4 (b),

$$\delta\sigma = \frac{e^2\nu^2\hbar}{2\pi}\mathrm{Tr}\left[V_x(p,\omega^-,\omega^+)\tilde{C}(p,p',\omega)V_x(p',\omega^+,\omega^-)\right] \tag{2.52}$$

where V_x is the current vertex (related to $\hat{j}_x$) connected two Green's functions as

$$V_x(p,\omega_1,\omega_2) = G^r(p_+,\omega_1)\tilde{v}_x(p,\omega_1,\omega_2)G^a(p_-,\omega_2) \tag{2.53}$$

with the renormalized vertex corrections $\tilde{v}_x = 2\Sigma^x$ (assuming background disorder $u\mathbb{I}$ dominating all of the disorder types). The Cooperon can be written as

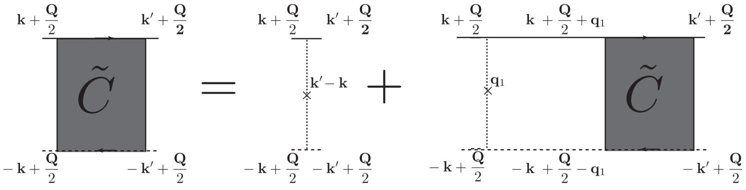

(2.54)

of which the mathematical form is

$$\tilde{C}(Q) = \left(1 - \int \left[VV(\mathbf{q}_1) \rightrightarrows (\mathbf{k} + \mathbf{q}_1)\right] d^2\mathbf{q}_1\right)^{-1} VV(\mathbf{k}', \mathbf{k}). \tag{2.55}$$

Combining the above operators we can easily write down the conductivity correction corresponding to the maximally crossed diagram.

$$\delta G_q = \frac{2e^2v^2\hbar}{\pi}\mathrm{Tr}\left[\Leftarrow\overset{j}{\underset{j}{\vdots}}\Leftarrow C\right] \tag{2.56a}$$

$$= \frac{2e^2v^2\hbar}{\pi}\int_{\mathbf{Q}}\sum_{i\in\text{poles}} \frac{\text{Residue}@\Gamma_i}{\frac{1}{2}\hbar v^2Q^2\tau_0 - i\hbar\omega + \Gamma_i + \frac{\hbar}{\tau_\phi}} \tag{2.56b}$$

where Γ_i is the pole. The $\frac{1}{2}v^2Q^2\tau_0$ comes from the first order correction in $\mathbf{Q}$ and $\tau_0 \sim \tau_u$ by approximation. τ_ϕ is the decoherence time which prevents the divergence of the integral.

The quantum conductivity is dominated by the $\frac{1}{2}\hbar v^2Q^2\tau_0$ channels, which is also called the singlet mode. Hence in the diffusive limit the Cooperon structure factor reduces to a projector onto this singlet mode. In contrast, these single modes are not important in the diffuson conductivity. This can be easily understood from the fact that the vertex renormalization does not depend on the vanishing modes, but only on its massive modes though not universal.

There is an important assumption about the vertex renormalization in the above calculation, which is that $u\mathbb{I}$ disorder dominates the transport (or the different disorder types are un-correlated). This assumption is valid for most experiments since long range onsite disorder is known to be the major disorder source near the Dirac points. Therefore, in the following examples, we explore various systems all with the assumption of large onsite disroder $u\mathbb{I}$. For a more general system, the vertex correction and conductivity can be solved mathematically.

Examples

From the above setup, we can evaluate the conductivity for different cases.

1. **spin-independent disorder** - $u\mathbb{I} + \sum_{s,l=\perp,z} u_{ls}\Lambda_l\Sigma_s$ where $\perp = x, y$.

    - **Poles** : 0, $(8u_{\perp\perp}^2 + 4u_{\perp z}^2)\pi\nu$, $(4u_{\perp\perp}^2 + 2u_{\perp z}^2 + 4u_{z\perp}^2 + 2u_{zz}^2)\pi\nu$ and $(u^2 + 4u_{\perp\perp}^2 + 2u_{\perp z}^2 + 2u_{z\perp}^2 + u_{zz}^2)\pi\nu$, many other poles with u^2.

- **Residues**: $\frac{2}{\pi\nu(u^2+4u_{\perp\perp}^2+2u_{\perp z}^2+2u_{z\perp}^2+u_{zz}^2)}$, $\frac{2}{\pi\nu(-u^2+4u_{\perp\perp}^2+2u_{\perp z}^2-2u_{z\perp}^2-u_{zz}^2)}$, -$\frac{4}{\pi\nu(u^2-2u_{z\perp}^2-u_{zz}^2)}$ and many others ...
- **Assumption**: with the approximation used in McCann's paper ($u^2 \gg u_{sl}^2$), we can ignore all the contributions from poles with u^2 because $1/u^2$ is small compare the the fist three poles. The leading contributions for the first three poles are residues $\frac{2}{\pi\nu u^2}(1,-1,-2) = \frac{2}{\pi\nu u^2}c_i$.
- **Conductivity**

$$\delta\sigma = \frac{2e^2\nu^2\hbar}{\pi}\frac{2}{\pi\nu u^2}\int_{\mathbf{Q}}\sum_i \frac{c_i}{\hbar DQ^2 - i\hbar\omega + \Gamma_i + \frac{\hbar}{\tau_\phi}} \tag{2.57}$$

$$= \frac{4e^2D}{\pi}\int_{\mathbf{Q}}\sum_i \frac{c_i}{\hbar DQ^2 - i\hbar\omega + \Gamma_i + \frac{\hbar}{\tau_\phi}} \tag{2.58}$$

$$= \frac{2e^2}{\pi h}\sum_i c_i \ln(\frac{\tau^{-1}}{\tau_\phi^{-1} + \Gamma_i/\hbar}) \tag{2.59}$$

and the magneto-conductance will be

$$\begin{gathered}\delta\sigma(B) = \frac{2e^2}{\pi h}\sum_i c_i F\left(\frac{B}{B_\phi + B_i}\right) \\ F(z) = \ln z + \psi\left(\frac{1}{2} + \frac{1}{z}\right), \quad B_i = \frac{\Gamma_i}{4De}\end{gathered} \tag{2.60}$$

We need to further consider another two diagrams of which each produces $-\frac{1}{4}$ of the above results. Therefore the total conductivity is

$$\delta\sigma(B) = \frac{e^2}{\pi h}\sum_i c_i F\left(\frac{B}{B_\phi + B_i}\right) \tag{2.61}$$

with $\Gamma_i = 0, (8u_{\perp\perp}^2 + 4u_{\perp z}^2)\pi\nu, (4u_{\perp\perp}^2 + 2u_{\perp z}^2 + 4u_{z\perp}^2 + 2u_{zz}^2)\pi\nu$ and $c_i = (1,-1,-2)$, which recovers the result in McCann's paper.

2. ***p*-orbital adatom: 0th order**

- **Poles**: $\pi\nu\,\big(2\lambda_i^2+2\lambda_{\mathrm{KM}}^2, 2V_i^2+2\lambda_{\mathrm{KM}}^2, V_i^2+\lambda_i^2+2\lambda_{\mathrm{KM}}^2, V_0^2+V_i^2+\lambda_i^2+\lambda_{\mathrm{KM}}^2,$ $\frac{(V_0-\lambda_{\mathrm{KM}})^2+(V_i+\lambda_i)^2}{2}, \frac{(V_0-\lambda_{\mathrm{KM}})^2+2V_i^2+2\lambda_i^2}{2}, \frac{V_0^2+3V_i^2-2V_i\lambda_i+3\lambda_i^2-2V_0\lambda_{\mathrm{KM}}+\lambda_{\mathrm{KM}}^2}{2}, \frac{(V_i-\lambda_i)^2+(V_0+\lambda_{\mathrm{KM}})^2}{2},$ $\frac{(V_0+\lambda_{\mathrm{KM}})^2+2(V_i^2+\lambda_i^2)}{2}, \frac{V_0^2+3V_i^2+2V_i\lambda_i+3\lambda_i^2+2V_0\lambda_{\mathrm{KM}}+\lambda_{\mathrm{KM}}^2}{2}\big).$
- **Residues** $2/(\nu\pi(V_0^2 + V_i^2 - \lambda_i^2 - \lambda_{\mathrm{KM}}^2)$, and many others...
- **Unitary**

3. ***p*-orbital adatom w/ SRD: 0th order**
    - **Poles**: $\pi\nu(2\lambda_i^2 + 2\lambda_{\mathrm{KM}}^2)$.
    - **Residues** $1/(\nu\pi(u^2 + 4u_{\perp\perp}^2 + 2u_{\perp z}^2 + V_0^2 + V_i^2 - \lambda_i^2 - \lambda_{\mathrm{KM}}^2) \sim 1/(\pi\nu u^2)$.
    - **Conductivity**

    $$\delta\sigma(B) = -\frac{e^2}{2\pi h} F\left(\frac{B}{B_\phi + B_\Gamma}\right) \tag{2.62}$$

    where $\Gamma = \pi\nu(2\lambda_i^2 + 2\lambda_{\mathrm{KM}}^2)$. This is still a Unitary behavior.

4. ***d*-orbital adatom** - no analytical solution if we consider full correlation.

5. ***d*-orbital adatom w/ SRD** - no analytical solution if we consider full correlation. If we somehow assume no correlation between different disorder type and take the approximation that $u^2 \gg \Gamma_{\perp z}, \Gamma_{\perp\perp} \gg a datom's\ coupling\ strength$.
    - **Poles**: the leading three contributions $\pi\nu\left(0, 4\lambda_{\mathrm{R}}^2, 2(\lambda_i^2 + 2\lambda_{\mathrm{KM}}^2 + \lambda_{\mathrm{R}}^2)\right) = \Gamma_i$.
    - **Residues**: The corresponding residue after approximation is $\frac{1}{\pi\nu u^2}(-1, 1, 2) = \frac{1}{\pi\nu u^2} c_i$,
    - **Conductivity**

    $$\sigma(B) = \frac{e^2}{2\pi h} \sum_i c_i F\left(\frac{B}{B_\phi + B_i}\right) \tag{2.63}$$

    where $B_i = \frac{\Gamma_i}{4eD}$ and c_i are the pole and sign of residue as shown above.

6. ***p*-orbital adatom w/ and wo/ SRD:: 1st order** - no analytical sol for either correlated or uncorrelated case.

2.3 Hidden symmetry approach - substrate disroder

As discussed in the last section, only massive modes contribute to diffuson modes while the divergent modes, singlet, contribute to the Cooperon. If we rewrite in the space spanned by *singlet* and *triplet*, we can find that the Cooperon and diffuson is diagonalized and can be easily solved, unless the hidden symmetry is broken. But the question is what is the singlet and triplet in this system?

Consider the basis to the representation of hidden symmetry (l, i, j) as shown in Fig. 2.5,

$$C(\{l, i, j\}) = \frac{1}{4} M_{lij}^\dagger C(\{\tau, \sigma, s\}) M_{lij} \tag{2.64}$$

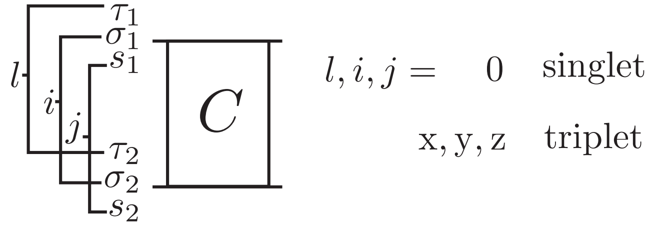

Figure 2.5: The transformation from the spaces $\tau \otimes \sigma \otimes s$ of two incoming particles to representation of hidden symmetry $l \otimes i \otimes j$.

with the transformation matrix $M_s^l = s^y s^j \Sigma^y \Sigma^i \Lambda^y \Lambda^l$ which is a 32×32 dimensional matrix. The two iso-spin (sublattice) of incoming and outgoing electrons together is transformed to another set of iso-spin by $\Sigma^y \Sigma^i$ and so are pseudo-spin (valley) and spin but by $\Lambda^y \Lambda^l$ and $s^y s^j$ respectively. This transformation does nothing but changes the basis of states such that the states for $l = 0, x, y, z$ (same for i, j) are singlet, triplet states for two incoming/outgoing states. Then we can rewrite the modified Cooperon as

$$\begin{aligned} C_{lij}^{l'i'j'}(Q,\omega) =& \delta_l^{l'} \delta_i^{i'} \delta_j^{j'} + \frac{1}{4} \sum_{l'',i'',j''} C_{l'',i'',j''}^{l',i',j'}(Q,\omega) \times \\ & \int \frac{d^2 p''}{(2\pi\hbar)^2} Tr\left[\langle V_{p_+ p''_+} M^\dagger_{lij} V_{p''_- p'_-} \rangle G^r(p''_+, \epsilon_+) M_{l''i''j''} \left[G^a(p''_-, \epsilon_-) \right]^T \right] \\ =& \delta_l^{l'} \delta_i^{i'} \delta_j^{j'} + \sum_{l'',i'',j''} \zeta_{l,i,j}^{l'',i'',j''}(Q,\omega) C_{l'',i'',j''}^{l',i',j'}(Q,\omega) \end{aligned} \tag{2.65}$$

and the equation of motion for modified Cooperon

$$\sum_{l'',i'',j''} \left[\delta_l^{l''} \delta_i^{i''} \delta_j^{j'} - \zeta_{l,i,j}^{l'',i'',j''}(Q,\omega) \right] C_{l'',i'',j''}^{l',i',j'}(Q,\omega) = \delta_l^{l'} \delta_i^{i'} \delta_j^{j'}. \tag{2.66}$$

Though there are many elements in C, only a few of them will contribute the conductivity. The relevant channels depend on the details of the system, and thus the corresponding quantum conductivities can show WAL/WL/U.

So far, we did nothing but re-wrote the Cooperon in the new bases. To simplify the calculation, here I made a few assumptions:

- Weak disorder regime $\lambda_F l_e \gg 1$
- Weak magnetic field effect $\omega_c \tau_e \ll 1$

- Other stronger disorder sources dominating the scatting process–intra-valley scattering $u\mathbb{I} > u_{nm}\Sigma^n\Lambda^m >$ adatom's couplings.
- Uncorrelated disorder correlators

This method is straightforward and easy in calculation with the last two assumptions. In this new basis, u all $\Lambda\Sigma$ combinations are all diagonalized as shown in the following derivation, and thus the corresponding channels are all gapped out and have little contribution to conductivity. Therefore, only 4 out of 64 are the leading contributions and their residuals are basically $\sim \tau_e$ times an number and we only need to evaluate a 4×4 Cooperon matrix.

In the following few subsections, we will re-examine the Cooperon obtained from this approach and derive the Cooperon for the homogeneous SOC.

Case I: Static disorder

Consider the most common onsite spin-independent disorder $u\hat{I}$ with correlation $\langle u(r)u(r')\rangle = u^2\delta(r-r')$ with density n_a. By plugging the correlator into Eq. (2.66), we find that only diagonal channels of $l = l'$ and $j = j'$ will survive and thus the equation of motion for $C(Q)$ can be reduced to

$$\begin{pmatrix} -i\omega\tau + \frac{1}{2}v^2Q^2\tau^2 & -\frac{i}{2}v_FQ_x\tau & -\frac{i}{2}v_FQ_y\tau & 0 \\ -\frac{i}{2}v_FQ_x\tau & \frac{1}{2} & 0 & 0 \\ -\frac{i}{2}v_FQ_x\tau & 0 & \frac{1}{2} & 0 \\ 0 & 0 & 0 & 1 \end{pmatrix} C^{lj} = 1 \tag{2.67}$$

where $\tau = \hbar/2\pi\gamma(p_F)n_au^2$. At low energy and weak disorder limit ($Q, \omega \to 0$), the divergence of the first element in C^{lj} (i.e. C^{l0j}_{l0j}) suggests that the modified Cooperon corresponding to iso-spin singlets $i = 0$ is the dominating scattering process in quantum transport. The Cooperon $\tilde{C}$ has a simple relationship with the modified Cooperon:

$$\tilde{C}^{lj}(Q) = u^2\zeta(Q,\omega)C^{lj} \sim u^2C^{lj} \tag{2.68}$$

and we can even rescale the Cooperon to $\bar{C}$ where $\bar{C}^{lij} = \frac{2\tau^2\pi\nu(p_F)}{\hbar}C^{lij}$ such that the rescaled Cooperon satisfies the Schrodinger equation

$$\left[D(i\nabla + \frac{2e}{c\hbar}A)^2 + \Gamma_{lij} + \tau_\phi^{-1} - i\omega\right]\bar{C}_{lij}(r,r') = \delta(r-r') \tag{2.69}$$

where τ_ϕ is the decoherence rate, the cutoff of the quantum interference. For onsite disorder $u\hat{I}$, the iso-spin triplets $i = x, y, z$ are all gapped out with the gap size

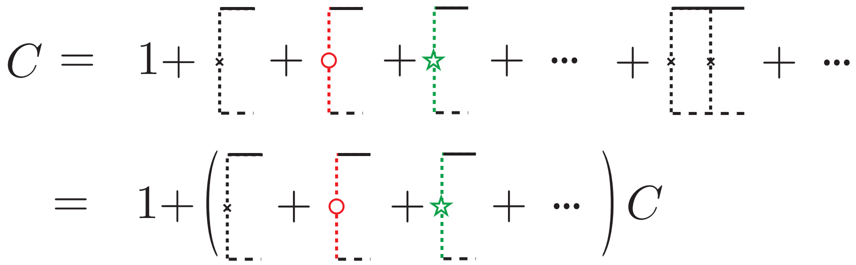

Figure 2.6: The modified Cooperon diagrams. Different colors represent different correlators.

$\Gamma_{lij} = 0$ have little contribution to the quantum transport. If we further consider more disorder types, including intervalley scattering, as shown in the paper [4], more channels will be gapped out, except for channels C^{00j}, which are isospin singlet and pseudo-spin singlet. Generally, the graphene experiments have lots of disorder, including both inter-valley and intra-valley scattering, from substrate or other sources; therefore in the following subsections, we assume that the graphene has strong disorder and only focus on the adatom effects on the aforementioned four Cooperon channels C^{00j}.

Case 2: d-orbital Adatoms

Consider the disorder induced by d-orbital adatoms as in Eq. (2.10) with correlation $\langle V(\mathbf{k},\mathbf{k}')V(\mathbf{k}',\mathbf{k})\rangle = nV_{\alpha,\gamma}V_{\delta,\beta}$ where $\alpha,\beta,\gamma,\delta$ refer to the quantum state $|\tau,\sigma,s\rangle$. With 25 different disorder correlators, the modified Cooperon can be grouped diagrammatically as in Fig. 2.6 which suggests ζ in Eq. (2.66) is simply the addition of all the possible correlators. After some simple algebra, we find that system will be largely gapped out with gaps

$$\begin{aligned} \Gamma_{000} &= 0 \\ \Gamma_{00x} = \Gamma_{00y} &= \tau^{-1}_{\lambda_i} + \tau^{-1}_{\lambda_{\mathrm{KM}}} + \tau^{-1}_{\lambda_R} \\ \Gamma_{00z} &= 2\tau^{-1}_{\lambda_R} \end{aligned} \tag{2.70}$$

where the SOCS rates are $\tau^{-1}_{\lambda_{i/KM}} = 2\pi n_a \nu \lambda^2_{i/KM} A_{\hexagon}/\hbar$ and $\tau^{-1}_{\lambda_{\mathrm{R}}} = \pi n_a \nu \lambda^2_{\mathrm{R}} A_{\hexagon}/\hbar$. Note that all off-diagonal in correlators only have higher order contribution in Q.

Case 3: p-orbital Adatoms

Consider momentum dependent disorder,

$$\zeta^{l,l''}_{s,s''}(\mathbf{Q},\omega) = \int d\mathbf{k}'\mathrm{Tr}\left[M^{l\dagger}_{s}V(\mathbf{q})G^{r}(\mathbf{k}',\epsilon_{+})M^{l''}_{s''}G^{a}(\mathbf{Q}-\mathbf{k}',\epsilon_{-})^{T}V(\mathbf{q})^{T}\right] \tag{2.71}$$

which can be view as

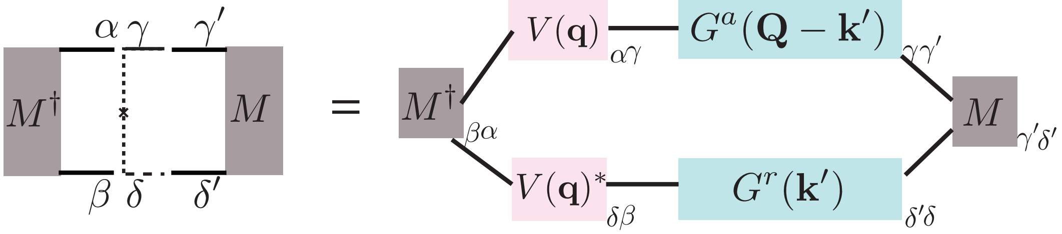

(2.72)

where the indices show how these matrices are connected. Note that $\mathbf{k}' - \mathbf{k} = \mathbf{q}$. The Cooperon gap is

$$\begin{aligned}
\Gamma_{000} &= 0 \\
\Gamma_{00x} &= \tau_{\lambda_i}^{-1} + \tau_{\lambda_{\mathrm{KM}}}^{-1} + 4\tau_{\lambda_i^{(1)}}^{-1} + 14\tau_{\lambda_{\mathrm{R}}^{(1)}}^{-1} \\
\Gamma_{00y} &= \tau_{\lambda_i}^{-1} + \tau_{\lambda_{\mathrm{KM}}}^{-1} + 4\tau_{\lambda_i^{(1)}}^{-1} + 10\tau_{\lambda_{\mathrm{R}}^{(1)}}^{-1} \\
\Gamma_{00z} &= 24\tau_{\lambda_{\mathrm{R}}}^{-1}
\end{aligned} \tag{2.73}$$

where $\hbar\tau_{\lambda_{\mathrm{R}}^{(1)}}^{-1} = n_a\pi\nu(\lambda_{\mathrm{R}}^{(1)})^2k^2a^2A_{\hexagon}$ and $\hbar\tau_{\lambda_i^{(1)}}^{-1} = n_a\pi\nu(\lambda_i^{(1)})^2k^2a^2A_{\hexagon}$.

Case 4: Homogeneous SOCs

If the induced SOCs, e.g. from the substrate, are homogeneous, the Green function of graphene needs to be modified as

$$G^r(p,\epsilon) = \frac{1}{\epsilon + i\eta - v\vec{\Sigma}\cdot\vec{p} - H_{so}}. \tag{2.74}$$

Strictly speaking, the homogeneous SOCs does not relax spin orientation since an electron traveling through the mesoscopic system is always in an eigenstate. However, if any background disorder, such as $u\mathbb{I} + \sum_{mn} u_{mn}\Lambda^m\Sigma^n$, exists, it will cause the spin relaxation with the none-zero ξ

$$\begin{aligned}
\zeta_{s,s''}^{l,l''}(Q,\omega) &= \frac{u^2}{4}\int\frac{d^2p}{(2\pi\hbar)^2}\mathrm{Tr}\left[M_s^{l\dagger}G^r(p,\epsilon_+)M_{s''}^{l''}G^a(Q-p,\epsilon_-)^T\right] \\
&= \delta_{ll''}\frac{u^2}{4}\int\frac{d^2\mathbf{k}}{(2\pi)^2}\mathrm{Tr}\left[\Sigma^s\Sigma^yG^r(p,\epsilon_+)\Sigma^y\Sigma^{s''}G^a(Q-p,\epsilon_-)^T\right]
\end{aligned} \tag{2.75}$$

For example, the KM SOC has extra contribution to Cooperon

$$\Gamma_{0,z}^l = -\frac{1}{2}\frac{\lambda^2}{E^2}\frac{1}{\tau_0} \longrightarrow 0 \tag{2.76a}$$

$$\Gamma_{x,y}^l = \frac{1}{2}\frac{\lambda^2}{E^2}\frac{1}{\tau_0} \longrightarrow \frac{\lambda^2}{E^2}\frac{1}{\tau_0} = \frac{1}{\tau_{KM}} \tag{2.76b}$$

, where the self-energy is shifted by absorbing the minus sign into the phase rates.

Magneto-conductivity

The magneto-conductivity can be greatly simplified in the hidden symmetry space too. Again, consider the only spin-independent scattering case which can be easily generalized to SOC scatters. The conductivity, current-current correlation, can be written as

$$\begin{aligned}\delta\sigma_{xx} &= 2\frac{e^2\hbar}{\pi}\mathrm{T}r\left[\tilde{V}_x(k,\omega^-,\omega^+)\tilde{C}(Q,\omega)\tilde{V}_x(Q-k,\omega^+,\omega^-)\right]\\ \tilde{V}_x(k,\omega_1,\omega_2) &= G^r(k,\omega_1)\tilde{v}_x(k,\omega_1,\omega_2)G^a(k,\omega_2)\end{aligned}$$

where $\tilde{V}_x$ is a current operator. 2 is from the spin degeneracy. If we work in the new basis $\{\Lambda,\Sigma\}$ with the inverse transform of basis changing equation

$$C^{\gamma\delta,\gamma'\delta'}_{\alpha\beta,\alpha'\beta'} = \frac{1}{4}\sum_{ll'ss'}\left(M^{l\dagger}_{s}\right)^{\delta\gamma}_{\beta\alpha}C^{ll'}_{ss'}\left(M^{l'}_{s'}\right)^{\gamma'\delta'}_{\alpha'\beta'} \tag{2.77}$$

where $M^l_s = \Sigma^y\Sigma^s\Lambda^y\Lambda^l$ and

$$\begin{aligned}\delta\sigma_{xx} &= \frac{e^2\hbar}{2\pi}\mathrm{T}r\left[\left(M^{l'}_{s'}\right)^{\gamma'\delta'}_{\alpha'\beta'}V_x(k,\omega^-,\omega^+)^{\delta'\gamma}_{\beta'\alpha}V_x(Q-k,\omega^+,\omega^-)^{\gamma'\delta}_{\alpha'\beta}\left(M^{l\dagger}_{s}\right)^{\delta\gamma}_{\beta\alpha}\tilde{C}^{ll'}_{ss'}(Q,\omega)\right]\\ &= \frac{e^2\hbar}{2\pi}\mathrm{T}r\left[V^t_x(Q-k,\omega^+,\omega^-)M^{l'}_{s'}V_x(k,\omega^-,\omega^+)M^{l*}_{s}\tilde{C}^{ll'}_{ss'}(Q,\omega)\right]\\ &= \frac{e^2\hbar}{2\pi}\mathrm{T}r\left[Z^{ll'}_{ss'}\tilde{C}^{ll'}_{ss'}(Q,\omega)\right]\end{aligned} \tag{2.78}$$

which can be further simplifed to

$$\delta\sigma_{xx} = -\frac{e^2\hbar}{2\pi}\mathrm{T}r\left[Z^0\left(\tilde{C}^x(Q,\omega)+\tilde{C}^y(Q,\omega)+\tilde{C}^z(Q,\omega)-\tilde{C}^0(Q,\omega)\right)\right] \tag{2.79}$$

because only $\tilde{C}^l_{00}$ is gapless, leading to $l = l'$. Also, $Z^l = -Z^0$ due to the property of M:

$$M^l = M^0\Lambda^l, \quad M^lM^{l*} = M^0\Lambda^lM^{0*}(\Lambda^l)^* = -M^0M^{0*} \tag{2.80}$$

and the operator Λ^l commutes with G and Γ_x. Now the only thing we need to figure out is Z^0,

$$\begin{aligned}Z^0 &= V^t_x(Q-k,\omega^+,\omega^-)\Sigma^y\Lambda^yV_x(k,\omega^-,\omega^+)\Sigma^y\Lambda^y\\ &= V^t_x(Q-k,\omega^+,\omega^-)\Sigma^yV_x(k,\omega^-,\omega^+)\Sigma^y\\ &= G^r(Q-k,\omega^+)\tilde{v}_x(Q-k,\omega^+,\omega^-)G^a(Q-k,\omega^-)\Sigma^yG^a(k,\omega^-)\tilde{v}_x(k,\omega^-,\omega^+)G^r(k,\omega^+)\Sigma^y.\end{aligned} \tag{2.81}$$

Since $C^l(Q, \omega)$ depends on the total momentum Q and the contribution from small Q dominates the summation, Z^0 can be replaced with

$$Z^0 = -\frac{2\pi^2}{v\eta^3}\frac{p_F}{(2\pi\hbar)^2}v^2 = -4\frac{E_F\tau^3}{\hbar^5} \tag{2.82}$$

$$\delta\sigma_{xx} = 4\frac{e^2\hbar}{2\pi}\frac{E_F\tau^3}{\hbar^5}\int\frac{d^2Q}{(2\pi)^2}\left(\tilde{C}^x(Q,\omega) + \tilde{C}^y(Q,\omega) + \tilde{C}^z(Q,\omega) - \tilde{C}^0(Q,\omega)\right) \tag{2.83}$$

in the limit of $Q = 0$ and $\omega = 0$. If we consider the other two diagrams as in the McCann (each of them contributes $-\frac{1}{4}$ of the above diagram) and re-organize the coefficient, the total conductivity correction reads

$$\delta\sigma_{xx} = \frac{2e^2}{\pi\hbar}\frac{v_F^2\tau}{2}\int\frac{d^2Q}{(2\pi)^2}\left(\bar{C}^x(Q,\omega) + \bar{C}^y(Q,\omega) + \bar{C}^z(Q,\omega) - \bar{C}^0(Q,\omega)\right) \tag{2.84a}$$

$$= \frac{2e^2}{\pi\hbar}D\int\frac{d^2Q}{(2\pi)^2}\left(\bar{C}^x(Q,\omega) + \bar{C}^y(Q,\omega) + \bar{C}^z(Q,\omega) - \bar{C}^0(Q,\omega)\right) \tag{2.84b}$$

$$= \frac{e^2}{\pi h}D\sum_{l=0,x,y,z} c_l \ln\left(\frac{\tau^{-1}}{\tau_\phi^{-1} + \Gamma^l}\right) \tag{2.84c}$$

where $D \longrightarrow D^*$ if we consider diffuson contribution. We can further include the magnetic field in this system and obtain magnetoconductivity,

$$\delta\sigma_{xx}(B) = 2\frac{e^2D}{\pi\hbar}\sum_{l=0,x,y,z} c_l\frac{eB}{\pi\hbar}\sum_{n=0}^{\tau_B/\tau} C^l(q_n) \tag{2.85a}$$

$$\Delta\sigma_{xx}(B) = \delta\sigma_{xx}(B) - \delta\sigma_{xx}(0) \tag{2.85b}$$

$$= -\frac{e^2D}{\pi h}\sum_{l=0,x,y,z} c_l F\left(\frac{B}{B_\phi + \Gamma^l}\right), \tag{2.85c}$$

$$B_i = \frac{\hbar c}{4De}\tau_i^{-1} \tag{2.85d}$$

$$F(z) = \ln z + \psi\left(\frac{1}{2} + \frac{1}{z}\right) \tag{2.85e}$$

where ψ is the Digamma function. The above derivation for spin-independent disorder can be easily generalized to be spin-dependent one with the modified MC

$$\delta\sigma_{xx}(B) = -\frac{e^2D}{2\pi\hbar}\sum_{l,j=0,x,y,z} c_l c_j F\left(\frac{B}{B_\phi + B_j^l}\right). \tag{2.86}$$

The indices l, j label the iso-spin and spin degrees of freedom. In the hidden symmetry approach, one can easily obtain the MC by calculating the Cooperon gaps.

2.4 Correlated versus uncorrelated disorder

So far we have used two approaches to evaluate the MC. The first approach is to directly solve for the Cooperon and the conductivity, and it is also easier to include the correlated disorder in this approach. However, we can only analytical solve a few uncorrelated and simply correlated cases since we always consider full dimension 64-by-64 matrix and its inversion can be technical/unsolvable. On the other hands, the calculation will be greatly simplified if we transform the system into a new basis -singlet, triplets- associated with hidden symmetries of the model and take the assumptions of $u \gg$ adatom's coupling. In the new basis, the Cooperon of the normal disorder $\mathbb{I}$ and $\Sigma_s \Sigma_l$ is diagonalized at zeroth order in momentum, and has big Cooperon gaps, leading to negligible MC. Due to these giant Cooperon gaps, SOCs's leading contribution is only important and can only be seen in four gapless channels. In this case, we can easily solve all types of uncorrelated disorders, but incorporation of correlated disorder is very difficult. We checked that both approaches give the same results for the uncorrelated cases.

To understand how the correlations affect the results, we numerically solve for the Cooperon gaps by using the first approach. We numerically solved Os adatom case with 0.1% coverage. The following singular points are the poles-Cooperon gaps ranging from 0 to $0.05eV$

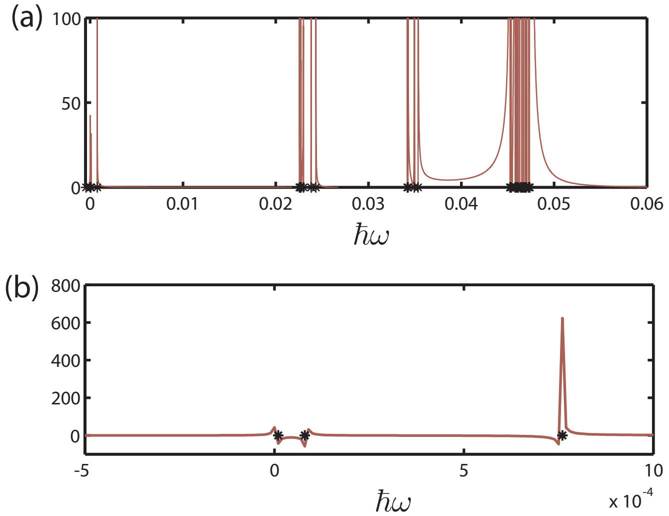

(2.87)

where only the smallest ones around 0 are the leading contribution in MC and the rest are negligible. If we further zoom in around origin point, we can see three peaks and these three peaks (blue dotted line below) are the extremely close to the value obtained analytically(solid red line)–$(0, 2\pi\nu\lambda_{\mathrm{KM}}^2 + 2\pi\nu\lambda_i^2 + 2\pi\nu\lambda_{\mathrm{R}}^2, 4\pi\nu\lambda_{\mathrm{R}}^2)$

throughout the whole studied carrier density range.

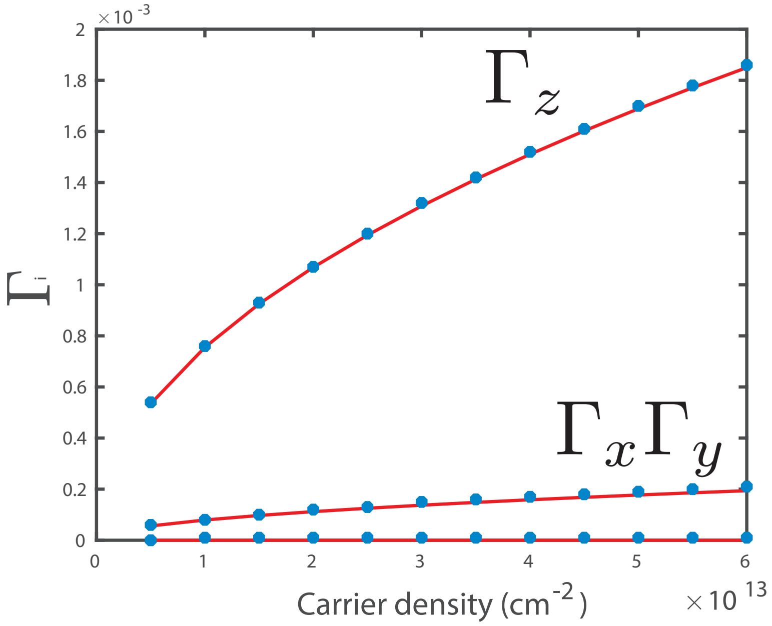

(2.88)

So it suggests that the correlation is negligible in Os case.

BIBLIOGRAPHY

[1] Shinobu Hikami, Anatoly I. Larkin, and Yosuke Nagaoka. Spin-orbit interaction and magnetoresistance in the two dimensional random system. *Progress of Theoretical Physics*, 63(2):707–710, 1980. doi: 10.1143/PTP.63.707.

[2] Denis Kochan, Susanne Irmer, and Jaroslav Fabian. Model spin-orbit coupling hamiltonians for graphene systems. *Phys. Rev. B*, 95:165415, Apr 2017. doi: 10.1103/PhysRevB.95.165415.

[3] E. McCann, K. Kechedzhi, Vladimir I. Fal'ko, H. Suzuura, T. Ando, and B. L. Altshuler. Weak-localization magnetoresistance and valley symmetry in graphene. *Phys. Rev. Lett.*, 97:146805, Oct 2006. doi: 10.1103/PhysRevLett.97.146805.

[4] Edward McCann and Vladimir I. Fal'ko. $z \rightarrow -z$ symmetry of spin-orbit coupling and weak localization in graphene. *Phys. Rev. Lett.*, 108:166606, Apr 2012. doi: 10.1103/PhysRevLett.108.166606.

[5] Jorgen Rammer. *Quantum Transport Theory*. CRC Press, 2018. ISBN 0429971389, 9780429971389.

Chapter 3

QUANTUM TRANSPORT THEORY

Transport experiments have been a great tool to measure electrical properties, probe phases of matter, and uncover novel physical phenomena. From the classical perspective, free electrons traveling in a spatially-periodic potential experience a series of collisions like pinballs according to the equations of motion. The electrical conduction is well-described by the *Drude model* [1] which yields the equation of motion,

$$\frac{d}{dt}\langle \mathbf{p}(t)\rangle = e\big(\mathbf{E} + \frac{\langle \mathbf{p}(t)\rangle \times \mathbf{B}}{m}\big) - \frac{\langle \mathbf{p}(t)\rangle}{\tau} \tag{3.1}$$

and a linear relationship between current density $\mathbf{J}$ and electric field $\mathbf{E}$

$$\mathbf{J} = \left(\frac{ne^2\tau}{m}\right)\mathbf{E}. \tag{3.2}$$

Here $\langle \mathbf{p}(t)\rangle$ is the average momentum per electron at time t, and e, m, n, τ are electron charge, mass, density, and mean free time between two collisions respectively. From the relationship between current and electric field $\mathbf{J} = \sigma\mathbf{E}$, we find the conductivity $\sigma = \frac{ne^2\tau}{m}$. This model provides a good explanation of DC and AC conductivity in metals, the Hall effect, and the magnetoresistance in metals near room temperature.

This model was later supplemented with the quantum theory by Arnold Sommerfeld and Hans Bethe, leading to the Drude-Sommerfeld model [1]. From this semi-classical perspective, electrons are wave packets (plane-waves or Bloch waves) $f(\mathbf{r}, \mathbf{p}, t)$ instead of pinballs and carry energy/momentum according to the band structure of the crystal. Electrons traveling into the device have an effective mass determined by the band structure and interactions; their scattering processes also reflect the disorder configuration in the system. Note that this is still a free electron model but the electrons are treated quantum mechanically—identical and indistinguishable, following Fermi-Dirac statistics. The evolution of the wave packets of state i can be described by

$$\frac{df_i}{dt} = I[f] \tag{3.3}$$

and the Boltzmann equation

$$\frac{df}{dt} = \frac{\partial f}{\partial t} + \mathbf{v}\nabla f + \dot{\mathbf{p}}\frac{\partial f}{\partial \mathbf{p}}. \tag{3.4}$$

At equilibrium, which is a stationary solution, there is no net flow of particles, i.e. $I[f] = 0$. Slightly away from equilibrium, $I[f] = -(f - f_{eq})/\tau$ is a linear function with scattering time τ derived from microscopic model such as Born approximation [1]. On the other hand, the Boltzmann equation describes the statistical behavior of a thermodynamic system out of equilibrium from which we can draw the connection between the electric field and current density yielding the conductivity. Consider an isotropic impurity potential $V(\mathbf{r}) = \sum_i v(\mathbf{r})$. For example, the conductivity for the free electron gas is

$$\sigma = \frac{1}{3}e^2(gv^2\tau)_{\epsilon=\mu} \tag{3.5}$$

where g is the density of states at energy ϵ. This expression can be traced back to the Drude conductivity $\sigma = \frac{ne^2\tau}{m}$.

At low temperature, when the system size is small enough with a long phase coherence length, the semi-classical theory is insufficient to describe such a *mesoscopic system*. When the electrons are coherent, different scattering processes interfere with each other. Although simple intuition suggests that the phases associated with multiple scattering average to zero and have no effect on the conductivity, all of the scattering paths and their time-reversal scattering paths, in fact, constructively interfere in a conventional 2-dimensional system, causing electrons to localize in the system. This quantum coherence effect in a conventional 2-dimensional system is also called *weak localization.* Depending on the details of the system and dimensionality, the quantum interference can be neutral, constructive, or destructive. There are a few approaches to study mesocopic systems: diagrammatic theory for a homogeneous, weakly disordered system (translationally invariant) in the thermodynamic limit and/or a quantum transport simulation for a non-homogeneous, small size system. We have explored the diagrammatic approach in the previous chapter. In this chapter, we will discuss how to simulate the transport of a mesocopic system efficiently.

Most simulations in this thesis are done with the Landauer-Büttiker approach [6, 7] as the foundation for numerical simulations of quantum transport. Therefore, we will present a pedagogical derivation of the Landauer theorem and describe the implementation of this theory for simulation of quantum transport in microscopic models. In the last section, we also briefly introduce another common tool for quantum transport: O(N) real-space algorithms of the diagonal Kubo formula [9], and comment on the discrepancies between the two tools.

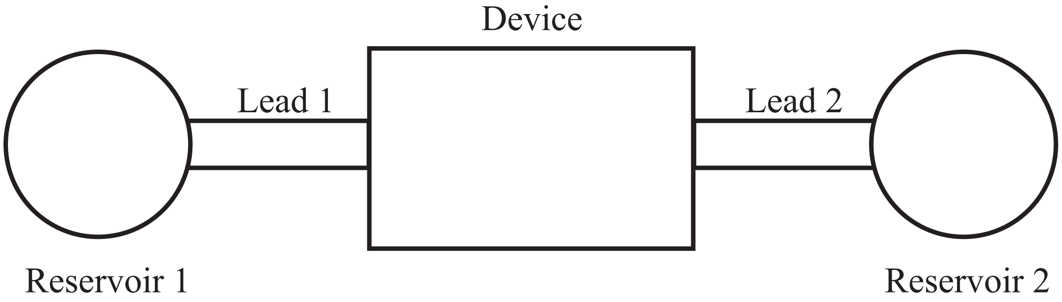

Figure 3.1: Typical setup for the Landauer-Büttiker formalism. Two (or more) reservoirs are connected via long and translational invariant leads to a mesoscopic device.

3.1 Landauer-Büttiker formalism

In 1957, Landauer proposed a new perspective on electron transport[6, 7]: “we can view the carriers introduced at the boundaries of the sample as the source of transport, and then ask how the resulting build-up of carriers produces fields." At that time, he treated the electrons semi-classically and assumed that scatterers act incoherently. This idea sparked many generalizations to the quantum coherent setting, most notably by Büttiker [2], where the conductance of a mesoscopic sample is related to the transmission properties of electrons. This theory is now called the Landauer-Büttiker formalism. It has wide applications and is the corner stone of quantum transport theory and simulation.

Consider a mesoscopic sample connected to electron reservoirs via leads, as shown in the Fig 3.1. The reservoirs provide thermalized electrons that flow into the metallic lead without dissipation. Furthermore, the leads are considered to be *perfect* (dissipation-less) and translationally-invariant in the propagating direction. Electrons from the reservoirs enter the leads without reflection, but the contact friction generates resistance - one of the main sources of resistance in the system. All of the incident electrons are either transmitted from one lead to another or are reflected back to the same leads. Hence, the conductance is related to the transmission rate $\mathcal{T}$. Therefore, the conductance of a two-terminal setup at zero temperature, for example, is described by the Landauer formula:

$$G = \frac{e^2}{h}\mathcal{T}. \tag{3.6}$$

As shown by Büttiker, this formula can be generalized to a multi-lead geometry and to the case in which a magnetic field is present. Since this formula is used to deal with a finite system, we need to be careful in dealing with finite size effects. First, the lead, though metallic in experiments, provides quantized transverse modes due to a finite width. Therefore, the wavefunctions in the leads can be written in the form $e^{ik_x x}\phi_m(y)$ where transverse modes $\phi_m(y)$ are also referred to as eigen-channels or extended Bloch waves with longitudinal wave numbers k_m. According to the Landauer formula, the conductance of a finite sample can be expressed as

$$G = \frac{e^2}{h}\sum_m T_m(E_F) \tag{3.7}$$

where the total transmission rate is a summation of the transmission probability T_m of channel m. Here below, I provide a heuristic, intuitive derivation of this formula, following S. Datta Electronic *Transport in Mesoscopic Systems* in Ref. [4]. Readers who are interested a more rigorous derivation are referred to Ref. [3].

Consider a two-probe setup with leads $\alpha = L, R$. The electrons in the leads, with wave vector k_x and energy E, obey the Fermi-Dirac distribution $f(E-\mu_\alpha)$ where μ_α is the chemical potentials of the connected reservoirs. Assuming the leads are ballistic and finite, each has M transverse modes. Then the m-th mode injected into the system from lead L will transmit to lead R with the average probability T_m. We know that the current carried by n non-interacting electrons per unit length with velocity v is env. Therefore, the transverse mode m of lead α carries an electric current,

$$I_{\alpha m}(E) = \frac{2e}{L}\sum_k v(k)T_m(E)f(E-\mu_\alpha), \tag{3.8}$$

across a sample of length L. The velocity $v(k)$ refers to group velocity and the factor of 2 arises from spin degeneracy. The net current is obtained by calculating the difference between the currents originating from two leads and summing over all quantum channels:

$$\begin{aligned} I &= \sum_m \left(I_{Ln}(E) - I_{Rn}(E)\right) \\ &= \frac{2e}{L}\sum_{n,k} T_m(E)v(k)\left[f(E-\mu_L) - f(E-\mu_R)\right]. \end{aligned} \tag{3.9}$$

We can further convert this into energy space as

$$I = \frac{2e}{h}\sum_m \int dE\, T_m(E)\left[f(E-\mu_L) - f(E-\mu_R)\right] \tag{3.10}$$

by using the definition of group velocity $v(k) = \frac{1}{\hbar}\frac{dE}{dk}$. This equation describes the current flowing in the sample with a potential drop between two leads: $V = (\mu_R - \mu_L)/e$. Hence, we can also obtain conductance $G = I/V$ by dividing Eq. (3.10) with the voltage V across the sample.

Assuming zero temperature, net current flow takes place entirely in the energy range $\mu_L > E > \mu_R$. We can further simplify Eq. (3.10) by Taylor expansion of $f(E - \mu_L) - f(E - \mu_R)$ in E around the Fermi energy, leading to $f(E - \mu_L) - f(E - \mu_R) \sim \delta(E - E_F)(\mu_L - \mu_R)$. Inserting these approximation into Eq. (3.10) and dividing by V, one would recover the Landauer formula:

$$G = \frac{2e^2}{h} \sum_n T_n(E_F) = \frac{2e^2}{h} \cdot \mathcal{T}(E_F). \tag{3.11}$$

We define the total transmission coefficient $\mathcal{T}$ as the sum of all transmission probabilities $T_m(E_F)$. The above derivation can easily be generalized to systems with more than two probes. In a N-probe system, the total current through lead α is the summation of all the current flowing out of lead-α and currents flowing into lead-α from other leads, which can be written as

$$I_\alpha = \frac{2e}{h} \sum_{\beta \neq \alpha} [\mathcal{T}_{\beta\alpha}(E_F)\mu_\alpha - \mathcal{T}_{\alpha\beta}(E_F)\mu_\beta] \tag{3.12}$$

where $T_{\alpha\beta}(E_F)$ is the total transmission coefficient from lead-α to lead-β. Since the current is conserved, the above equation can be simplified with the property- $\sum_\alpha \mathcal{T}_{\alpha\beta} = \sum_\beta \mathcal{T}_{\alpha\beta}$. After some algebra, we obtain the conductance between leads α, β as desired,

$$G_{\alpha\beta} = \frac{2e^2}{h} \mathcal{T}_{\alpha\beta}(E_F). \tag{3.13}$$

The is the generalized Landauer formula for a multi-terminal setup. In the next section, we will discuss how to implement this formalism from microscopic point of view.

3.2 Fisher-Lee relation: connecting the transmission coefficient to the Green's function

The transmission coefficient can be expressed in terms of the Green's function by using Fisher-Lee relation [5]. The Landauer formula describes the conductance in terms of transmission probability,

$$G = \frac{2e^2}{h} \cdot \mathcal{T}(E_F) = \frac{2e^2}{h} Tr[t^\dagger t] \tag{3.14}$$

and the probability $\mathcal{T}$ can be further connected to the transmission matrix across the system t in the scattering S matrix:

$$S = \begin{pmatrix} r & t' \\ t & r' \end{pmatrix}. \tag{3.15}$$

This scattering matrix element can be expressed in terms of Green's function between two interfaces $G^r_{LR}(y_R, y_L)$ as

$$s_{nm} = -\delta_{nm} + i\hbar\sqrt{v_n v_m} \int\int \chi_n(y_R)\left[G^r_{RL}(y_R, y_L)\right]\chi_m(y_L) dy_R dy_L \tag{3.16}$$

which is the Fisher-Lee relation. Parameters v_c and $\chi_c(y_\alpha)$ are, respectively, the longitudinal propagation velocity and the transverse wave function in the propagating channel c of lead α. The integration runs over the contact interface region at L/R leads; $n \in L$ and $m \in R$. Plugging Eq. (3.16) into Eq. (3.14), we obtain

$$\begin{aligned}
T &= \sum_n \sum_m s_{nm} s^*_{mn} \\
&= \hbar^2 v_n v_m \int\int\int\int dy_R dy_L dy'_R dy'_L \chi_n(y_R)\left[G^r_{RL}(y_R, y_L)\right]\chi_m(y_L)\chi_m(y'_L)\left[G^r_{LR}(y'_L, y'_R)\right]^* \chi_n(y'_R) \\
&= \hbar^2 v_n v_m \int\int\int\int dy_R dy_L dy'_R dy'_L \chi_n(y_R)\left[G^r_{RL}(y_R, y_L)\right]\chi_m(y_L)\chi_m(y'_L)\left[G^a_{RL}(y'_R, y'_L)\right]\chi_n(y'_R) \\
&= \int\int\int\int dy_R dy_L dy'_R dy'_L \chi_n(y'_R)\hbar v_n \chi_n(y_R)\left[G^r_{RL}(y_R, y_L)\right]\chi_m(y_L)\hbar v_m \chi_m(y'_L)\left[G^a_{RL}(y'_R, y'_L)\right] \\
&= \int\int\int\int dy_R dy_L dy'_R dy'_L \Gamma_R(y'_R, y_R)\left[G^r_{RL}(y_R, y_L)\right]\Gamma_L(y_L, y'_L)\left[G^a_{RL}(y'_R, y'_L)\right] \\
&= \mathrm{T}r\left[\Gamma_R G^r_{RL}\Gamma_L G^a_{RL}\right] \\
&= \mathrm{T}r\left[\Gamma_R G^r_{RL}\Gamma_L \left(G^r_{RL}\right)^\dagger\right]
\end{aligned} \tag{3.17}$$

where

$$\Gamma_L(y_L, y'_L) = \sum_m \chi_m(y_L)\hbar v_m \chi_m(y'_L) \tag{3.18}$$

is the broadening function. Therefore, we can rewrite the Landauer formula as

$$G = \frac{2e^2}{h}\mathrm{T}r\left[\Gamma_L G^r_{LR}\Gamma_R G^a_{LR}\right] = \mathrm{T}r\left[\Gamma_R G^r_{RL}\Gamma_L \left(G^r_{RL}\right)^\dagger\right] \tag{3.19}$$

with the Green's functions across the mesoscopic device G_{LR}/G_{RL} and the broadening function describing the coupling of the device to the leads. The latter can be derived from self-energy Σ,

$$\Gamma = i\left[\Sigma - \Sigma^\dagger\right]. \tag{3.20}$$

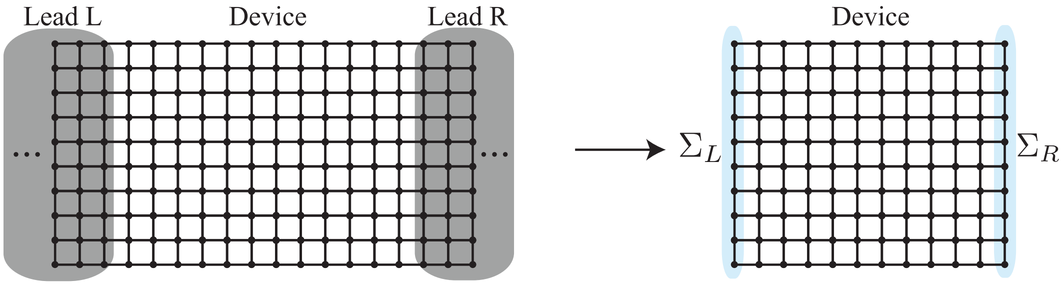

Figure 3.2: The semi-infinite leads can be integrated out and taken into account as self-energy corrections to the device.

The above equations constitute a theoretical framework to calculate the conductance from a microscopic model. However, it is computational expensive and even impossible in practice since the Green's function including semi-infinite leads has infinite lattice sites. In the following, I will describe efficient numerical methods to calculate the Green's function and the self-energy resulting from leads.

3.3 Lattice Green's Function Method

In this section, I will describe an efficient method for calculating the Green's function and broadening function by following the work in Ref. [8]. Given a total Hamiltonian H composed of both device and leads,

$$H = H_D + \sum_i (H_L^i + V_{LD}^i + V_{DL}^i), \tag{3.21}$$

the Green's function is described by

$$G(E) = [E + i\eta - H]^{-1} . \tag{3.22}$$

The term H_D is the Hamiltonian for the device, H_L^i is the Hamiltonian for the lead i, and V_{LD}^i describes the hopping between the lead and the device. Simplifying the above Green's function computation can be accomplished by integrating out the lead degrees of freedom and evaluating their energy contribution to the device Σ_p. This turns out to be easy due to the (half)-translational symmetry. We can rewrite G as

$$G = \left[[E + i\eta]\,\mathbf{I} - \langle i | H_D + \sum_{p=L,R} \Sigma_p | i \rangle \right]^{-1} \tag{3.23}$$

with $\Sigma_p = (V_{LD}^p)^\dagger g_L^p V_{LD}^p$. In the following two subsections, I will explain how to efficiently deal with the device Green's function and the self-energy correction from the leads.

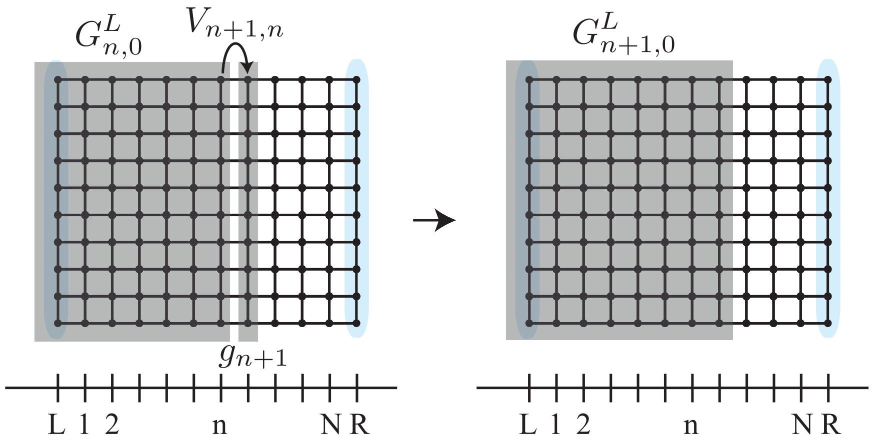

Figure 3.3: By Dyson's equation, the total Green's function can be obtained by stitching each slices together.

Recursive Green's function Method

3.4 Lattice Green's Function Method

Instead of evaluating the total device Green's function at once, it is more efficient to divide the lattice of the device into several sections, calculate the Green's function of each section and glue them together by Dyson's equation,

$$G = g + gVG. \tag{3.24}$$

As shown in the Fig. 3.4, g is the Green's function of disconnected sections, V describes the hopping between the sections, and G is the Green's function of the connected system. Specifically, we first slice the system into N pieces. For each column $i = 1, 2, \ldots, N$, the isolated Greens function g_i is calculated by direct inversion,

$$\begin{aligned} g_i &= \left[[E + i\eta]\,\mathbf{I} - \langle i|H_d|i\rangle\right]^{-1}, \\ g_p &= \left[[E + i\eta]\,\mathbf{I} - \langle i|H_d + \Sigma_p|i\rangle\right]^{-1}. \end{aligned} \tag{3.25}$$

The Hamiltonian for each slice of the device is described by H_d, with the exception of the first and the last columns which also include the self-energy Σ_p ($p = L, R$) of the leads. Then we start from the left end of the device and add the single column one by one. The recursive relation of the conductance can be summarized in the following two equations:

$$G^L_{n+1,n+1} = \left[\mathbf{I} - g_{n+1}V_{n+1,n}G^L_{nn}V_{n,n+1}\right]^{-1} g_{n+1,n+1} \tag{3.26}$$
$$G^L_{n+1,0} = G^L_{n+1,n+1}V_{n+1,n}G^L_{n0}. \tag{3.27}$$

After all the slices are connected, we obtain the left Green's function G^L_{N1}. Similarly, we derive the right Green's function starting from right lead with the recursive relations:

$$G^R_{n,n} = \left[\mathbf{I} - g_nV_{n,n+1}G^R_{n+1,n+1}V_{n+1,n}\right]^{-1} g_{n,n} \tag{3.28}$$
$$G^R_{n,N+1} = G^R_{n,n}V_{n,n+1}G^R_{n+1,N+1}. \tag{3.29}$$

The full Green's function is then

$$G_{n,n} = \left[E - h_n - V_{n,n+1}G^L_{n+1,n+1}V_{n+1,n} - V_{n,n-1}G^L_{n-1,n-1}V_{n-1,n}\right]^{-1} \tag{3.30}$$
$$G_{n,0} = G_{n,n}V_{n,n-1}G^L_{n-1,0} \tag{3.31}$$
$$G_{n,N+1} = G_{n,n}V_{n,n+1}G^R_{n+1,N+1} \tag{3.32}$$
$$G_{n,n-1} = G_nV_{n,n-1}G^L_{n-1,n-1} \tag{3.33}$$
$$G_{n+1,n} = G^R_{n+1,n+1}V_{n+1,n}G_{n,n}. \tag{3.34}$$

If only transmission matrices are required, we can simply close either sweep with a connection to both ends:

1. For the left sweep

   $$G_{N+1,N+1} = \left[\mathbf{I} - g_{N+1}V_{N+1,N}G^L_{N,N}V_{N,N+1}\right]^{-1} g_{N+1} \tag{3.35}$$
   $$G_{N+1,0} = G_{N+1,N+1}V_{N+1,N}G^L_{N0}. \tag{3.36}$$

   where $g_{N+1} = g_R$.

2. For the right sweep

   $$G_{0,0} = \left[\mathbf{I} - g_0V_{0,1}G^R_{1,1}V_{1,0}\right]^{-1} g_0 \tag{3.37}$$
   $$G_{0,N+1} = G_{0,0}V_{0,1}G^R_{1,N+1}. \tag{3.38}$$

   where $g_0 = g_L$.

The above equations yield the right-to-left and left-to-right Green's functions. For systems with inversion symmetry, we expect $G_{00} = G_{N+1,N+1}$ and $G_{0,N+1} = G_{N+1,0}$

and therefore only one sweep is necessary to evaluate the whole scattering matrix. Also, for symmetric leads, and in the absence of an external magnetic field (i.e., time-reversal symmetric systems), the Green's functions satisfy the relation

$$\left[G^r_{N+1,0}\right]^\dagger = \left[G^r_{0,N+1}\right]^* = G^a_{N+1,0} = G^a_{0,N+1} \tag{3.39}$$

and only one sweep is necessary, i.e.

$$G = \frac{2e^2}{h}\mathrm{T}r\left[\Gamma_L G^r_{LR}\Gamma_R\left(G^r_{LR}\right)^\dagger\right]. \tag{3.40}$$

Otherwise, both sweeps are required. From the above setup, we find that this method is only applicable to short-range or finite-range interactions on tight-binding models. For longer range interactions, we have to extend the size of each slice to ensure that each isolated slice only has its H_d and energy contribution V from its nearest-neighbor slices. In this case, the efficiency of the method decreases.

Self-energy of semi-infinite leads

Although the leads are infinite (thermodynamically large), the self-energy can still be greatly simplified by using the recursive Green's function method because of periodicity. The Green's function of a semi-infinite lead has a form of

$$g_L = \left[E + i\eta - H_l\right]^{-1} \tag{3.41}$$

$$= \begin{pmatrix} d & -A & 0 & 0 & . \\ -B & D & -A & 0 & . \\ 0 & -B & D & -A & . \\ 0 & 0 & -B & D & . \\ . & . & . & . & . \end{pmatrix} \tag{3.42}$$

which can be rescaled to another matrix, similar to the original structure but with new elements,

$$d' = d - AD^{-1}B \tag{3.43}$$

$$D' = D - AD^{-1}B - BD^{-1}A \tag{3.44}$$

$$A' = AD^{-1}A \tag{3.45}$$

$$B' = BD^{-1}B \tag{3.46}$$

$$g'_{r,1} = g_{2r-1,1} \tag{3.47}$$

where $r = 2, 3, \ldots$. After sufficient rescaling, A', B' is negligible, the new Green's function of the lead will be $g_{11} \approx d_n^{-1}$. The corresponding retarded self-energy can be determined by

$$[E + i\eta - (h_l + \Sigma_l)]\, g_{11} = 1 \tag{3.48}$$

or

$$\Sigma_L^r(E) = u_L g_L^r u_L^\dagger \quad and \quad \Sigma_R^r(E) = u_R^\dagger g_R^r u_R; \tag{3.49}$$

Either equation yields the same self-energy. Thus, the broadening function Γ can be obtained by using relationship $\Gamma = i\left[\Sigma - \Sigma^\dagger\right]$. With both Green's functions of the device and the self-energy contribution from the leads, one can easily simulate the quantum transport of any system.

3.5 An alternative quantum simulation method-$O(N)$ real-space methods

Another common approach to calculate the static conductivity of a disordered metal is to consider linear response of a system at equilibrium, perturbed by an external voltage—Kubo formulae. In the linear response framework, when the temperature is much lower than the Fermi temperature, the real part of the diagonal conductivity can be well-described by the zero temperature limit conductivity:

$$\mathrm{Re}\ \sigma_{xx}(\epsilon_F, \omega) = \frac{\hbar}{\pi\Omega}\mathrm{Tr}\left[\hat{j}_x \mathrm{Im}\hat{G}^R_{\epsilon_F}\hat{j}_x \mathrm{Im}\hat{G}^R_{\epsilon_F - \hbar\omega}\right]. \tag{3.50}$$

By expanding the above equation on a basis of orthogonal polynomials and by using real-space recursion principle, Roche developed a $O(N)$ *real-space methods* which can efficiently simulate quantum transport in the presence of magnetic field—quantum Hall effect. The key point of this algorithm is to rescale the density of states and then make a polynomial expansion of the associated Kubo formula; thus, instead of diagonalizing the total Hamiltonian, one only needs to take N recursion steps to obtain conductivity. We refer the readers to Ref. [9] for more details.

The Kubo formalisms and Landauer formalism are equivalent and can be derived from one to another. Landauer formalism is particularly convenient if we want to study a complex geometric system where there is no equivalent to the Kubo description. Though Landauer formulae has higher flexibility in dealing complicated system, it is also very time consuming since diagonalizing an N-state Hamiltonian requires CPU time scaling as $O(N^3)$. Even with recursive Green's function method, the scaling is still $O(N^2)$. $O(N)$ real-space methods provides an efficient route to tackle larger, strongly disordered, quasiperiodic, and inhomogeneous systems. Note that this method implicitly requires taking the limit of an infinite system. In this thesis, we focus on small weak disordered system, probing magneto-conductance; therefore, Landauer-Büttiker formalism, though more time-consuming, is a proper choice in this context.

BIBLIOGRAPHY

[1] N. VV. Ashcroft and N. D. Mermin. *Solid State Physics*. Sannderg College. Philadel phia., 1965.

[2] M. Büttiker. Absence of backscattering in the quantum hall effect in multiprobe conductors. *Phys. Rev. B*, 38:9375–9389, Nov 1988.

[3] Horia D. Cornean, Arne Jensen, and Valeriu Moldoveanu. A rigorous proof of the landauer–büttiker formula. *Journal of Mathematical Physics*, 46(4):042106, 2005.

[4] Supriyo Datta. *Electronic Transport in Mesoscopic Systems*. Cambridge University Press, 3 edition, 1995.

[5] Daniel S. Fisher and Patrick A. Lee. Relation between conductivity and transmission matrix. *Phys. Rev. B*, 23:6851–6854, Jun 1981.

[6] R. Landauer. Spatial variation of currents and fields due to localized scatterers in metallic conduction. *IBM J. Res. Dev.*, 1(3):223–231, July 1957.

[7] Rolf Landauer. Electrical resistance of disordered one-dimensional lattices. *Philosophical Magazine*, 21(172):863–867, 1970.

[8] Caio H. Lewenkopf and Eduardo R. Mucciolo. The recursive green's function method for graphene. *J. Comput. Electron.*, 12(2):203–231, June 2013.

[9] Stephan Roche. Quantum transport by means of O(n) real-space methods. *Phys. Rev. B*, 59:2284–2291, Jan 1999.

Chapter 4

QUANTUM TRANSPORT SIMULATION RESULTS

We use the Landauer Büttiker formalism to study devices with hexagonal structures and explore various variations of the graphene device. In this chapter, we will discuss how to model graphene-based devices effectively and efficiently, including the device itself, external leads, disorder, and magnetic fields; then we will discuss a few elements that arise in the realistic simulation of a topological insulator—contact mismatch minimization, finite size effects, diffusiveness, and magnetoconductance.

4.1 Landauer-Büttiker implementation on graphene

Modeling graphene device

Consider a graphene-based device of width w and length L. We employ operators $c^\dagger_{\mathbf{r}\alpha}$ to create a spin-α electron on the carbon atom at site $\mathbf{r}$; throughout, indices such as α are implicitly summed when suppressed. The minimum Hamiltonian for graphene is given by

$$H_g = -t \sum_{\langle \mathbf{r}\mathbf{r}' \rangle} (c^\dagger_{\mathbf{r}} c_{\mathbf{r}'} + h.c.). \tag{4.1}$$

To minimize the evaluation time $O(w^3 \times L)$, we slice each column in which $\frac{2}{a\sqrt{3}}w$ number of carbon atoms reside, as shown in Fig. 4.1. This single column setup is still applicable with the inclusion of second-nearest hopping (e.g. Kane-Mele SOC), spin-flip hopping (e.g. Rashba SOC),

$$H_{KM} = it_2 \sum_{\langle\langle \mathbf{r},\mathbf{r}' \rangle\rangle} \nu_{\mathbf{r}\mathbf{r}'} c^\dagger_{\mathbf{r}} s^z c_{\mathbf{r}'}, \tag{4.2}$$

$$H_R = i\frac{t_1}{a} \sum_{\langle \mathbf{r},\mathbf{r}' \rangle} c^\dagger_{\mathbf{r}} \left(s \times d_{\mathbf{r}\mathbf{r}'}\right)_z c_{\mathbf{r}'}, \tag{4.3}$$

and adatoms described by a tight-binding model. Though the Hamiltonian of each column and interaction between two consecutive slices are not exactly the same everywhere, one can still easily stitch them together by Dyson's equation.

Modeling lead

In an experiment, the leads are metallic and provide numerous electrons. The interface of the leads and the device is a low resistance junction—an Ohmic contact. To satisfactorily model the leads, we choose a similar hexagonal structure in the leads

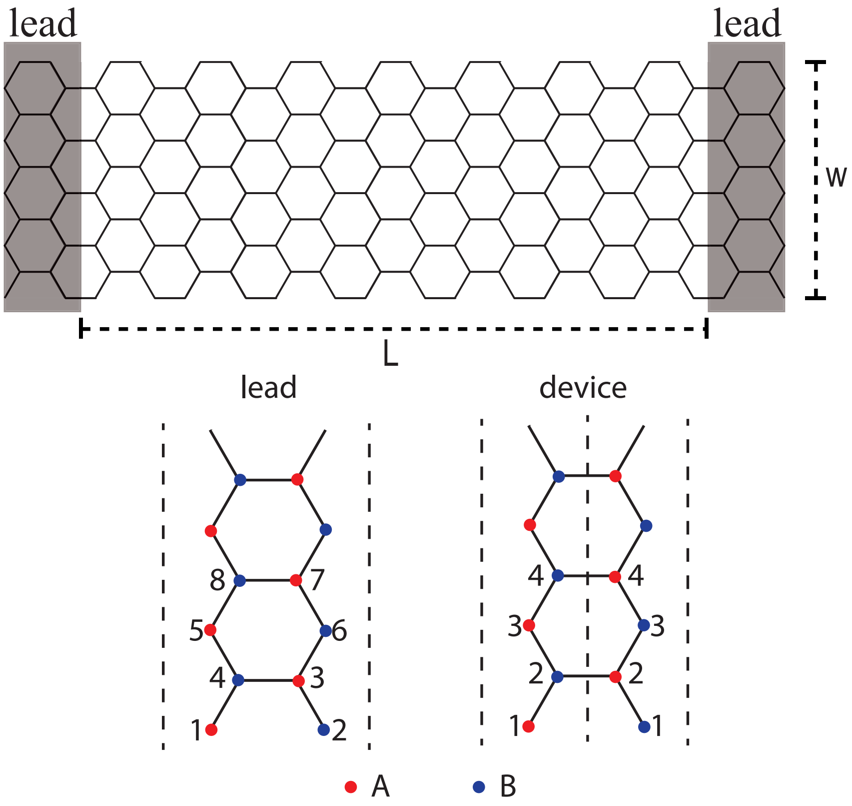

Figure 4.1: Upper panel is the cartoon picture of lattices of the device and leads. Lower panel shows the minimum column for the device and leads.

to minimize the contact mismatch, and adjust the chemical potentials to ensure the high density of states. Note that, in principle, the leads can be modeled by any type of semi-infinite lattice, and one can experiment with different structures to obtain the best performance for the device of interest.

The Hamiltonian of leads is chosen to be graphene structure,

$$H = \mu \sum_{\mathbf{r}} c^\dagger_{\mathbf{r}} c_{\mathbf{r}} - t \sum_{\langle \mathbf{r}\mathbf{r}' \rangle} (c^\dagger_{\mathbf{r}} c_{\mathbf{r}'} + h.c.). \tag{4.4}$$

The nearest-neighbor hopping amplitude t is the same as the device (graphene) and the chemical potential is shifted to -4 eV in order to maximize the density of states and maintain the symmetric V-shape of conductance versus Fermi energy $G(E_F)$ relationship. If $|\mu_{lead}| > 4$ eV, the conductance curve becomes U-shaped; on the contrary, if $|\mu_{lead}| < 4$ eV, the curve is asymmetric and unable to provide enough electrons from the leads.

Modeling disordered device

Many different types of disorder are unavoidable in a real graphene sample. Common sources of disorder include charges density inhomogeneities (charge puddles), substrate irregularities, intrinsic and extrinsic ripples, strain fields, surface molecular adsorption, vacancies, irregular edges, lattice bulk defects, and so on. Their effects are investigated in many research works [2, 7, 9, 11]. Most of the above can be studied using the recursive Green's function method. However, this method is suboptimal in modeling long-range disorder.

In this thesis, we apply the diagonal disorder

$$H = \sum_{\mathbf{r}} V(\mathbf{r}) c^{\dagger}_{\mathbf{r}} c_{\mathbf{r}} - t \sum_{\langle \mathbf{r},\mathbf{r}' \rangle} \left[c^{\dagger}_{\mathbf{r}} c_{\mathbf{r}'} + h.c. \right] \tag{4.5}$$

as the major source that, depending on the correlation $V(\mathbf{r})$, yields inter-valley and intra-valley scattering. To generate the disorder potential $V(r)$, which has correlations with disorder strength K_0 (dimensionless) and correlation length ξ, we firstly create a continuous potential landscape satisfying

$$\langle V(x)V(x+r) \rangle = K_0 \frac{(\hbar v_F)^2}{2\pi\xi^2} e^{-\frac{r^2}{2\xi^2}}, \tag{4.6}$$

then map the potential on the discrete lattice. Here $\langle \cdots \rangle$ stands for the average over disorder realizations and the average disorder potential $\langle V(x) \rangle$ is 0. This disorder potential simulates finite-range correlations, but can be used to model short- and long-range correlations by adjusting the correlation length. When $\xi \rightarrow 0$, the disorder correlation $\langle V(x)V(x+r) \rangle$ goes to 0, except at $x = 0$; this is similar to white noise disorder. On the other hand, when $\xi \rightarrow \infty$, the system has infinite correlation as in the case of no disorder at all.

In order to make the random disorder landscape satisfy Eq. (4.15), we can move to momentum space and randomize the phase.

$$V(q) = \sqrt{\frac{K_0}{A}} \hbar v_F \exp(-\frac{q^2\xi^2}{4}) \exp(i\phi(q)) \tag{4.7}$$

where A is the area of graphene and $\phi(q)$ is a random phase which depends on q, and $\phi(q) = -\phi(-q)$. We choose random phases for each q and then Fourier transform back to real space, such that the $V(r)$ satisfies the Eq. (4.15). Note that maximum possible value of $V(r)$ is $\frac{\hbar v_F}{\pi\xi^2}\sqrt{AK_0}$ and that the average height of the potential is $\sqrt{\frac{K_0}{2\pi}} \frac{\hbar v_F}{\xi}$. Here, we present two examples of disorder landscapes with different correlation lengths ξ.

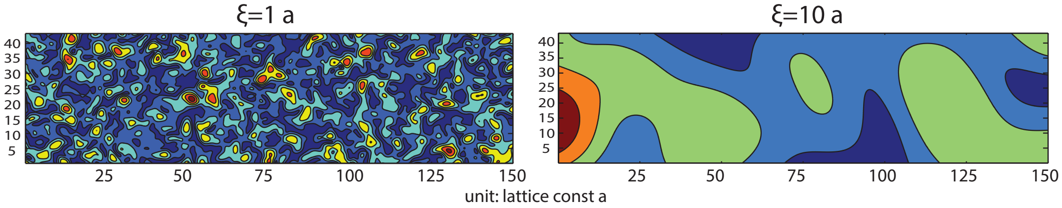

Figure 4.2: The disorder landscape modeled on the device. The unit for both axes are lattice constant a.

Modeling magnetic field

In the Landauer-Büttiker simulation, we need to incorporate a magnetic field into the tight-binding representation. Consider an electron moving in a uniform magnetic field **B**. The electron obtains a phase by hopping between different sites. This phase can be well-described by a Peierls substitution

$$t \longrightarrow t e^{i\frac{e}{\hbar}\int_i^f \vec{A}\cdot d\vec{l}} \tag{4.8}$$

where **A** is the vector potential of the magnetic field $\mathbf{B} = \nabla \times \mathbf{A}$. Note that only a perpendicular magnetic field applied to the sample will have an influence on the orbital of the electrons since we are considering a 2D system. This substitution fails when the magnetic length is smaller than the lattice spacing,

$$l_B = \sqrt{\frac{\hbar}{eB}} = \frac{26\text{n}m}{\sqrt{B}} > a = 0.142\text{n}m. \tag{4.9}$$

This constraint can be easily satisifed as long as $B \lesssim 100T$ in our simulation.

In the quantum mechanical simulation, we want to apply a magnetic field to the device in order to measure the magneto-contanctance at zero magnetic field $B \longrightarrow 0$. To realize such a setup, we consider a small uniform magnetic field B applied perpendicularly to the graphene plane $\mathbf{B} = B\mathbf{e}_z$ and choose a corresponding gauge

$$\vec{A} = \begin{cases} 0 & \text{, for } x < 0 \\ B_0 x\hat{y} & \text{, for } 0 < x < L \\ B_0 L\hat{y} & \text{, for } L < x \end{cases} . \tag{4.10}$$

Here we choose the $x-$coordinate of first slice of atoms to be 0 while that of the last slice to be L. This gauge is chosen for two reasons: one is to keep the periodicity in $\hat{y}$ direction if we study a nanotube structure; another is to ensure the continuity at the interface.

4.2 Conductance quantization

In this section, we will discuss quantized conductance arising from finite size effect. Consider a graphene nano-ribbon with width w and length L. Each edge is terminated in an armchair geometry (the same calculation applies to zigzag as well). Due to confinement, the wave-vector in $y-$direction is quantized as

$$k_n = \frac{\pi n}{W + \sqrt{3}a} + \frac{2\pi}{3\sqrt{3}a} \tag{4.11}$$

to satisfy the boundary conditions. Each quantum number n corresponds to a state in the band structure. As shown in Fig. 4.3, we expect to obtain a quantized conductance in the quantum simulation if the leads are perfectly metallic.

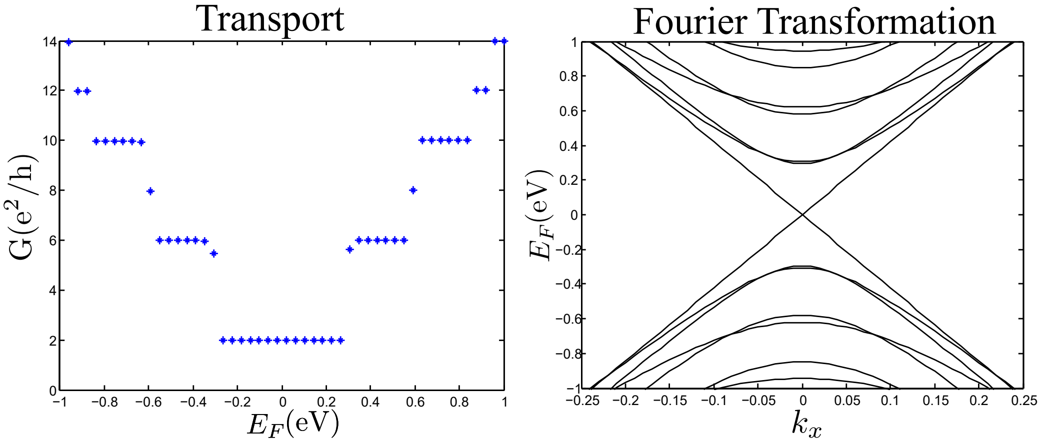

Figure 4.3: Conductance simulation for perfect metallic leads and PFT of pristine graphene nano-ribbon. $(w, L) = (43, 45)a$.

However, the leads in a real simulation have a finite density of states and thus the energy level mismatch causes contact resistance. Therefore, in real quantum transport, we obtain a jagged continuous curve instead of quantized conductance. The jagged features not only depend on the contact resistance, but also reflect the Febry-Perot oscillations due to the finite system length L as shown in Fig. 4.4.

4.3 Confinement and tunneling effect

Confinement

Confinement (finite size effect) may introduce a gap in a gapless Hamiltonian for different edge geometries. For a graphene nanoribbon terminated with armchair edges, the system could be either semi-conducting or metallic depending on the width. The finite size gap closes when $w = (3n + 1)\frac{\sqrt{3}}{2}a$ where n is the number of

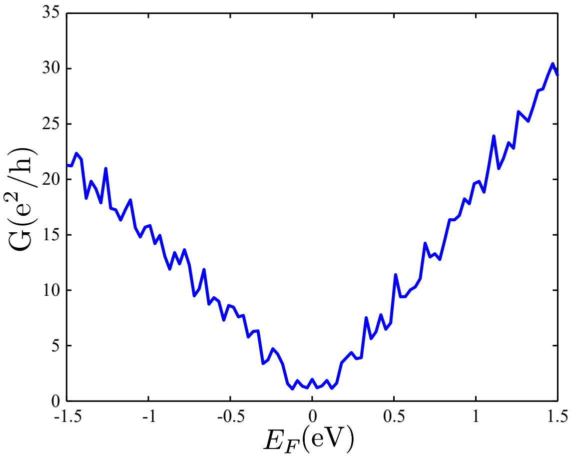

Figure 4.4: Conductance simulation with metallic leads for a pristine graphene nano-ribbon of size $(w, L) = (87.5, 150)a$. a is the bond length of graphene.

rows; otherwise, a gap of size $\sim \delta \sim v_F \frac{\pi}{w+\sqrt{3}a/2}$ opens (the actual value is slighter smaller in simulation as shown in Table 4.1). Since we are interested in gapped systems (e.g. topological insulators), we need to carefully choose a large enough width to observe the "true gap" of the system. In the next subsection, we will discuss how to extract the gap size from simulation results.

number of rows N_y	21	52	100	201	300	400
finite size gap	0.4eV	0.2eV	0.1eV	0.05eV	0.04eV	0.02eV

Table 4.1: The confinement gap size measured in the quantum mechanical simulation. The width w is $\frac{\sqrt{3}}{2}N_y a$.

Tunneling effect and minimum conductance

A major problem preventing us from observing the gap is quantum tunneling. Since the simulated system is so small, there is always some tunneling current found in the gap, a phenomenon which is also seen in experiments and is known as the *minimum conductance* problem. Let us focus on the behavior of the minimum conductance in two extreme limits: $W/L \longrightarrow \infty$ and $w/L \longrightarrow 0$. In the first case, $W/L \longrightarrow \infty$, the leads are close to each other and thus current can tunnel through the device. With this tunneling current, the conductivity ($\sigma = G\frac{L}{W}$) is predicted to converge to a fixed value,

$$\sigma_{\mathrm{m}in} = \frac{4e^2}{\pi h}. \tag{4.12}$$

In the other limit $W/L \to 0$, the tunneling current is very weak and the conductance would gradually decrease since electrons have higher chances to back scatter into other channels throughout the infinite strip. However, L/W grows much faster than G such that conductivity goes to infinity while $L/W \to \infty$. Both predictions are consistent with our results shown in Fig. 4.5.

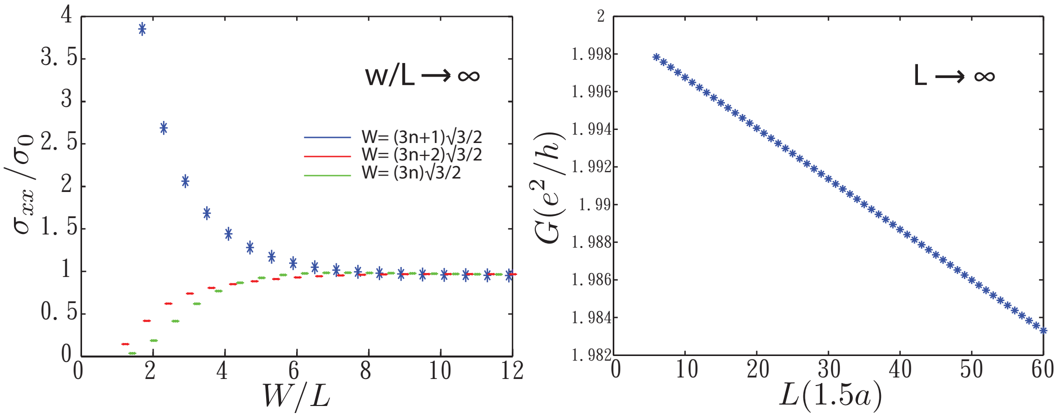

Figure 4.5: Checking the limits of a graphene strip. (a) is the relative conductivity σ_{xx}/σ_0 change by varying W/L and (b) is the conductance G change respect to L. In the $W/L \to \infty$ limit, the conductivity converges to σ_0 as predicted. In the other limit, L increases and the conductance gradually drops to an insignificant value. It indicates that backscattering is not very important in our system.

Due to quantum tunneling, zero conductance is no longer a good indicator for an energy gap. A more reliable way to extract the gap size is by finite size scaling: the conductance in the gap decays exponentially with the system size,

$$G(L) = G(0)e^{-L/l_{\text{loc}}}. \tag{4.13}$$

The finite-size gap can be easily identified by increasing system size as shown in the Fig. 4.6. Concluding from the above discussion, to see the transport gap Δ of a gapped Hamiltonian, one should choose a large system, for which the finite-size gap is smaller than Δ from the Hamiltonian. However, it doesn't guarantee the appearance of a perfect gap with zero conductance inside and non-zero conductance outside; the tunneling effect is unavoidable and oscillations near the gap makes it hard to define the size of the transport gap. One reliable way to measure the tranport gap is to ensure the finite size gap is smaller than the target system's gap, and then measure the gap size by finite-size scaling, to avoid confusion of tunneling current.

As shown in Fig. 4.7, current in a gap decays exponentially as the system grows longer while it decays insignificantly and linearly out side of a gap.

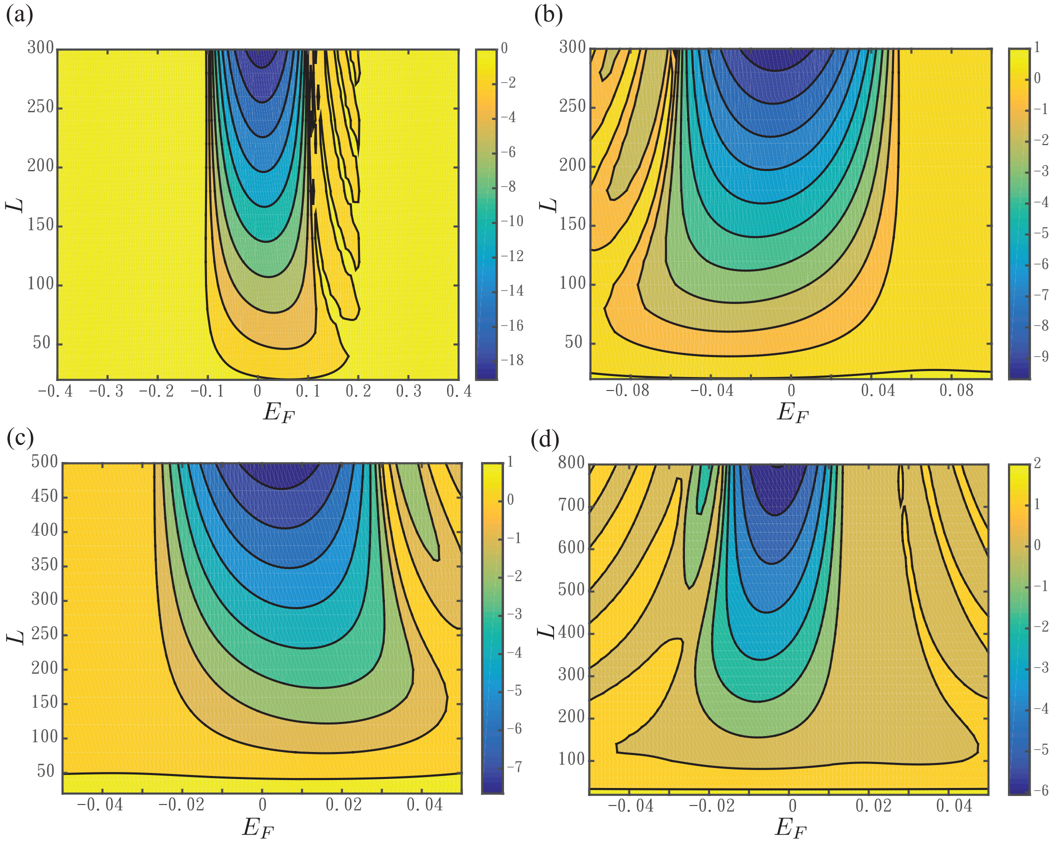

Figure 4.6: Finite size gaps for device's width $w = N_y \frac{\sqrt{3}}{2}$ (a) $N_y = 51a$,(b) $N_y = 100a$, (c) $N_y = 201a$, (d) $N_y = 400a$. The corresponding finite size gaps are 0.2 eV, 0.1 eV, 0.05 eV, and 0.01 eV respectively. L is in the unit of $1.5a$. The color bar unit is $\log(G(\frac{e^2}{h}))$

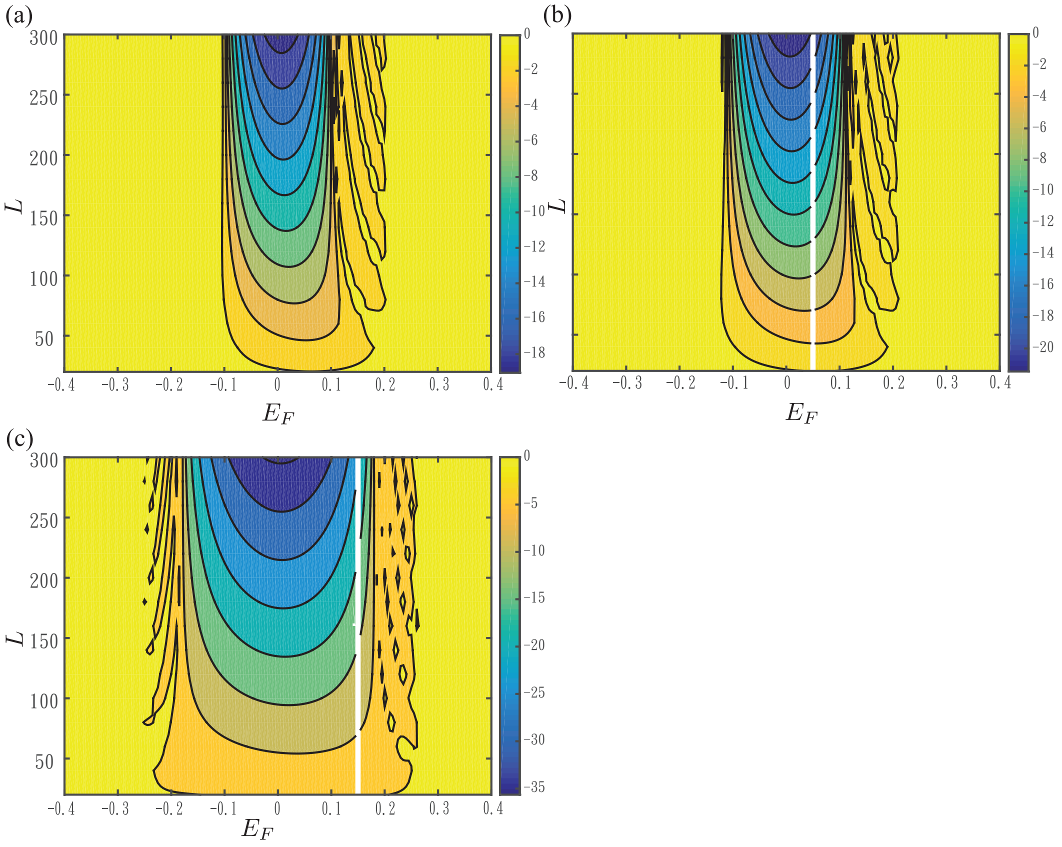

Figure 4.7: Pristine graphene transport simulation of different mass gap Δ. (a) $\Delta = 0$ eV, (b) $\Delta = 0.1$ eV, (c) $\Delta = 0.3$ eV. The width of the device is $w = 51\frac{\sqrt{3}}{2}a$, corresponding to a finite-size gap 0.2 eV. L is in the unit of $1.5a$. The color bar unit is $\log(G(\frac{e^2}{h}))$

4.4 Disorder and diffusiveness

One of the most important sources of scattering in a generic graphene sample are charged (i.e. Coulomb) impurities, especially in the low carrier density regime. The random charged impurities at the graphene-substrate interface lead to inhomogeneous electron-hole puddles; its long-range disorder nature results in the linear behavior of the conductivity as the density (or Fermi energy) increases. Analytically, we can study this problem with a long-range Coulomb potential by semi-classical Boltzmann theory. Numerically, however, it is difficult to simulate the long-rang disorder. Instead, we use the non-interacting electron model with a Gaussian disorder landscape and apply a self-consistent RPA (considering the electron screening effect) to estimate the relevant variables. For some high-mobility samples, a sublinear conductivity is found in experiments. This result suggests that short-range disorder plays a dominant role in the system. In this thesis, we strive to model both types of disorder, and study its effects on magneto-transport.

In this section, we will address a few issues regarding modeling disorder in graphene and compare the simulation results with analytical transport theory. Firstly, we will discuss two disorder models—simple onsite disorder and finite range disorder. Next, we investigate how short- and long-range disorder affects the conductance $G(E_F)$ and compare this to the analytical results. Finally, we will describe how to extract mean free path from the simulation results.

Disorder Models

Let us start with disordered graphene in the simplest setup. Consider disorder on a carbon at site r_{dis}. Its Hamiltonian is

$$H_{disorder} = -\mu_{dis} \sum_{r} \delta(r - r_{dis}) c_r^{\dagger} c_r \tag{4.14}$$

where μ_{dis} is the energy shift caused by the disorder with the assumption that the average disorder strength $\langle \mu_{dis} \rangle$ is 0. From Fig. 4.8, we can see that the conductance decreases as more or stronger impurities are placed on graphene. Furthermore, the conductance curve $G(E)$ shows sub-linearity due to the short-range nature of simple onsite disorder, a result that is consistent with analytical prediction in the Ref. [9],

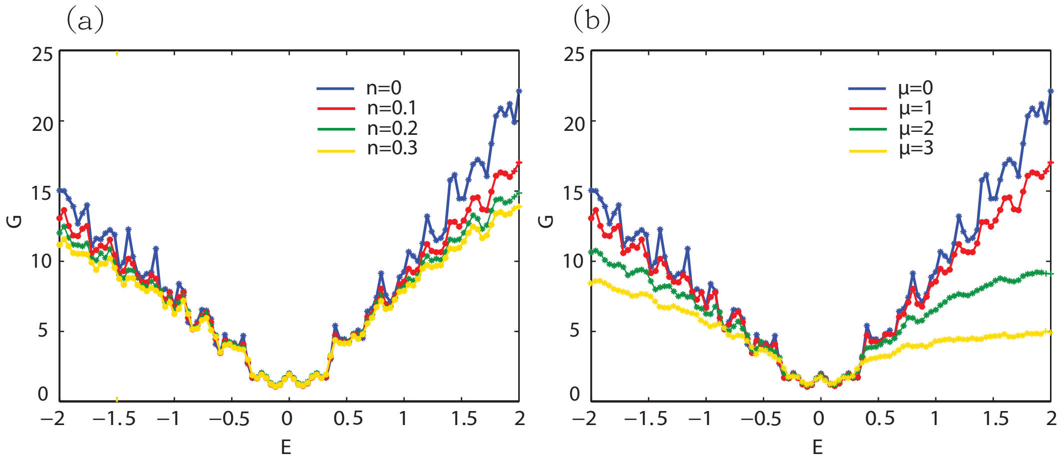

Figure 4.8: (a)The conductance change by tuning the density of disorder n. The system parameters are $(w, L) = (50, 20)$ and $\mu_{dis} = 1$; conductance G is in the unit of $\frac{e^2}{h}$ and the Fermi energy E is in the unit of eV. (b) The conductance change by tuning the disorder strength. The density is fixed to 0.1. The above data are averaged over 100 different disorder distributions.

Now, we consider a more generalized model—Gaussian correlated disorder—which is a finite-range disorder that can be used to model short- and long-range disorder with the appropriate choice of correlation length,

$$\langle V(x)V(x+r)\rangle = K_0\frac{(\hbar v_F)^2}{2\pi\xi^2}e^{-\frac{r^2}{2\xi^2}}. \tag{4.15}$$

where K_0 is the dimensionless disorder strength and ξ is the correlation length. When ξ is smaller than the bond length, this disorder model is short-ranged and leads to sub-linear conductance at higher carrier concentration, as shown in the left panel of Fig. 4.9. On the other hand, we find that the finite-range disorder, similar to the case of long-range disorder, results in the linearity of the conductance (right panel of Fig. 4.9). Although this model may not fully capture the properties of long- or short-range disorder, it can well approximate the disorder that generates intra- and inter-valley scatterings (see next subsection) as desired for magneto-conductance calculations. Therefore, we adopt this model in all of our simulation results.

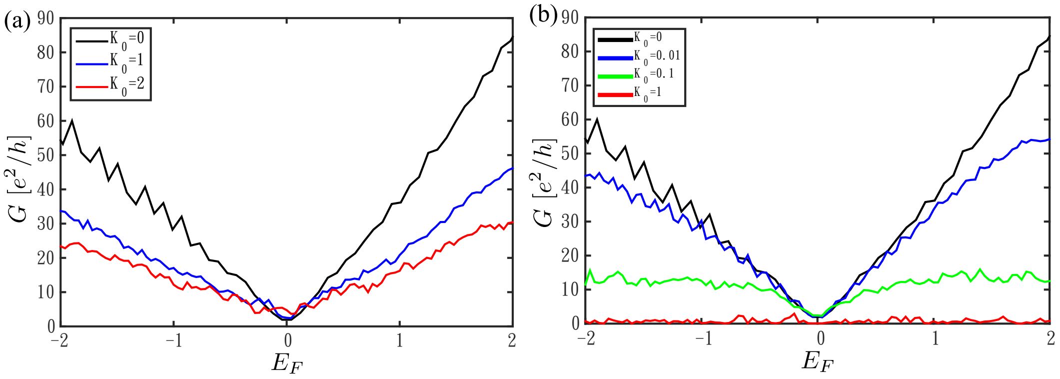

Figure 4.9: (a) Transport measure of graphene with different long range disorder strength. Parameters $(w, L, bc, \xi) = (173a, 90a, 1, 4a)$.(b)Transport measure of graphene with different short range disorder strength. Parameters $(w, L, bc, \xi) = (173a, 90a, 1, 0.5a)$.

Compare to Boltzmann theory

In the weak disorder limit $k_F l_e \gg 1$, we can analytically derive the mean free path and conductivity for intra-valley scattering and inter-valley scattering for the Gaussian disorder case:

1. intra-valley scattering

$$l_{MFP} = \frac{2k^2\xi^2}{K_0 I_1(k^2\xi^2)} e^{k^2\xi^2} \tag{4.16}$$

$$\sigma = \frac{4e^2}{h} \frac{k^2\xi^2}{K_0 I_1(k^2\xi^2)} e^{k^2\xi^2} \tag{4.17}$$

2. inter-valley scattering

   The transport scattering time is

$$\begin{aligned} \frac{1}{\tau_t} &= \frac{NA}{4} \int \frac{d^2k'}{(2\pi)^2} W_{kk'}(1-\cos\theta) \\ &= \frac{NK_0\pi}{2\hbar}(\hbar v_F)^2 \int \frac{d^2k'}{(2\pi)^2} \exp(-(q^2+\eta^2)\xi^2/2)(1+\cos\theta)(1-\cos\theta) \\ &\times (\cosh(\xi^2 q_y \eta) + 2\cosh(-\xi^2 q_x \frac{\sqrt{3}}{2})\cosh(\xi^2 q_y \eta/2))\delta(E_{k'}-E_k) \end{aligned} \tag{4.18}$$

$$l_{MFP} = v_F \tau_t \tag{4.19}$$

$$\sigma = \frac{e^2 v_F^2 \tau}{\hbar}\left(\frac{4k_F}{\pi\hbar v_F}\right) \tag{4.20}$$

by Boltzmann theory. (See Appendix 8 for derivation details.) The total mean free path is the inverse of the sum of each l_{mfp}^{-1}. From Fig. 4.10, we see that the inter-valley scattering becomes important only when $\xi < 1$, which suggests short-range disorder. For long-range or finite-range disorder, Boltzmann theory predicts insignificant inter-valley scattering encountered within the system size in simulation.

These disorder parameters in the Gaussian disorder case can be associated to real disorder sources such as charged impurities from the substrate. Shaffique *et al.* have established a relationship in Ref. [1] which extracts the corresponding parameters from experiments—

$$K_0 = \frac{1}{4r_s^2}\left(\frac{D_0}{C_0}\right)^2 \tag{4.21}$$

$$\xi = \frac{1}{\sqrt{n_{imp}}} \frac{D_0}{4\pi r_s^2} \frac{1}{(C_0)^{3/2}} \tag{4.22}$$

(a) $E_F = 0$ eV

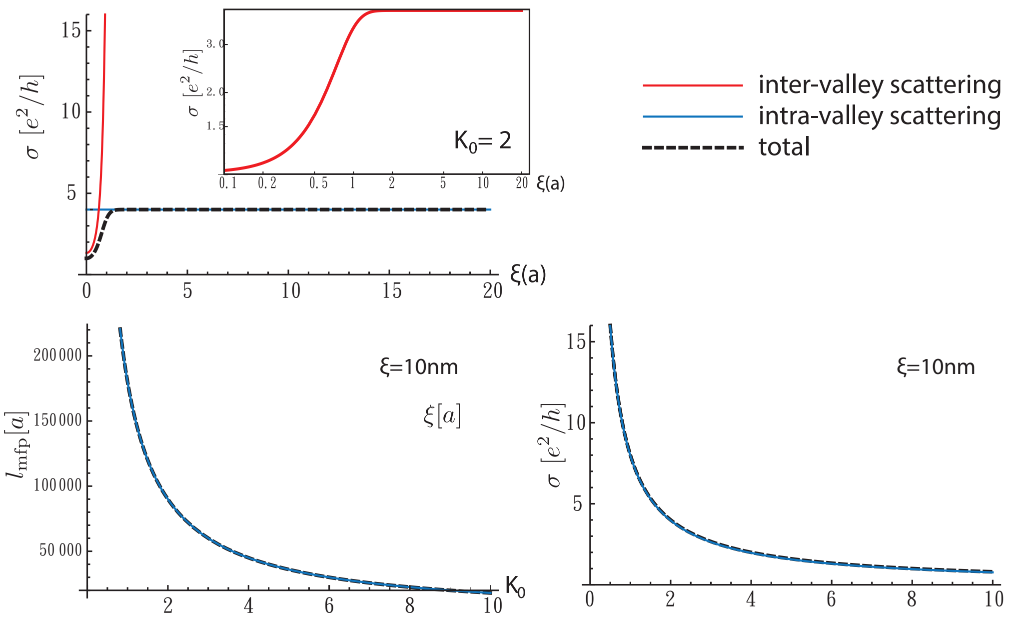

(b) $E_F = 0.3$ eV

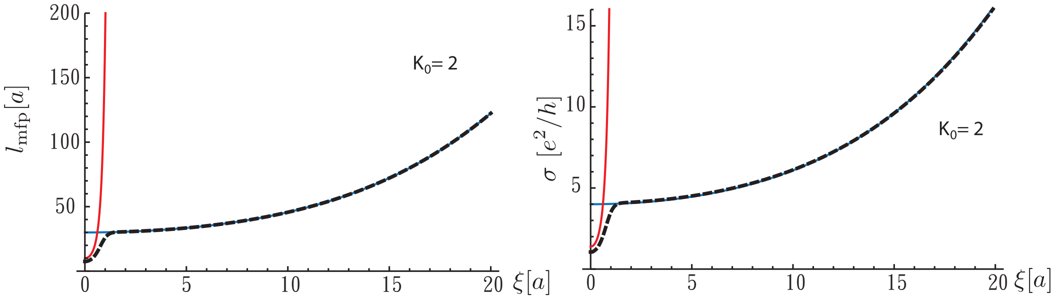

Figure 4.10: The conductivity change by changing different correlation length ξ at Fermi energy (a)$E_F = 0$ eV and (b)$E_F = 0.3$ eV. The inter-valley scattering is only important when $\xi < 1a$.

where $r_s = e^2/\kappa\gamma$ and κ is the effective dielectric constant that depends on the choice of substrate. The coefficients C_0 and D_0 are respectively

$$C_0(z) = -1 + \frac{4E_1(z)}{(2+\pi r_s)^2} + \frac{2e^{-z}r_s}{1+2r_s} + (1+2zr_s)e^{2zr_s}(E_1[2zr_s] - E_1[z(1+2r_s)]) \tag{4.23}$$

$$D_0(z) = 1 - \frac{8r_s z E_1[z]}{(2+\pi r_s)^2} + \frac{8e^{-z}r_s}{(2+\pi r_s)^2} - \frac{2e^{-z}r_s}{1+2r_s} - 2zr_s e^{2zr_s}(E_1[2zr_s] - E_1[z(1+2r_s)]). \tag{4.24}$$

These disorder parameters in the Gaussian disorder case can be associated to real disorder sources such as charged impurities from the substrate. Shaffique *et al.* have established a relationship in Ref. [1] which extracts the corresponding parameters from experiments—

$$K_0 = \frac{1}{4r_s^2}(\frac{D_0}{C_0})^2 \tag{4.25}$$

$$\xi = \frac{1}{\sqrt{n_{imp}}}\frac{D_0}{4\pi r_s^2}\frac{1}{(C_0)^{3/2}} \tag{4.26}$$

where $r_s = e^2/\kappa\gamma$ and κ is the effective dielectric constant that depends on the choice of substrate. The coefficients C_0 and D_0 are respectively

$$C_0(z) = -1 + \frac{4E_1(z)}{(2+\pi r_s)^2} + \frac{2e^{-z}r_s}{1+2r_s} + (1+2zr_s)e^{2zr_s}(E_1[2zr_s] - E_1[z(1+2r_s)]) \tag{4.27}$$

$$D_0(z) = 1 - \frac{8r_s z E_1[z]}{(2+\pi r_s)^2} + \frac{8e^{-z}r_s}{(2+\pi r_s)^2} - \frac{2e^{-z}r_s}{1+2r_s} - 2zr_s e^{2zr_s}(E_1[2zr_s] - E_1[z(1+2r_s)]). \tag{4.28}$$

Here, $z = 4k_F d$ and $E_1(x) = \int_x^\infty t^{-1}e^{-t}dt$. Typical experimental conditions correspond to K_0 between 1 and 3. The correlation length is about 10nm. Combining the above prediction for parameters and the results from Boltzmann theory, only intra-valley scattering processes will happen in the transport experiment if we use this model to simulate the charged impurities. However, even though the main disorder source is believed to be charged impurities from the substrate, almost all the magneto-conductance experiments show weak localization, resulting from inter-valley scattering, A recent work proposes that the intervalley scattering comes from edge disorder [9] . However, we find that our system size is too small for edge disorder to induce strong enough inter-valley scattering. Therefore, we strike the balance between simulating the real disorder landscape and capturing the inter-valley scattering in MC, by adopting short-range disorder $\xi < 1a$. We will address the issue of choosing the proper disorder for magneto-conductance simulations in the next section.

In Fig. 4.11, we present the conductivity results from the Landauer Büttiker simulation and Boltzmann theory analysis. General trend (blue-red) and scales are roughly in agreement, but the relation σ with respect to K_0 and ξ, are not ideal. Therefore, it is crucial to develop a method to identify the disorder phases and extract the corresponding mean free path numerically. We will discuss this topic in the following.

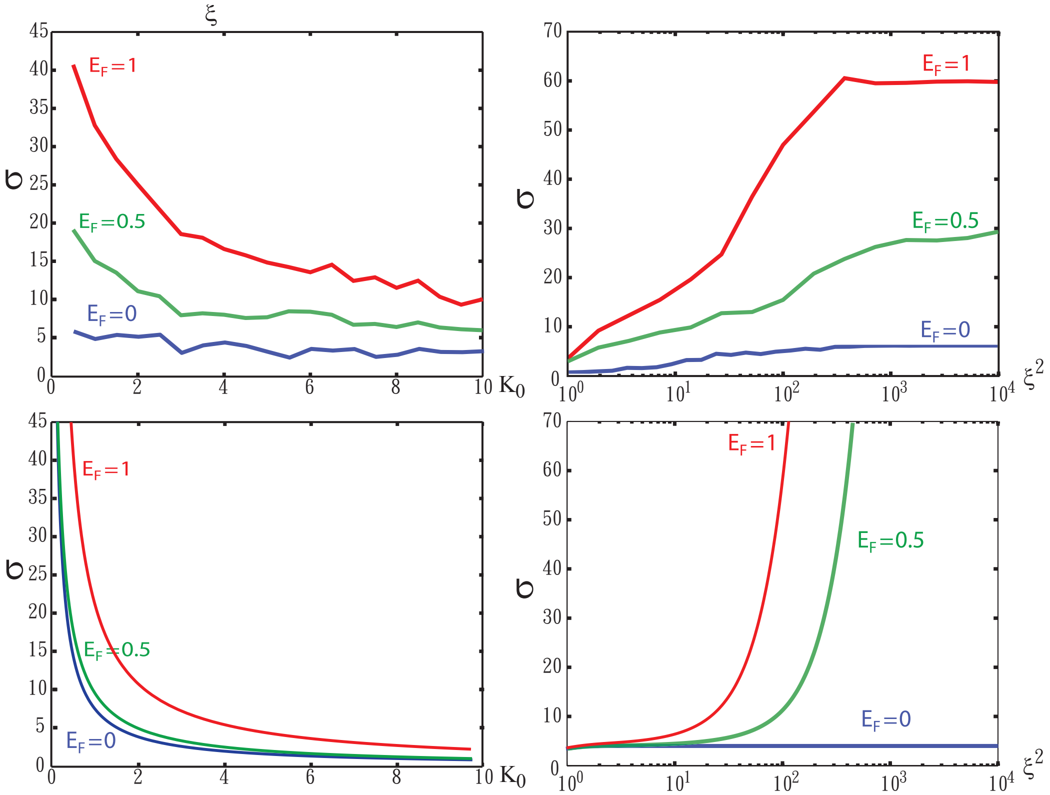

Figure 4.11: Conductance change respect to (a) disorder strength K_0 (where $\xi = 5a$) and (B) correlation length ξ (where $K_0 = 2$) in Landauer Büttikar simulation. (c) and (d) are the same as (a) and (b) but estimated from Boltzmann theory. The conductivity is in units of $\frac{e^2}{h}$ and the variance ξ is measured by lattice bond length a.

Mean free path extracted from simulation

One crucial length scale in studying diffusive transport is the mean free path. When the mean free path l_{mfp} is longer than the device, the system is metallic; on the other hand, the system is diffusive if $l_{\text{mfp}} < L$. However, if the disorder is too strong, the system changes its nature qualitatively from diffusive, where the wave functions are spatially extended, to localized, where the wave functions are spatially localized. Here, we present a way to distinguish these three phases from simulation results, and extract the mean free path/localization length if applicable.

In Landauer Büttiker formalism, the resistance in a diffusive system has two sources: contact resistance and classical Ohm's resistance:

$$R_{\text{measured}} = R_c + R_{cl} = \frac{h}{2N_{ch}e^2} + \frac{h}{2N_{ch}e^2}\frac{L}{L_0} = \frac{1}{T}\frac{h}{2e^2}. \tag{4.29}$$

Here R_c is the contact resistance, R_{cl} is the classical Ohm's resistance, N_{ch} the the number of channels in the device, and T is the transmission coefficient. Following the statistical criteria for disorder phases as shown in Refs. [5, 6, 8], we can distinguish the diffusiveness or localization for a given E, L. In the diffusive regime, the transmission coefficient T satisfies

$$\frac{\Delta T}{\langle T \rangle} < 1 \tag{4.30}$$

with mean free path

$$l_{\mathrm{mfp}} = L\left(\frac{N_{ch}}{T} - 1\right)^{-1}. \tag{4.31}$$

Here ΔT is the standard deviation of the transmission coefficient, and $\langle T \rangle$ is the average T over disorder realizations. In contrast, electrons in the localized regime move across the device by tunneling through localized states and thus T fluctuates considerably between very small values and values close to 1. One is deep in this regime when

$$\frac{\Delta \ln T}{\langle \ln T \rangle} < 1 \quad \mathrm{a}nd \quad \frac{\Delta T}{\langle T \rangle} > 1, \tag{4.32}$$

with localization length $\xi_{\mathrm{l}oc}$,

$$\langle \ln T \rangle \propto -L/\xi_{\mathrm{l}oc}. \tag{4.33}$$

Combining these statistical criteria and by finite-size scaling of the conductance (or its logarithm), we can distinguish the weak disorder and localization phases as well as extract the corresponding L_{mft} or ξ_{loc}. We can also identify the metallic properties with the criteria $l_{\mathrm{mfp}} > L$. This will be an important step in preparing a weakly disordered phase to study magneto-conductance in simulation.

4.5 Magneto-transport

Before discussing the simulation results, we note that Peierls substitution in graphene under a magnetic field is accurate as long as the lattice spacing a is much smaller than the magnetic length,

$$l_B = \sqrt{\frac{\hbar}{eB}} = \frac{26nm}{\sqrt{B}} > a = 0.142\mathrm{nm}. \tag{4.34}$$

One should be careful about the field range applied to the system while studying magneto-transport.

Strong magnetic field-QHE

The tight binding model of clean graphene with an applied magnetic field is,

$$\begin{aligned} H_g = -t \sum_A \quad & (\exp(-i\pi \frac{\Phi}{\Phi_0}(n_A + 1/6))c_A^\dagger c_{A+\delta_1} \\ & + \exp(i\pi \frac{\Phi}{\Phi_0}(n_A + 1/6))c_A^\dagger c_{A+\delta_2} \\ & + c_A^\dagger c_{A+\delta_3}) + h.c \end{aligned} \tag{4.35}$$

where $\Phi_0 = \frac{h}{e}$ and $\Phi = 3\frac{\sqrt{3}}{2}B_0a^2$. $n_A = 1, 2, 3, ..., 2L$. The corresponding low energy spectrum is

$$E_\pm(N) = \pm\omega_c\sqrt{N}, \tag{4.36}$$

with $\omega_c = \sqrt{2}\frac{v_F}{l_B}$. The zero-mode Landau level is the anomaly observed in the graphene quantum Hall effect. From the density of states of the carbon nanotube in Fig. 4.12, we observe the peaks corresponding to the extended states of each Landau level. Also, since only electrons in the Landau levels can propagate, we observe conduction peaks at the Landau levels. However, the peaks are too narrow and the gap is too small to observe the peaks as the system size increases. Therefore, at large system size, the conductance drops to zero around the Dirac point, even though we can see these states in the DOS. Note that the magnetic field is high because of small system size; it does not represent the exact value in experiments.

To observe the Landau levels, we can put some disorder in the system which broadens the peaks. We consider a larger size $(w, L) = (43a, 75a)$ which shows no Landau levels in the transport simulation. After placing some disorder in the device, the Landau level peaks are seen again. However, compared to the theoretical values, the position of the peaks are slightly shifted toward to zero energy instead of simply broadening.

Now let's look at the magneto-transport of both a nano-strip (open boundary condition, OBC) and a nano-tube (periodic boundary condition, PBC) at high magnetic field. In the nano-tube geometry, the conductance quickly drops to zero as magnetic field increases; only when Landau levels pass through the Fermi energy, one might observe a little peak in the conductance if the system is small enough. In the nano-strip geometry, the sample presents a quantized plateau showing edge currents. However, if the strip geometry tends to be qausi-1D, the edge channels from different edges may scatter into each other, leading to smaller conductance as shown in Fig. 4.14.

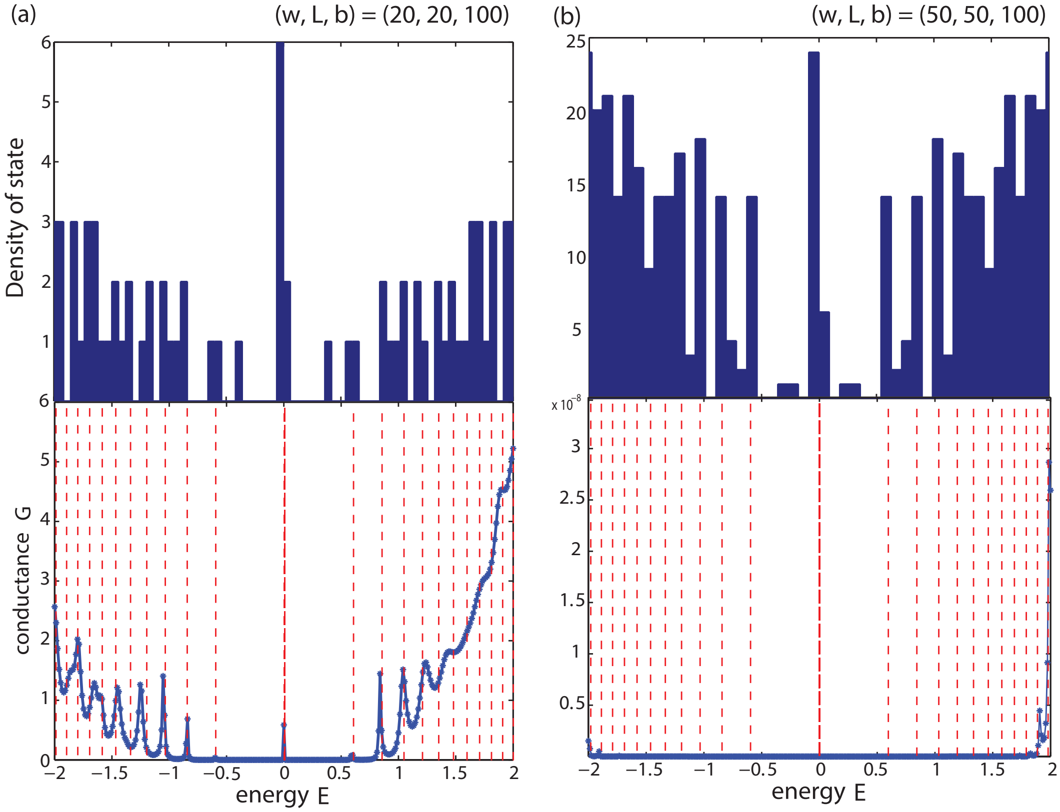

Figure 4.12: (a) The DOS and the conductance of the carbon nanotube with parameters $(w, L, B) = (17a, 30a, 100\mathrm{T})$ and (b) is the same as (a), except $(w, L) = (43a, 75a)$. The red dashed lines are the analytical value of Landau levels, $E = \pm\hbar\omega_c = 0.06\sqrt{B}\sqrt{N}$. Note that, if we look into the spatial distribution of some states at zero energy, some states come from the edge states at end of the nanotube, but they does not help conduct current in the bulk.

Adding disorder also broadens the conductance peak where the Landau level is located. Interestingly, short-range and long-range disorder of the same K_0 have different effects on magneto-transport. For long-range disorder (LRD), the disorder landscape creates numerous charge puddles which assist current tunneling through the device. As shown in Fig. 4.15, we observe the broadened conductance peaks with LRD; however, when the LRD is too strong, current can easily tunnel through the device and thus the conductance increases. For short-range disorder (SRD) of the same K_0, the *average* disorder strength $\langle V^2 \rangle$ is so much stronger; thus disorder with only $K_0 \sim 0.01$ can broaden the peak more than in the case of LRD with $K_0 \sim 0.1$. Furthermore, SRD with $K_0 = 1$ drives the system into Anderson localization as in Fig. 4.15. We see that $K_0 = 1$ is too strong for studying weak disorder phenomena such as weak localization. This can be also checked by the aforementioned statistical

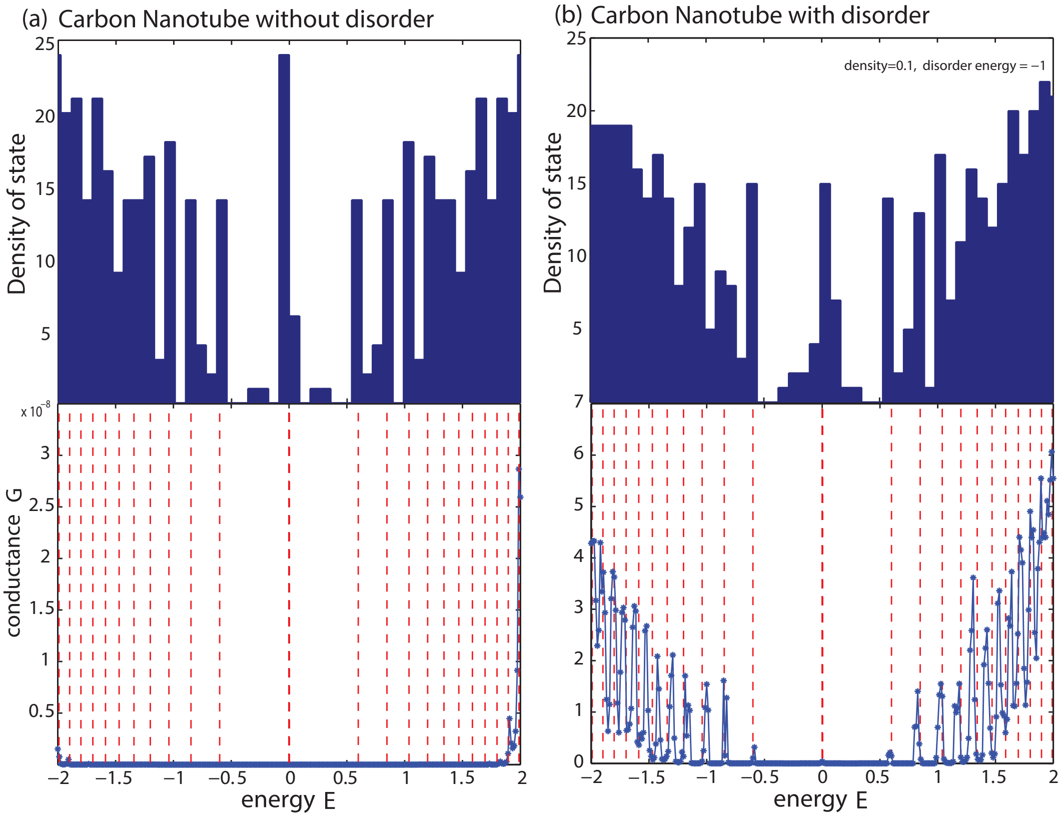

Figure 4.13: (a) is the DOS and the conductance of the carbon nanotube with parameters $(w, L, B) = (43a, 75a, 100T)$ and (b) is the same as (a), but with disorder $(\mu_{disorder}, n) = (-1, 0.1)$. One can find that the disorder broadens the peaks of the Landau levels and makes them easier to observe.

criteria as well.

Weak magnetic field-quantum interference

Between the metallic and localized phases, the weak (anti-)localization phase has drawn great attention for its interesting physics and applicability in revealing SOC in 2D materials. Weak (anti-)localization is a manifestation of quantum interference in a 2D diffusive mesoscopic system. This phenomena can be measured by magneto-conductance with a weak magnetic field.

As mentioned in Chapter 1, weak (anti-)localization (WL/WAL) is a quantum phenomena which can only be measured when all the scattering paths are coherent in phase. Any inelastic scattering from, or entanglement with the environment, e.g., phonons, system size, or magnetic field, will destroy such coherence and make the system effectively classical. Therefore, the applicable magnetic field range for measuring WL/WAL is determined by the (temperature-dependent) characteristic scale

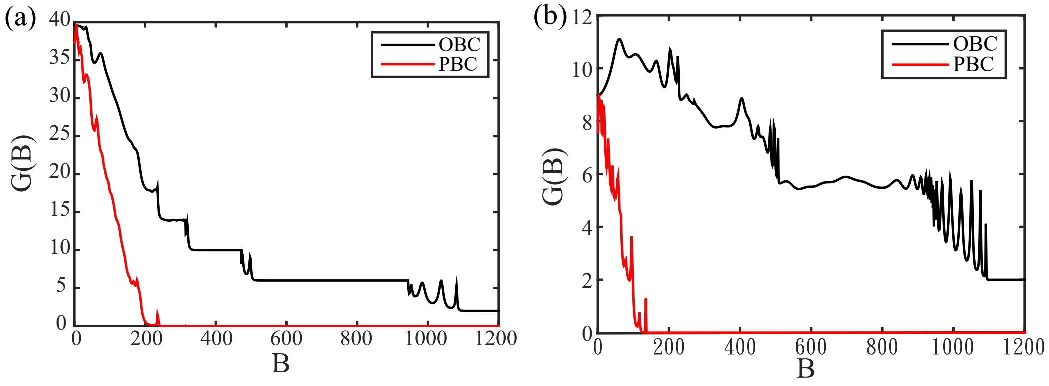

Figure 4.14: QHE in (a) 2D $(w, L) = (173a, 90a)$ and (b) quasi-1D $(w, L) = (43a, 150a)$ graphene samples. $E_F = 1eV$. Conductance has the unit e/h and magnetic field has unit T.

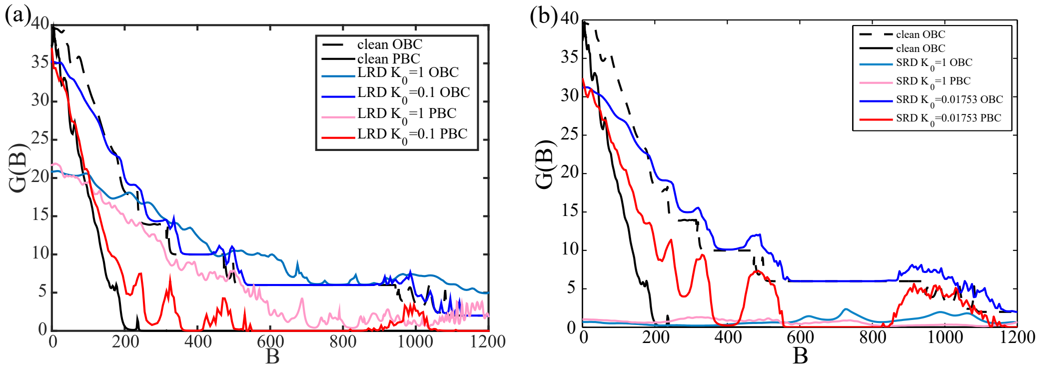

Figure 4.15: QHE in 2D dimension with (a) LRD $(K_0, \xi) = (1, 4a)$ and (b) SRD $(K_0, \xi) = (1, 0.5a)$, graphene samples. $(w, L) = (173a, 90a), E_F = 1$ eV. Conductance has the unit e/h and magnetic field has unit T.

of the magnetic field $B_\phi = \hbar/4D|e|\tau_\phi$, which is related to the coherence rate τ_ϕ. Here $D = v^2\tau_{tr}/2$ is the diffusion constant. In other words, for WL/WAL, one would expect to see the most obvious changes in conductance by applying magnetic fields for which magnetic length is comparable to the phase coherence length, $l_B \sim L_\phi$, or equivalently, $\omega_c\tau \sim \hbar/\epsilon_F\tau_\phi$.

Another related length worth mentioning is that of classical magnetoresistance $B_{cl} \sim m/|e|\tau$, as $B_\phi \sim B_{cl}\hbar/\epsilon_F\tau_\phi$. The classical magneto-conductance effect is governed by the orbit bending scale, $\omega_c\tau \sim 1$, in a metallic system, whereas the weak-localization quantum effect sets in when a loop of typical area L_ϕ^2 encloses a flux quanta in a diffusive system. Classical magneto-conductance mostly vanishes in a diffusive system.

Here are two criteria to observe weak (anti-)localization in MC in a simulation:

- Diffusive mesocopic system: $l_e < l_\phi = L^*$
- Magnetic field: $l_B > L_\phi$. $B < \left(\frac{26\text{n}m}{L*}\right)^2$.

Pristine graphene MC

Technically, clean graphene without disorder does not have WL/WAL because there is no scattering process leading to quantum interference. However, in a finite size system, electrons can scatter from the boundaries and cause quantum interference, such as the Fabry-Perot effect. This interferences induces a conductivity oscillation with the frequency $\frac{\pi}{L}$ of the increasing wave-vector k. As shown in the Fig. 4.5 (b), one can observe a large periodic oscillation in conductance along with many smaller oscillations, which are probably due to the low reflectivity of the zigzag interface. After applying a magnetic field, one will see the magneto-conductance having large peaks with some mild oscillations. These high peaks also correspond to the small sharp peaks in the no-B field graphene. Fortunately, these oscillation peaks coming from boundary scattering are washed away with a diffusive bulk.

Here, we also notice that the magneto-conductance oscillation is observed when $E > 0.2\text{e}V$ in our system setup. When $E < 0.2\text{e}V$, the wavelength is longer than the system so that the electron will travel through the system with little scattering.

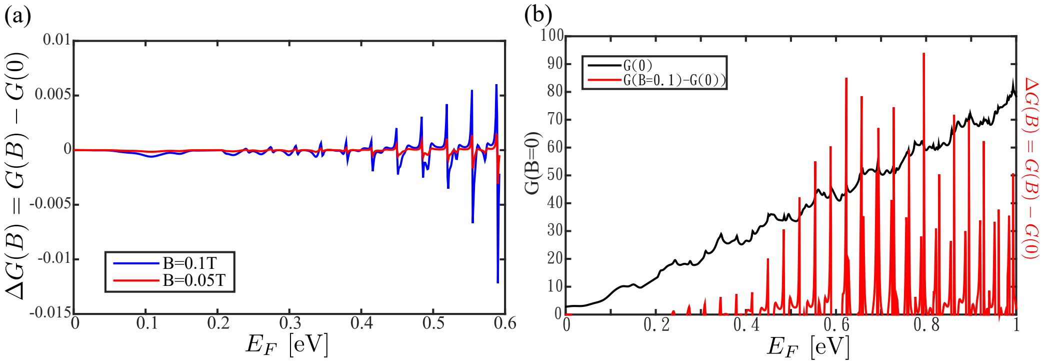

Figure 4.16: (a) Magnetoconductance of pristine graphene strips of which size is $(w, L) = (346a, 120a)$. (b) Conductance of pristine graphene without a magnetic field and the conductance change with magnetic field. Note that G(B)-G(0) is rescaled as $10,000$ times larger for convenience in presentation.

Disordered graphene

Due to its unusual chirality, graphene with smooth disorder is predicted to exhibit WAL [4]. However, strong inter-valley scattering, which typically arises in ordinary-quality samples, suppresses the chirality-related WAL and generates weak localization (WL) [10, 12]. We have confirmed these WL/WAL behaviors in our simulations. In Fig. 4.17, we place *long range disorder*—$\xi = 4a$—on a graphene sheet, check the diffusiveness, and then measure the magneto-conductance. We find that magneto-conductance is mostly WAL, except at $E_F = 0.6$eV. This is due to the fact that electrons at higher energy are closer to their neighboring Dirac cones in momentum space and thus it is easier to hop between two valleys. Applying the same algorithm to SRD, we find that the system which is diffusive shows WL as expected, except at $E_F < 0.3$ where the system is apparently ballistic. Here, again, we confirm numerically that the real WL/WAL signatures can only be observed in the diffusive regime.

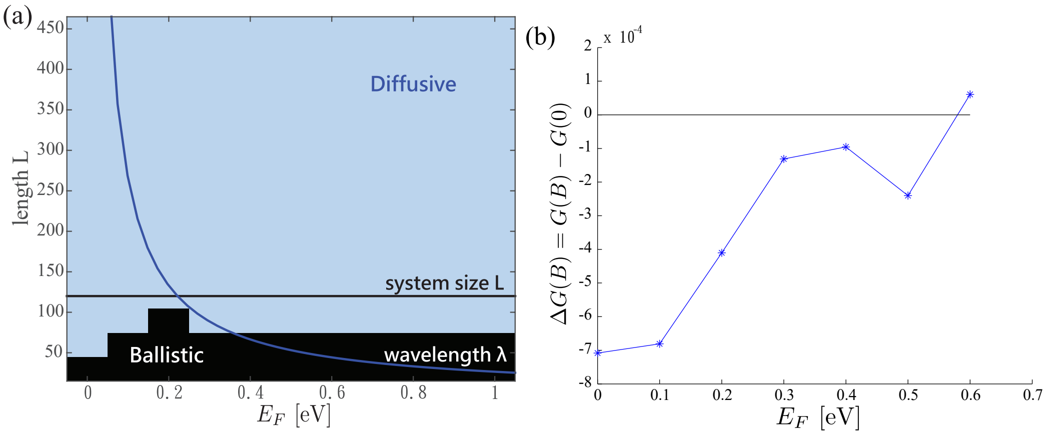

Figure 4.17: (a) Transport property map and (b) magnetoconductance of LRD graphene strips of which size is $(w, L) = (346a, 120a)$. The disorder strength is $(K_0, \xi) = (1.5, 4a)$. We average over 100 disorder realizations and $B = 0.5$T.

Universal conductance fluctuation

Another important physical phenomenon in the multiple-scattering regime is the presence of universal conductance fluctuations (UCF). The phase coherences for different disorder configurations are completely different and this difference leads to a unique signature of each configuration in conductance. Naively, one would expect such fluctuations in 2D to vanish in the thermodynamic limit $L \rightarrow \infty$. However, this is not the case in the mesoscopic regime where $L < L_\phi$. The fluctuations around the average value do not depend on disorder, but depend only on the geometry of

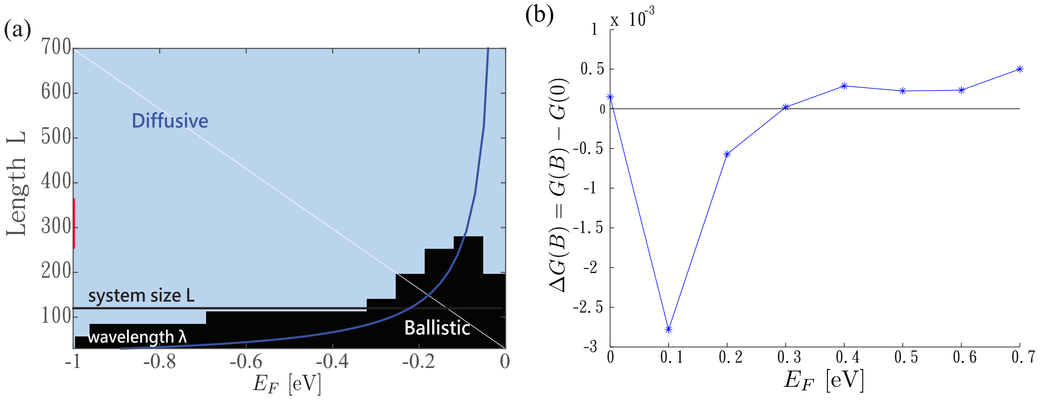

Figure 4.18: (a) Transport property map and (b) magnetoconductance of SRD graphene strips of which size is $(w, L) = (346a, 120a)$. The disorder strength for (a) is $(K_0, \xi) = (0.088, 0.5a)$ and for (b) is $(K_0, \xi) = (0.1, 0.5a)$. We average over 100 disorder realizations and $B = 0.5$T.

the conductor: so called UCF—

$$\overline{\delta G^2} = \overline{G^2} - \overline{G}^2 \sim \left(\frac{e^2}{h}\right)^2 . \tag{4.37}$$

The origin of UCF is beyond the scope of this thesis, and we refer the readers to Ref. [3]. The UCF increases the difficulty in measuring WL/WAL signatures; the MC change $\Delta G = G(B) - B(0)$ is much smaller than UCF $\sim e^2/h$ due to the small-size system in our simulation. Therefore, we need to average over more disorder realization to identify the true WL/WAL signals as shown in Fig. 4.5.

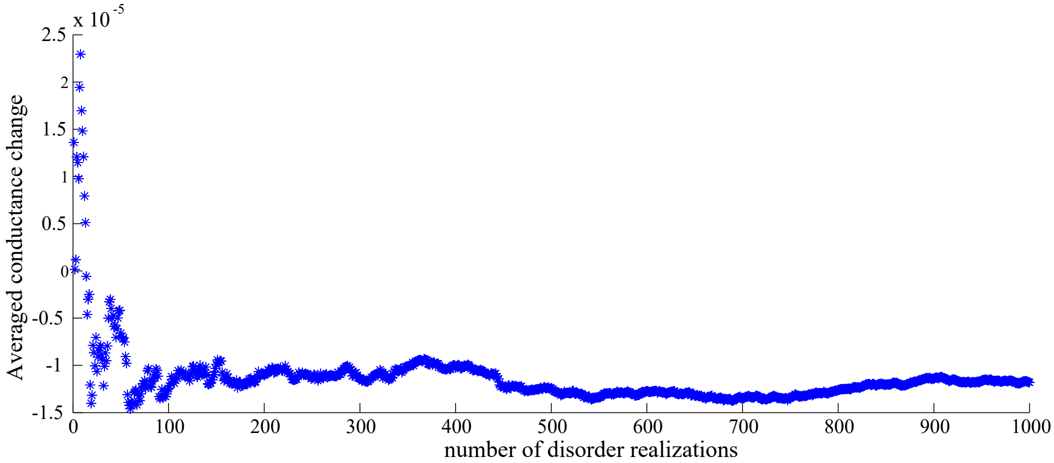

Figure 4.19: Averaged MC change with increase the number of disorder realizations. System info: $(w, L, K, \xi, E, B) = (346a, 120a, 1.5, 4a, 0.247\text{eV}, 0.1\text{T})$.

Recipe for MC simulation

In the aforementioned subsections, we discussed many aspects of the transport simulation. To successfully study the quantum interference effect numerically, we list a few things which should be carefully treated or considered in magneto-conductance simulation.

- Prepare a diffusive graphene device with enough inter-valley scattering by placing short range disorder. (Note that the disorder can't be too strong to turn the system into a strongly localized phase.)
- Apply magnetic field of which the magnetic field length l_B is larger than coherence length l_ϕ.
- The system size is the only determining factor for decoherence length. Larger systems show more significant MC change.
- Perform the same calculation with multiple disorder realizations to obtain the real WL/WAL signatures.

BIBLIOGRAPHY

[1] S. Adam, S. Cho, M. S. Fuhrer, and S. Das Sarma. Density inhomogeneity driven percolation metal-insulator transition and dimensional crossover in graphene nanoribbons. *Phys. Rev. Lett.*, 101:046404, Jul 2008.

[2] Shaffique Adam, Piet W. Brouwer, and S. Das Sarma. Crossover from quantum to boltzmann transport in graphene. *Phys. Rev. B*, 79:201404, May 2009.

[3] Akkermans and Montambaux. *Mesoscopic Physics of Electrons and Photons*. Cambridge University Press, 2007.

[4] Tsuneya Ando, Takeshi Nakanishi, and Riichiro Saito. Berry's phase and absence of back scattering in carbon nanotubes. *Journal of the Physical Society of Japan*, 67(8):2857–2862, 1998.

[5] Denis A. Areshkin, Daniel Gunlycke, and Carter T. White. Ballistic transport in graphene nanostrips in the presence of disorder: Importance of edge effects. *Nano Letters*, 7(1):204–210, 2007. PMID: 17212465.

[6] REMI AVRILLER, STEPHAN ROCHE, FRANCOIS TRIOZON, XAVIER BLASE, and SYLVAIN LATIL. Low-dimensional quantum transport properties of chemically-disordered carbon nanotubes: From weak to strong localization regimes. *Modern Physics Letters B*, 21(29):1955–1982, 2007.

[7] A. H. Castro Neto, F. Guinea, N. M. R. Peres, K. S. Novoselov, and A. K. Geim. The electronic properties of graphene. *Rev. Mod. Phys.*, 81:109–162, Jan 2009.

[8] Alessandro Cresti and Stephan Roche. Range and correlation effects in edge disordered graphene nanoribbons. *New Journal of Physics*, 11(9):095004, 2009.

[9] S. Das Sarma, Shaffique Adam, E. H. Hwang, and Enrico Rossi. Electronic transport in two-dimensional graphene. *Rev. Mod. Phys.*, 83:407–470, May 2011.

[10] E. McCann, K. Kechedzhi, Vladimir I. Fal'ko, H. Suzuura, T. Ando, and B. L. Altshuler. Weak-localization magnetoresistance and valley symmetry in graphene. *Phys. Rev. Lett.*, 97:146805, Oct 2006.

[11] E R Mucciolo and C H Lewenkopf. Disorder and electronic transport in graphene. *Journal of Physics: Condensed Matter*, 22(27):273201, 2010.

[12] F. V. Tikhonenko, D. W. Horsell, R. V. Gorbachev, and A. K. Savchenko. Weak localization in graphene flakes. *Phys. Rev. Lett.*, 100:056802, Feb 2008.

Chapter 5

GRAPHENE ON WS_2

Tunable spin-orbit coupling and symmetry-protected edge states in graphene/WS_2

5.1 Introduction

Electron pseudospin in graphene and the associated chirality yield remarkable transport consequences including the half-integer quantum Hall effect [53] and intrinsic weak anti-localization (WAL) [2]. Physical spin, by contrast, is often largely a spectator that couples weakly to momentum due to carbon's low mass, leading to much longer spin diffusion lengths (> 1 μm at room temperature) than normal conductors [17, 42]. Graphene's extremely weak spin-orbit coupling (SOC) clearly has merits, yet greatly hinders the observation of important spin-dependent phenomena including the quantum spin Hall effect [24] and quantum anomalous Hall effect [28, 35, 37, 46].

Fortunately, the open two-dimensional honeycomb structure allows tailoring the SOC strength by coupling to foreign atoms or materials [6, 10, 13, 19, 23, 29, 45]. Several experiments have pursued approaches of graphene hydrogenation [4, 25] or fluorination [18] as well as heavy-adatom decoration [7, 21]; these methods tend to decrease the transport quality, and moreover the induced SOC appears either difficult to reproduce [4, 25] or to detect [7, 18, 21]. A different approach has recently been employed by several groups: placing graphene on target substrates featuring heavy atoms. Proximity to the substrates not only provides desirable properties such as ferromagnetic ordering and large SOC, but also reduces adverse effects on the target materials [3, 22, 43, 44].

Here we employ magneto-conductance (MC) measurements to demonstrate enhanced SOC in graphene proximity-coupled to multilayer WS_2. We quantify the spin-relaxation rate caused by Rashba SOC by fitting to WAL data, and further show that the Rashba strength is tunable via transverse electric fields. Guided by first-principles calculations, we also predict that WS_2-covered graphene additionally features a prominent 'valley-Zeeman' SOC that mimics a Zeeman field with opposite signs for the two valleys. The interplay between these two SOC terms opens a non-topological gap at the Dirac point that supports symmetry-protected sub-gap edge states along certain boundaries. Though the gap is too small to be detected in our experiments, theory suggests that graphene/WS_2 may provide a simple model system for studying such an unusual gapped phase.

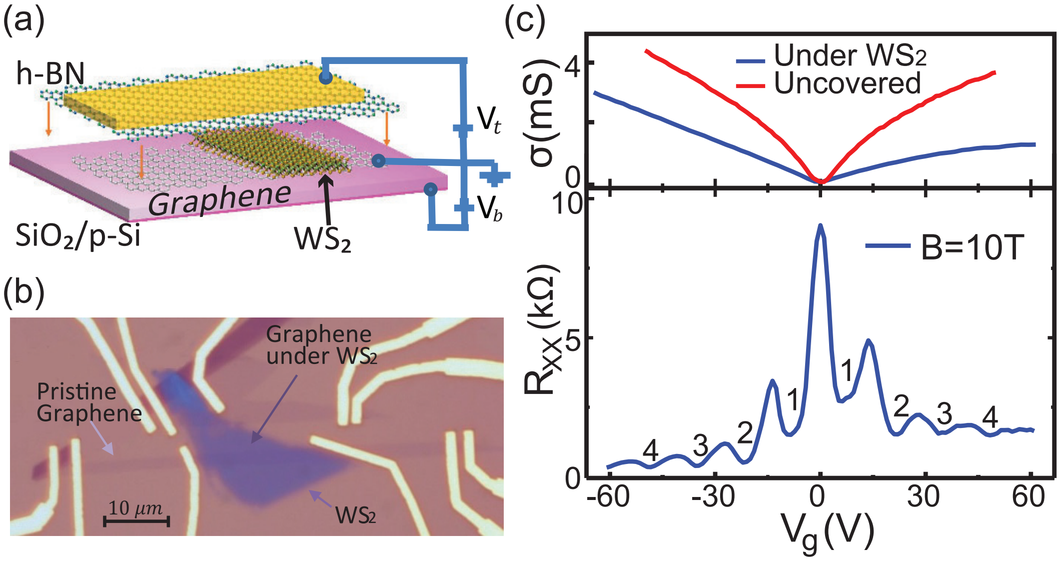

Figure 5.1: (a) Device geometry. Bottom to top: SiO_2, graphene, WS_2, h-BN, and Au top-gate. h-BN serves as the dieletric for the top gate, and is transferred onto graphene/WS_2 after deposition of Au contacts. (b) Optical image of graphene/WS_2 before h-BN transfer. Two parallel graphene devices share the same WS_2 flake (dark blue) and each has WS_2-covered and uncovered channels that can be probed independently. All single-layer-graphene data shown in this paper were taken from the lower device. (c) Top: conductivity of uncovered (red) and WS_2-covered (blue) graphene devices. Bottom: Shubnikov-de Haas oscillations of WS_2-covered graphene measured at 2 K and 10 T. The evenly spaced peaks up to the 4th order on both sides confirm the absence of carrier-density saturation.

5.2 Experimental Setup.

Figure 5.1(a) sketches the dual-gated graphene devices used in our study. Both single-layer graphene and multilayer WS_2 flakes were first exfoliated from their respective bulk materials and subsequently placed onto a Si/SiO_2 (280 nm) wafer. Since multilayer WS_2 flakes can be much thicker and stiffer, we chose to transfer the WS_2 flake instead of graphene to avoid trapped bubbles in between, thereby yielding a larger effective overlap area. Figure 5.1(b) shows an optical image of the device prior to top-gate fabrication. Notice that only part of the graphene channel directly contacts with WS_2; the left uncovered channel serves as a control sample that allows direct comparison with the right part under WS_2 (dark blue).

Transport measurements were performed at 2K (unless specified otherwise) using a Quantum Design's Physical Property Measurement System. Figure 5.1(c), top, shows the conductivity of graphene versus the back gate voltage. Interestingly, for both top and back gate sweeps, the device does not show the conductivity saturation (up to ±60V with back gate) reported recently by other groups [3, 43]. Conductivity saturation in the latter studies was attributed to saturation in carrier density from either the large density of states associated with sulfide defects [3] or screening by electrons in the WS_2/SiO_2 interface [43]. In our WS_2-covered device, the lack of conductivity saturation on either side suggests that the Fermi level resides within the band gap of WS_2, consistent with our DFT calculations (see below). The absence of the carrier density saturation in graphene is verified by Shubnikov-de Haas oscillations of the WS_2-covered graphene as a function of the gate voltage in a 10 T magnetic field; see Figure 5.1(c). On both sides, the Landau Levels are evenly spaced up to the 4th level, indicating that the carrier density is proportional to the gate voltage. This property allows us to access the high-density regions, which is important for understanding the origin of enhanced SOC and accurately determining its strength. The field effect mobility, calculated from capacitance of the SiO_2 [8] layer, is higher in the uncovered graphene ($\sim 7000\,\mathrm{cm^2 s^{-2} V^{-1}}$) than the WS_2-covered graphene ($\sim 4000\,\mathrm{cm^2 s^{-2} V^{-1}}$ on the hole side, and $\sim 2000\,\mathrm{cm^2 s^{-2} V^{-1}}$ on the electron side). Despite the relatively low mobility, our devices manifest clear low-field magneto-conductance (MC) over a much larger carrier-density range than in previous studies [3, 43].

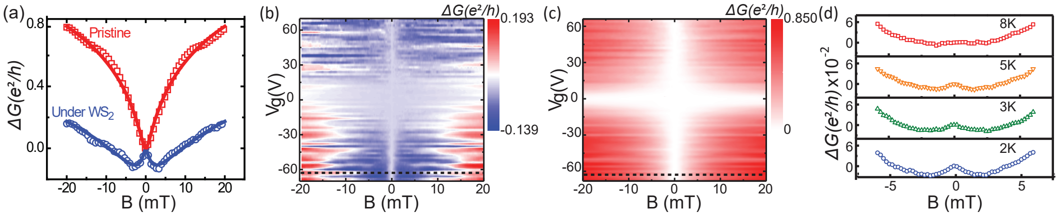

Figure 5.2: (a) MC comparison between WS_2-covered (blue circles) and uncovered (red squares) graphene channels at carrier density $n = 5 \times 10^{12}\mathrm{cm^{-2}}$ [dotted lines in (b) and (c)]. Solid blue and red curves represent fits using Eq. (5.1) and Ref. [30], respectively. (b,c) Gate-voltage dependence of MC for (b) WS_2-covered and (c) uncovered devices. The narrow white vertical region near $B = 0$ in (b) represents the WAL *peak* in WS_2-covered graphene, whereas a WL *dip* near $B = 0$ appears for all gate voltages in uncovered graphene (c). (d) Temperature dependence of the WAL in a bilayer graphene device, with carrier density $n = 8 \times 10^{12}\mathrm{cm^{-2}}$.

5.3 Rashba SOC Signature.

Due to its unusual chirality, graphene with smooth disorder is predicted to exhibit WAL [2]. However, strong inter-valley scattering, which typically arises in ordinary-quality samples, suppresses the chirality-related WAL and generates weak localization (WL) [30, 40]. Introducing strong Rashba SOC allows the spin relaxation rate τ_{R}^{-1} to exceed the inelastic dephasing rate τ_{ϕ}^{-1}. In this case, before quantum dephasing occurs the electron spin precesses around the effective magnetic field and acquires an additional π phase in the interference [31]—reviving WAL due to spin. Intrinsic (Kane-Mele) and valley-Zeeman SOC terms, by contrast, break a pseudo time reversal symmetry and thus place the system in the unitary class (suppressed WL) [20, 31].

Figure 5.2(a) contrasts the low-temperature MC $\Delta G = G - G(B = 0)$ for uncovered and $\mathrm{WS_2}$-covered devices at approximately the same carrier density, $n = -5 \times 10^{12}\mathrm{cm}^{-2}$ [corresponding to the black dashed lines in Figs. 5.2(b) and (c)]. The uncovered graphene shows WL as expected given the modest mobility. More interestingly, in $\mathrm{WS_2}$-covered graphene the MC clearly exhibits the hallmark WAL feature at low fields. In both cases this behavior persists over a broad range of gate voltages as shown in Figs. 5.2(b) and (c). The robust WAL feature appearing only in the $\mathrm{WS_2}$-covered graphene—despite its lower mobility which naively further promotes WL—provides strong evidence of Rashba SOC acquired from $\mathrm{WS_2}$ on both electron and hole sides. This result differs qualitatively from the strongly asymmetric characteristic reported in Ref. [3]; there the induced SOC was only observed on the electron side, which was attributed to the asymmetric density-of-states due to sulfur vacancies.

To further confirm the proximity-induced SOC, we fabricated a $\mathrm{WS_2}$-covered bilayer-graphene device. Unlike in single-layer graphene, WL is expected independent of inter-valley scattering strength in bilayer graphene due to its associated 2π Berry phase [15]. Consequently, the emergence of WAL in a bilayer graphene—which we indeed detect—gives direct evidence of Rashba SOC inherited from $\mathrm{WS_2}$ (i.e., the competing pseudospin interpretation disappears here). Figure 5.2(d) shows the observed WAL feature in a bilayer-graphene device at different temperatures. Note that we only measure a clear WAL signature when the carrier density exceeds $\sim 8 \times 10^{12}\mathrm{cm}^{-2}$, suggesting that the dominant dephasing mechanism in bilayer graphene is electron-electron interaction. In this scenario, increasing the carrier density suppresses dephasing, and WAL appears once the dephasing rate drops below the spin relaxation rate. The WAL feature also disappears on raising temperature, due naturally to thermally enhanced dephasing.

It is worth mentioning that the MC data shown in Figure 5.2 are from single field-sweep measurements, as opposed to an ensemble average [41, 43] over many curves taken over a gate-voltage range corresponding to the Thouless energy. Our device length ($\sim 20\mu$m $\times$ 2μm) greatly exceeds the coherence length ($\sim 1\mu$m); hence the conductivity self-averages resulting in suppressed universal conductance fluctuations (UCF) [9].

5.4 Quantitative Analysis

When inter- and intra-valley scattering rates are much larger than the dephasing and spin relaxation rates, MC in graphene is well-described at low magnetic fields by the following expression from diagrammatic perturbation theory [31]:

$$\Delta G = \frac{-e^2}{2\pi h}\left[F\left(\frac{B}{B_\phi}\right) - F\left(\frac{B}{B_\phi + 2B_{\text{asy}}}\right) - 2F\left(\frac{B}{B_\phi + B_{\text{asy}} + B_{\text{sym}}}\right)\right]. \tag{5.1}$$

Here $F(z) = \ln(z) + \Psi\left(\frac{1}{2} + \frac{1}{z}\right)$ (Ψ is the digamma function) and $B_{\phi,\text{asy},\text{sym}} = \frac{\hbar}{4De}\tau^{-1}_{\phi,\text{asy},\text{sym}}$ with D the diffusion constant. The spin relaxation rate τ^{-1}_{asy} is determined by the $z \to -z$ asymmetric Rashba SOC λ_{R}, i.e., $\tau^{-1}_{\text{asy}} = \tau^{-1}_{\text{R}}$, while τ^{-1}_{sym} follows from those $z \to -z$ symmetric SOCs including the intrinsic SOC λ_{I}, and valley-Zeeman SOC λ_{VZ}. (Additional SOC terms that may be present due to the system's low symmetry are assumed negligible for simplicity.)

The intrinsic SOC relaxation rate τ^{-1}_{I} obeys the Elliot-Yafet mechanism [12, 33, 49]: $\tau^{-1}_{\text{I}} = \tau^{-1}_{e}\left(\lambda^2_{\text{I}}/E^2_{\text{F}}\right)$, where τ^{-1}_{e} is the momentum relaxation rate and E_{F} is the Fermi energy. This rate is thus negligibly small compared to the typical dephasing rate in graphene when $\lambda^2_{\text{I}}/E^2_{\text{F}} \ll 1$. Here we deliberately focus on the high-carrier-density region ($n > 4 \times 10^{12}\text{cm}^{-2}$ and $E_F > 0.2\text{eV}$) where we can reasonably approximate $\tau^{-1}_{\text{sym}} \approx 0$. The λ_{VZ} coupling meanwhile is inherited from WS_2 due to sublattice symmetry breaking [48]. Since this term imposes an opposite Zeeman field for the two valleys, it generates *non-degenerate*, spin-polarized momentum eigenstates whose spin orientations do not relax (except due to the interplay with other SOCs). Thus the valley-Zeeman SOC relaxation rate is also negligible. With these assumptions only τ^{-1}_{ϕ} and τ^{-1}_{R} remain in Eq. (5.1), and both can be extracted by fitting to the experimental data [see, e.g., blue curve in Fig. 5.2(a)].

Figure 5.3(a) shows the resulting τ^{-1}_{R} for WS_2-covered graphene as a function of the momentum scattering rate τ^{-1}_{e} calculated from the device mobility [38]. As

τ_e^{-1} increases, the Rashba SOC relaxation rate decreases almost monotonically, indicating that the spin relaxation is dominated by the Dyakonov-Perel mechanism [11] [$\tau_{\mathrm{R}}^{-1} = 2\tau_e(\lambda_{\mathrm{R}}/\hbar)^2$]. This behavior stands in marked contrast to standalone graphene, in which the Elliot-Yafet mechanism dominates spin relaxation over a broad range of carrier density [17, 25]. Furthermore, the spin relaxation rate of $\mathrm{WS_2}$-covered graphene ($\tau_{\mathrm{R}}^{-1} \approx 0.2\mathrm{ps}^{-1}$) exceeds that for standalone graphene (e.g., $\sim 3\times 10^{-3}\mathrm{ps}^{-1}$ [17]) by two orders of magnitude—indicating strong SOC introduced by the proximity coupling with $\mathrm{WS_2}$.

Figure 5.3(b) displays the density dependence of the characteristic relaxation rates. All data correspond to $\mathrm{WS_2}$-covered graphene except the inter-valley scattering rate τ_i^{-1}. The latter is extracted by fitting our WL data for uncovered graphene with the theory of Ref. [30] instead of Eq. (5.1); as an example, see the red curve in Fig. 5.2(a). [Equation (5.1) can also provide a good fit for our low-field WL measurements in the absence of any SOC terms, but does not reveal τ_i^{-1}.] We assume that τ_i^{-1} inferred from uncovered graphene sets a lower bound for the corresponding rate in $\mathrm{WS_2}$-covered graphene,which is quite natural given its lower mobility. From Fig. 5.3(b) we then see that $\tau_i^{-1} \gg \tau_{\mathrm{R}}^{-1}$—a prerequisite for Eq. (5.1)—is indeed satisfied for $\mathrm{WS_2}$/graphene. Moreover, the dephasing rate τ_ϕ^{-1} can be extracted independently from the WAL, or the UCF by the autocorrelation function [27] (see Supplementary Material for details), and both methods agree quite well. These facts support the applicability of Eq. (5.1) and suggest that the spin relaxation rates we extracted from the high-carrier density region are reliable.

Our dual-gated graphene device [Fig. 5.1(a)] allows us to study the influence of an applied transverse electric field on the Rashba SOC. In particular, the dual gate enables independent control of the carrier density (thus the momentum scattering rate) and the transverse electric field [39]. Figure 5.3(c) shows the spin relaxation rate τ_{R}^{-1} extracted at fixed $\tau_e^{-1} = 12\mathrm{ps}^{-1}$ but at different transverse electric fields E_a (for $E_a > 0$ the field points from $\mathrm{WS_2}$ to graphene). Interestingly, τ_{R}^{-1} increases monotonically with the applied field, changing by 18% over the range -60V/300nm to 60V/300nm. This increase can be interpreted as an enhancement of the Rashba SOC: The positive electric field lifts the graphene Dirac bands towards the $\mathrm{WS_2}$ conduction bands [51]; hence graphene's π orbitals acquire a stronger hybridization with the tungsten d orbitals, substantially strengthening Rashba SOC.

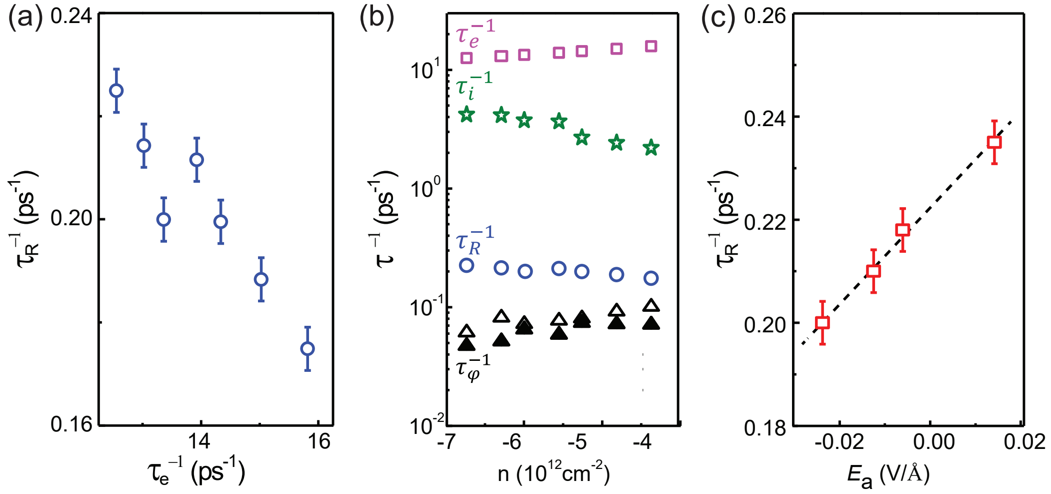

Figure 5.3: (a) Rashba SOC relaxation rates as a function of the momentum scattering rates at carrier density $n = 6.8 \times 10^{12}\text{cm}^{-1}$. Error bar indicate the fitting uncertainty. (b) Characteristic rates in WS_2-covered graphene as a function of the carrier density, except inter-valley scattering rates (stars) which are extracted from uncovered graphene. Squares denote the momentum scattering rates, circles are the Rashba spin relaxation rates, and open (filled) triangles are the inelastic dephasing rates extracted from WAL (UCF). (c) Rashba SOC spin relaxation rates extracted at different transverse electric fields. Dashed line is a guide to the eyes.

5.5 Origin and implications of SOC

To explain these experimental findings we performed density-functional theory (DFT) calculations using a large supercell in the lateral plane (9 × 9 graphene on 7 × 7 WS_2) that minimizes the lattice mismatch (0.35%) between these two materials. With the van der Waals correction, the optimized interlayer distance is 3.34, and a small buckling (< 0.08) is found in the graphene layer. The Dirac cones in Fig. 5.4(a) still center around the Fermi level, indicating negligible charge transfer between WS_2 and graphene as seen experimentally [in all our devices the graphene is slightly p-doped ($n = 0 \sim 1.5 \times 10^{12}\text{cm}^{-2}$), as generally observed for SiO_2 substrates]. The zoom-in of the band structure reveals a sizable spin splitting and a gap at the Dirac point due to SOC and the loss of sublattice symmetry. To diagnose the origin of the SOC terms, we adjust the SOC strength of each element selectively; see rightmost panels of Fig. 5.4(a). When SOC of carbon is excluded, the band structure remains essentially unchanged. However, eliminating the SOC for tungsten removes the spin splitting and yields a trivial mass gap, unrelated to SOC, that simply reflects the staggered sublattice potential induced by WS_2. Enhanced SOC of graphene is thus primarily induced by hybridization with tungsten atoms.

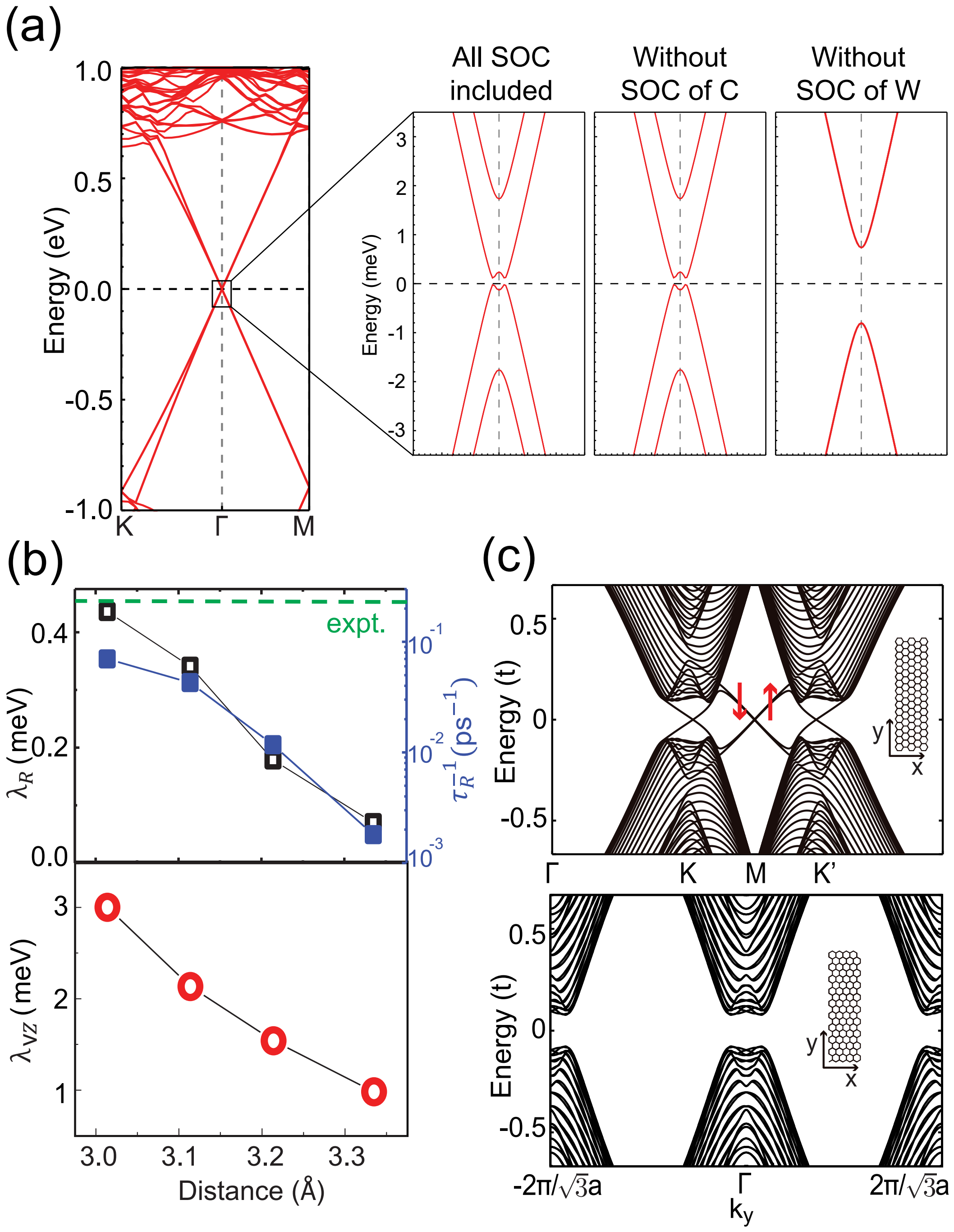

Figure 5.4: (a) Calculated band structure for graphene/WS_2 heterostructure (left panel), and zoom-ins near the Dirac point (right panel) with SOC selectively included for different atoms. The leftmost zoom-in includes SOC for all atoms, while the middle and right exclude SOC for carbon and tungsten, respectively. (b) Upper panel: calculated Rashba SOC and its associated spin relaxation rate versus interlayer distance. Green dashed line indicates the value of the experimentally extracted spin relaxation rate. Lower panel: interlayer distance dependence of valley-Zeeman SOC. (c) Energy bands for a graphene strip with zigzag edges (top) and armchair edges (bottom) using $\lambda_{VZ}/t = 0.3$ and $\lambda_R/t = 0.1$ (t is the nearest-neighbor hopping strength for carbon).

We analytically model our DFT results with the low-energy Hamiltonian

$$\begin{aligned} H_{\mathrm{e}ff} &= \hbar v_{\mathrm{F}}(\tau_z\sigma_x p_x - \sigma_y p_y) + M\sigma_z \\ &+ \lambda_{\mathrm{I}}\tau_z\sigma_z s_z + \lambda_{\mathrm{R}}(\tau_z\sigma_x s_y - \sigma_y s_x) + \lambda_{\mathrm{VZ}}\tau_z s_z. \end{aligned} \tag{5.2}$$

The first line represents the standard Dirac theory supplemented by a staggered sublattice potential M, while the second encodes symmetry-allowed SOC terms [1]. DFT bands near the Dirac point for the optimized structure can be well-fit using Eq. (5.2) with the following parameters: $M = 0.79$meV, $\lambda_{\mathrm{R}} = 0.03$meV, $\lambda_{\mathrm{VZ}} = 0.96$meV and $\lambda_{\mathrm{I}} \approx 0$meV.

The fitted SOC strengths do, however, depend sensitively on the interlayer distance in the DFT simulations. Figure 5.4(b) presents the interlayer-distance dependence of the two dominant SOCs, λ_{R} and λ_{VZ}. The Rashba spin relaxation rates shown are calculated through $\tau_{\mathrm{R}}^{-1} = 2\tau_e\left(\lambda_{\mathrm{R}}/\hbar\right)^2$, with a value $\tau_e = 12\mathrm{ps}^{-1}$ comparable to that extracted from experiment. We find that DFT for the optimized structure underestimates the Rashba coupling λ_{R} seen experimentally, but that this difference can be mitigated by using $\sim 5\%$ smaller interlayer distances. This 'correction' is not unreasonable given imperfections in our samples and the neglect of the weak force between graphene and WS_2 in DFT calculations. The reduced distance also increases λ_{VZ} in DFT; its effect, however, is likely artificially enhanced by the use of a parallelogram supercell that breaks sublattice symmetry, which is arguably restored in an average sense by the incommensuration of real samples. On the contrary, we expect that incommensuration more weakly impacts λ_{R}, which only requires $z \longrightarrow -z$ asymmetry.

Together, these two SOCs open a gap at the neutrality point—λ_{VZ} lifts spin degeneracy while λ_{R} gaps the remaining carriers via spin-flip processes. This gapped state is not a topological insulator (contrary to the reports of previous DFT studies [14, 43]), as can be verified by the existence of an even number of counter-propagating edge states and explicit calculations of the topological invariant in a lattice model. Figure 5.4(c) shows the tight-binding band structure for a strip with zigzag (top) and armchair (bottom) edges, including both λ_{R} and λ_{VZ} SOCs. In the zigzag case two copies of edge states appear at K, K' points due to band inversion, as observed in Ref. [14], but two more edge states also appear at the M-point. These edge states are protected by time reversal and crystalline symmetries, but do not have a topological origin. For an armchair geometry, no edge states appear.

---

[1] Note that inter-valley terms are excluded here even though the system is a $3n \times 3n$ superlattice; the supplementary material provides evidence that they are unimportant in this case.

This gapped phase, while topologically trivial, exhibits edge-state properties that differ markedly from those of the valley Hall effect driven by an ordinary mass gap [39, 47]. Both exhibit edge states along zigzag boundaries, but with very different spin polarizations. For the SOC gap, the M-point edge states exhibit out-of-plane spin polarization while those at K and K' exhibit in-plane polarization. In contrast, valley-Hall-effect edge modes are spin degenerate and thus do not naturally support spin currents. The nontrivial spin structure for the edge modes in our problem, combined with the prospect of electrically tuning Rashba coupling and hence the band gap, underlie tantalizing applications for spintronics that warrant further pursuit.

5.6 Conclusion

We have demonstrated a dramatic and tunable enhancement of Rashba SOC in graphene by coupling to WS_2. In the high carrier-density region, we determined the Rashba coupling strength by analyzing the low-field MC. First-principles calculations indicate that the induced SOC originates from the band hybridization between graphene π orbitals and tungsten states. The combination of Rashba and a theoretically predicted valley-Zeeman SOC creates novel edge states that are interesting to pursue further by engineering heterostructures with different substrates as well as improving the device mobilities. In addition, we show that Rashba SOC induced by substrate proximity can be tuned with a transverse electric field; this method could be applied on magnetic insulating substrates [36, 52] to enhance both the exchange field and SOC needed to reveal the quantum anomalous Hall effect.

5.7 Acknowledgments

We gratefully acknowledge Roger Mong for valuable discussions. This work was supported by the DOE BES award No. DE-FG02-07ER46351 (BY and JS) and award No. DE-FG02-05ER46237 (JW and RW); NSF through grant DMR-1341822 (MT and JA); the Caltech Institute for Quantum Information and Matter, an NSF Physics Frontiers Center with support of the Gordon and Betty Moore Foundation; and the Walter Burke Institute for Theoretical Physics at Caltech. DFT simulations were performed on the U.S. Department of Energy Supercomputer Facility (NERSC).

5.8 Appendix

Method and experimental setup

The target WS_2 flake was identified with an optical microscope and then transferred to cover part of the long graphene channel. To promote adhesion, the wafer was annealed in O_2 at $300C$ for 3 hours. Standard electron beam lithography and electron beam evaporation were used to connect the graphene with multiple 80nm thick Au electrodes. The electrodes allow independent four-terminal resistivity measurements in the covered and uncovered areas. After electrodes fabrication, an h-BN flake was transferred to cover the whole device to serve as a top gate dielectric, followed by the top Au gate metal fabrication with similar electron-beam lithography procedures. No additional annealing was performed thereafter.

Reproducible WAL in a single-layer graphene on WS_2 device.

Here we present a second device that has the similar characteristics as the first one shown in the main text. However, instead of transferring WS_2 onto graphene, this time we transferred graphene onto WS_2, in order to show that the absence of density saturation is independent of the transfer sequence and robustness of WAL exists. Figure 5.5 (a) shows the conductivity of the graphene as a function of the gate voltage. This device exhibits almost the same properties as the device in the main text, despite that it has a lower mobility ($\sim 3000\text{cm}^{-1}\text{s}^{-1}\text{V}^{-1}$ on the hole side, and $\sim 2000\text{cm}^{-1}\text{s}^{-1}\text{V}^{-1}$ on the electron side), which is mainly due to the bubbles in the device. As clearly seen in the inset, bubbles (small black dots) are all over the graphene flake. We did not intentionally choose a bubble-free area in order to minimize the UCFs. Figure 5.5 (b) shows the gate voltage dependent WAL observed in this device. MC is smaller in this device. We symmetrize the data to show clearer temperature dependence, as is shown in Figure 5.5 (c). Just as in the first device, WAL is present on both hole and electron sides and disappears quickly as temperature increases.

Distinctions between spin and pseudospin resulted WAL at intermediate magnetic field

To justify the spin origin of WAL that appears in the WS_2-covered graphene, one can also look at the change of the MC curve in the intermediate magnetic fields. Here we present a heuristic way to explain the idea and one can find the same result through a more complete diagrammatic perturbation theory. Magnetic field not only reveals the WAL/WL by changing the phase of quantum interference but also

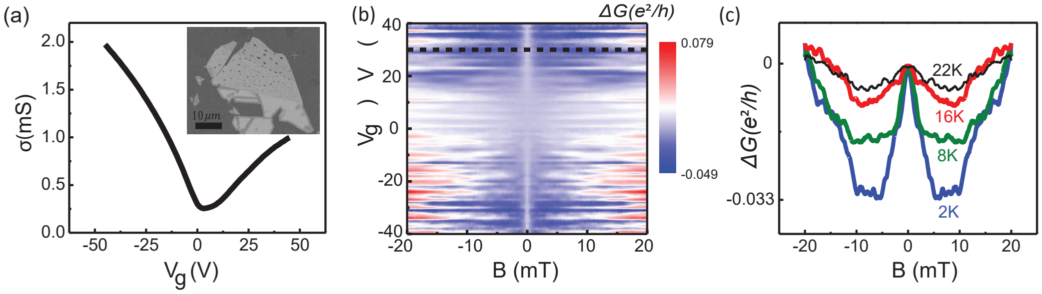

Figure 5.5: (a) Conductivity vs. gate voltage. Inset: SEM image of graphene on WS_2 before electrode fabrication. Bubbles are visible after graphene is transferred onto WS_2. (b) MC and its dependence on the temperature (c). The Fermi level is located on the electron side indicated by the black dotted line in (b).

shorten the dephasing length in which the system can be considered as a coherence mesoscopic system. In a WL system, for example, the constructive interference of electron and its time reversal partner makes electrons tend to localize in the system. When we apply magnetic field, the excessive phase it brings in will destroy the constructive interference and result in positive MC as what we see in zero magnetic field. When we go on higher magnetic field, the dephasing length is shorten and may drive the system into WAL-like once the dephasing length is shorter than the inter-valley scattering. This is because when inter-valley scattering is no longer in the quantum interference, the resulting interference in each little mesocpoic system turns to be destructive (but not complete destructive as at zero magnetic field) and thus mimics WAL behavior. The detail of MC behavior can be well described by diagrammatic perturbation theory which predicts the quantum interference results at different magnetic field.

Figure 5.6 shows a $\tau_B^{-1}/\tau_\phi^{-1}$ vs. τ_B^{-1}/τ_R^{-1} diagram, indicating the regions where covered and uncovered graphene are separated by a dashed line: $\tau_\phi^{-1} = \tau_R^{-1}$, where $\tau_B^{-1} = \frac{4DeB}{\hbar}$ and D is the diffusion constant. In the uncovered graphene channel, we estimate τ_R^{-1} from the total spin relaxation rate obtained in reference [17] (i.e., $\tau_R^{-1} = 3 \times 10^{-3}\mathrm{ps}^{-1}$), and $\tau_\phi^{-1} = 8 \times 10^{-2}\mathrm{ps}^{-1}$ is calculated from the WL with the theory in Ref. [30]. Note that the intervalley scattering rate τ_i^{-1} can be calculated from the same WL curve ($\sim 2\mathrm{ps}^{-1}$, as shown in Figure 5.3(d)), and is much greater than τ_R^{-1}. Therefore, in this regime WL appears [40, 41], as is indicated below the dashed line in Figure 5.6. In contrast, if sufficiently strong Rashba SOC is introduced so that $\tau_R^{-1} > \tau_\phi^{-1}$ in the WS_2-covered graphene channel, WAL can occur at small fields in the upper left region. As the magnetic field strength increases, it plays a similar role to inelastic dephasing which destroys the quantum interference when $\tau_B^{-1} > \tau_{\mathrm{R}}^{-1}$, i.e., the effect of the additional π phase is diminished and the WL behavior is restored. This particular crossover occurs from left to right in Figure 5.6 and is characteristic of Rashba SOC. On the other hand, if this WAL arises from pseudospin, it can only occur when τ_ϕ^{-1} is greater than the inter- and intra-valley scattering rates [41], i.e., the π phase due to intervalley scattering is already screened by the large τ_ϕ^{-1}. As the magnetic field increases, there is no more WL since the coherence is lost.

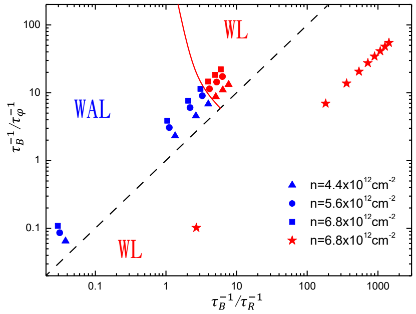

Figure 5.6: A diagram of the transition of MC between WAL and WL. The dashed line stands for $\tau_\phi^{-1} = \tau_{\mathrm{R}}^{-1}$. The red solid line represents $\Delta G = 0$ calculated from Eq. 5.1 assuming $\tau_{\mathrm{VZ}}^{-1} = 0$. Filled (Open) points are experimental values at different carrier densities in $\mathrm{WS_2}$-covered (uncovered) channel.

Temperature dependence of MC

Figure 5.7(a) shows the temperature dependence of the MC data of the $\mathrm{WS_2}$-covered graphene. Since compared with the spin diffusion length and the SO scattering rate [17], the inelastic dephasing rate τ_ϕ^{-1} is much more sensitive to temperature at low temperatures, the dramatic decrease of the WAL signal can be primarily attributed to the significantly increased inelastic dephasing rate. We extract the dephasing rate τ_ϕ^{-1} as a function of temperature and plotted it in Figure 3b. We find that τ_ϕ^{-1} obeys approximately a linear temperature dependence which can be explained by the electron-electron scattering in the diffusive regime [1],

$$\tau_\phi^{-1} = \alpha \frac{k_B T}{2E_F\tau_0} \ln(\frac{E_F\tau_0}{\hbar}) \tag{5.3}$$

where α is a correction coefficient equal to 2.4. If the mobility of the graphene is extremely high, the sample will reach the ballistic regime ($k_B T\tau_0/\hbar \gg 1$) and the temperature dependence of τ_ϕ^{-1} will turn parabolic [32]. Under this circumstance, Eqs. (5.1) will also be rendered invalid since both are developed for the diffusive regime. However, since our device has a moderate mobility of $\sim 4,000\,\mathrm{cm^2s^{-1}V^{-1}}$, it is well in the diffusive transport regime ($k_B T\tau_0/\hbar \ll 1$); therefore Eqs. (5.1) is applicable. At low temperatures, the dephasing time τ_ϕ^{-1} seems to start deviating from the straight line. In principle, at low temperatures, the electron-electron scattering may not be the dominant inelastic scattering mechanism, as compared with electron-phonon interactions, the spin-flip scattering of electrons from localized spins [31], etc.

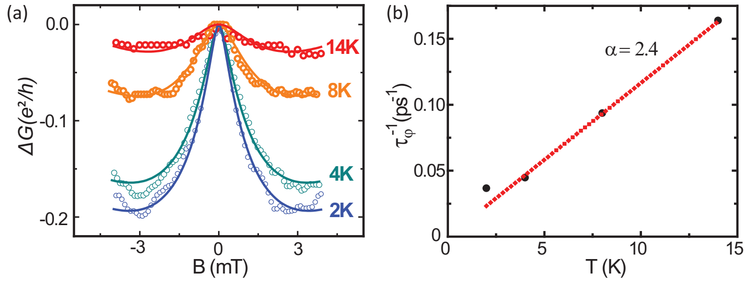

Figure 5.7: (a) Temperature dependence of MC for WS2-covered graphene at carrier density $n = 5\times10^{12}\mathrm{cm}^{-2}$ (open circles). Solid lines are fits assuming a temperature-independent SOC rate. The dephasing rate extracted from the fitting is shown in (b). The temperature dependence of the dephasing rate (black dots) is approximately linear in temperature. The red dotted line is the dephasing rate calculated from Eq. (5.3) with $\alpha = 2.4$.

Universal conduction fluctuation (UCF)

Universal conductance fluctuations can be extracted by removing the WAL background in the magneto-conductance, as shown in FIG. 5.8 a). The WAL curve is fitted by equation 5.3 and describes the experimental data quite well up to 50 mT. In addition to the reproducibility of the MC curves, the nearly symmetric fluctuations in conductance as a function of B is another evidence that the fluctuation is UCF.

In order to calculate the phase coherence length l_ϕ from the UCF, we utilized the autocorrelation function $F(\Delta B) = \langle\delta\sigma(B+\Delta B)\delta\sigma(B)\rangle$ to find the characteristic magnetic field $B_\phi(B_\phi l_\phi^2 = h/2e)$, which is determined by $F(B_\phi) = \frac{1}{2}F(0)$. FIG. 5.8 b) shows the normalized autocorrelation function at different gate voltages. When the device approaches a higher carrier density, the characteristic field B_ϕ clearly decreases, indicating an increase in the phase coherence length l_ϕ, due to the weaker electron-electron interaction than the Dirac region. l_ϕ' s extracted from UCFs agree reasonably well with those extracted from WAL, as shown in FIG 5.8. c), suggesting the validity of equation 5.1 and thus the extracted spin orbit scattering rates. It is also worth mentioning the l'_ϕ s extracted from WAL with $\lambda_{VZ} = 0.5$meV or $\lambda_{VZ} = 0$meV are completely overlapped, further supporting that these two boundaries are not distinguishable in the fitting given by equation 5.1.

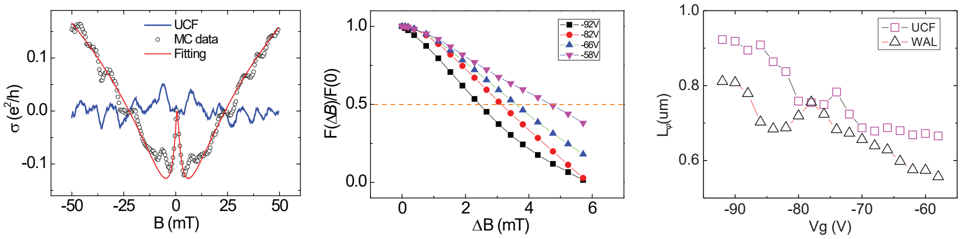

Figure 5.8: a) UCF extracted from MC by removing the WAL background. b) Normalized autocorrelation functions at different gate voltages. $F(B_\phi)/F(0) = 1/2$ gives the characteristic magnetic field B_ϕ. c) Phase coherence length extracted from UCF and WAL.

Computational details

Our first-principles calculations were carried out using the projected augmented plane-wave method [5, 26] as implemented in Vienna ab initio simulation package. The valence electron configuration for C, W, and S is $2s^2 22p^2$, $5d^4 6s^2$, and $3s^2 3p^4$, respectively. Generalized gradient approximation of Perdew-Burke-Ernzerhof type was used for the description of exchange-correlation interactions among electrons [34]. The spin-orbit coupling was included in the self-consistent calculation level. We employed $5 \times 5 \times 1$ K-point grid for Graphene/WS$_2$ heterostructure containing 162 C, 49 W and 98 S atoms. A large supercell is adopted to minimize the lattice mismatch; graphene layers expanded as 9×9 in the lateral plane and WS$_2$ monolayer as 7×7. Slab structures are separated by $\sim$ 13 vacuum along the surface normal. The energy cutoff for the plane-wave-basis expansion was set to 400eV. Positions of all atoms are fully relaxed until the convergence of total energies becomes better than 0.1meV. In order to treat the van der Waals force properly, we adopted DFT-D3 method suggested by [16].

The size effect of the supercell on the low energy states

Since we used 9×9 graphene unit cell, Dirac cones are folded to Γ point and the interaction of two different Dirac cones from K and K' points can be artificially incorporated into our calculations. In order to verify that the induced SOC of graphene is not sensitive to the cell size we have chosen, we do the same calculation for a different cell size. We adopted 5×5 graphene in contact with 4×4 WS_2 monolayer to place Dirac cones separately at K and K' point. The lattice mismatch is increased to 2.49% and the separation between graphene and WS_2 is decreased to 3.21. Even though we used a different supercell, the low energy states remain the same as shown in Figure S1 (a). We also found that the Dirac cones are very sensitive to the SOC strength. Figure S1 (b) shows that the band order is inverted at K point by SOC. Therefore, we can conclude that the enhancement of SOC is not much affected by the specific atomic configuration and that inter-valley scattering is a less important factor even if Dirac cones are shifted to the same point.

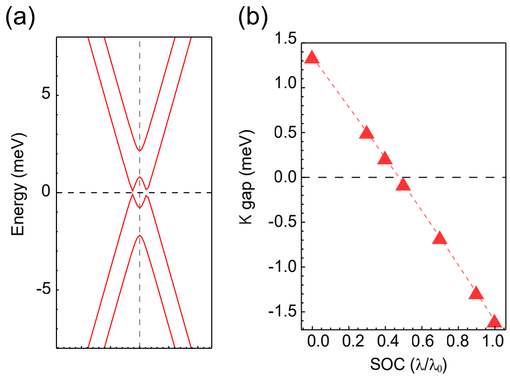

Figure 5.9: (a) Calculated band structure for the slab structure of WS_2 monolayer (4×4) on graphene (5×5). (b) The energy gap of the Dirac cone as a function of the spin-orbit coupling strength, which is adjusted from zero to the true value set as 1.

Variation of the energy gap of the unbuckled graphene

When WS2 layer is placed on the top of graphene, the graphene layer becomes buckled because we use a finite size of supercell and A-B sites are no longer equivalent to each other. For a more precise description of an incommensurate Gra/WS2 structure in which AB symmetry breaking is expected to be canceled out, we fixed carbon atoms to be flattened while maintaining the average distance between graphene and WS2 layer. The unbuckled graphene have a very small trivial gap close to zero but the energy gap difference (2.0 meV) caused by SOC is similar to that of unbuckled one (1.9 meV) [Figure S2(a), (b)]. It is worth to mention that the large SOC effect is not originated from graphene layer itself. Figure S2(c) shows that the effect of SOC on the energy gap is negligible in the absence of WS2 layer and that the gap variation upon the electric field is not observed.

When WS_2 layer is placed on the top of graphene, the graphene layer becomes buckled because we use a finite size of supercell and A-B sites are no longer equivalent to each other. For a more precise description of an incommensurate G/WS2 structure in which AB symmetry breaking is expected to be canceled out, we fixed carbon atoms to be flattened while maintaining the average distance between graphene and WS_2 layer. The unbuckled graphene have a very small trivial gap close to zero but the energy gap difference (2.0meV) caused by SOC is similar to that of unbuckled one (1.9meV) [Figure 5.10(a), (b)]. It is worth to mention that the large SOC effect is not originated from graphene layer itself. Figure 5.10 (c) shows that the effect of SOC on the energy gap is negligible in the absence of WS_2 layer and that the gap variation upon the electric field is not observed.

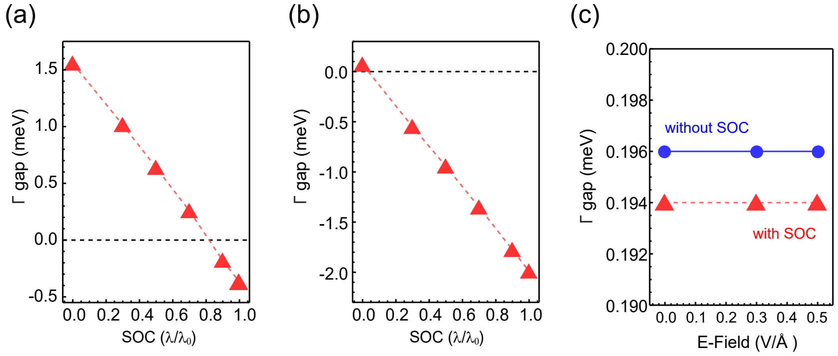

Figure 5.10: The energy gap of the Dirac cone of (a) the buckled (relaxed) and (b) the unbuckled (unrelaxed) graphene as a function of the spin-orbit coupling strength, which is adjusted from zero to the true value set as 1. (c) The energy gap of the Dirac cone with (red triangles) and without SOC (blue dots) upon varying electric field in the buckled graphene without WS_2 layer.

The effect of WS_2 multi-layer and SiO_2 substrate

We also investigate the effect of WS_2 multi-layer and SiO_2 substrate on the Dirac cone of graphene [Figure 5.11]. The Dirac cone was little affected by the additional stacking of WS_2 layer on graphene. The low energy states of graphene are almost the same regardless of the thickness of WS_2 layer. Even if we consider the effect of SiO_2 substrate into our calculations, it does not make noticeable changes except that the mass gap being increased by ~ 3meV due to the presence of SiO_2. In structural point of view, the distance between graphene and WS_2 is elongated by ~ 0.2.

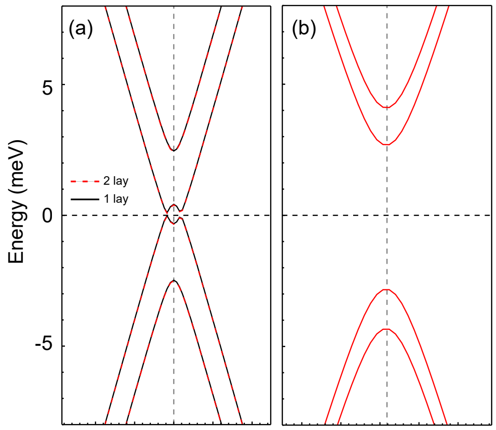

Figure 5.11: (a) Calculated band structure for the slab structure of a single layer or double layers of WS2 (4 × 4) on graphene (5 × 5). (b) Calculated band structure for the slab structure of WS_2 monolayer (4 × 4) on graphene (5 × 5) with SiO_2 (3 × 3) substrate terminating with oxygen atoms. The zero energy is set to be in the middle of Dirac cone for the comparison.

The model Hamiltonian fitting to first-principles calculations

By comparison the model Hamiltonian with DFT calculations, we determined the physical quantities: $M = 0.01(0.04$meV, ?$R = 0.07(0.18)$meV, ?$VZ = 0.98(1.539)$meV and ?I 0(0)meV for 3.34(3.21). The excellent matching of DFT with the model demonstrates the validity of the SOC values extracted from DFT calculations. Figure 5.12 shows that the quality of fitting is well maintained regardless of the separation between graphene and WS2.

The full Hamiltonian of WS_2/Graphene and topological number calculation

In WS_2/graphene system, the sub-lattice and z-inversion symmetries are both broken, and thus the only symmetries left are $2\pi/3$ rotational symmetry, the reflection symmetry along the armchair direction and time reversal symmetry. Since tungsten and sulfur bands are far away from Fermi level which is sitting at Dirac point, we can reasonable treat the conduction bands from WS_2 as perturbation and model the

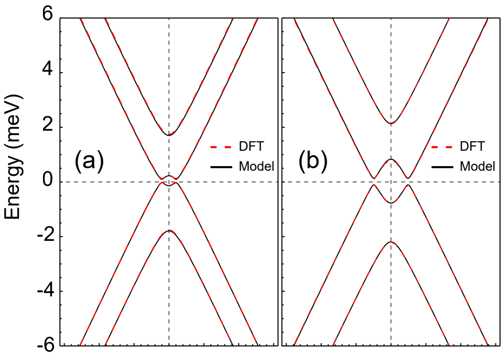

Figure 5.12: Calculated band structure from DFT and the model Hamiltonian for the slab structure with the interlayer distance of (a) 3.34 and (b) 3.21.

system by a effective minimum tight-binding Hamiltonian,

$$\begin{aligned} H \;=\; & \left[t_0 \sum_r a_r^\dagger a_r + \xi t_0 \sum_r b_r^\dagger b_r\right] - t \sum_{\langle rr'\rangle} (a_r^\dagger b_{r'} + b_r^\dagger a_{r'}) \\ & + \left[i t_1 \sum_{\langle rr'\rangle} a_r^\dagger (\vec{S} \times d_{rr'}) b_{r'} + h.c \right] + \left[t_3 \sum_{\langle\langle rr'\rangle\rangle} a_r^\dagger a_{r'} + \kappa t_3 \sum_{\langle\langle rr'\rangle\rangle} b_r^\dagger b_{r'} \right] \\ & + \left[i t_2 \sum_{\langle\langle rr'\rangle\rangle} v_{rr'} a_r^\dagger s_z a_{r'} + i \mu t_2 \sum_{\langle\langle rr'\rangle\rangle} v_{rr'} b_r^\dagger s_z b_{r'} \right] \\ & + \left[i t_4 \sum_{\langle\langle rr'\rangle\rangle} a_r^\dagger (\vec{S} \times d_{rr'}) a_{r'} + i \varsigma t_4 \sum_{\langle\langle rr'\rangle\rangle} b_r^\dagger (\vec{S} \times d_{rr'}) b_{r'} \right] \end{aligned} \tag{5.4}$$

where $a_r^\dagger / b_r^\dagger$ is a spinor which adds an electron to honeycomb site r of sub-lattice A(B). The first term describes onsite potential with t_0; the second term t allows nearest-neighbor hopping for graphene; the third term t_1 is nearest-bright hopping including spin-flipping process, which is also the origin of Rashba SOC; the fourth term t_3 is next-nearest-neighbor(n.n.n) hopping; the fifth is n.n.n hopping with s_z conserved SOC; and the last one is the n.n.n hopping with spin-flipping. The parameters ξ, κ, μ, and η describes the asymmetry of sub-lattice. At low energy, this Hamiltonian can be expanded around Dirac cone up to zeroth order

$$\begin{aligned} H = H_t + t_0\left(\frac{1+\xi}{2} + \sigma_z \frac{1-\xi}{2}\right) + \frac{3}{2} t_1 (\tau_z \sigma_x s_y - \sigma_y s_x) \\ - 3t_3\left(\frac{1+\kappa}{2} + \sigma_z \frac{1-\kappa}{2}\right) - 3\sqrt{3} t_2 \tau_z s_z \left(\frac{1-\mu}{2} + \sigma_z \frac{1+\mu}{2}\right) \end{aligned} \tag{5.5}$$

where τ describes valley; σ is for sub-lattice; s is for spin. The parameters are defined as:$\frac{3}{2} t_1 = \lambda_R$, $\frac{1-\xi}{2} t_0 - 3t_3 \frac{1-\kappa}{2} = M$, $3\sqrt{3} t_2 \frac{1-\mu}{2} = \lambda_{VZ}$, and $3\sqrt{3} t_2 \frac{1+\mu}{2} = \lambda_{so}$.

By fitting this Hamiltonian with DFT, we find that the low energy model is governed by valley-Zeeman SOC and Rashba SOC, and thus it creates a w-shaped gap of size $\approx \lambda_R$ in this case. Based on the theory in Ref. [50], we find that the evolution of Wannier function center of two states is trivially connected, which means one can cut across even number(two in this case) of states for arbitrary Θ along k_y-direction. It suggests that the system is topological trivial.

Our results are different from the previous studies by Avsar [3] and Wang [43]. Avsar's work shows that the the WS_2 has no significant SOC introduced by the WS_2 unless with sulphur vacancy in the bulk WS_2; while Wang's work gives that the SOC λ_{VZ} is huge and opens up a topological gap with the aid of Rashba SOC. However, we later confirmed with authors in Wang's paper that this gap is indeed topologically trivial.

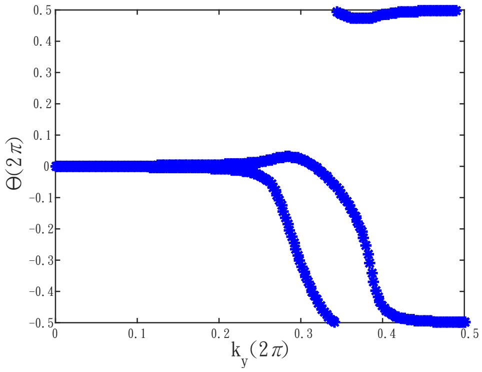

Figure 5.13: The evolution of the Wannier function center, described by a phase factor Θ, for the effective 1D system with k_y.

Adiabatic connection between WS_2/graphene and topological trivial system

Edge states on WS_2/graphene system are robust against weak bulk disorder and even magnetic field because of the large momentum separation of edge states near K-point. However, we that a type edge disorder which can make the system smoothly connected to a trivial insulator without closing the gap. As seen in Figure **??**, the edge states are lifted upward/downward when we assign the opposite on-site energy for different edges. The broken sub-lattice symmetry yields asymmetric zigzag edges, so they have opposite energy.

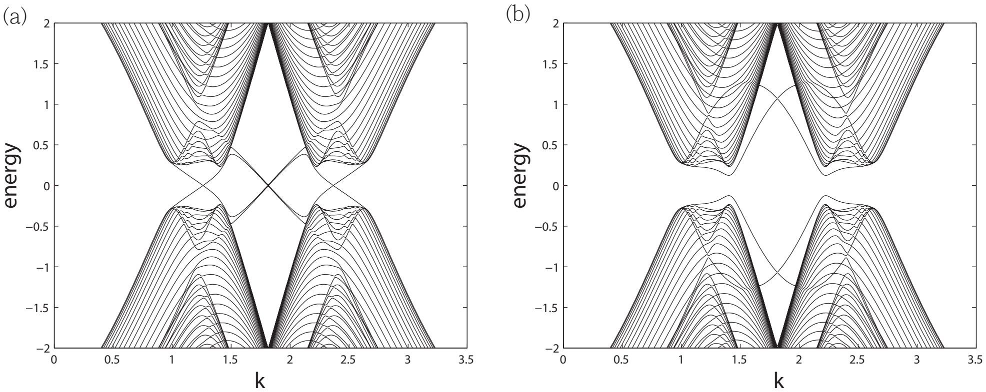

Figure 5.14: (a) One dimensional energy bands for zigzag-edge strip of graphene modeled with $\lambda_{\mathrm{VZ}}/t = 0.3$ and $\lambda_{\mathrm{R}}/t = 0.1$. (b) is the energy bands for the same model in (a), except that the upper/lower edge has onsite energy $0.5t/{-0.5t}$.

Spin relaxation rates of valley-Zeeman SOC

Valley-Zeeman spin orbit coupling is like Zeeman effect but with opposite sign at two valleys due to time reversal symmetry. Consider a graphene with valley-Zeeman SOC, $H = \hbar v_F(\tau_z\sigma_x p_x - \sigma_y p_y) + \lambda_{\mathrm{VZ}}\tau_z s_z$, the corresponding eigenstates are still the same as the ones of uncovered graphene but the energy spectrum for spin up/down shifts in opposite direction. The spin of an injecting electron in z-direction will not be relaxed in an elastic scattering process because $[H, s_z] = 0$ and the spin degree of freedom is totally decoupled from momentum. On the other hand, an electron with spin at in-plane direction will rotate with a constant rate $\frac{2\lambda_{VZ}}{h}$ which is unaffected by intra-valley scattering. The rotation direction are opposite for different valleys, so the spin will change direction after inter-valley scattering and the random spin precession can be derived as

$$\Delta\phi^2(t) = (\omega\tau_i)^2\frac{1}{\tau_i}t \tag{5.6}$$

where $\Delta\phi^2(\tau_s) \sim 1$

$$\tau_s^{-1} = \omega^2\tau_i \tag{5.7}$$

. Therefore, the total spin relaxation rate is

$$\tau_{VZ}^{-1} = \frac{2\lambda_{VZ}}{h}(1 + \frac{2\lambda_{VZ}}{h}\tau_i) \tag{5.8}$$

The second term can be ignored because inter-valley scattering time is the shortest time scale compared to the SOC relaxation time, i.e. $\frac{2\lambda_{VZ}}{h} \ll \tau_i^{-1}$. Thus, one can use the scattering rate $\tau_{VZ}^{-1} = \frac{2\lambda_{VZ}}{h}$ to extract valley-Zeeman SOC strength λ_{VZ}.

BIBLIOGRAPHY

[1] B L Altshuler, A G Aronov, and D E Khmelnitsky. Effects of electron-electron collisions with small energy transfers on quantum localisation. *Journal of Physics C: Solid State Physics*, 15(36):7367, 1982.

[2] Tsuneya Ando, Takeshi Nakanishi, and Riichiro Saito. Berry's phase and absence of back scattering in carbon nanotubes. *Journal of the Physical Society of Japan*, 67(8):2857–2862, 1998. doi: 10.1143/JPSJ.67.2857.

[3] A. Avsar, J. Y. Tan, T. Taychatanapat, J. Balakrishnan, G.K.W. Koon, Y. Yeo, J. Lahiri, A. Carvalho, A. S. Rodin, E.C.T. O'Farrell, G. Eda, A. H. Castro Neto, and B. Ozyilmaz. Spin-orbit proximity effect in graphene. *Nat Commun*, 5:4875, Sep 2014. doi: 10.1038/ncomms5875.

[4] J. Balakrishnan, G. K. W. Koon, M. Jaiswal, A. H. C. Neto, and B. Colossal Ozyilmaz. enhancement of spin-orbit coupling in weakly hydrogenated graphene. *Nat. Phys.*, 9:284–287, Mar 2013. doi: doi:10.1038/nphys2576.

[5] P. E. Blöchl. Projector augmented-wave method. *Phys. Rev. B*, 50:17953–17979, Dec 1994. doi: 10.1103/PhysRevB.50.17953.

[6] A. H. Castro Neto and F. Guinea. Impurity-induced spin-orbit coupling in graphene. *Phys. Rev. Lett.*, 103:026804, Jul 2009. doi: 10.1103/PhysRevLett.103.026804.

[7] U. Chandni, Erik A. Henriksen, and J. P. Eisenstein. Transport in indium-decorated graphene. *Phys. Rev. B*, 91:245402, Jun 2015. doi: 10.1103/PhysRevB.91.245402.

[8] J.-H Chen, C. Jang, S. Adam, M. S. Fuhrer, E. D. Williams, and M. Ishigami. Charged-impurity scattering in graphene. *Nat Phys*, 4:377–381, April 2008. doi: 10.1038/nphys935.

[9] Supriyo Datta. *Electronic Transport in Mesoscopic Systems*. Cambridge University Press, 3 edition, 1995. ISBN 9780511805776.

[10] Jun Ding, Zhenhua Qiao, Wanxiang Feng, Yugui Yao, and Qian Niu. Engineering quantum anomalous/valley hall states in graphene via metal-atom adsorption: An *ab-initio* study. *Phys. Rev. B*, 84:195444, Nov 2011. doi: 10.1103/PhysRevB.84.195444.

[11] MI Dyakonov and VI Perel. Spin relaxation of conduction electrons in noncentrosymmetric semiconductors. *Soviet Physics Solid State, Ussr*, 13(12): 3023–3026, 1972.

[12] R. J. Elliott. Theory of the effect of spin-orbit coupling on magnetic resonance in some semiconductors. *Phys. Rev.*, 96:266–279, Oct 1954. doi: 10.1103/PhysRev.96.266.

[13] Aires Ferreira, Tatiana G. Rappoport, Miguel A. Cazalilla, and A. H. Castro Neto. Extrinsic spin hall effect induced by resonant skew scattering in graphene. *Phys. Rev. Lett.*, 112:066601, Feb 2014. doi: 10.1103/PhysRevLett.112.066601.

[14] Martin Gmitra, Denis Kochan, Petra Högl, and Jaroslav Fabian. Trivial and inverted dirac bands and the emergence of quantum spin hall states in graphene on transition-metal dichalcogenides. *Phys. Rev. B*, 93:155104, Apr 2016. doi: 10.1103/PhysRevB.93.155104.

[15] R. V. Gorbachev, F. V. Tikhonenko, A. S. Mayorov, D. W. Horsell, and A. K. Savchenko. Weak localization in bilayer graphene. *Phys. Rev. Lett.*, 98:176805, Apr 2007. doi: 10.1103/PhysRevLett.98.176805.

[16] Stefan Grimme, Jens Antony, Stephan Ehrlich, and Helge Krieg. A consistent and accurate ab initio parametrization of density functional dispersion correction (dft-d) for the 94 elements h-pu. *The Journal of Chemical Physics*, 132 (15):154104, 2010. doi: http://dx.doi.org/10.1063/1.3382344.

[17] Wei Han and R. K. Kawakami. Spin relaxation in single-layer and bilayer graphene. *Phys. Rev. Lett.*, 107:047207, Jul 2011. doi: 10.1103/PhysRevLett.107.047207.

[18] X. Hong, S.-H. Cheng, C. Herding, and J. Zhu. Colossal negative magnetoresistance in dilute fluorinated graphene. *Phys. Rev. B*, 83:085410, Feb 2011. doi: 10.1103/PhysRevB.83.085410.

[19] Jun Hu, Jason Alicea, Ruqian Wu, and Marcel Franz. Giant topological insulator gap in graphene with $5d$ adatoms. *Phys. Rev. Lett.*, 109:266801, Dec 2012. doi: 10.1103/PhysRevLett.109.266801.

[20] K.-I. Imura, Y. Kuramoto, and K. Nomura. Anti-localization of graphene under the substrate electric field. *EPL (Europhysics Letters)*, 89(1):17009, 2010.

[21] Zhenzhao Jia, Baoming Yan, Jingjing Niu, Qi Han, Rui Zhu, Dapeng Yu, and Xiaosong Wu. Transport study of graphene adsorbed with indium adatoms. *Phys. Rev. B*, 91:085411, Feb 2015. doi: 10.1103/PhysRevB.91.085411.

[22] Zilong Jiang, Cui-Zu Chang, Chi Tang, Peng Wei, Jagadeesh S. Moodera, and Jing Shi. Independent tuning of electronic properties and induced ferromagnetism in topological insulators with heterostructure approach. *Nano Letters*, 15(9):5835–5840, 2015. doi: 10.1021/acs.nanolett.5b01905. PMID: 26288309.

[23] Kyung-Hwan Jin and Seung-Hoon Jhi. Proximity-induced giant spin-orbit interaction in epitaxial graphene on a topological insulator. *Phys. Rev. B*, 87: 075442, Feb 2013. doi: 10.1103/PhysRevB.87.075442.

[24] C. L. Kane and E. J. Mele. Quantum spin hall effect in graphene. *Phys. Rev. Lett.*, 95:226801, Nov 2005. doi: 10.1103/PhysRevLett.95.226801.

[25] A. A. Kaverzin and B. J. van Wees. Electron transport nonlocality in monolayer graphene modified with hydrogen silsesquioxane polymerization. *Phys. Rev. B*, 91:165412, Apr 2015. doi: 10.1103/PhysRevB.91.165412.

[26] G. Kresse and D. Joubert. From ultrasoft pseudopotentials to the projector augmented-wave method. *Phys. Rev. B*, 59:1758–1775, Jan 1999. doi: 10.1103/PhysRevB.59.1758.

[27] P. A. Lee, A. Douglas Stone, and H. Fukuyama. Universal conductance fluctuations in metals: Effects of finite temperature, interactions, and magnetic field. *Phys. Rev. B*, 35:1039–1070, Jan 1987. doi: 10.1103/PhysRevB.35.1039.

[28] Chao-Xing Liu, Shou-Cheng Zhang, and Xiao-Liang Qi. The quantum anomalous hall effect: Theory and experiment. *Annu. Rev. of Condens. Matter Phys.*, 7:301–321, 2016.

[29] Dongwei Ma, Zhongyao Li, and Zhongqin Yang. *Carbon*, 50(1):297 – 305, 2012. ISSN 0008-6223. doi: http://dx.doi.org/10.1016/j.carbon.2011.08.055.

[30] E. McCann, K. Kechedzhi, Vladimir I. Fal'ko, H. Suzuura, T. Ando, and B. L. Altshuler. Weak-localization magnetoresistance and valley symmetry in graphene. *Phys. Rev. Lett.*, 97:146805, Oct 2006. doi: 10.1103/PhysRevLett.97.146805.

[31] Edward McCann and Vladimir I. Fal'ko. $z \rightarrow -z$ symmetry of spin-orbit coupling and weak localization in graphene. *Phys. Rev. Lett.*, 108:166606, Apr 2012. doi: 10.1103/PhysRevLett.108.166606.

[32] B. N. Narozhny, Gábor Zala, and I. L. Aleiner. Interaction corrections at intermediate temperatures: Dephasing time. *Phys. Rev. B*, 65:180202, May 2002. doi: 10.1103/PhysRevB.65.180202.

[33] H. Ochoa, A. H. Castro Neto, and F. Guinea. Elliot-yafet mechanism in graphene. *Phys. Rev. Lett.*, 108:206808, May 2012. doi: 10.1103/PhysRevLett.108.206808.

[34] John P. Perdew, Kieron Burke, and Matthias Ernzerhof. Generalized gradient approximation made simple. *Phys. Rev. Lett.*, 77:3865–3868, Oct 1996. doi: 10.1103/PhysRevLett.77.3865.

[35] Zhenhua Qiao, Shengyuan A. Yang, Wanxiang Feng, Wang-Kong Tse, Jun Ding, Yugui Yao, Jian Wang, and Qian Niu. Quantum anomalous hall effect in graphene from rashba and exchange effects. *Phys. Rev. B*, 82:161414, Oct 2010. doi: 10.1103/PhysRevB.82.161414.

[36] Zhenhua Qiao, Wei Ren, Hua Chen, L. Bellaiche, Zhenyu Zhang, A. H. MacDonald, and Qian Niu. Quantum anomalous hall effect in graphene proximity coupled to an antiferromagnetic insulator. *Phys. Rev. Lett.*, 112:116404, Mar 2014. doi: 10.1103/PhysRevLett.112.116404.

[37] Yafei Ren, Zhenhua Qiao, and Qian Niu. Topological phases in two-dimensional materials: a review. *Rep. on Prog. Phys.*, 79(6):066501, 2016.

[38] R. Rengel and M. J. Martín. Diffusion coefficient, correlation function, and power spectral density of velocity fluctuations in monolayer graphene. *Journal of Applied Physics*, 114(14):143702, 2013. doi: http://dx.doi.org/10.1063/1.4824182.

[39] Mengqiao Sui, Guorui Chen, Liguo Ma, Wen-Yu Shan, Dai Tian, Kenji Watanabe, Takashi Taniguchi, Xiaofeng Jin, Wang Yao, Di Xiao, and Yuanbo Zhang. Gate-tunable topological valley transport in bilayer graphene. *Nat Phys*, 11: 1027–1031, Dec 2015. doi: 10.1038/nphys3485.

[40] F. V. Tikhonenko, D. W. Horsell, R. V. Gorbachev, and A. K. Savchenko. Weak localization in graphene flakes. *Phys. Rev. Lett.*, 100:056802, Feb 2008. doi: 10.1103/PhysRevLett.100.056802.

[41] F. V. Tikhonenko, A. A. Kozikov, A. K. Savchenko, and R. V. Gorbachev. Transition between electron localization and antilocalization in graphene. *Phys. Rev. Lett.*, 103:226801, Nov 2009. doi: 10.1103/PhysRevLett.103.226801.

[42] Nikolaos Tombros, Csaba Jozsa, Mihaita Popinciuc, Harry T. Jonkman, and Bart J. van Wees. Electronic spin transport and spin precession in single graphene layers at room temperature. *Nature*, 448:571–574, Aug 2007. doi: 10.1038/nature06037.

[43] Zhe Wang, Dong-Keun Ki, Hua Chen, Helmuth Berger, Allan H. MacDonald, and Alberto F. Morpurgo. Strong interface-induced spin-orbit interaction in graphene on ws2. *Nat Commun*, 6:8339, Sep 2015. doi: doi:10.1038/ncomms9339.

[44] Zhiyong Wang, Chi Tang, Raymond Sachs, Yafis Barlas, and Jing Shi. Proximity-induced ferromagnetism in graphene revealed by the anomalous hall effect. *Phys. Rev. Lett.*, 114:016603, Jan 2015. doi: 10.1103/PhysRevLett.114.016603.

[45] Conan Weeks, Jun Hu, Jason Alicea, Marcel Franz, and Ruqian Wu. Engineering a robust quantum spin hall state in graphene via adatom deposition. *Phys. Rev. X*, 1:021001, Oct 2011. doi: 10.1103/PhysRevX.1.021001.

[46] Hongming Weng, Rui Yu, Xiao Hu, Xi Dai, and Zhong Fang. Quantum anomalous hall effect and related topological electronic states. *Adv. in Phys.*, 64:227, May 2015. doi: 10.1080/00018732.2015.1068524.

[47] Di Xiao, Wang Yao, and Qian Niu. Valley-contrasting physics in graphene: Magnetic moment and topological transport. *Phys. Rev. Lett.*, 99:236809, Dec 2007. doi: 10.1103/PhysRevLett.99.236809.

[48] Di Xiao, Gui-Bin Liu, Wanxiang Feng, Xiaodong Xu, and Wang Yao. Coupled spin and valley physics in monolayers of mos_2 and other group-vi dichalcogenides. *Phys. Rev. Lett.*, 108:196802, May 2012. doi: 10.1103/PhysRevLett.108.196802.

[49] Y. Yafet. *Solid State Physics*, volume 14. Academic, New York, 1963.

[50] Rui Yu, Xiao Liang Qi, Andrei Bernevig, Zhong Fang, and Xi Dai. Equivalent expression of F_2 topological invariant for band insulators using the non-abelian berry connection. *Phys. Rev. B*, 84:075119, Aug 2011. doi: 10.1103/PhysRevB.84.075119.

[51] Young-Jun Yu, Yue Zhao, Sunmin Ryu, Louis E. Brus, Kwang S. Kim, and Philip Kim. Tuning the graphene work function by electric field effect. *Nano Letters*, 9(10):3430–3434, 2009. doi: 10.1021/nl901572a. PMID: 19719145.

[52] Jiayong Zhang, Bao Zhao, Yugui Yao, and Zhonggin Yang. Quantum anomalous hall effect in graphene-based heterostructure. *Scientific Reports*, 5:10629, May 2015. doi: 10.1038/srep10629.

[53] Yuanbo Zhang, Yan-Wen Tan, Horst L. Stormer, and Philip Kim. Experimental observation of the quantum hall effect and berry's phase in graphene. *Nature*, 438:201–204, 2005. doi: 10.1038/nature04235.

Chapter 6

ADATOM DOPED GRAPHENE

6.1 Introduction

Enhancing spin-orbit coupling (SOC) in graphene has attracted much interest in recent years, for its application in spintronic devices and realization of exotic physics phenomena such as quantum spin Hall effect[19] and quantum anomalous Hall effect[28]. Due to the light mass of carbon atoms, the SOC on pristine graphene is exceedingly weak[4, 11, 26, 36], leading to long spin relaxation length and unobservable (topological) SOC gap ($\sim 10^{-3}$meV). Therefore, to study the SOC related phenomena, several theories and first principle simulations have proposed tailoring the SOC strength on the open 2-dimensional honeycomb structure by coupling to heavy adatoms, codopant, or other materials with hexagonal structure [5, 8, 10, 14, 18, 23, 32, 35, 37]. Some experiments have confirmed the existence of Rashba SOC arising from crystal with structural inversion asymmetry[3, 13, 20, 34]; however, interestingly intrinsic (Kane-Mele) SOC which respects the full symmetries of pristine graphene has not been observed in experiments. Moreover, no sign of SOC was observed experimentally [7, 16] on the adatom decorated graphene samples which are predicted to host significant SOC gap by first principle simulation[14, 32]. Therefore, it is important to investigate the reason for the absence of SOC signals in the hope of bringing first principle calculation and experiments into consistency.

In an adatom-doped graphene model, the tunneling between two carbon atoms through adatom orbitals opens or enhances channels in graphene and these channels in the low energy effectively induce spin-conserving SOC or spin-flipping SOC. For example, adatom with p outer-shell will only induce spin-conserving SOC such as $\tau^y\sigma^y s^z$ and intrinsic SOC, without the detrimental factor-Rashba SOC. Therefore, this type of atoms can effectively stabilize QSE phase and may induce sizable topological gap with strong SOC adatoms, e.g. In and Tl as predicted in the previous work. [32] On the other hand, both spin-conseving and spin-flipping SOCs exist on graphene near the Dirac points by coupling to d orbital adatoms. Thus, only when the induced intrinsic SOC is greater than the Rashba SOC, the system will turn to QSHE phase by proximity. Interesting, for some specific d-orbital adatoms, such as Os [14], they do not simply follow the aforementioned proximity scheme, but still generate a topological gap with substantial adatom coverage. The energy bands of these adatoms dominate the low energy physics and open a SOC gap which essentially comes from adatoms instead of conventional gap in Dirac physics.

The above SOC signatures can be possibly identified by the magneto-conductivity (MC) transport experiment[12]. The SOC in conventional 2D electron gas will turn the disorder class from weak-localization (WL) to weak anti-localization (WAL) by changing the quantum interference. However, the contribution of SOC in quantum conductivity is more complicated in graphene due to its unusual chirality [1, 38]. Graphene with smooth disorder is predicted to exhibit WAL [1]; However, strong inter-valley scattering, which typically arises in ordinary-quality samples, suppresses the chirality-related WAL and generates weak localization (WL) [24, 31]. While introducing strong Rashba SOC, the electron spin precesses around the effective magnetic field and acquires an additional π phase in the interference [25]—reviving WAL due to spin. Intrinsic (Kane-Mele) SOC terms, by contrast, break an effective time reversal symmetry and thus place the system in the unitary class (suppressed WL) [25]. Note that the SOC has to strong enough to participate in the interference before the electron dephasing out—i.e. the relaxation rate exceeds the inelastic dephasing rate. Though intrinsic SOC is the most important SOC to realized quantum spin Hall phase, it is hard to pinpoint its existence by MC since unitary behavior can come from not only intrinsic SOC, but also other decoherence sources as well. Therefore, in this work, we investigate the MC signatures in $l = p, d$-orbital adatom doped graphene, We also proposed a scheme to hunt for the SOC signatures this case and derive the corresponding magneto-conductivity formula and spin-relaxation rates.

In the section 6.2, we will first derive the effective Hamiltonians for graphene with sparse, randomly distributed adatoms of which outer-shell is p- or d-orbitals. Then we will explore how the randomness and disorder brought in by adatoms would affect the quantum spin Hall phase by Landauer Buttiker simulation in section 6.3. In section **??**, we derive the magento-conductance and the related SOCs for all the possible SOCs induced by both adatoms and substrate. Finally, we discuss the current difficulties of measuring SOCs in experiments and propose a potential scheme to pin down their signatures in sections 6.5, 6.6.

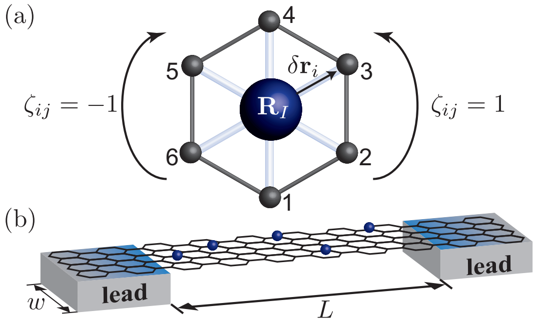

Figure 6.1: (a) Cartoon picture of graphene with adatom at the center of the plaquette and (b)the device setup in the transport simulation.

6.2 Effective Hamiltonians for adatom-decorated graphene

Throughout we consider either *d*- or *p*-orbital adatoms residing at ‘hollow sites’ in the graphene sheet [see Fig. 6.1(a)]. The hollow site allows the adatoms to most effectively mediate the spin-dependent second-neighbor hopping present in the Kane-Mele model while avoiding competing effects that arise in other positions with fewer symmetries; moreover, this position is predicted to be energetically favorable for many atomic species [2, 6, 22, 29, 30, 32]. In this section, we construct a microscopic Hamiltonian describing a single adatom on graphene, then obtain an effective graphene-only Hamiltonian, and finally derive a continuum model for graphene with multiple randomly distributed adatoms.

Following Refs. [5, 9, 14, 32], we model graphene with a *single* adatom using a tight-binding Hamiltonian

$$H = H_g + H_a + H_c, \tag{6.1}$$

where H_g, H_a, and H_c respectively describe disordered graphene, the adatom, and the graphene-adatom hybridization. We employ operators $c^\dagger_{\mathbf{r}\alpha}$ to create a spin-α electron on the carbon atom at site $\mathbf{r}$ and $d^\dagger_{m\alpha}$ to create a spin-α electron on orbital m of the adatom; throughout, indices such as α are implicitly summed when suppressed. The graphene-only part of the Hamiltonian is given by

$$H_g = -t \sum_{\langle \mathbf{r}\mathbf{r}'\rangle} (c^\dagger_{\mathbf{r}} c_{\mathbf{r}'} + h.c.) + H_{dis}. \tag{6.2}$$

The first term describes nearest-neighbor hopping with amplitude t while the second encodes a ‘background’ disorder arising, for example, from the substrate but explicitly *not* from the adatom. The adatom Hamiltonian reads

$$\begin{aligned}H_a = &\sum_{m=-l}^{m=l} \epsilon_{|m|} d_m^\dagger d_m + \sum_{m=-l}^{l} \Lambda_m \big(d_m^\dagger s^z d_m^\dagger - d_{-m}^\dagger s^z d_{-m}^\dagger\big) \\ &+ \sum_{m=-l}^{l} \sqrt{2}\Lambda_m' \big(d_{-m+1}^\dagger s^- d_{-m} + d_{m-1}^\dagger s^+ d_m^\dagger + h.c.\big).\end{aligned} \tag{6.3}$$

Here $l = 1$ for the p-orbital case while $l = 2$ for the d-orbital case, and s^z and $s^\pm = (s^x \pm i s^y)/2$ act on the spin degrees of freedom ($s^{x,y,z}$ are Pauli matrices). Crystal fields and atomic spin-orbit coupling respectively split the adatom's orbitals through $\epsilon_{|m|}$ and Λ_m, $\Lambda_{m'}$ couplings. Finally, the adatom-graphene hybridization terms are

$$H_c = -\sum_{m=-l}^{l} (t_{|m|} C_{m\mathbf{R}}^\dagger d_m + h.c.). \tag{6.4}$$

In Eq. (6.4), we introduced operators

$$C_{m\mathbf{R}\alpha} = \frac{1}{\sqrt{6}} \sum_{j=1}^{6} e^{-i\frac{\pi}{3}m(j-1)} c_{\mathbf{R}+\delta\mathbf{r}_j\alpha}, \tag{6.5}$$

where $\mathbf{R}$ designates the impurity site and $\delta\mathbf{r}_j$ points from the impurity to one of the six neighboring carbon atoms as illustrated in Fig. 6.1(a). The couplings t_m are constrained by symmetries; all are real except t_1, which is purely imaginary.

To understand how graphene is affected by the adatom, it is illuminating to integrate out the adatom degrees of freedom. Focusing on energies that are far from the adatom levels, one obtains an effective graphene Hamiltonian that is modified in the vicinity of the adatom (see Appendix **??** and Refs. [5, 9, 32]),

$$H_{\text{eff}} = H_g + \delta H_{\mathbf{R}}. \tag{6.6}$$

The second term describes additional channels mediated by the adatom:

$$\begin{aligned}\delta H_{\mathbf{R}} = &\sum_{i} T_0 c_i^\dagger c_i \\ &+ \Bigg[\sum_{\langle ij\rangle} [T_1 c_i^\dagger c_j + i\zeta_{ij} T_1' c_i^\dagger s^z c_j + iT_1'' c_i^\dagger (\mathbf{s}\times\mathbf{d}_{ij}) c_j] \\ &+ \sum_{\langle\langle ij\rangle\rangle} [T_2 c_i^\dagger c_j + i\zeta_{ij} T_2' c_i^\dagger s^z c_j + iT_2'' c_i^\dagger (\mathbf{s}\times\mathbf{d}_{ij}) c_j] \\ &+ \sum_{\langle\langle\langle ij\rangle\rangle\rangle} [T_3 c_i^\dagger c_j + iT_3'' c_i^\dagger (\mathbf{s}\times\mathbf{d}_{ij}) c_j] + h.c.\Bigg].\end{aligned} \tag{6.7}$$

Parameter relations		
d-orbital case	p-orbital case	low-energy limit
$T_0 = -\frac{1}{6}(\frac{t_0^2}{\epsilon_0} + 2\frac{\lvert t_1\rvert^2}{\epsilon_1} + 2\frac{t_2^2}{\epsilon_2})$	$T_0 = -\frac{1}{6}(\frac{t_0^2}{\epsilon_0} + 2\frac{\lvert t_1\rvert^2}{\epsilon_1})$	$3T_0\mathbb{I}$
$T_1 = -\frac{1}{6}(\frac{t_0^2}{\epsilon_0} + \frac{\lvert t_1\rvert^2}{\epsilon_1} - \frac{t_2^2}{\epsilon_2})$	$T_1 = -\frac{1}{6}(\frac{t_0^2}{\epsilon_0} + \frac{\lvert t_1\rvert^2}{\epsilon_1})$	$-3T_1 e^{i\Delta\mathbf{K}\cdot\mathbf{R}\tau^z}\tau^x\sigma^x$
$T_2 = -\frac{1}{6}(\frac{t_0^2}{\epsilon_0} - \frac{\lvert t_1\rvert^2}{\epsilon_1} - \frac{t_2^2}{\epsilon_2})$	$T_2 = -\frac{1}{6}(\frac{t_0^2}{\epsilon_0} - \frac{\lvert t_1\rvert^2}{\epsilon_1})$	$-3T_2\mathbb{I}$
$T_3 = -\frac{1}{6}(\frac{t_0^2}{\epsilon_0} - 2\frac{\lvert t_1\rvert^2}{\epsilon_1} + \frac{t_2^2}{\epsilon_2})$	$T_3 = -\frac{1}{6}(\frac{t_0^2}{\epsilon_0} - 2\frac{\lvert t_1\rvert^2}{\epsilon_1})$	$3T_3 e^{i\Delta\mathbf{K}\cdot\mathbf{R}\tau^z}\tau^x\sigma^x$
$T_1' = \frac{1}{2\sqrt{3}}(\frac{\lvert t_1\rvert^2}{\epsilon_1^2}\Lambda_1 + \frac{t_2^2}{\epsilon_2^2}\Lambda_2)$	$T_1' = \frac{1}{2\sqrt{3}}\frac{\lvert t_1\rvert^2}{\epsilon_1^2}\Lambda_1$	$3\sqrt{3}T_1' e^{i\Delta\mathbf{K}\cdot\mathbf{R}\tau^z}\tau^y\sigma^y s^z$
$T_2' = \frac{1}{2\sqrt{3}}(\frac{\lvert t_1\rvert^2}{\epsilon_1^2}\Lambda_1 - \frac{t_2^2}{\epsilon_2^2}\Lambda_2)$	$T_2' = \frac{1}{2\sqrt{3}}\frac{\lvert t_1\rvert^2}{\epsilon_1^2}\Lambda_1$	$3\sqrt{3}T_2'\tau^z\sigma^z s^z$
$T_1'' = -i\frac{\sqrt{2}}{3a}(2\frac{t_1t_2}{\epsilon_1\epsilon_2}\Lambda_2' - \frac{t_1t_0}{\epsilon_1\epsilon_0}\Lambda_1')$	$T_1'' = i\frac{\sqrt{2}}{3a}\frac{t_1t_0}{\epsilon_1\epsilon_0}\Lambda_1'$	$-3T_1''(\tau^z\sigma^x s^y + \sigma^y s^x)$
$T_2'' = i\frac{\sqrt{2}}{3a}\frac{t_1t_0}{\epsilon_1\epsilon_0}\Lambda_1'$	$T_2'' = i\frac{\sqrt{2}}{3a}\frac{t_1t_0}{\epsilon_1\epsilon_0}\Lambda_1'$	$O(k_x, k_y)$
$T_3'' = i\frac{\sqrt{2}}{3a}(\frac{t_1t_2}{\epsilon_1\epsilon_2}\Lambda_2' + \frac{t_1t_0}{\epsilon_1\epsilon_0}\Lambda_1')$	$T_3'' = i\frac{\sqrt{2}}{3a}\frac{t_1t_0}{\epsilon_1\epsilon_0}\Lambda_1'$	$3T_3''(\tau^z\sigma^x s^y + \sigma^y s^x)$

Table 6.1: Relationship between parameters in various models. The first two columns relate couplings in Eqs. (6.3), (6.4), and (6.7) for the d- and p-orbital cases, respectively. The third column gives the lowest-order contribution to the continuum Dirac Hamiltonian arising from each microscopic process.

Here i, j denote carbon sites surrounding the impurity as labeled in Fig. 6.1; the couplings for d- and p-orbital adatoms appear in Table 6.1; $\zeta_{ij} = \pm 1$ denotes the circulation of an electron hopping around the plaquette (see Fig.6.1); $\mathbf{s}$ is a vector of Pauli matrices; and $\mathbf{d}_{ij} = \delta\mathbf{r}_i - \delta\mathbf{r}_j$. The T_0 coupling simply represents a potential induced by the adatom on the neighboring carbon sites, while the $T_{1,2,3}$ terms are first-, second-, and third-neighbor hoppings mediated by the adatom. All other terms represent induced spin-orbit couplings, with $T'_{1,2}$ designating S^z-conserving processes and $T''_{1,2,3}$ non-S^z-conserving processes. The latter arise because the adatom locally breaks structural inversion symmetry.

We now make the leap to many randomly distributed (but sparse) adatoms on graphene by considering the Hamiltonian

$$H_{\text{eff}} = H_g + \sum_{\mathbf{R}} \delta H_{\mathbf{R}}. \tag{6.8}$$

Focusing on low-energy physics in the vicinity of graphene's Dirac points, we can further distill the model by deriving a continuum Dirac Hamiltonian perturbed by the adatom-mediated couplings. To this end we decompose the lattice fermion operators for honeycomb sublattices A and B in terms of slowly varying continuum

Dirac fields via

$$\begin{aligned} c_{\mathbf{r}\in A,\alpha} &\approx \sqrt{A_{\hexagon}}\left(\psi_{KA\alpha}e^{i\mathbf{K}\cdot\mathbf{r}} + \psi_{K'A\alpha}e^{i\mathbf{K}'\cdot\mathbf{r}}\right) \\ c_{\mathbf{r}\in B,\alpha} &\approx \sqrt{A_{\hexagon}}\left(\psi_{KB\alpha}e^{i\mathbf{K}\cdot\mathbf{r}} + \psi_{K'B\alpha}e^{i\mathbf{K}'\cdot\mathbf{r}}\right), \end{aligned} \tag{6.9}$$

where $\mathbf{K} = (\frac{4\pi}{3\sqrt{3}a}, 0)$, $\mathbf{K}' = -\mathbf{K}$, $A_{\hexagon}$ is the unit-cell area, and a is the nearest-neighbor carbon separation.

Inserting this decomposition into Eq. (6.8) and then expanding in powers of momenta away from the Dirac points yields the desired continuum model, which we write as

$$H_{\text{cont}} = \int d\mathbf{r}\, \psi^{\dagger}\left(\mathcal{H}_g + \sum_{\mathbf{R}_I} \delta\mathcal{H}_{\mathbf{R}}\right)\psi. \tag{6.10}$$

The first term on the right side,

$$\mathcal{H}_g = \hbar v_F\left(-i\partial_x\sigma^x\tau^z - i\partial_y\sigma^y\right) + \mathcal{H}_{\text{d}is}, \tag{6.11}$$

is the usual graphene Dirac Hamiltonian supplemented by a disorder potential $\mathcal{H}_{\text{d}is}$ that encodes both intra- and inter-valley scattering. We note that $\mathcal{H}_{\text{d}is}$ is the continuum analogue of $H_{\text{d}is}$ from Eq. (6.2), and is thus is unrelated to the adatoms. Here and below $\tau^{x,y,z}$ and $\sigma^{x,y,z}$ are Pauli matrices that act in the valley and sublattice sectors, respectively. The second term in Eq. (6.10) contains the continuum form of the adatom-mediated couplings in Eq. (6.7). Interestingly, this part of the Hamiltonian differs qualitatively for *d*- and *p*-orbital adatoms, so we now examine these two cases separately.

d-orbital adatoms

For *d*-orbital adatoms, we find

$$\begin{aligned} \delta\mathcal{H}^{(d)}_{\mathbf{R}} = A_{\hexagon}\delta(\mathbf{r}-\mathbf{R})\Big[&V_0 + \lambda_{\text{R}}(\tau^z\sigma^x s^y + \sigma^y s^x) \\ &+ \lambda_{\text{KM}}\tau^z\sigma^z s^z + e^{i\Delta\mathbf{K}\cdot\mathbf{R}\tau^z}(V_{\text{i}}\tau^x\sigma^x + \lambda_{\text{i}}\tau^y\sigma^y s^z)\Big] \end{aligned} \tag{6.12}$$

upon retaining only terms with no spatial derivatives. All couplings are defined in Table 6.2. (See also the last column of Table 6.1 for the low-energy contribution arising from each microscopic channel.) The first term in Eq. (6.12) represents a local potential due to the adatoms; the second encodes Kane-Mele SOC that favors a QSH phase; the third is Rashba-like SOC, which breaks structural inversion symmetry and does not conserve S^z; and finally the last line allows inter-valley

Parameters in the continuum Dirac Hamiltonian	
d-orbital case, Eq. (6.12)	*p*-orbital case, Eqs. (6.14), (6.15)
$V_0 = -\frac{3}{2}\frac{\lvert t_1\rvert^2}{\epsilon_1} - \frac{3t_2^2}{2\epsilon_2}$	$V_0 = -\frac{3}{2}\frac{\lvert t_1\rvert^2}{\epsilon_1}$
$V_\mathrm{i} = \frac{3\lvert t_1\rvert^2}{2\epsilon_1} - \frac{3t_2^2}{2\epsilon_2}$	$V_\mathrm{i} = -V_0$
$\lambda_\mathrm{KM} = -\frac{3t_2^2}{2\epsilon_2^2}\Lambda_2 + \frac{3\lvert t_1\rvert^2}{2\epsilon_1^2}\Lambda_1$	$\lambda_\mathrm{KM} = \frac{3\lvert t_1\rvert^2}{2\epsilon_1^2}\Lambda_1$
$\lambda_\mathrm{i} = \frac{3\lvert t_1\rvert^2}{2\epsilon_1^2}\Lambda_1 + \frac{3t_2^2}{2\epsilon_2^2}\Lambda_2$	$\lambda_\mathrm{i} = \frac{3\lvert t_1\rvert^2}{2\epsilon_1^2}\Lambda_1$
$\lambda_\mathrm{R} = 3i\sqrt{2}\frac{t_1 t_2}{\epsilon_1\epsilon_2}\Lambda_2'$	$\lambda_R^{(1)} = i\frac{3}{4}\frac{t_0 t_1 \Lambda_1'}{\sqrt{2}\epsilon_0\epsilon_1}$

Table 6.2: Definition of parameters in the adatom-mediated part of our continuum Dirac Hamiltonians.

scattering with a phase that varies between different impurity sites ($\Delta\mathbf{K} = \mathbf{K}' - \mathbf{K}$ is the momentum difference between the valleys).

Equation (6.12) describes different types of scattering and spin-relaxation processes induced by adatoms. The intra-valley V_0 and inter-valley V_i scattering processes show that adatoms can be viewed as a disorder source, and thus lead to lower conductivity. We also see, however, that adatoms bring in three types of SOC: λ_i, $\lambda_{\mathrm{K}M}$, and λ_R. If one spatially averages the terms above, inter-valley processes drop out leaving

$$\overline{\delta\mathcal{H}_\mathbf{R}^{(d)}} = n_I\Big[V_0 + \lambda_\mathrm{KM}\tau^z\sigma^z s^z + \lambda_\mathrm{R}(\tau^z\sigma^x s^y + \sigma^y s^x)\Big] \tag{6.13}$$

with n_I the adatom coverage: the fraction of unit cells occupied with an adatom. Within this very crude treatment the *d*-orbital adatoms mediate a QSH phase provided $\lambda_{\mathrm{K}M} > \lambda_R$. [19] Previous work on related systems has shown that a QSH phase can indeed appear even when the adatoms are randomly positioned in the lattice [17, 32]; see also Sec. 6.5 below. Our main interest, however, is understanding how the adatom-mediated processes encoded in the more exact Eq. (6.12) impact transport signatures, especially magnetoconductance. We will address this problem in Sec. 6.3 and 6.4.

p-orbital adatoms

Next we turn to p-orbital adatoms. Again retaining only terms with no derivatives, the second piece in Eq. (6.10) now becomes

$$\begin{aligned}\delta\mathcal{H}^{(p,0)}_{\mathbf{R}} = A_{\bigcirc}\delta(\mathbf{r}-\mathbf{R}_I)\big[&V_0 + \lambda_{\mathrm{KM}}\tau^z\sigma^z s^z \\ &+ e^{i\Delta\mathbf{K}\cdot\mathbf{R}_I\tau^z}(V_{\mathrm{i}}\tau^x\sigma^x + \lambda_{\mathrm{i}}\tau^y\sigma^y s^z)\big].\end{aligned} \tag{6.14}$$

Table 6.2 defines the couplings above in terms of microscopic parameters. Comparing to Eq. (6.12) for the d-orbital case, we see that Rashba-like SOC is conspicuously absent here—which reflects destructive interference among certain microscopic processes that p-orbital adatoms mediate for electrons at the Dirac point [32]. Hence Eq. (6.14) preserves structural inversion symmetry even though the adatoms clearly violate this symmetry microscopically. We note that Ref. [27] found that a (small) Rashba-like term can arise if one includes spin-dependent hopping between carbon atoms and a p-orbital adatom. Due to carbon's tiny intrinsic SOC, we expect that such terms will be exceedingly weak and thus neglect them in this paper. At low energies, Kane-Mele SOC $\lambda_{\mathrm{K}M}$ and the inter-valley scattering term λ_{i} then furnish the dominant spin-dependent interactions, making p-orbital adatoms an appealing mediator of QSH physics in graphene. Measuring these SOC's through magnetoconductance is, however, challenging due to their relatively weak signature in transport [15, 25]. Fortunately, inversion symmetry is broken by higher-order corrections in the adatom-mediated part of the Hamiltonian. Retaining terms with one derivative, we find corrections

$$\begin{aligned}\psi^\dagger\delta\mathcal{H}^{(p,1)}_{\mathbf{R}}\psi = a\lambda^{(1)}_{\mathrm{R}}&A_{\bigcirc}\delta(\mathbf{r}-\mathbf{R}) \\ &\times\big[\psi^\dagger\mathbf{\Omega}\cdot\big(-i\nabla\psi\big) + h.c.\big] + \cdots\end{aligned} \tag{6.15}$$

with

$$\begin{aligned}\Omega_x &= s^y - \tau^z\sigma^y s^x + \sigma^x s^y \\ &\quad - e^{i\Delta\mathbf{K}\cdot\mathbf{R}_I\tau^z}\big(\tau^x s^y - \tau^y\sigma^z s^x + \tau^x\sigma^x s^y\big), \\ \Omega_y &= -s^x + \tau^z\sigma^y s^y + \sigma^x s^x \\ &\quad - e^{i\Delta\mathbf{K}\cdot\mathbf{R}_I\tau^z}\big(\tau^x s^x + \tau^y\sigma^z s^y - \tau^x\sigma^x s^x\big).\end{aligned} \tag{6.16}$$

Above we explicitly displayed only Rashba-like SOC's that are odd under structural inversion symmetry and thus break the 'accidental' symmetry present in Eq. (6.14); Table 6.2 defines the corresponding coupling $\lambda^{(1)}_{\mathrm{R}}$. Appendix **??** shows that various other terms with one derivative also exist, which we represent with the ellipsis above. Such terms are expected to be qualitatively unimportant, however, so we neglect

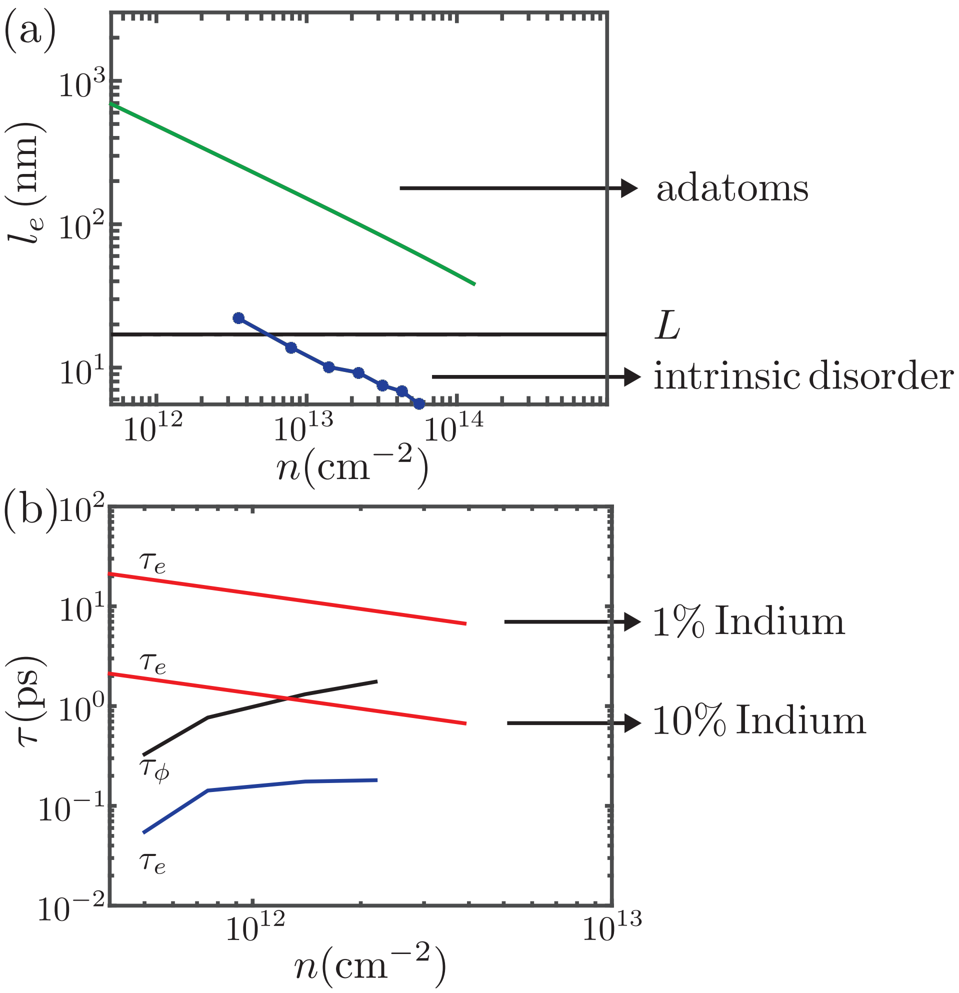

Figure 6.2: (a) Elastic scattering length of graphene with 25% estimation by Drude model (Green), compared to the scattering length of intrinsic disorder source (blue) used in the later MC simulation to ensure the diffusiveness. The black line is the system length in simulation L. (b) Elastic scattering time of graphene with randomly distributed 1% and 10% Tl atoms. The coherence and elastic time are extracted from the experiment[16]. In both simulation and experiment, we can see that the disorder from adatoms is much weaker than other disorder.

them for simplicity in our analytical calculations below. In the following sections, we instead explore how the higher-order Rashba-like SOC's modify magnetotransport in graphene.

6.3 Scattering rates and conductivties

Two major sources of disorder on adaotm-decorated graphene experiments are background disorder $\mathcal{H}_{\mathrm{d}is}$ and adatoms $\delta\mathcal{H}_{\mathbf{R}}$, which are assumed to be uncorrelated with each other. Background disorder enhances both intra- and inter-valley scatterings, and so do adatoms particularly if randomly distributed. However, we should be more careful in treating different types of scattering process within $\delta\mathcal{H}_{\mathbf{R}}$, since they are from the same adatom and thus highly correlated with each other. In this section, we will derive the scattering times and conductivities for adatom-decorated graphene with and without background disorder $\mathcal{H}_{\mathrm{d}is}$. Then we show that the correlation between different scattering process within adatoms is negligible in some specific situations.

After averaging over disorder, the propagation of an electron on adatom-doped graphene can be described by retarded and advanced Green's functions $\bar{G}^{r/a}$,

$$\left[E - \mathcal{H}_{g,0} - \Sigma^{r/a} \pm i\eta\right] \bar{G}^{r/a} = \mathbb{I}. \tag{6.17}$$

Pristine graphene, without any disorder, is described by $\mathcal{H}_{g,0} = -i\hbar v_F \left(\partial_x \sigma^x \tau^z + \partial_y \sigma^y\right)$, and all the scattering processes caused by either intrinsic disorder or adatoms are encoded in the self-energy $\Sigma^{r/a}$. We firstly consider graphene with weak adatom potential $\delta\mathcal{H}_{\mathbf{R}}$ only and expand $\bar{G}$ around the bare Green's funciton G_0 to the leading order in $(\delta\mathcal{H})^2$,

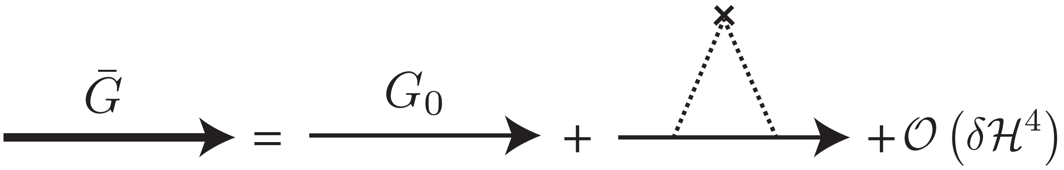

with the leading order correction of self energy Σ_0,

$$\Sigma_0^{r,a}(\mathbf{k}, \omega) = \int \frac{d^2\mathbf{k}'}{(2\pi)^2} \langle \delta\mathcal{H}(\mathbf{k}, \mathbf{k}') G_0^{r,a}(\mathbf{k}', \omega) \delta\mathcal{H}(\mathbf{k}', \mathbf{k}) \rangle. \tag{6.18}$$

Here $\langle \cdots \rangle$ represents averaging over disorder realizations. Since an adatom scatterer contains multiple scattering types, the self-energy matrix has non-zero off-diagonal elements reflecting the high correlation properties between different scattering types. Therefore, the conventional Matthiessen rule for total scattering is no longer applicable, and we also need to re-define the average scattering time of an electron. Now we will derive the average scattering time for both $d-$ and $p-$orbital adatoms.

d-orbital adatoms

We consider pristine graphene with randomly distributed $d-$orbital adatoms with coverage n_I, and derive the scattering time matrix $\tau = -\frac{\hbar}{2\mathrm{Im}\Sigma^R}$ from the leading order self-energy Σ_0. Due to the high correlation, τ is a non-diagonal matrix with eigenvalues

$$\tau_+ = \frac{\hbar}{\Gamma_a - \Gamma_c}, \qquad \tau_0 = \frac{\hbar}{\Gamma_a}, \qquad \tau_- = \frac{\hbar}{\Gamma_a + \Gamma_c}, \tag{6.19}$$

where

$$\begin{aligned} \Gamma_a &= \pi \nu n_I A_{\hexagon}(V_0^2 + \lambda_{\mathrm{KM}}^2 + 2\lambda_{\mathrm{R}}^2 + V_{\mathrm{i}}^2 + \lambda_{\mathrm{i}}^2), \\ \Gamma_c &= 2\pi \nu n_I A_{\hexagon}\lambda_{\mathrm{R}}(V_0 + \lambda_{\mathrm{KM}}). \end{aligned} \tag{6.20}$$

There is no unique life time for correlated disorder, and three of the scattering times together determine the transport properties, e.g. conductivity and magneto-conductance. The self-energy components Γ_a describes the self-energy contribution from uncorrelated part, while Γ_c reflects the correlation between different types of disorder within $\delta\mathcal{H}$. Density of states per valley per spin at Fermi energy ϵ_F is $\nu(\epsilon_F) = \frac{\epsilon_F}{2\pi\hbar^2 v_F^2}$. If different scattering types induced by adatoms are uncorrelated, then Γ_c will vanish and three life times are identical $\tau_\pm = \tau_0$ which is simply the addition of scattering rate for each scattering type. If we further include the background disorder $\mathcal{H}_{\mathrm{d}is}$ in the system, the corresponding scattering times are the same as Eq. (6.19), except that $\Gamma_a \longrightarrow \Gamma_a + \Gamma_{\mathrm{b}g}$ where $\Gamma_{\mathrm{b}g}$ denotes the imaginary self-energy resulted by background disorder.

The classical diagonal conductivity $\sigma_{xx}(\omega)$ for a system of volume Ω at zero temperature is given by Kubo-Greenwood formula,

$$\sigma_{xx} = \frac{\hbar}{\pi\Omega}\mathrm{ReTr}\,[j_x G^r j_x G^a] \tag{6.21}$$

where $j_x = -e v_F \tau^z \sigma^x$ is the current operator. After disorder averaging, the leading three scattering mechanisms are Drude-Boltzmann(bare), diffuson, and Cooperon scattering (which corresponding to the maximally crossed diagram),

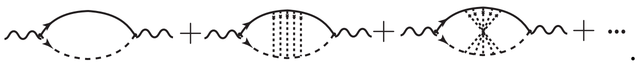

The former two describe classical conductivity and the last one shows the quantum interference correction which we will discuss in the next section. By plugging the Green's function in Eq. (6.17) with the approximated self energy in Eq. (6.18) into the first diagram, we derive the bare conductivity

$$\sigma_0(\omega) = e^2\nu(\epsilon_F)v_F^2\left(\frac{\hbar}{\Gamma_a + \Gamma_c - i\hbar\omega} + \frac{\hbar}{\Gamma_a - \Gamma_c - i\hbar\omega}\right) \tag{6.22}$$

which can be reduced to

$$\sigma_0(\omega = 0) = e^2\nu(\epsilon_F)v_F^2(\tau_+ + \tau_-) \tag{6.23}$$

for DC conductivity. By comparing to the conventional Drude conductivity for Dirac fermion, we identify the "elastic scattering rate" $\tau_e = \frac{\tau_+ + \tau_-}{2}$. Again, we can simply replace Γ_a with $\Gamma_a + \Gamma_{\mathrm{b}g}$ if background disorder is included in the system.

We obtain some insights for this system by considering the following limits: *uncorrelated limit* $\Gamma_a + \Gamma_{\mathrm{b}g} \gg \Gamma_c$ and *correlated limit* $\Gamma_a + \Gamma_{\mathrm{b}g} \ll \Gamma_c$. When the background disorder $\Gamma_{\mathrm{b}g}$ or, more precisely, the uncorrelated part of self-enegy—$\Gamma_a + \Gamma_{\mathrm{b}g}$—is much stronger than adatom disorder, this equation will recover the conventional uncorrelated results,

$$\tau_+ + \tau_- = 2\tau_0 \left(1 + \varepsilon^2 + O(\varepsilon^4)\right) \tag{6.24}$$

with $\varepsilon = \frac{\Gamma_c}{\Gamma_a + \Gamma_{\mathrm{b}g}}$, despite the none-zero correlation between scattering types induced by adatoms. The background disorder $\Gamma_{\mathrm{b}g}$ can be estimated as $\hbar/\tau_e'$ with the elastic scattering τ_e' caused by background disorder. Therefore, in a strong disordered graphene sample, the correlation between different scattering types can be neglected. On the other hand, in a clean system or for some specific adatoms where $\Gamma_a + \Gamma_{\mathrm{b}g} \ll \Gamma_c$, the correlation becomes important and should be considered in the conductivity and MC.

The total classical conductivity includes both the bare conductivity and diffuson scattering, which can be renormalized into the current operator as

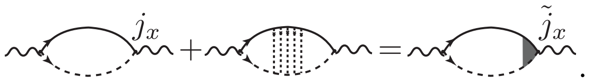

The normalized current operator can be written as

$$\tilde{j}_x = (1 - (\delta\mathcal{H}_I \otimes \delta\mathcal{H}_I)(G^r \otimes G^r))^{-1} j_x, \tag{6.25}$$

and the explicit index contraction and derivation can be found in Appendix. **??**. Though there is no nice general analytical form for this normalized factor, the above equation can be simplified to $\tilde{j}_x \sim 2j_x$ in the *uncorrelated* limit. Therefore, total classical conductivity, i.e. Drude conductivity, of the uncorrelated disorder system is simply, and widely known as

$$\sigma_{\mathrm{cl}} = 4e^2\nu(\epsilon_F)D \tag{6.26}$$

with diffusion coefficient $D = v_F^2\tau_{tr}/2 = v_F^2\tau_e$. If the correlation between different scattering types in adatoms is not negligible, this factor will change accordingly and can be estimated numerically for the given details of adatoms.

p-orbital adatoms

The same derivation applies to p-orbital adatoms as well, with the corresponding self-energy, up to first order in momentum,determined by

$$\begin{aligned}\Gamma_a =& \pi \nu n_I \left[V_0^2 + V_{\mathrm{i}}^2 + \lambda_{\mathrm{i}}^2 + \lambda_{\mathrm{KM}}^2 + \mathcal{O}(k_F^2)\right] A_{\hexagon} \\ \Gamma_b =& 2\pi \nu n_I k_F a \lambda_{\mathrm{R}}^{(1)} \left[V_0 - V_i\right]\end{aligned} \tag{6.27}$$

and other correlation-related Γs listed in the Appendix. **??**. The inclusion of background disorder, again, only modifies Γ_a to be $\Gamma_a + \Gamma_{bg}$. The corresponding bare conductivity reads

$$\begin{aligned}\sigma_0(\omega) =& e^2 \nu(\epsilon_F) v_F^2 \times \\ & \left(\frac{\hbar}{\Gamma_a + \Gamma_b(\epsilon_F) - i\hbar\omega} + \frac{\hbar}{\Gamma_a - \Gamma_b(\epsilon_F) - i\hbar\omega}\right).\end{aligned} \tag{6.28}$$

At Dirac points $k_F = 0$, the correlated term Γ_b vanishes and the system can be viewed as independent.

We estimated that the conductivity is dominated by background disorder in adatom-decorated graphene with In and Tl, based on the parameter values given by Ref. [32]. Figure 6.2(a) and (b) show the comparison of elastic time/length of adatoms and background disorder in both the experiment [16] and our simulations. In Fig. 6.2(a), we estimate the elastic length(green line) with $l_e/v_F = \tau_e \sim \hbar/\Gamma_a$ for 25% In-decorated graphene and find that it is shorter than the system size in all the studied range. This is consistent with our quantum transport simulation results: the system is always ballistic. In the later analysis and simulation, we will include the intrinsic disorder (blue line) to ensure our system diffusive and having strong short range disorder to study the quantum interference effect. In Fig. 6.2(b), the intrinsic disorder (e.g. ripple, charge puddles) in adatom-doped experiments induces strong scattering compared to the low coverage adatoms. Again, τ_e(red lines) are roughly estimated by $\sim \hbar/\Gamma_a$. However, we should clarify that, in an experiment, extra “disorder" might be induced to graphene in the process of doping adatoms, but this type of disorder comes from, for example, charge-puddle or ripple enhancement instead of the adatom itself. To sum up, we find that the correlation property of the disorder induced by adatoms has little effect on conductivity and elastic time, when the background disorder is strong. On the contrary, in the case of clean graphene strongly coupled to heavy adatoms, conductivity may increase due to correlation.

6.4 spin-relaxation rates and magneto-conductance

In this section, we derive all spin relaxation rates arising from both local impurity and homogeneous SOCs, and compute their respective contributions to the magneto-conductance. Here homogeneous SOCs emerge through proximity of the graphene sheet to a homogeneous substrate. Impurity SOCs arise from adatom doping as in Eqs. (6.12), (6.14). From each SOC's contribution individually, we can understand the resulting magneto-conductance behavior qualitatively. However, one should keep in mind that the total quantum conductance is determined by the interplay of all of the scattering and spin-relaxation rates, so the exact quantitative contribution is not always simply the sum of each rates and is case-dependent.

A few assumptions are made in the following evaluation of the quantum corrections to the magneto-conductance.

- Weak magnetic field effect $\omega_c \tau_e \ll 1$
- Weak disorder regime $\lambda_F l_e \gg 1$
- Intrinsic disorder dominating the scatting process.
- Uncorrelated disorder correlators

The first points is the minimum requirement to observe quantum interference by MC and the second one states the limit of the perturbation theory. l_e and τ_e are the elastic scattering length and time; $\omega_c = \sqrt{2}\frac{v_F}{l_B}$ with magnetic length $l_B = \sqrt{\hbar/eB}$ is the cyclotron frequency. The third assumption is justified in the previous subsection. In the following analysis, we will consider other disorder sources which include both strong intra- and inter-valley scattering. The fourth assumption is more subtle. Since all scatterings are induced from the same atom, they are highly correlated and all the cross-term correlators need to be taken into consideration. However, we show that the conductivity contributed from the extra correlators is negligible in In/Tl and Os cases. Therefore, we can still get a general understanding of MC in the adatom-graphene model by treating these scatterings uncorrelated.

Impurity SOC from adatom doping

Consider adatom decorated graphene with the coverage n_a per unit cell. The adatom-induced local SOC effects emerges at low-energy given in Eq. (6.12) and (6.14). We assume these SOCs $\sum_I \delta H_I$ are perturbative effects on top of strongly disordered graphene, $H_g + V_{\mathrm{i}ntrinsic}(r)$, where $V_{intrinsic}(r)$ describe all the possible momentum-independent, uncorrelated, time-reversal symmetric disorder. (For more details of intrinsic disorder, please see the appendix.) With the above setup, We use diagrammatic techniques [12, 24, 25] to calculate the weak-localization correction $\delta\sigma$ to the conductivity for both p and d adatom cases.

The classical conductivity mainly determines the total conductivity, whereas the quantum correction has weaker contribution and can be detected by applying weak magnetic field. For d-orbital doped graphene with strong short range disorder, the magneto-conductivity is

$$
\begin{aligned}
\Delta G &= -\frac{e^2}{2\pi h}\left[F\left(\frac{B}{\mathcal{B}_\phi}\right) - \sum_{j=x,y,z} F\left(\frac{B}{\mathcal{B}_\phi + \mathcal{B}_j}\right)\right] \\
B_\phi &= \frac{\hbar}{4eD}\tau_\phi^{-1}, \quad B_j = \frac{\Gamma_j}{4eD}, \\
F(z) &= \ln z + \psi\left(\tfrac{1}{2} + \tfrac{1}{z}\right).
\end{aligned}
\tag{6.29}
$$

where ψ denotes the digamma function, $D = v^2\tau_e$, and $\Gamma_{sym/asy}$ denotes the Cooperon gap for ($z \longrightarrow -z$) symmetric/anti-symmetric SOCs as

$$
\begin{aligned}
\Gamma_{x,y} &= 2n_I\pi\nu A_{\hexagon}(\lambda_{\mathrm{i}}^2 + \lambda_{\mathrm{KM}}^2 + \lambda_{\mathrm{R}}^2) \\
\Gamma_z &= 2n_I\pi\nu\lambda_{\mathrm{R}}^2 A_{\hexagon}.
\end{aligned}
\tag{6.30}
$$

We can relate the above gap to the spin-relaxation and scattering rates as in the Table. 6.4. When an electron on graphene sheets bumps into an adatom, it experiences the local SOC and may relaxes its original spin orientation. These spin relaxation rates determine quantum conduction correction and are also the key to decipher the presence of SOCs and their strength. Note that the local intrinsic SOC and Rashba SOC do not obey the well-known Elliot-Yafel and D'yakonov-Perel relation which obey different relaxation mechanisms. The corresponding spin relaxation rates are listed in the Table 6.4.

For p-orbital adatom doped graphene, we derive magneto-conductance with

$$
\begin{aligned}
\Gamma_x &= n_I\pi\nu A_{\hexagon}(2\lambda_{\mathrm{i}}^2 + 2\lambda_{\mathrm{KM}}^2 + 14k_F^2a^2(\lambda_{\mathrm{R}}^{(1)})^2) \\
\Gamma_y &= n_I\pi\nu A_{\hexagon}(2\lambda_{\mathrm{i}}^2 + 2\lambda_{\mathrm{KM}}^2 + 10k_F^2a^2(\lambda_{\mathrm{R}}^{(1)})^2) \\
\Gamma_z &= 24n_I\pi\nu A_{\hexagon}(k_Fa\lambda_{\mathrm{R}}^{(1)})^2.
\end{aligned}
\tag{6.31}
$$

Interestingly, we find that the $\Gamma_x \neq \Gamma_y$ in contrast to the general MC equation.

A big concern of the applicability of the above equations is the high correlation between different disorder types, which has some technical difficulties to be solved analytically. To resolve this issue, we numerically calculate the Cooperon gaps Γ for Os and Tl cases and compare with Eq. (6.30) and (6.31). For a 0.1% Os-doped graphene, we can see that the correlation has negligible effect on the Cooperon gap in Fig.6.3, and so is the 0.4% case, above which coverage the Dirac physic no longer applies. The main reasons of negligible correlation's effects are, firstly, the strong intrinsic disorder induces huge Cooperon gaps, which are the sub-leading contribution to MC; also, the strength of correlation between different disorder types are small compared to the ones within the same type (uncorrelated). For more details, we refer the readers to the appendix. For the zeroth-order-in-momentum Hamiltonian of p-orbital graphene-adatom model, the leading contribution to MC of correlated case is the same as the uncorrelated one. If the Fermi energy moves away from Dirac points, the induced Rashba SOCs have some non-trivial correlation with the other disorder types from the adatom. Such correlation is also negligible since $k_F a \lambda_{\mathrm{R}}^{(1)}$ is extremely small (less than 10% of other adatom's parameters, with carrier density up to $n = 5 \times 10^{13} cm^{-2}$).

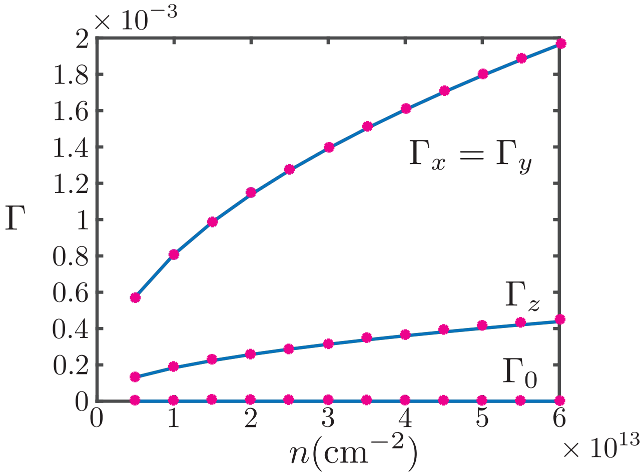

Figure 6.3: The value of Cooperon gaps $\Gamma_{0,x,y,z}$ for correlated (red dotted line) and uncorrelated types of disorder (blue solid line) for Os-doped graphene with coverage 1%.

Homogeneous SOC: substrate

Here we consider proximity induced phenomena or periodically functionalized structure. SOCs induced from periodically structures are homogeneous and thus undergo different spin relaxation process than the local adatom case. These SOCs may be induced to any graphene samples on a substrate which breaks different symmetries. In the work of Denis Kochan *e*t al. [21] who have constructed low energy effective model for structures with global point group symmetries D_{6h}, D_{3d} , D_{3h}, C_{6v}, and C_{3v} that represent, for example, pristine graphene, graphene mini-ripple, planar boron nitride, graphene on a substrate, and free standing graphone,respectively. By reducing symmetry step by step, they find the emergence of certain spin-orbit couplings by specific point group symmetries. Based on their work, we will further derive the spin-relaxation rates for these SOCs and briefly discussed how to measure them.

(i) Pristine graphene D_{6h}. The only SOC which respects the full symmetry of pristine graphene is intrinsic SOC-$\lambda_i \tau^z \sigma^z s^z$. Though the intrinsic SOC is homogeneous, it still contributes to Γ_{sym} through other static disorder, such as $u\mathbb{I}$ with the rate τ_i^{-1} following the Elliot-Yafet mechanism

$$\tau_i^{-1} = \frac{\lambda_i^2}{\epsilon_F^2} \tau_e^{-1} \tag{6.32}$$

where Fermi energy is ϵ_F, gap size is Δ, and momentum relaxation rate is τ_e^{-1}. Interesting the intrinsic SOC rate is larger around the Dirac points and thus one can possibly see the Unitary behavior around the gap through MC, $\Gamma_{x,y} = \frac{\hbar}{\tau_i}$ and $\Gamma_z = 0$, given that the system is still diffusive.

Spin-independent relaxation rates	
decoherence rate τ_φ^{-1}	intra-valley scattering rate τ_*^{-1}
elastic scattering rate $\tau_0^{-1} = \tau_*^{-1} + \tau_{\text{inter}}^{-1}$	inter-valley scattering rate τ_{inter}^{-1}
Spin relaxation rates (impurity effect)	
$\lambda_{\text{KM}} A_{\hexagon} \tau^z \sigma^z s^z$	$\tau_{\text{K}M}^{-1} = n_a \lambda_{\text{KM}}^2 \pi \nu A_{\hexagon}$
$\lambda_i A_{\hexagon} \tau^y \sigma^y s^z$	$\tau_i^{-1} = n_a \lambda_i^2 \pi \nu A_{\hexagon}$
$\lambda_{\text{R}} A_{\hexagon} (\tau_z \sigma^x s^y - \sigma^y s^x)$	$\tau_R^{-1} = 2 n_a \lambda_{\text{R}}^2 \pi \nu A_{\hexagon}$
$\lambda_{\text{R}}^{(1)}(\ldots)$	$\tau_{R^{(1)}}^{-1} = 14 n_a (\lambda_{\text{R}}^{(1)} k a)^2 \pi \nu A_{\hexagon}$
ν is the density of state per spin, per valley.	
Spin relaxation rates (homogeneous effect)	
$\lambda_i \tau^z \sigma^z s^z$	$\tau_i^{-1} = \frac{\lambda_i^2}{\epsilon_F^2} \frac{1}{\tau_0}$
$\lambda_{\text{PIA}} \sigma^0 (k_x s^y - k_y s^x)$	$\tau_{\text{PIA}}^{-1} = 2 \frac{k^2 (\lambda_{\text{PIA}})^2}{\hbar^2} \tau_0$
$\lambda_{\text{VZ}} \tau^z s^z$	$\tau_{\text{VZ}}^{-1} = 2 \frac{\lambda_R^2}{\hbar^2} \tau_0$
$\lambda_R (\tau_z \sigma^x s^y + \sigma^y s^x)$	$\tau_R^{-1} = 2 \frac{\lambda_R^2}{\hbar^2} \tau_0$

(ii) Rippling structure D_{3d}. Structures, like graphane, silicene, and graphene miniripple, break the mirror symmetries respected $x, y, z = 0$ plane but preserve time-reversal $\mathcal{T}$ and inversion $\mathcal{I}$ symmetries. In the structure, one expects to obtain the presence of λ_I and a *momentum-dependent* Rashba SOC $\lambda_{\text{PIA}}\sigma^0(k_x s^y - k_y s^x)$ where PIA is shorthand for the"pseudospin inversion asymmetry". (Note that there is no terminological consensus.) Its SOC relaxation rate

$$\tau_{\text{PIA}}^{-1} = 2\frac{k^2(\lambda_{\text{PIA}})^2}{\hbar^2}\tau_e. \tag{6.33}$$

is dominated by the D'yakonov-Perel scattering process. Due to spin-asymmetry and momentum dependence, the Cooperon gap is $\Gamma_{x,y} = \frac{\hbar}{\tau_{\text{PIA}}}$ and $\Gamma_z = \frac{2\hbar}{\tau_{\text{PIA}}}$ and thus one would expect to see an increasing change of MC to negative value (WAL) away from Dirac point.

(iii) Sublattice inversion asymmetry D_{3h}. Materials like planar boron nitride, aluminum nitride, or any other planar system with two nonequivalent interpenetrating triangular lattices A and B would lead to not only the mass gap σ^z but also the valley-Zeeman SOC [33] $\lambda_{\text{VZ}}\tau^z s^z$. Though it is spin-symmetric, its spin relaxation rate follows D'yakonov-Perel mechanism as

$$\tau_{\text{VZ}}^{-1} = 2\frac{\lambda_R^2}{\hbar^2}\tau_e. \tag{6.34}$$

In a MC measurement of graphene with valley-Zeeman SOC, one would expect to see the suppressed WL with the inverse dependence of τ_e with Cooperon gaps $\Gamma_{x,y} = \frac{\hbar}{\tau_{\text{VZ}}}$ and $\Gamma_z = 0$.

(iv) Transverse electric field C_{6v}. By applying external field or depositing graphene on a substrate, one would break the $z \to -z$ mirror symmetry and induce Rashba SOC (and PIA SOC for higher order contribution). Rashba SOC obeys D'yakonov-Perel mechanism

$$\tau_R^{-1} = 2\frac{\lambda_R^2}{\hbar^2}\tau_e \tag{6.35}$$

which has been measured in many quantum transport experiments. The corresponding Cooperon gaps are $\Gamma_{x,y} = \frac{\hbar}{\tau_R}$ and $\Gamma_z = \frac{2\hbar}{\tau_R}$ and MC shows WAL.

Generally, most materials or layered graphene-based structures include more than one type of SOC due to limited symmetries. However, the net Cooperon gaps may

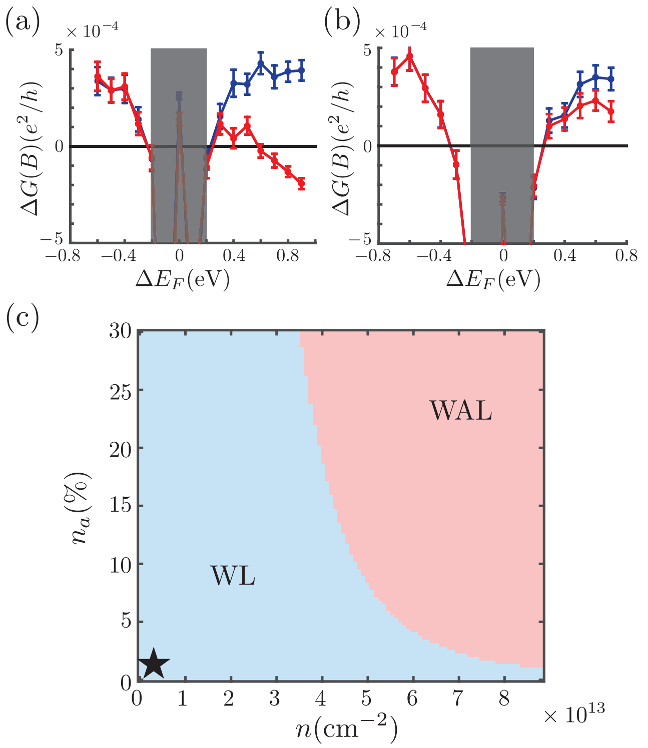

Figure 6.4: MAGNETO-CONDUCTANCE $\Delta G(B) = G(B) - G(B = 0)$ and Fermi energy respect to the shifted Dirac point $E_F - E_{\mathrm{DP}}$ for (a) 20% and (b) 1% Tl-doped graphene sheet. The blue curves describe Tl *w*ithout SOC and the red curves describe Tl *w*ith SOC. The simulated system information: system size $(w, L) =$ $(49, 17)$nm, short range disorder (besides adatom) $\langle V(x)V(x + r)\rangle = K_0 \frac{(\hbar v_F)^2}{2\pi\xi^2} e^{-\frac{r^2}{2\xi^2}}$ with $(K_0, \xi) = (0.1, 0.5a)$, and Tl adatoms parameters extracted from DFT [32] $t = 2.82$eV; $\delta\mu = 0.5$eV; $\epsilon_0 = 2.5eV$, $\epsilon_1 = 1.8eV$; $t_0 = 2eV$, $t_1 = 0.95eV$; and $\Lambda_{so} = \Lambda_{so}^{'} = 0.31eV$. The disorder class diagram respect to carrier density n and coverage n_a in an experiment.The experiment information: $\tau_\phi(l_\phi)$ is taken from the experimental paper [16]. The star is a guide for eyes about the range of previous adatom doped graphene experiments..

not be simply the sum of contribution from different SOCs, because the potential correlation between different types of SOCs. In the hope of diagnosing the nature of each SOC and its strength, one may need to combine the theoretical symmetry analysis, first principle simulation, and proper designed MC experiments/schemes.

6.5 Graphene doped with In and Tl

As mentioned in Sec. 6.2, adatoms with p orbitals such as In and Tl modify the low energy physics by inducing large intrinsic spin-orbit coupling, however, with the absence of Rashba SOC at Dirac points. Given the aforementioned difficulties of measuring intrinsic SOC, we propose a way to measure the SOC indirectly: the idea is to look for signatures of the SOCs induced at the next order in momentum (Eq. 6.14) which has a clear WAL signatures in MC away from Dirac points.

Firstly, we simulate transport measurements of a Tl-doped graphene sheet and measure the change in the magneto-conductance. With 20% Tl in Fig.6.4(a), we observe a sign change in the magneto-conductance which indicates a transition from WL (positive) to WAL (negative) by increasing the electron doping concentration. If we remove the SOC in Tl, the conductance will decrease, but $\Delta G(B)$ is still positive (WL). Therefore, such a transition suggests that the SOC is successfully induced on graphene. Note that the transition only occurs on the electron side which is also where the In bands lie. On the contrary, the spin relaxation for low enough n_a may be too weak to have an appreciable influence on the quantum interference; therefore, we will only see a mild change but not a transition to negative $\Delta G(B)$ as shown in Fig.6.4(b).

To quantitatively describe such transition, we calculated the disorder class by using the MC Eq.6.31 at infinitesimal amount of magnetic field. Combining with existing experimental data (τ_ϕ from Ref.[16]), we found that the graphene-Tl model turns from WL to WAL at high carrier density and high coverage as shown in the Fig.6.4(c); the transition happens roughly at

$$\frac{\hbar}{\tau_\phi} \sim 10\Gamma_z = 240 n_a \pi \nu A_{\hexagon} (\lambda_{\mathrm{R}}^{(1)} k a)^2 \tag{6.36}$$

which is a result of competition among decoherence rate, carrier density concentration, adatom's SOC strength, and adatom coverage. Therefore, one can arrive WAL by not only increasing carrier density and adatom coverage, but also using p-orbital adatom with stronger SOC (such as Tl) and making the sample with long coherent length. In the previous In-doped graphene experiments, the coverage $n_a \sim 0.25\%$ and the carrier density $n \sim 1-5\times 10^{12}\mathrm{cm}^{-2}$, as shown as the star sign in Fig.6.4(c), are too low to drive the graphene to WAL. Also, In has only $1/3$ of the SOC strength of Os, so it requires both stronger SOC rates and longer coherence time to observe WAL. This result provides a potential explanation for the absence of WAL signature in the previous experiments and plots a road map to look for it.

6.6 Graphene doped with Os

As mentioned in the introduction, Os-doped graphene can hold quantum spin Hall phase through two completely different mechanism. In the lower panel of Fig. 6.5

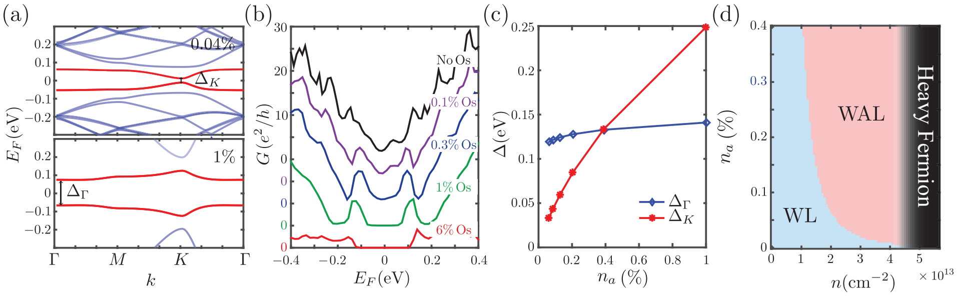

Figure 6.5: (a) The band diagrams of graphene doped with 0.04% (upper panel) and 1% (lower panel). The gap at Γ is Δ_Γ and the one at K is Δ_K. Tight-binding model - $(\epsilon_0, \epsilon_1, \epsilon_2, t_0, t_1, t_2, \Lambda_1, \Lambda_2, \delta_{01}, \delta_{12}) = (-1.5, -0.5, -1.4, 1.5, 1.5, 1.5, 0.2, 0.1, 0.2\sqrt{2}, 0.1\sqrt{2})$. (b) The transport simulation of a graphene nanotube doped with various Os coverage. System information: $(w, L) = (49, 17)$ nm. (c) The competition of Δ_Γ and Δ_K. By increasing the coverage, the dominant gap changes from Δ_K to Δ_Γ at 0.4%. (d) The disorder class diagram for Os. The grey area means the Fermi energy lies in the d-orbital flat banks.

(a), with a few percentage of Os coverage, the $l = \pm 1$ orbitals of Os form two bands across the Dirac point and lead to a large topological gap $\sim 0.2eV$, called“Γ *gap* Δ_Γ". On the other hand, if the coupling between graphene and the adatoms is too weak or if the adatoms have extremely dilute coverage, the low energy spectrum of adatom doped graphene remains Dirac-like as shown in the upper panel of Fig. 6.5(a) and has a smaller but still topological gap at the high symmetry point K, named as “K *gap* Δ_K". This gap is governed by Dirac physics and thus the gate voltage may be shifted if excessive charges are doped into graphene. These two types of gaps are formed by different mechanisms and there is a crossover at 0.4% in Fig. 6.5 (c). In addition, our simulation results as shown in figure 6.5(b) also suggest that the topological gap sustains with random distributed Os.

The Δ_K and Δ_Γ regimes are both topological and smoothly connected but many of their physics properties are different. Firstly, the Dirac point will shift toward electron side in the Δ_Γ phase since the Os is a hole-dopant. On the other hand, we don't need to worry about the relation of charge transfer and shift of gate voltage in this case since since all the excessive will gather around Osmium because of 5d flat bands. Note that the DP doesn't shift in Fig 6.5 because we don't consider the excessive holes doping in the simulation, but it should be there and is confirmed by experiments. Furthermore, the low physics in Δ_Γ regime is not no longer Dirac physics, but is mainly dominated by the d-band of Os hybridized with a little

p_z orbital from carbons. Therefore, the MC prediction Eq. (6.30) is no longer applicable. Anyway, though there is no appropriate MC equation to describe this regime yet, we still expect to see WAL around the band gap since these d-bands have strong SOC which is split by the crystal field, including the broken $z \to -z$ inversion symmetry.

The MC of Os is easier to detect than the p-orbital case since Rashba SOC is not canceled out and the adatoms bands are much closer to the Dirac points. As shown in Fig 6.5(d), one can observe the WAL at relatively lower n_a and n, given the same coherence rates as in Tl-doped case. Note that even though Rashba SOC is not canceled out at the Dirac points for Os-doped graphene, we may still not be able to observe WAL because the SOC rate at low energy may be too small, compared to the coherence rate, to play a role in quantum interference. Therefore, to observe WAL, one still needs to go on higher carrier density and keep a clean, coherent sample.

BIBLIOGRAPHY

[1] Tsuneya Ando, Takeshi Nakanishi, and Riichiro Saito. Berry's phase and absence of back scattering in carbon nanotubes. *Journal of the Physical Society of Japan*, 67(8):2857–2862, 1998. doi: 10.1143/JPSJ.67.2857.

[2] C. Ataca, E. Aktürk, S. Ciraci, and H. Ustunel. High-capacity hydrogen storage by metallized graphene. *Applied Physics Letters*, 93(4):043123, 2008. doi: 10.1063/1.2963976.

[3] J. Balakrishnan, G. K. W. Koon, M. Jaiswal, A. H. C. Neto, and B. Colossal Ozyilmaz. enhancement of spin-orbit coupling in weakly hydrogenated graphene. *Nat. Phys.*, 9:284–287, Mar 2013. doi: doi:10.1038/nphys2576.

[4] J. C. Boettger and S. B. Trickey. First-principles calculation of the spin-orbit splitting in graphene. *Phys. Rev. B*, 75:121402, Mar 2007. doi: 10.1103/PhysRevB.75.121402. URL `https://link.aps.org/doi/10.1103/PhysRevB.75.121402`.

[5] A. H. Castro Neto and F. Guinea. Impurity-induced spin-orbit coupling in graphene. *Phys. Rev. Lett.*, 103:026804, Jul 2009. doi: 10.1103/PhysRevLett.103.026804. URL `http://link.aps.org/doi/10.1103/PhysRevLett.103.026804`.

[6] Kevin T. Chan, J. B. Neaton, and Marvin L. Cohen. First-principles study of metal adatom adsorption on graphene. *Phys. Rev. B*, 77:235430, Jun 2008. doi: 10.1103/PhysRevB.77.235430. URL `https://link.aps.org/doi/10.1103/PhysRevB.77.235430`.

[7] U. Chandni, Erik A. Henriksen, and J. P. Eisenstein. Transport in indium-decorated graphene. *Phys. Rev. B*, 91:245402, Jun 2015. doi: 10.1103/PhysRevB.91.245402. URL `http://link.aps.org/doi/10.1103/PhysRevB.91.245402`.

[8] Jun Ding, Zhenhua Qiao, Wanxiang Feng, Yugui Yao, and Qian Niu. Engineering quantum anomalous/valley hall states in graphene via metal-atom adsorption: An *ab-initio* study. *Phys. Rev. B*, 84:195444, Nov 2011. doi: 10.1103/PhysRevB.84.195444. URL `http://link.aps.org/doi/10.1103/PhysRevB.84.195444`.

[9] F. J. dos Santos, D. A. Bahamon, R. B. Muniz, K. McKenna, E. V. Castro, J. Lischner, and A. Ferreira. The impact of complex adatom-induced interactions on quantum spin hall phases. *ArXiv e-prints*, December 2017.

[10] Aires Ferreira, Tatiana G. Rappoport, Miguel A. Cazalilla, and A. H. Castro Neto. Extrinsic spin hall effect induced by resonant skew scattering in

graphene. *Phys. Rev. Lett.*, 112:066601, Feb 2014. doi: 10.1103/PhysRevLett.112.066601. URL `http://link.aps.org/doi/10.1103/PhysRevLett.112.066601`.

[11] M. Gmitra, S. Konschuh, C. Ertler, C. Ambrosch-Draxl, and J. Fabian. Band-structure topologies of graphene: Spin-orbit coupling effects from first principles. *Phys. Rev. B*, 80:235431, Dec 2009. doi: 10.1103/PhysRevB.80.235431. URL `https://link.aps.org/doi/10.1103/PhysRevB.80.235431`.

[12] Shinobu Hikami, Anatoly I. Larkin, and Yosuke Nagaoka. Spin-orbit interaction and magnetoresistance in the two dimensional random system. *Progress of Theoretical Physics*, 63(2):707–710, 1980. doi: 10.1143/PTP.63.707.

[13] X. Hong, S.-H. Cheng, C. Herding, and J. Zhu. Colossal negative magnetoresistance in dilute fluorinated graphene. *Phys. Rev. B*, 83:085410, Feb 2011. doi: 10.1103/PhysRevB.83.085410. URL `http://link.aps.org/doi/10.1103/PhysRevB.83.085410`.

[14] Jun Hu, Jason Alicea, Ruqian Wu, and Marcel Franz. Giant topological insulator gap in graphene with 5*d* adatoms. *Phys. Rev. Lett.*, 109:266801, Dec 2012. doi: 10.1103/PhysRevLett.109.266801. URL `http://link.aps.org/doi/10.1103/PhysRevLett.109.266801`.

[15] K.-I. Imura, Y. Kuramoto, and K. Nomura. Anti-localization of graphene under the substrate electric field. *EPL (Europhysics Letters)*, 89(1):17009, 2010. URL `http://stacks.iop.org/0295-5075/89/i=1/a=17009`.

[16] Zhenzhao Jia, Baoming Yan, Jingjing Niu, Qi Han, Rui Zhu, Dapeng Yu, and Xiaosong Wu. Transport study of graphene adsorbed with indium adatoms. *Phys. Rev. B*, 91:085411, Feb 2015. doi: 10.1103/PhysRevB.91.085411. URL `https://link.aps.org/doi/10.1103/PhysRevB.91.085411`.

[17] Hua Jiang, Zhenhua Qiao, Haiwen Liu, Junren Shi, and Qian Niu. Stabilizing topological phases in graphene via random adsorption. *Phys. Rev. Lett.*, 109:116803, Sep 2012. doi: 10.1103/PhysRevLett.109.116803. URL `https://link.aps.org/doi/10.1103/PhysRevLett.109.116803`.

[18] Kyung-Hwan Jin and Seung-Hoon Jhi. Proximity-induced giant spin-orbit interaction in epitaxial graphene on a topological insulator. *Phys. Rev. B*, 87:075442, Feb 2013. doi: 10.1103/PhysRevB.87.075442. URL `http://link.aps.org/doi/10.1103/PhysRevB.87.075442`.

[19] C. L. Kane and E. J. Mele. Quantum spin hall effect in graphene. *Phys. Rev. Lett.*, 95:226801, Nov 2005. doi: 10.1103/PhysRevLett.95.226801.

[20] A. A. Kaverzin and B. J. van Wees. Electron transport nonlocality in monolayer graphene modified with hydrogen silsesquioxane polymerization. *Phys. Rev. B*, 91:165412, Apr 2015. doi: 10.1103/PhysRevB.91.165412. URL `http://link.aps.org/doi/10.1103/PhysRevB.91.165412`.

[21] Denis Kochan, Susanne Irmer, and Jaroslav Fabian. Model spin-orbit coupling hamiltonians for graphene systems. *Phys. Rev. B*, 95:165415, Apr 2017. doi: 10.1103/PhysRevB.95.165415.

[22] Xiaojie Liu, C. Z. Wang, M. Hupalo, Y. X. Yao, M. C. Tringides, W. C. Lu, and K. M. Ho. Adsorption and growth morphology of rare-earth metals on graphene studied by ab initio calculations and scanning tunneling microscopy. *Phys. Rev. B*, 82:245408, Dec 2010. doi: 10.1103/PhysRevB.82.245408.

[23] Dongwei Ma, Zhongyao Li, and Zhongqin Yang. *Carbon*, 50(1):297 – 305, 2012. ISSN 0008-6223. doi: http://dx.doi.org/10.1016/j.carbon.2011.08.055. URL `http://www.sciencedirect.com/science/article/pii/S0008622311007020`.

[24] E. McCann, K. Kechedzhi, Vladimir I. Fal'ko, H. Suzuura, T. Ando, and B. L. Altshuler. Weak-localization magnetoresistance and valley symmetry in graphene. *Phys. Rev. Lett.*, 97:146805, Oct 2006. doi: 10.1103/PhysRevLett.97.146805. URL `http://link.aps.org/doi/10.1103/PhysRevLett.97.146805`.

[25] Edward McCann and Vladimir I. Fal'ko. $z \to -z$ symmetry of spin-orbit coupling and weak localization in graphene. *Phys. Rev. Lett.*, 108:166606, Apr 2012. doi: 10.1103/PhysRevLett.108.166606. URL `http://link.aps.org/doi/10.1103/PhysRevLett.108.166606`.

[26] Hongki Min, J. E. Hill, N. A. Sinitsyn, B. R. Sahu, Leonard Kleinman, and A. H. MacDonald. Intrinsic and rashba spin-orbit interactions in graphene sheets. *Phys. Rev. B*, 74:165310, Oct 2006. doi: 10.1103/PhysRevB.74.165310. URL `http://link.aps.org/doi/10.1103/PhysRevB.74.165310`.

[27] Alexandre Pachoud, Aires Ferreira, B. Özyilmaz, and A. H. Castro Neto. Scattering theory of spin-orbit active adatoms on graphene. *Phys. Rev. B*, 90:035444, Jul 2014. doi: 10.1103/PhysRevB.90.035444. URL `https://link.aps.org/doi/10.1103/PhysRevB.90.035444`.

[28] Zhenhua Qiao, Shengyuan A. Yang, Wanxiang Feng, Wang-Kong Tse, Jun Ding, Yugui Yao, Jian Wang, and Qian Niu. Quantum anomalous hall effect in graphene from rashba and exchange effects. *Phys. Rev. B*, 82:161414, Oct 2010. doi: 10.1103/PhysRevB.82.161414. URL `http://link.aps.org/doi/10.1103/PhysRevB.82.161414`.

[29] Filipe J. Ribeiro, J. B. Neaton, Steven G. Louie, and Marvin L. Cohen. Mechanism for bias-assisted indium mass transport on carbon nanotube surfaces. *Phys. Rev. B*, 72:075302, Aug 2005. doi: 10.1103/PhysRevB.72.075302. URL `https://link.aps.org/doi/10.1103/PhysRevB.72.075302`.

[30] H. Sevinçli, M. Topsakal, E. Durgun, and S. Ciraci. Electronic and magnetic properties of $3d$ transition-metal atom adsorbed graphene and graphene nanoribbons. *Phys. Rev. B*, 77:195434, May 2008. doi: 10.1103/PhysRevB.77.195434.

[31] F. V. Tikhonenko, D. W. Horsell, R. V. Gorbachev, and A. K. Savchenko. Weak localization in graphene flakes. *Phys. Rev. Lett.*, 100:056802, Feb 2008. doi: 10.1103/PhysRevLett.100.056802.

[32] Conan Weeks, Jun Hu, Jason Alicea, Marcel Franz, and Ruqian Wu. Engineering a robust quantum spin hall state in graphene via adatom deposition. *Phys. Rev. X*, 1:021001, Oct 2011. doi: 10.1103/PhysRevX.1.021001. URL `http://link.aps.org/doi/10.1103/PhysRevX.1.021001`.

[33] Bowen Yang, Min-Feng Tu, Jeongwoo Kim, Yong Wu, Hui Wang, Jason Alicea, Ruqian Wu, Marc Bockrath, and Jing Shi. Tunable spin–orbit coupling and symmetry-protected edge states in graphene/ws 2. *2D Materials*, 3 (3):031012, 2016. URL `http://stacks.iop.org/2053-1583/3/i=3/a=031012`.

[34] Bowen Yang, Mark Lohmann, David Barroso, Ingrid Liao, Zhisheng Lin, Yawen Liu, Ludwig Bartels, Kenji Watanabe, Takashi Taniguchi, and Jing Shi. Strong electron-hole symmetric rashba spin-orbit coupling in graphene/monolayer transition metal dichalcogenide heterostructures. *Phys. Rev. B*, 96:041409, Jul 2017. doi: 10.1103/PhysRevB.96.041409. URL `https://link.aps.org/doi/10.1103/PhysRevB.96.041409`.

[35] Yingping Yang, Shifei Qi, and Xiaohong Xu. High-temperature quantum spin hall insulator in compensated n-p codoped graphene. *Journal of Physics D: Applied Physics*, 49(7):075004, 2016. URL `http://stacks.iop.org/0022-3727/49/i=7/a=075004`.

[36] Yugui Yao, Fei Ye, Xiao-Liang Qi, Shou-Cheng Zhang, and Zhong Fang. Spin-orbit gap of graphene: First-principles calculations. *Phys. Rev. B*, 75: 041401, Jan 2007. doi: 10.1103/PhysRevB.75.041401. URL `http://link.aps.org/doi/10.1103/PhysRevB.75.041401`.

[37] Hongbin Zhang, Cesar Lazo, Stefan Blügel, Stefan Heinze, and Yuriy Mokrousov. Electrically tunable quantum anomalous hall effect in graphene decorated by $5d$ transition-metal adatoms. *Phys. Rev. Lett.*, 108:056802, Feb 2012. doi: 10.1103/PhysRevLett.108.056802. URL `https://link.aps.org/doi/10.1103/PhysRevLett.108.056802`.

[38] Yuanbo Zhang, Yan-Wen Tan, Horst L. Stormer, and Philip Kim. Experimental observation of the quantum hall effect and berry's phase in graphene. *Nature*, 438:201–204, 2005. doi: 10.1038/nature04235.

Chapter 7

CONCLUSION

In this thesis, we studied two types of structures, graphene with WS_2 and adatom-doped graphene. In the first structure, we have demonstrated a dramatic and tunable enhancement of Rashba SOC in graphene by coupling to WS2. In the high carrier-density region, we determined the Rashba coupling strength by analyzing the low-field MC. First-principles calculations indicate that the induced SOC originates from the band hybridization between graphene π orbitals and tungsten states. The combination of Rashba and a theoretically predicted valley-Zeeman SOC creates novel edge states that are interesting to pursue further by engineering heterostructures with different substrates as well as improving the device mobilities. In addition, we show that Rashba SOC induced by substrate proximity can be tuned with a transverse electric field; this method could be applied to magnetic insulating substrates to enhance both the exchange field and SOC needed to reveal the quantum anomalous Hall effect.

In the adatom-doped graphene, we provided a rationale for the missing SOC signatures, particularly in the recent adatom-doped graphene experiment. By using diagrammatic techniques and a Landauer-Buttiker transport simulation, we found that the induced spin-orbit couplings from $p-$orbital adatoms can contribute to magneto-conductance differently from conventional intrinsic and Rasbha spin-orbit couplings. Moreover, we showed that the WAL - the SOC signature - appears away from the Dirac points unlike conventional Rashba SOC with which WAL appears in all range ("at all momenta" instead of "in all range"?). For $d-$orbital adatoms (particularly Os), we investigated the gap-changing mechanisms and discussed their SOC signatures under various coverages, chemical potentials, and disorder types.

The search of 2D TIs is still an ongoing mission which needs more collaboration among experimentalists, numericists, and theorists. We have established a roadmap for studying magneto-transport experiments by using simulation tools, and found that the induced SOCs may have different spin-relaxation mechanisms and SOC rates depending on the origin of the SOCs. Building on this work, one could continue seeking more possibilities by combining different materials and pushing the limit of current experimental techniques in the hope of finding the next superstar material!

Chapter 8

APPENDIX

8.1 Mean Free Path Calculation for Intra-Valley Scattering

Disorder Potential on Graphene Lattice

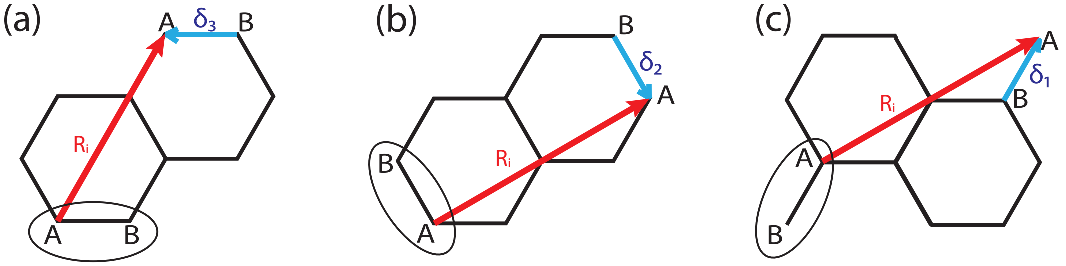

Consider a graphene sample with gaussian correlation disorder. The effective Hamiltonian close to Dirac point is $H = \sigma \cdot \mathbf{p} + V$. The disorder landscape V is discrete and can be described as following,

$$V = \sum_{R_i} V^A(R_i) c_A^\dagger(R_i) c_A(R_i) + V^B(R_i) c_B^\dagger(R_i) c_B(R_i) \tag{8.1}$$

where $R_i (= n_1 \vec{a}_1 + n_2 \vec{a}_2)$ is a lattice vector. We want the correlation between $V^{A(B)}$ also satisfying Gussian correlation as Eq. 4.15 so that the matrix version of disorder potential is

$$\begin{aligned} \langle V(\vec{R}_i) V(\vec{R}_i + \vec{r}) \rangle &= \langle \begin{pmatrix} V^A(\vec{R}_i) V^A(\vec{R}_i + \vec{r}) & V^A(\vec{R}_i) V^B(\vec{R}_i + \vec{r}) \\ V^B(\vec{R}_i) V^A(\vec{R}_i + \vec{r}) & V^B(\vec{R}_i) V^B(\vec{R}_i + \vec{r}) \end{pmatrix} \rangle \\ &= K_0 \frac{(\hbar v_F)^2}{2\pi \xi^2} \begin{pmatrix} \exp(-r^2/2\xi^2) & \exp(-(\vec{r} - \vec{r}_{AB})^2/2\xi^2) \\ \exp(-(\vec{r} + \vec{r}_{AB})^2/2\xi^2) & \exp(-r^2/2\xi^2) \end{pmatrix} \end{aligned} \tag{8.2}$$

where $\vec{r}_{AB} = \vec{r}_A - \vec{r}_B$ which is depending on the choice of unit cell, shown in the above figure. We can also do the Fourier transform on the left-hand side and obtain,

$$\langle V(\vec{R}_i) V(\vec{R}_i + \vec{r}) \rangle = A \int \frac{d^2k}{(2\pi)^2} e^{-ikx} \begin{pmatrix} V^A(k) V^A(-k) & V^A(k) V^B(-k) \\ V^B(k) V^A(-k) & V^B(k) V^B(-k) \end{pmatrix} \tag{8.3}$$

By comparing the above two equations, we can get $V(k)V(-k)$ by Fourier transformation,

$$\begin{cases} V^A(k)V^A(-k) = (\hbar v_F)^2 \frac{K_0}{A} \exp(-k^2\xi^2/2) \\ V^A(k)V^B(-k) = (\hbar v_F)^2 \frac{K_0}{A} \exp(-k^2\xi^2/2) \exp(i\vec{k} \cdot \vec{r}_{AB}) \\ V^B(k)V^A(-k) = (\hbar v_F)^2 \frac{K_0}{A} \exp(-k^2\xi^2/2) \exp(-i\vec{k} \cdot \vec{r}_{AB}) \\ V^B(k)V^B(-k) = (\hbar v_F)^2 \frac{K_0}{A} \exp(-k^2\xi^2/2) \end{cases} \tag{8.4}$$

From the above relation, we can reasonable guess the form of $V(K)$

$$\begin{pmatrix} V^A(k) \\ V^B(k) \end{pmatrix} = \hbar v_F \sqrt{\frac{K_0}{A}} e^{-k^2\xi^2/4} \begin{pmatrix} 1 \\ e^{-i\vec{k}\cdot\vec{r}_{AB}} \end{pmatrix} e^{i\alpha(k)}$$

where $\alpha(k)$ is the random phase and $\alpha(-k) = -\alpha(k)$. The proper physics explanation of $V^{A(B)}(k)$ is the scattering strength for the scattering happening at A(B) sites. Since we will calculate the scattering matrix $\langle f|V_{q=k'-k}|i\rangle$, we want the basis and fourier transformation of V and wave function are consistent. Consider the first unit cell choice(a), we apply a gauge transformation $c_k^B \longrightarrow c_k^B e^{i\mathbf{k}\cdot\delta 3}$ in the low energy Hamiltonian, Eq. (8.6), so that the potential would be modified as

$$\begin{pmatrix} V^A(k) \\ V^B(k) \end{pmatrix} = \hbar v_F \sqrt{\frac{K_0}{A}} e^{-k^2\xi^2/4} \begin{pmatrix} 1 \\ 1 \end{pmatrix} e^{i\alpha(k)} \tag{8.5}$$

The above equation holds if we choose other unit cell, because the phase will be absorbed into the gauge transformation. The only difference in these three cases are that the momentum of the wave function will differ by $2\pi/3$ angle and it will not make differences in scattering rates.

Wavefunction of electrons in Graphene

After applying the gauge $c_k^B \longrightarrow c_k^B e^{i\mathbf{k}\cdot\delta 3}$ as in the disorder potential, the low energy Hamiltonian can be expanded around two Dirac points, K and K'.

$$\begin{aligned} H(\mathbf{k}+\mathbf{K}) &= -\hbar v_F(\sigma_y k_x + \sigma_x k_y) \\ H(\mathbf{k}+\mathbf{K'}) &= -\hbar v_F(\sigma_y k_x - \sigma_x k_y) \end{aligned} \tag{8.6}$$

where $\hbar v_F = 3at/2$, σ is the Pauli matrix for sub-lattice. The wave functions of a Dirac electron around K and K' is a pseudo-spinor (A,B),

$$\begin{aligned}
\phi^{(1)}_{k+K}(\mathbf{r}) &= \frac{1}{\sqrt{2}}\begin{pmatrix} ie^{i\theta_k} \\ 1 \end{pmatrix} e^{i(\mathbf{k}+\mathbf{K})\cdot\mathbf{r}} \\
\phi^{(2)}_{k+K}(\mathbf{r}) &= \frac{1}{\sqrt{2}}\begin{pmatrix} ie^{i\theta_k} \\ -1 \end{pmatrix} e^{i(\mathbf{k}+\mathbf{K})\cdot\mathbf{r}} \\
\phi^{(1)}_{k+K'}(\mathbf{r}) &= \frac{1}{\sqrt{2}}\begin{pmatrix} ie^{-i\theta_k} \\ 1 \end{pmatrix} e^{i(\mathbf{k}+\mathbf{K}')\cdot\mathbf{r}} \\
\phi^{(2)}_{k+K'}(\mathbf{r}) &= \frac{1}{\sqrt{2}}\begin{pmatrix} ie^{-i\theta_k} \\ -1 \end{pmatrix} e^{i(\mathbf{k}+\mathbf{K}')\cdot\mathbf{r}}
\end{aligned}$$

where $\theta = \tan^{-1}(\frac{k_y}{k_x})$ and $\mathbf{k}$ is the momentum defined around Dirac points. $\phi^{(1)}_{K(K')}$ are conduction states and $\phi^{(2)}_{K(K')}$ are valence states.

Transition Rate and Scattering Rate

By Fermi golden rule, the transition probability is

$$\frac{2\pi}{\hbar}|H_{k'k}|^2\delta(E_{k'} - E_k) \tag{8.7}$$

where $H_{k'k}$ is the scattering mechanism which is composed of the scattering in two valleys separately. The scattering probability in valley K is

$$H_{k'k} = \frac{1}{2}\int \frac{d^2\mathbf{q}}{(2\pi)^2}(V^A(\mathbf{q})e^{i(\theta_k-\theta_{k'})} + V^B(\mathbf{q}))\delta^2(\mathbf{k} + \mathbf{q} - \mathbf{k}') \tag{8.8}$$

Since $V^*(\mathbf{q}) = V(-\mathbf{q})$, one can easily derive the scattering probability,

$$\begin{aligned}
|H_{k'k}|^2 &= H^*_{k'k}H_{k'k} \\
&= \frac{1}{2}(\hbar v_F)^2\frac{K_0}{A}\int \frac{d^2\mathbf{q}}{(2\pi)^2}\exp(-q^2\xi^2/2)(1 + \cos(\theta_{k'} - \theta_k))\delta^2(\mathbf{k} + \mathbf{q} - \mathbf{k}')
\end{aligned} \tag{8.9}$$

and the scattering probability in valley K' is the same. Now let us assume that $\theta_k = 0$, $\theta_{k'} = \theta$ and obtain $q = 2k\sin(\theta/2)$ by momentum conservation. Then the above equation can be simplified as

$$|H_{k'k}|^2 = \frac{1}{2}(\hbar v_F)^2\frac{K_0}{A}\exp(-2k^2\xi^2\sin^2(\theta/2))(1 + \cos\theta) \tag{8.10}$$

Now we can estimate the mean free path with this scattering mechanism. By the Bozeman theory, the transport scattering rate $\frac{1}{\tau_t}$ of electron going through potential $V(r)$ is

$$\frac{1}{\tau_t} = NA\int \frac{d^2k}{(2\pi)^2} W_{kk'}(1-\cos(\theta_k-\theta_{k'}))f_{k'}(1-f_k) \tag{8.11}$$

where N is the degeneracy of the system, $W_{kk'}$ is the transition rate from state k to k', and f_k is the Fermi distribution which is $\frac{1}{2}$ if we consider zero temperature. The factor $1-\cos\theta$ accounts for the scattering probability in the transport direction.

The scattering rate of intra-valley is

$$\begin{aligned}
\frac{1}{\tau_t} &= 2\frac{NA}{4}\int \frac{d^2k'}{(2\pi)^2} W_{kk'}(1-\cos\theta) \\
&= \frac{NK_0}{2}\frac{\pi}{\hbar}(\hbar v_F)^2 \int \frac{d^2k'}{(2\pi)^2}\exp(-q^2\xi^2/2)(1+\cos\theta)(1-\cos\theta)\delta(E_{k'}-E_k) \\
&= \frac{\pi K_0}{\hbar}\hbar v_F \int \frac{k'dk'd\theta}{(2\pi)^2}\exp(-q^2\xi^2/2)(1-\cos^2\theta)\delta(k'-k) \\
&= \frac{\pi K_0}{(2\pi)^2\hbar}\hbar v_F \int d\theta k \exp(-q^2\xi^2/2)(1-\cos^2\theta) \\
&= \frac{K_0 v_F k}{2k^2\xi^2}e^{-k^2\xi^2} I_1(k^2\xi^2) \qquad (8.12)
\end{aligned}$$

where $N=2$ for spin degeneracy. Thus, we can easily write down the mean free path and conductivity,

$$\begin{aligned}
l_{MFP} &= v_F\tau_t \\
&= \frac{2k^2\xi^2}{kK_0 I_1(k^2\xi^2)}e^{k^2\xi^2} \qquad (8.13) \\
\sigma &= \frac{e^2v_F^2\tau}{\hbar}\left(\frac{4k_F}{\pi\hbar v_F}\right) \\
&= = \frac{4e^2}{h}\frac{k^2\xi^2}{K_0 I_1(k^2\xi^2)}e^{k^2\xi^2} \qquad (8.14)
\end{aligned}$$

The above result is consistent with the result of Das Sarma's work in 2009.

8.2 Mean Free Path Calculation for Inter-Valley Scattering

At short range disorder, inter-valley scattering becomes more important. The leading order of disorder potential has three terms, for example, the scattering from valley K to K' is

$$V(\mathbf{q}) = V(\mathbf{q}+\eta_1) + V(\mathbf{q}+\eta_2) + V(\mathbf{q}+\eta_3) \tag{8.15}$$

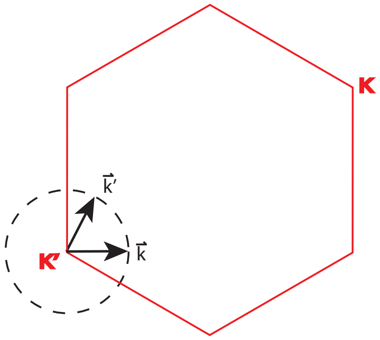

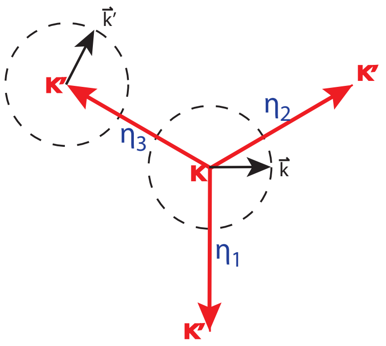

where η are shown in the above figure. For scattering of K' to K, $V(\mathbf{q}) = V(\mathbf{q} - \eta_1) + V(\mathbf{q} - \eta_2) + V(\mathbf{q} - \eta_3)$. The $V = (V^A, V^B)^\top$ as used in intra-valley scattering. Then we employ the wave function in the same basis.

$$\begin{aligned}\phi^{(1)}_{k+K}(\mathbf{r}) &= \frac{1}{\sqrt{2}}\begin{pmatrix} ie^{i\theta_k} \\ 1 \end{pmatrix} e^{i(\mathbf{k}+\mathbf{K})\cdot\mathbf{r}} \\ \phi^{(1)}_{k+K'}(\mathbf{r}) &= \frac{1}{\sqrt{2}}\begin{pmatrix} ie^{-i\theta_k} \\ 1 \end{pmatrix} e^{i(\mathbf{k}+\mathbf{K}')\cdot\mathbf{r}} \end{aligned} \tag{8.16}$$

The wave functions are the eigenstates of the low energy Hamiltonian.

The scattering process from a state k to a state k' include six terms

$$|H_{k'k}|^2 = \sum_{i=1}^{3} |\langle k'@(K+\eta_i)|V_{K'K}|k@K\rangle|^2 + |\langle k'@(K'-\eta_i)|V_{KK'}|k@K'\rangle|^2 \tag{8.17}$$

Let's assume that the $\theta_k = 0$ and $\theta_{k'} = \theta$ and insert Eq. (8.15, 8.16) to Eq. (8.17). After some algebra, one will obtain scattering mechanism

$$\begin{aligned}|\langle k'@(K+\eta_i)|V_{K'K}|k@K\rangle| &= \frac{1}{2}\int \frac{d^2\mathbf{q}}{(2\pi)^2}(V^A(\mathbf{q}+\eta_i)e^{i(\theta_k+\theta_{k'})} + V^B(\mathbf{q}+\eta_i))\delta^2(\mathbf{k}+\mathbf{q}-\mathbf{k}') \\ |\langle k'@(K'-\eta_i)|V_{KK'}|k@K'\rangle| &= \frac{1}{2}\int \frac{d^2\mathbf{q}}{(2\pi)^2}(V^A(\mathbf{q}-\eta_i)e^{i(\theta_k+\theta_{k'})} + V^B(\mathbf{q}-\eta_i))\delta^2(\mathbf{k}+\mathbf{q}-\mathbf{k}')\end{aligned}$$

Let's remove the Delta function for momentum conservation and replace $|q| =$

$2k \sin\theta/2$.

$$
\begin{aligned}
|H_{k'k}|^2 &= H^*_{k'k} H_{k'k} \\
&= \frac{1}{2}(\hbar v_F)^2 \frac{K_0}{A} \sum_i \exp(-(\mathbf{q} + \eta_i)^2 \xi^2/2)(1 + \cos(\theta_{k'} + \theta_k)) \\
&+ \frac{1}{2}(\hbar v_F)^2 \frac{K_0}{A} \sum_i \exp(-(\mathbf{q} - \eta_i)^2 \xi^2/2)(1 + \cos(\theta_{k'} + \theta_k)) \\
&= (\hbar v_F)^2 \frac{K_0}{A} \exp(-(q^2 + \eta^2)\xi^2/2)(1 + \cos\theta) \\
&\quad (\cosh(\xi^2 q_y \eta) + \exp(-\xi^2 q_x \eta \frac{\sqrt{3}}{2}) \cosh(\xi^2 q_y \eta/2) + \exp(\xi^2 q_x \eta \frac{\sqrt{3}}{2}) \cosh(\xi^2 q_y \eta/2)) \\
&= (\hbar v_F)^2 \frac{K_0}{A} \exp(-(q^2 + \eta^2)\xi^2/2)(1 + \cos\theta) \\
&\quad (\cosh(\xi^2 q_y \eta) + 2\cosh(-\xi^2 q_x \eta \frac{\sqrt{3}}{2}) \cosh(\xi^2 q_y \eta/2))
\end{aligned}
$$

where $\eta = |\eta_i|$, $q_x = -2k \sin^2(\theta/2)$ and $q_y = k \sin\theta$.

The transport scattering time will be

$$
\begin{aligned}
\frac{1}{\tau_t} &= \frac{NA}{4} \int \frac{d^2k'}{(2\pi)^2} W_{kk'}(1 - \cos\theta) \\
&= \frac{NK_0\pi}{2\hbar}(\hbar v_F)^2 \int \frac{d^2k'}{(2\pi)^2} \exp(-(q^2 + \eta^2)\xi^2/2)(1 + \cos\theta)(1 - \cos\theta) \\
&\quad (\cosh(\xi^2 q_y \eta) + 2\cosh(-\xi^2 q_x \frac{\sqrt{3}}{2}) \cosh(\xi^2 q_y \eta/2))\delta(E_{k'} - E_k)
\end{aligned}
$$